



Level 2 products and performances for mantle studies with *Swarm*

Alexei Kuvshinov¹, Jakub Velimsky^{1,2}, Pascal Tarits³, Alexey Semenov¹,
Oleg Pankratov⁴, Lars Tøffner-Clausen⁵, Zdenek Martinec^{6,2}, Nils Olsen⁵,
Terence J. Sabaka⁷ and Andrew Jackson¹

¹ETH, Institut für Geophysik, Zürich, Switzerland

²Charles University, Department of Geophysics, Prague, Czech Republic

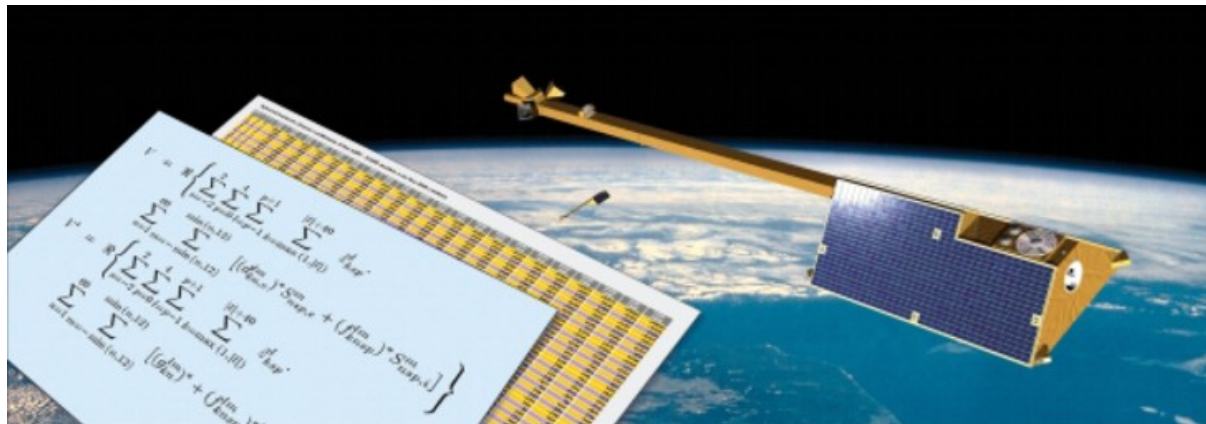
³Universite de Bretagne Occidental, Brest, France

⁴IZMIRAN, Russian Academy of Sciences, Troitsk, Russia

⁵DTU Space, Technical University Denmark, Copenhagen, Denmark

⁶Dublin Institute for Advanced Studies, Geophysics Section, Dublin, Ireland

⁷Geodynamics Branch, NASA GSFC, Greenbelt/MD, USA



Final Report



Swarm Science Study

This page is intentionally left blank



ESA STUDY CONTRACT REPORT			
<p>No ESA Study Contract Report will be accepted unless this sheet is inserted at the beginning of each volume of the Report.</p>			
ESA CONTRACT No 22656/09/NL/FF	SUBJECT Level 2 products and performances for mantle studies with Swarm		CONTRACTOR ETH Zurich
* ESA CR()No 22656	* STAR CODE	No of volumes 1 This is Volume No 1	CONTRACTOR'S REFERENCE
ABSTRACT: <p>This report describes the results of activities performed during the Science Study “Level 2 products and performances for mantle studies with <i>Swarm</i>” (ESTEC Contract No. 22656/09/NL/FF).</p> <p>The objective of this and the previous study “Mapping 3-D mantle conductivity from <i>Swarm</i> constellation data” (ESTEC Contract No. 20944/07/NL/JA) is the development of independent 3-D inversion algorithms and software, with the goal of recovery of the 3-D conductivity distribution in the mantle from <i>Swarm</i> magnetic data. Four approaches have been developed during these studies: The first method is a frequency-domain approach and deals with the 3-D inversion of <i>C</i>-responses. The second method is a time-domain approach that concerns the 3-D inversion of time series of internal spherical harmonic coefficients describing the induced part of the magnetic field. The third and fourth methods are frequency domain approaches that deal with the 3-D inversion of time-spectra of internal coefficients, respectively of <i>Q</i>-responses.</p>			
<p>The work described in this report was done under ESA Contract. Responsibility for the contents resides in the author or organisation that prepared it.</p>			
<p>Names of authors: Alexei Kuvshinov, Jakub Velimsky, Pascal Tarits, Alexey Semenov, Oleg Pankratov, Lars Tøffner-Clausen, Zdenek Martinec, Nils Olsen, Terence J. Sabaka and Andrew Jackson</p>			
** NAME OF ESA STUDY MANAGER Jonas Amneus Roger Haagmans DIRECTORATE: Earth Observation Programmes	** ESA BUDGET HEADING		



This page is intentionally left blank

Contents

1	Introduction	8
1.1	Background and objective	8
1.2	Structure of the report	9
2	Frequency domain C-response inversion	11
2.1	Data preparation	11
2.1.1	List of notations	11
2.1.2	Generation of ultimate ground-based C -responses	12
2.1.3	Generation of realistic ground-based and satellite-based C -responses	12
2.2	Frequency-domain quasi 3-D inversion: methodology and tests	24
2.2.1	Inverse problem formulation	24
2.2.2	Simple quasi 1-D inversion of ultimate ground-based data set	24
2.3	Frequency-domain full 3-D inversion: methodology	29
2.3.1	Inverse problem formulation	29
2.3.2	Choice of the optimization scheme	31
2.3.3	Test of different regularization schemes. 1-D case	35
2.4	Efficient calculation of the gradient of the misfit function	38
2.4.1	Definition of the operators G_{3D}^{ej} , G_{3D}^{eh} , G_{3D}^{eg}	38
2.4.2	Derivatives of the Z:Y C -responses	39
2.4.3	Gradient of the data misfit (Z:Y case)	41
2.4.4	Reciprocity of operator G_{3D}^{ej}	42
2.5	Estimates of CPU time needed to perform a full cycle of 3-D inversion	42
2.6	Forward modeling scheme: integral equation (IE) approach	43
2.6.1	Governing equations	43
2.6.2	Optimization of the IE solution within 3-D inversion	44
2.6.3	Explicit forms for Green's tensor G_{1D}^{eh}	45
2.6.4	Explicit forms for Green's tensors G_{1D}^{eg}	53
2.7	Frequency-domain full 3-D inversion: proof of the concept	54
2.7.1	Derivatives of the Z:H C -responses	54
2.7.2	Gradients of the data misfit (Z:H case)	55
2.7.3	Tests of calculation of Green's tensor G_{1D}^{eh}	55
2.7.4	Test of adjoint scheme to calculate gradient of the data misfit	59
2.7.5	Inputs and outputs of 3-D inversion code	59
2.7.6	Tests of full FD 3-D inversion code	59



3 Time domain internal coefficient inversion	71
3.1 Formulation of the 3-D adjoint problem in time domain	71
3.1.1 Forward problems with Dirichlet, external and mixed boundary conditions	71
3.1.2 Misfit and misfit derivative in the model space	73
3.1.3 Adjoint method	74
3.2 3-D time-domain forward solver	80
3.2.1 Semi-implicit scheme	80
3.2.2 Crank-Nicolson scheme and iterative approach	81
3.2.3 Crank-Nicolson scheme with factorization of full matrix	81
3.3 Checkerboard tests of the inversion	82
3.3.1 Checkerboard model	82
3.3.2 Synthetic excitation model	82
3.3.3 Accuracy of time-integration schemes	83
3.3.4 Conjugate gradient inversion	83
3.4 E2E-based tests of the inversion	88
3.4.1 E2E resistivity model	88
3.4.2 E2E external field model	88
3.4.3 Regularization and LMQN inversion	89
4 Frequency domain internal coefficient inversion	99
4.1 Some general remarks	99
4.2 The numerical model	99
4.2.1 Solution for the normal field	102
4.2.2 Solution for the anomalous field	102
4.2.3 Numerical considerations	104
4.3 Data analysis	105
4.4 Inversion	109
4.4.1 Accounting for the coast effect	110
4.4.2 Calculation of the distortion kernels	111
4.4.3 Results of the 3-D inversion	112
4.5 Conclusion	112
4.6 Appendices	114
4.6.1 Appendix A1: expansion of a vector into generalized spherical harmonics (GSH)	114
4.6.2 Appendix A2: expansion of the Maxwell's equations into GSH	115
4.6.3 Appendix A3: SHE of external and internal coefficients	115
4.6.4 Appendix A4: solution for satellite data	116
5 Frequency-domain Q-responses inversion	117
5.1 Concept	117
5.2 Adjoint approach to calculate data misfit gradients	120
5.3 Inverse problem scheme and its numerical verification	122
6 Preparation of 3-D synthetic data sets	125
6.1 Calculation of induced time series of spherical harmonic expansion coefficients using smooth 3-D mantle conductivity model (idealistic data)	125
6.2 Calculation of induced time series of spherical harmonic expansion coefficients using blocky 3-D mantle conductivity model (realistic data I)	126



6.3	Recovery of magnetospheric and induced time series of spherical harmonic expansion coefficients from realistic <i>Swarm</i> constellation data ((realistic data II))	126
6.3.1	Comprehensive Inversion	128
6.3.2	Computation of “magnetospheric” residuals from recovered model	129
6.3.3	Estimations of magnetospheric and induced fields for various model parametrizations	130
7	Benchmarking of 1-D inversion approaches	139
7.1	1-D inversion of 1-D synthetic data	139
7.2	1-D inversion of idealistic data	140
7.2.1	Frequency domain approach	141
7.2.2	Time domain approach	141
7.3	1-D inversion of realistic data II	143
7.3.1	Frequency domain approach	143
7.3.2	Time domain approach	143
7.4	Summary of 1-D benchmarking inversions	145
8	Benchmarking of 3-D inversion approaches	153
8.1	3-D inversion of idealistic data	153
8.1.1	Frequency domain inversion of internal coefficients	153
8.1.2	Frequency domain inversion of C -responses	155
8.1.3	Time domain inversion of internal coefficients	155
8.2	3-D inversion of realistic data I	155
8.2.1	Frequency domain inversion of internal coefficients	155
8.2.2	Frequency domain inversion of C -responses	160
8.2.3	Time domain inversion of internal coefficients	160
8.3	3-D inversion of realistic data II	160
8.3.1	Frequency domain inversion of internal coefficients	160
8.3.2	Time domain inversion of internal coefficients	160
8.4	Summary of 3-D benchmarking inversions	160
9	Summary of the results and the impact of these results on the proposed Development Plan	168
9.1	Summary of results	168
9.2	Definition of the baseline 1-D inversion method	168
9.3	Definition of two baseline 3-D inversion methods to be studied further	168

Chapter 1

Introduction

This report describes the results of activities performed during the Science Study “Level 2 products and performances for mantle studies with *Swarm*” (ESTEC Contract No. 22656/09/NL/FF). Parts of the report have been derived during the previous Science Study “Mapping 3-D mantle conductivity from *Swarm* constellation data” (ESTEC Contract No. 20944/07/NL/JA) and the present report is partly an update of the final report of that study. Chapters 2 to 4 are (updated) versions of corresponding chapters from the previous study report. In particular, all maps showing conductivities have been updated and harmonized. Chapters 5 to 9 are completely new and report on the findings of the present study.

1.1 Background and objective

The study of lateral variability in physical properties of Earth’s mantle using geophysical methods is a topic of present-day fundamental science. It gives insight into geodynamic processes such as mantle convection, the fate of subducting slabs and the origin of continents. Global seismic tomography provides today a variety of three-dimensional (3-D) mantle velocity models that can be interpreted in terms of cratonic roots, mantle plumes and slab graveyards. The goal of global electromagnetic (EM) induction studies is to identify complementary large-scale spatial variations (3-D structures) in the electrical conductivity of the mantle. This is an important issue since conductivity reflects the connectivity of constituents as fluids, partial melt, and volatiles (all of which may have profound effects on rheology and, ultimately, mantle convection and tectonic activity), while seismology ascertains bulk mechanical properties.

Traditionally, ground-based observatory recordings of the geomagnetic field along with long-period magnetotelluric (MT) measurements have been used to derive regional mantle conductivity profiles (1-D profiles, i.e. conductivity varies only with depth). But global images of lateral variations of mantle conductivity can hardly be obtained at present or in the foreseeable future with the use of ground-based data alone due to the sparse and very irregular distribution of geomagnetic observatories and long-period MT sites. For instance, the three quarters of the globe that are occupied by oceans is almost free of ground geomagnetic observatories.

In contrast to ground-based data, satellite-borne measurements provide an excellent spatio-temporal coverage with high-precision data of uniform quality. Since more and more satellite data are becoming available, and especially with the satellite mission *Swarm*, global images of 3-D mantle heterogeneities come into reach. Moreover, mapping of 3-D electrical conductivity of the Earth’s upper mantle has been identified as one of the scientific objectives of the *Swarm* constellation mission.

The main objective of the work done in the present and previous studies was to develop and validate inversion algorithms and codes to determine 3-D mantle conductivity from *Swarm* constellation

magnetic field observations.

1.2 Structure of the report

Because 3-D induction in a spherical geometry from satellite data was at such a rudimentary stage at the beginning of this study, the main thrust of the project was to produce a methodology for recovering 3-D electrical conductivity variations. As is normal in research, the exact path by which this would be achieved was not entirely clear; many approaches presented themselves as possibilities, but each had pros and cons. Not least amongst the challenges to be met was the question of how to efficiently perform the computations, since the recovery of three-dimensional structure in the Earth naturally leads to very large-scale inverse problems.

Thus it was not foreseen at the beginning of the activities described in this report that so many different approaches would prove fruitful. The net result of the coordinated and yet independent studies, performed by ETH, IZMIRAN, Charles University, Prague (CUP) and Universite de Bretagne Occidental (UBO), are the Chapters 2-5 that make up the major part of this report. In these chapters we document the different approaches that have been developed. Within each approach independent 3-D inversion algorithms and software have been developed. They have been tested in their ability to recover a target structure, from which synthetic data has been calculated.

The first approach is based on a frequency-domain (FD) setting and deals with a 3-D inversion of C -responses (3-D FD C -responses inversion). The results of this activity are summarised in Chapter 2. C -responses depend on measurements of ratios of properties of the magnetic field in the frequency domain, and can be calculated at any point on a grid on the Earth's surface. In this respect the data are rather intuitive, and Chapter 2 shows how this approach works exceptionally well in recovering a target image.

The second approach is based on a time-domain (TD) 3-D setting and deals with a 3-D inversion of time series of internal coefficients, describing the induced part of the magnetic field (3D TD inversion). The results of this activity are summarised in Chapter 3. This approach was not envisaged at the outset to be the focus of studies, indeed it was an entirely optional approach beyond the “core activities” of the original mandate. The ability of team scientists to develop this rather difficult approach has surpassed our wildest expectations. This method lives in spectral (spherical harmonic) space within the physical domain, and in the time domain; as such it is in an entirely “opposite” space to method 1 of Chapter 2. The extent to which these methods are able to recover test structures is extremely gratifying.

The third approach is, like Chapter 2, based on a frequency domain setting but deals with a 3-D inversion of the Fourier spectra of internal spherical harmonic coefficients (in a similar manner to Chapter 3). We refer to this method as FD internal coefficient inversion. The results of this activity are summarised in Chapter 4, and again we see excellent performance.

The fourth approach is also based on a frequency domain setting and presents a theoretical background for 3-D inversion of the so-called Q -responses (see Chapter 5). We refer to this method as FD Q -response inversion.

The attentive reader will have realised that our 4 main chapters cover 3 of the 4 possible combinations of frequency/time and physical space/spherical harmonic wavenumber. The fourth possibility has not been investigated and would be a strange combination of time domain methods at points on a physical grid. Table 1.1 summarises the situation.

An important task of the study activities was the preparation of test data sets for benchmarking the various approaches for mantle conductivity determination. This is described in Chapter 6.

The results of a benchmarking of different 1-D approaches are presented in Chapter 7, obtained using simple synthetic data from a 1-D conductivity distribution, as well as a more realistic data from

Method	Time or Frequency	Physical Space or SH (Wavenumber)	Chapter	Comment
Frequency domain C-response inversion	Frequency	Space	2	Intuitively similar to method of 1-D MT and GDS
Time domain internal coefficient inversion	Time	Wavenumber	3	Time series fitting avoiding Fourier analysis
Frequency domain internal coefficient inversion	Frequency	Wavenumber	4	
Frequency domain Q -response inversion	Frequency	Wavenumber	5	

Table 1.1: Summary of the different methods and their respective chapters in the report. MT and GDS refer to the classic methods of magnetotellurics and geomagnetic deep sounding. SH stands for spherical harmonic.

the 3-D conductivity structure discussed in Chapter 6. All approaches demonstrated their ability to recover the input 1-D mantle conductivity structures; however, there are some expected deviations due to the non-uniqueness of the inverse problem.

Chapter 8 presents the result of a benchmarking of approaches for determination of the 3-D mantle conductivity structure, based on the synthetic data that have been generated as discussed in Chapter 6.

Finally, Chapter 9 summarizes the obtained results and describes possible directions of future study activities.

Chapter 2

Frequency domain C -response inversion

2.1 Data preparation

2.1.1 List of notations

In this section we introduce the notations that we will use through this chapter

- $\omega = 2\pi/T$ is the angular frequency, T is the period of the variation in consideration;
- $\mathbf{r} = (r, \vartheta, \varphi)$ is the position vector, ϑ, φ and r are colatitude, longitude and radial distance from the Earth's center, respectively;
- The time-harmonic dependency is $e^{-i\omega t}$, $i = \sqrt{-1}$;
- μ_0 is the magnetic permeability of free space;
- $\mathbf{B} = \mu_0 \mathbf{H}$, where \mathbf{B} is the magnetic field;
- $\nabla_\tau f$ defines the tangential part of the gradient

$$\nabla_\tau f = \frac{1}{r} \frac{\partial f}{\partial \vartheta} + \frac{1}{r \sin \vartheta} \frac{\partial f}{\partial \varphi} \quad (2.1)$$

- $\nabla_\tau \cdot \mathbf{a}$ defines the tangential part of the divergence

$$\nabla_\tau \cdot \mathbf{a} = \frac{1}{r \sin \vartheta} \left(\frac{\partial (a_\vartheta \sin \vartheta)}{\partial \vartheta} + \frac{\partial a_\varphi}{\partial \varphi} \right); \quad (2.2)$$

- The Z:Y C -response is defined as

$$C(\omega) = -\frac{B_r}{\nabla_\tau \cdot \mathbf{B}}. \quad (2.3)$$

- the Z:H C -response is defined as

$$C(\omega) = -\frac{r \tan \vartheta_d}{2} \frac{B_r}{B_\vartheta}, \quad (2.4)$$

where ϑ_d is geomagnetic colatitude. Eq. (2.3) reduces to (2.4) in the case that the source includes only the first zonal harmonic.

2.1.2 Generation of ultimate ground-based C -responses

2.1.2.1 3-D models under consideration

We consider three conductivity models of the Earth

The first model is a radially-symmetric (1-D) section consisting of a relatively resistive 400 km thick layer of 0.004 S/m, a 300 km thick transition layer of 0.04 S/m, and an inner uniform sphere of 2 S/m.

The second model is a 3-D model that consists of a surface shell of laterally varying conductance and a 1-D conductivity model underneath. The shell conductance (see conductance distribution in the upper panel of Fig. 2.4) is obtained by considering contributions both from sea water and from sediments. The conductance of the sea water is taken from [Manoj et al. \[2006\]](#). Conductance of the sediments (in continental as well as oceanic regions) is based on the global sediment thickness given by map of [Laske and Masters \[1997\]](#). These two models are used for the ocean correction of C -responses when performing a quasi 3-D inversion.

The third model is a 3-D model that incorporates a surface shell and a 1-D model underneath containing a 1 S/m 300 km thick large-scale conductivity anomaly in the upper mantle (see conductivity distribution in the lower panel of Fig. 2.4). This anomaly describes a hypothetical conductor beneath the Pacific Ocean plate. The 3-D model was split in vertical direction into 3 inhomogeneous spherical sublayers of thickness 10 km (surface shell), 150 km and 150 km (deep anomaly), respectively; each spherical sublayer was discretized in horizontal direction in 180×90 cells of size $2^\circ \times 2^\circ$.

2.1.2.2 Calculation of ultimate ground-based C -responses

The forward modelling code described above has been used to obtain C -responses at the surface of the Earth on a uniform 180×90 mesh. The C -responses have been calculated for the 3 conductivity models described in the previous subsection. For this data set the models are excited by an elementary magnetospheric source in the form of a symmetric (in geomagnetic coordinates) magnetospheric ring current. The responses have been calculated for 11 periods between 1.88 days and 60 days, with geometric step size of $\sqrt{2}$. Figs. 2.1-2.3 present the real (left panels) and imaginary (right panels) parts of the C -responses at the three periods: 2.66, 10.66 and 60.33 days. The upper panel of each Figure show C -responses calculated by eq. (2.3) (Z:Y method), while the lower panel show those calculated using the simplified version (Z:H method) of eq. (2.4).

2.1.3 Generation of realistic ground-based and satellite-based C -responses

2.1.3.1 3-D model under consideration

The 3-D conductivity model that we consider consists of an inhomogeneous conducting surface shell, three local conductors of 0.04 S/m at depths from the bottom of that shell down to 400 km, and a deep-seated regional conductor of 1 S/m located between 400 km and 700 km depth. The local and regional conductors are embedded in a radially symmetric section consisting of a relatively resistive 400 km thick layer of 0.004 S/m, a 300 km thick transition layer of 0.04 S/m, and an inner uniform sphere of 2 S/m.

Figure 2.4 shows global maps of these anomalous structures. The top panel presents the adopted surface shell conductance. It approximates the nonuniform distribution of oceans and continents. The conductance of the shell is chosen as realistic as possible and includes contributions from sea water and from sediments. The conductance of the oceans has been derived from the global $5' \times 5'$ NOAA ETOPO map of bathymetry, multiplying the water depth by a mean seawater conductivity of 3.2 S/m. The conductance of the sediments has been derived from the global sediment thickness given by the $1^\circ \times 1^\circ$ map of [Laske and Masters \[1997\]](#) with the use of a heuristic procedure similar to that described in [Everett et al. \[2003\]](#).

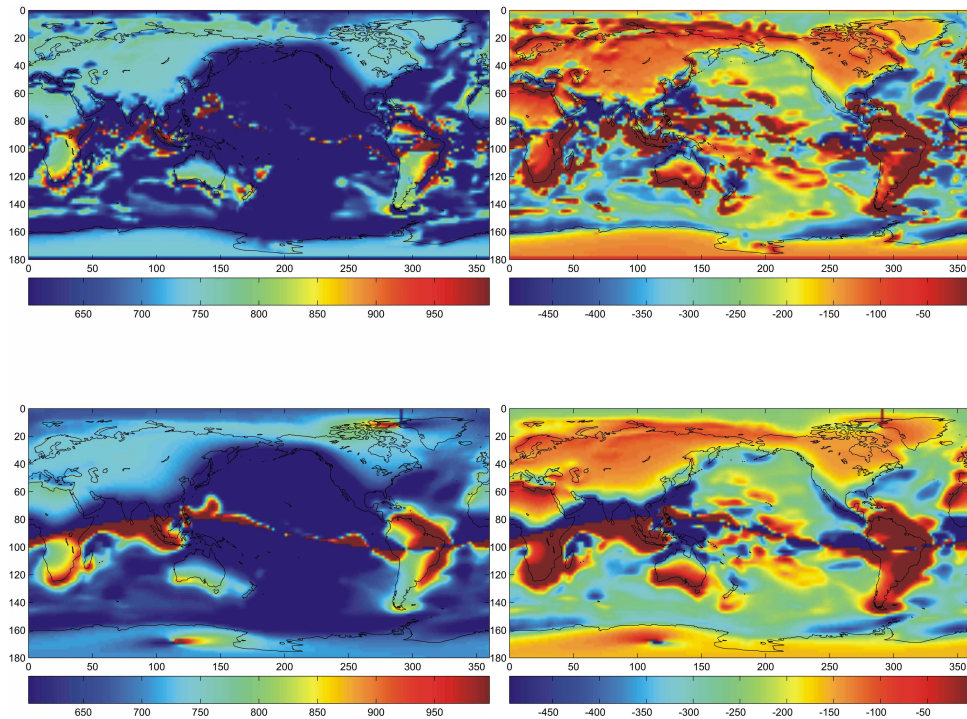


Figure 2.1: Real (left) and imaginary (right) parts of C -responses (in km) from 3-D model at period of 2.66 days, calculated by Z:Y (top) and Z:H (bottom) method.

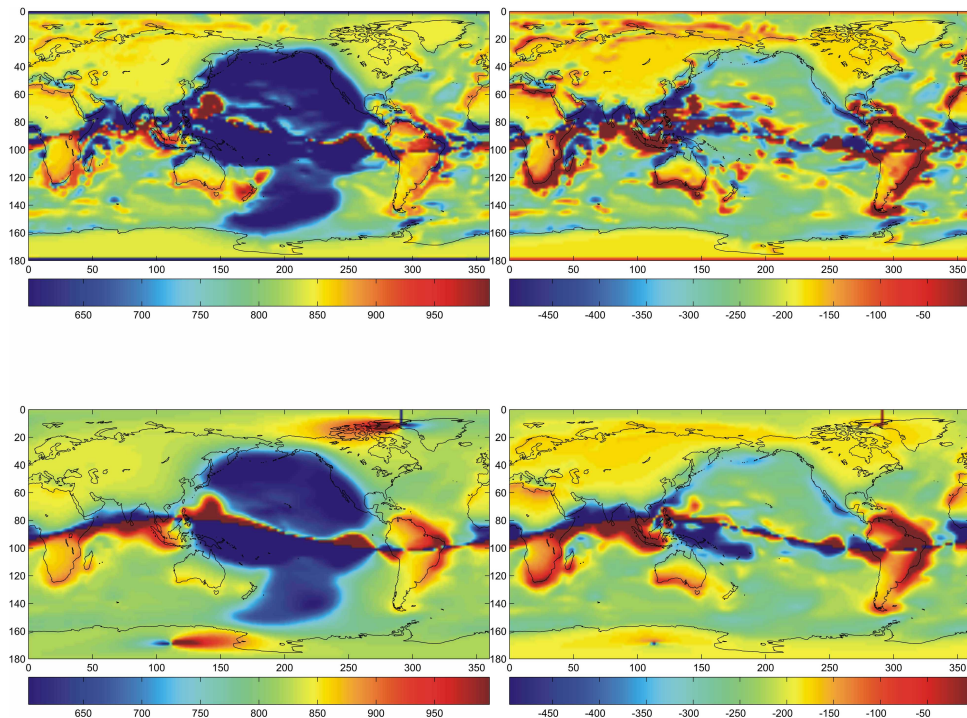


Figure 2.2: Real (left) and imaginary (right) parts of C -responses (in km) from 3-D model at period of 10 days, calculated by the Z:Y (top) and Z:H (bottom) method.

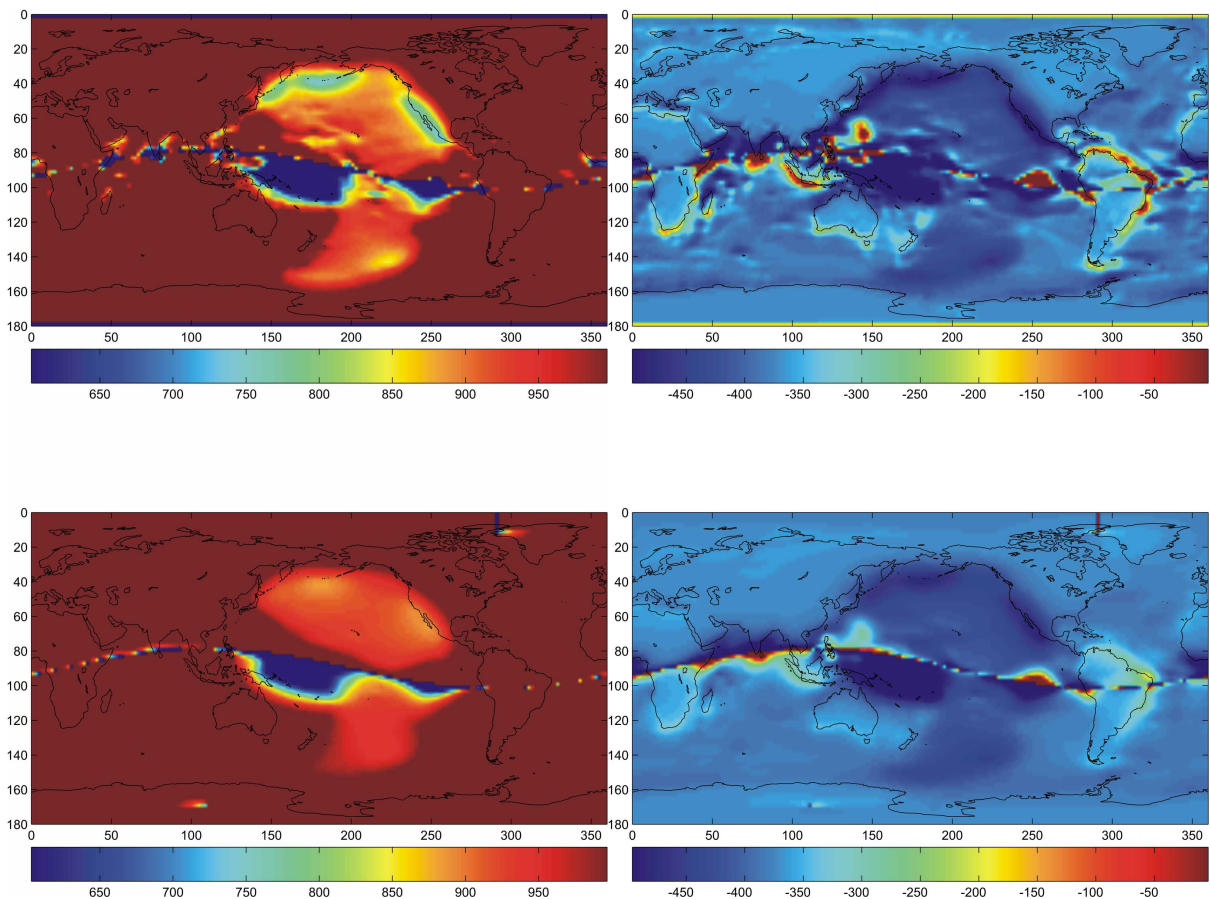


Figure 2.3: Real (left) and imaginary (right) parts of C -responses (in km) from 3-D model at period of 60 days, calculated by $Z:Y$ (top) and $Z:H$ (bottom) method.

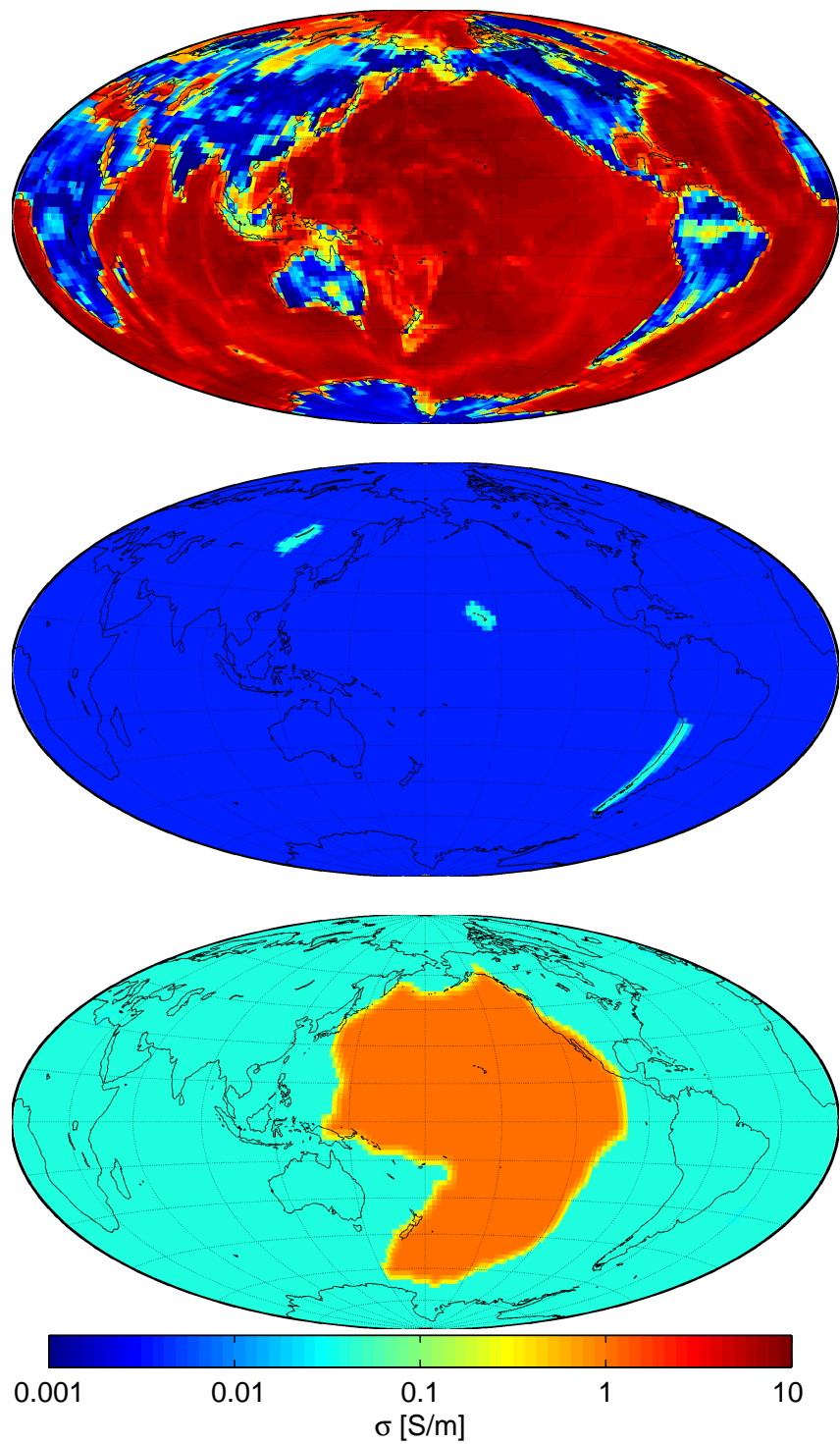


Figure 2.4: Top: Surface shell conductance in units of S. Middle: Conductivity [S/m] at depths from 1 km down to 400 km. Bottom: Conductivity [S/m] at depths from 400 km down to 700 km. The results are presented in logarithmic (with base 10) scale. The range of the colorbar for the conductance is between 1.2 and 4.3. Hereinafter the conductivity distributions will be presented in logarithmic scale.

Two local conductors of horizontal size $600 \times 1200 \text{ km}^2$ describe hypothetic plumes beneath the Baikal and Hawaii [Constable and Heinson, 2004]; the third conductor of size of $600 \times 3000 \text{ km}^2$ represents a hypothetic subduction zone along the western margin of South America. This part of the model is shown in the middle panel of the Figure and was suggested by Steve Constable [2003; private communication]. Finally, the deep-seated large scale structure describing a hypothetic conductor beneath the Pacific Ocean plate is presented in the bottom panel of the Figure. The aim of this model is not to be identical to the “true” world (e.g., we do not claim that there really exists a plume under the Baikal), but to provide a test model for our retrieval algorithm. The model was split in the vertical direction into 4 inhomogeneous spherical sublayers of thickness 1, 150, 250, and 300 km, respectively; each spherical sublayer was discretized in horizontal direction in 180×90 cells of size $2^\circ \times 2^\circ$.

2.1.3.2 Derivation of time series of magnetic field and its spatial derivatives on 2-D grid

To derive these time series we follow the procedure described in [Kuvshinov et al., 2006] and shown in Figure 2.5. Using this scheme we produce time series of magnetic field and its spatial derivatives due to magnetospheric sources at the surface of the Earth for a given 3-D spherical conductivity model of the Earth and for a given time series of hourly mean values of external (inducing) coefficients $q_n^m(t)$ and $s_n^m(t)$ ($n = 1, 2, \dots, N_\varepsilon$, $m = 0, 1, \dots, n$) of the magnetic potential (details of how the inducing coefficients have been derived are given in Olsen et al. [2006]). This procedure follows in general the scheme described in Olsen and Kuvshinov [2004] and Kuvshinov and Olsen [2005b] and consists of the following steps:

1. The time series of the external coefficients $q_n^m(t)$ and $s_n^m(t)$ are Fourier transformed to obtain complex coefficients $\tilde{q}_n^m(\omega)$ and $\tilde{s}_n^m(\omega)$ at a set of frequencies, ω_i , $i = 1, 2, \dots, N_d$, where $N_d = \frac{P}{2\Delta t}$. By performing discrete Fourier transform of a time series of external coefficients on an interval $[0, P]$ we implicitly assume that our time series are represented by a finite trigonometric series. Due to the quasi-regular nature of the magnetospheric signal at a long time scale (in our case $P = 5$ years) we believe that such a representation is accurate enough for our time-domain simulations.
2. EM induction simulations are performed using the above described 3-D model of electrical conductivity in the frequency domain for N_s logarithmically spaced frequencies, ω_j , $j = 1, 2, \dots, N_s$, covering the frequency range from $\omega_1 = \frac{2\pi}{P}$ to $\omega_{N_s} = \frac{2\pi}{2\Delta t}$ (here $\Delta t = 1$ hour). For each frequency the simulations are performed for a set of preselected elementary harmonics, $Y_n^m(\vartheta, \varphi) = P_n^{|m|}(\cos \vartheta) e^{im\varphi}$ of the external field (in our case for all harmonics up to degree $N_\varepsilon = 3$). To simulate the magnetic fields the frequency domain 3-D numerical solution described above is used. Note that there is no need to calculate the fields at all involved frequencies, ω_i , of the inducing field. Due to the smoothed (with respect to frequency) nature of the induced field we calculate the response at a coarse grid of frequencies, ω_j (with 9 frequencies per frequency decade), with subsequent interpolation to all frequencies (see Step 4).
3. For each elementary harmonic, $Y_n^m(\vartheta, \varphi)$ ($n = 1, 2, \dots, N_\varepsilon$, $m = -n, -n+1, \dots, n$) and each frequency, ω_j , a spherical harmonic analysis of the simulated induced part of B_r (from step 2) is performed, resulting in arrays of coefficients of the induced part of the potential, $Q_{nk}^{ml}(\omega_j)$ for all harmonics up to degree N_i (where N_i is determined from the chosen horizontal discretization of the 3-D model. Here $N_i = 45$). $Q_{nk}^{ml}(\omega_j)$ is the field of degree k and order l that is induced by a magnetospheric source, $Y_n^m(\vartheta, \varphi)$, of degree n and order m .
4. The arrays $Q_{nk}^{ml}(\omega_j)$ are spline interpolated from the coarse logarithmically-spaced frequency

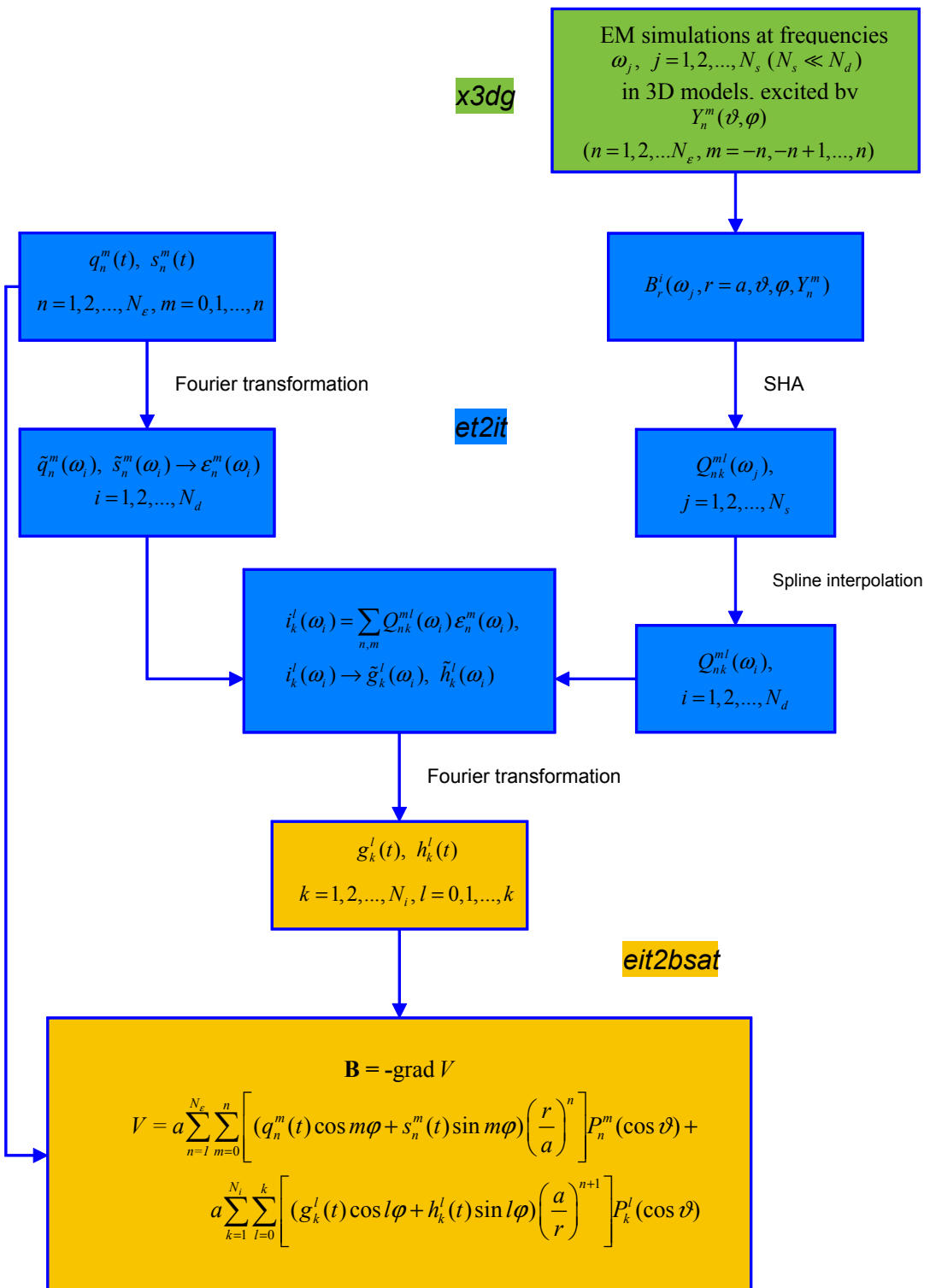


Figure 2.5: Scheme describing the calculation of induced field contributions.

set ω_j to the actual (denser) frequency set ω_i , and the resulting coefficients arrays $\iota_k^l(\omega_i)$ ($k = 1, 2, \dots, N_i$, $l = -k, -k+1, \dots, k$) are calculated as [Olsen, 1999]

$$\iota_k^l(\omega_i) = \sum_{n=1}^{N_\varepsilon} \sum_{m=-n}^n Q_{nk}^{ml}(\omega_i) \varepsilon_n^m(\omega_i), \quad (2.5)$$

where

$$\varepsilon_n^m = \begin{cases} \frac{\tilde{q}_n^m - i\tilde{s}_n^m}{2}, & m > 0 \\ \frac{\tilde{q}_n^{|m|} + i\tilde{s}_n^{|m|}}{2}, & m < 0 \\ \tilde{q}_n^m, & m = 0 \end{cases}$$

This step gives frequency domain coefficients of the induced part of the potential produced by given external coefficients ε_n^m .

5. The complex coefficients $\iota_k^l(\omega_i)$ are transformed to the real coefficients $\tilde{g}_k^l(\omega_i)$ and $\tilde{h}_k^l(\omega_i)$ ($k = 1, 2, \dots, N_i$, $l = 0, 1, \dots, k$) as $\tilde{g}_k^l = \iota_k^{-l} + \iota_k^l$ and $\tilde{h}_k^l = -i(\iota_k^{-l} - \iota_k^l)$ for $l \neq 0$, and $\tilde{g}_k^l = \iota_k^l$ for $l = 0$. Then, the coefficients $\tilde{g}_k^l(\omega)$ and $\tilde{h}_k^l(\omega)$ are Fourier transformed to the time domain, resulting in time series of hourly values of the coefficients $g_k^l(t)$ and $h_k^l(t)$ of the induced part of the potential.
6. Magnetic field $\mathbf{B} = -\nabla V$ at $5^\circ \times 5^\circ$ grid at the Earth's surface is obtained from the scalar magnetic potential V , which is approximated by the spherical harmonic expansion

$$V = a \sum_{n=1}^{N_\varepsilon} \sum_{m=0}^n \left[(q_n^m(t) \cos m\varphi + s_n^m(t) \sin m\varphi) \left(\frac{r}{a} \right)^n \right] P_n^m(\cos \vartheta) + a \sum_{k=1}^{N_i} \sum_{l=0}^k \left[(g_k^l(t) \cos l\varphi + h_k^l(t) \sin l\varphi) \left(\frac{a}{r} \right)^{k+1} \right] P_k^l(\cos \vartheta), \quad (2.6)$$

with $a = 6371.2$ km as the mean Earth's radius.

7. Further we calculate time series of $\nabla_\tau \cdot \mathbf{H}$ using the following equation

$$\begin{aligned} \nabla_\tau \cdot \mathbf{H} = & \frac{1}{r} \sum_{n=1}^{N_\varepsilon} \sum_{m=0}^n \left[n(n+1)(q_n^m(t) \cos m\varphi + s_n^m(t) \sin m\varphi) \left(\frac{r}{a} \right)^{n-1} \right] P_n^m(\cos \vartheta) \\ & + \frac{1}{r} \sum_{k=1}^{N_i} \sum_{l=0}^k \left[k(k+1)(g_k^l(t) \cos l\varphi + h_k^l(t) \sin l\varphi) \left(\frac{a}{r} \right)^{k+2} \right] P_k^l(\cos \vartheta). \end{aligned} \quad (2.7)$$

2.1.3.3 Calculation of realistic ground-based C-responses

Following the notation introduced in the last section, we expand the magnetic potential V in a series of spherical harmonics

$$V = a \operatorname{Re} \left\{ \sum_{n,m} \left(\epsilon_n^m(\omega) \left(\frac{r}{a} \right)^n + \iota_n^m(\omega) \left(\frac{a}{r} \right)^{n+1} \right) P_n^m(\cos \theta) \exp(im\phi) \right\} \quad (2.8)$$



where $\epsilon_n^m = q_n^m - is_n^m$ and $\iota_n^m = g_n^m - ih_n^m$ are complex expansion coefficinets for a given angular frequency ω . The magnetic vertical component at Earth's surface ($r = a$) follows as

$$\begin{aligned} Z(\omega, r = a, \theta, \phi) &= \operatorname{Re} \left\{ \sum_{n,m} (n\epsilon_n^m(\omega) - (n+1)\iota_n^m(\omega)) P_n^m(\cos \theta) \exp(im\phi) \right\} \\ &= \operatorname{Re} \left\{ \sum_{n,m} z_n^m(\omega) P_n^m(\cos \theta) \exp(im\phi) \right\} \end{aligned} \quad (2.9)$$

with $z_n^m = n\epsilon_n^m - (n+1)\iota_n^m$. The horizontal divergence of the magnetic horizontal components follows as

$$\begin{aligned} \nabla_\tau \cdot \mathbf{B}_H = -\nabla_\tau^2 V = \mathcal{Y} &= \operatorname{Re} \left\{ \sum_{n,m} n(n+1) (\epsilon_n^m(\omega) + \iota_n^m(\omega)) P_n^m(\cos \theta) \exp(im\phi) \right\} \\ &= \operatorname{Re} \left\{ \sum_{n,m} y_n^m(\omega) P_n^m(\cos \theta) \exp(im\phi) \right\} \end{aligned} \quad (2.10)$$

with $y_n^m = n(n+1) (\epsilon_n^m + \iota_n^m)$.

From the time series of ϵ_n^m (up to $n = 3$) and ι_n^m (up to $n = 30$) we have calculated times series of z_n^m and y_n^m , from which time series of $Z(\theta, \phi)$ and $\mathcal{Y}(\theta, \phi)$ have been synthesized for points on a regular $5^\circ \times 5^\circ$ in colatitude θ and longitude ϕ consiting of $N_\theta \times (N_\phi - 1) = 37 \times 72 = 2664$ grid points. For the results presented here we only used one year (1998) of data.

For each grid point we then calculated the C -response

$$C(\omega) = \frac{Z(\omega)}{\mathcal{Y}(\omega)} \quad (2.11)$$

using the section-averaging method of [Olsen \[1998a\]](#)) for periods between 1.8 and 80 days.

As an example, Figure 2.6 shows squared coherence coh^2 and obtained responses for a $\theta = 45^\circ, \phi = 0^\circ$. The red curve represents the 1-D response (for $n = 1$) that has been used for calculating the synthetic data.

Maps of the C -response for various periods are shown in Figures 2.7 to 2.9. Grey regions indicate data with $\text{coh}^2 < 0.5$.

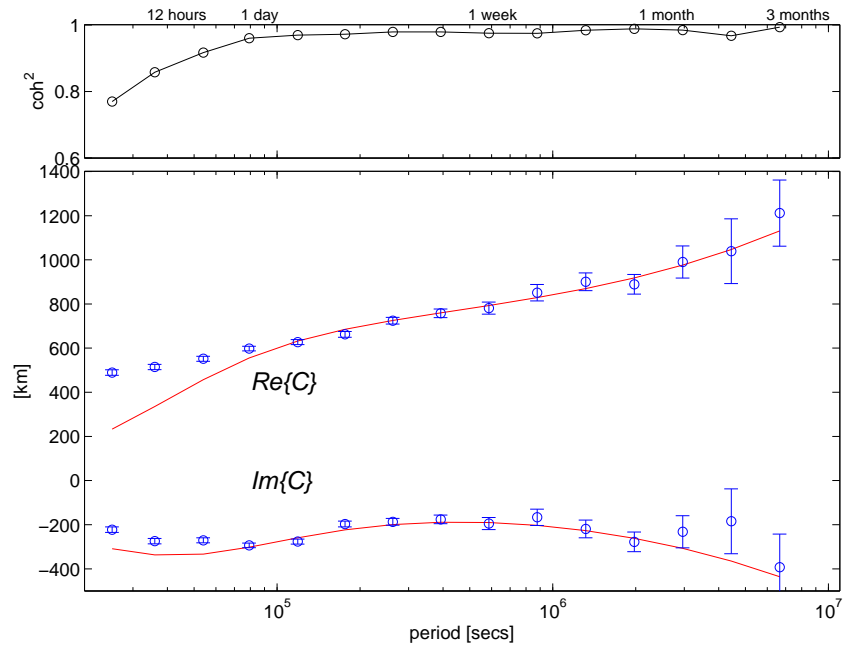


Figure 2.6: Squared coherence and C -response (for $\theta = 45^\circ, \phi = 0^\circ$, determined from one year of time series of ε_n^m and ι_n^m . The red curve represents the 1-D response (for $n = 1$) that has been used for calculating the synthetic data.

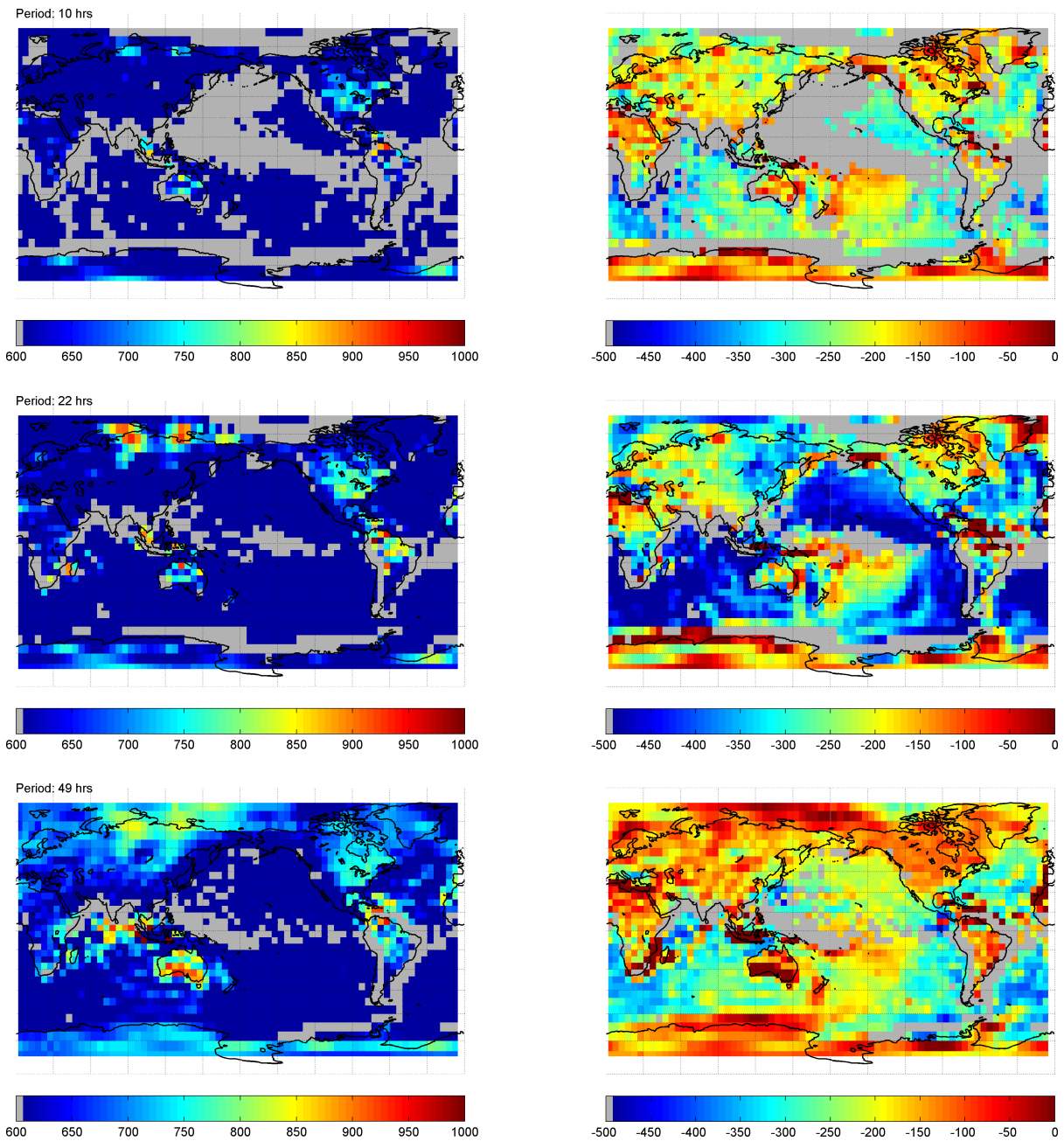


Figure 2.7: Map of real (left) and imaginary (right) part of the C -response (in km), determined from one year of time series of ϵ_n^m and ι_n^m . Regions with $\text{coh}^2 < 0.5$ are shown in grey.

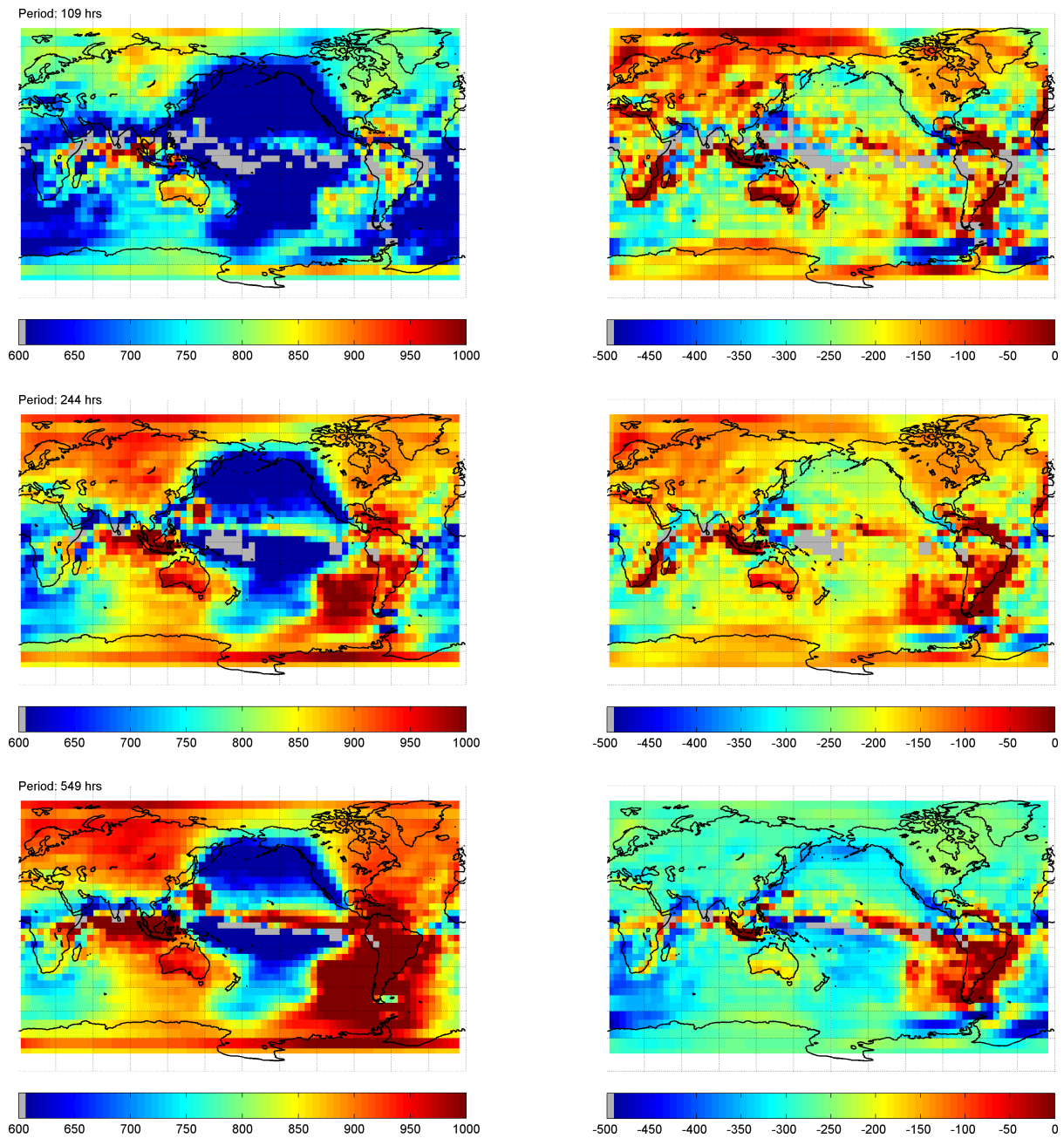


Figure 2.8: Map of real (left) and imaginary (right) part of the C -response (in km), determined from one year of time series of ϵ_n^m and ι_n^m . Regions with $\text{coh}^2 < 0.5$ are shown in grey.

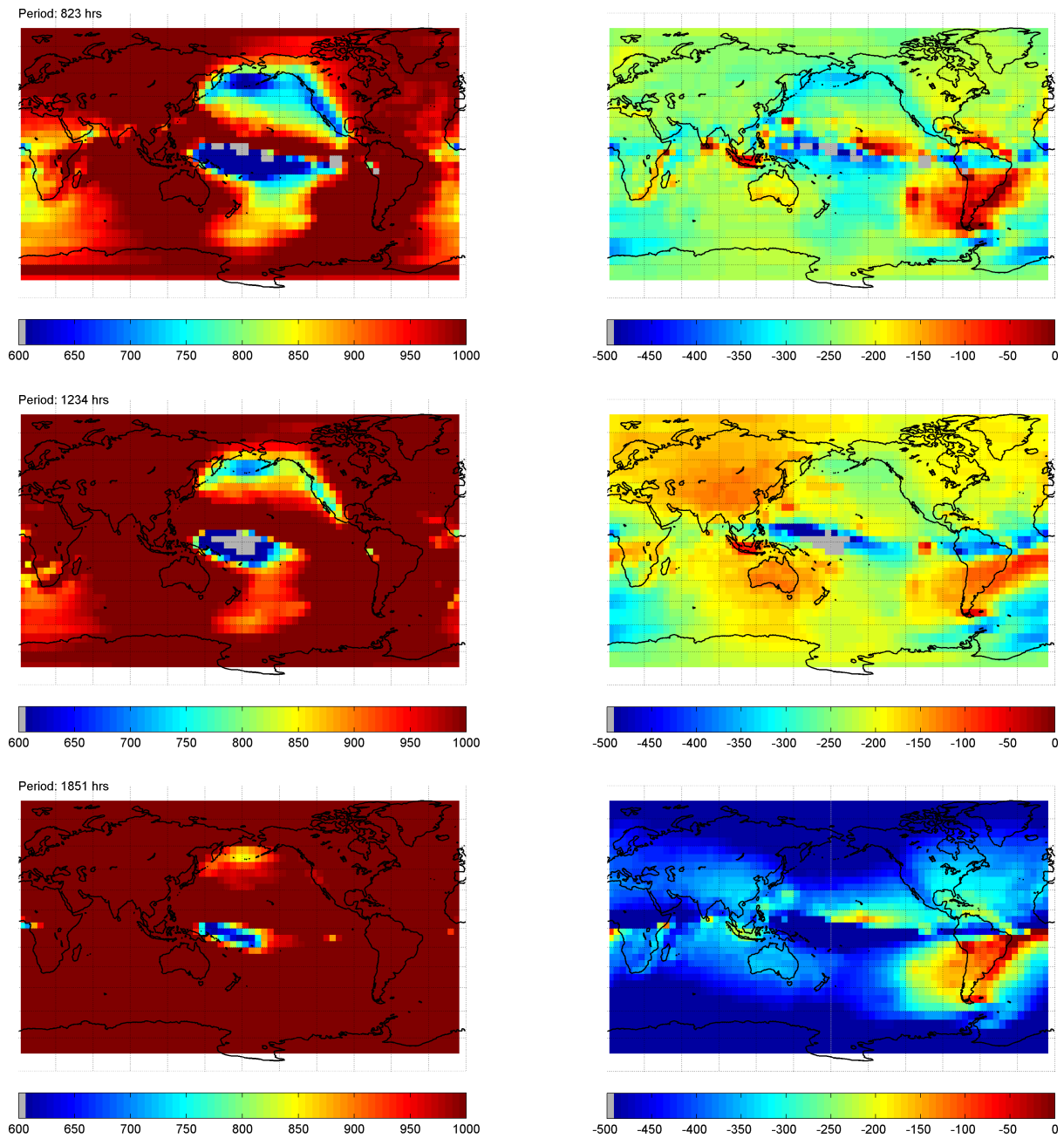


Figure 2.9: Map of real (left) and imaginary (right) part of the C -response (in km), determined from one year of time series of ϵ_n^m and ι_n^m . Regions with $\text{coh}^2 < 0.5$ are shown in grey.

2.1.3.4 Calculation of realistic satellite-based C -responses

We use simulated *Swarm* satellite data of constellation # 4; creation and availability of these data are given in section 2.4 and 2.5 of [Olsen et al. \[2007\]](#).

In following we only use the magnetospheric and secondary, induced, part of the magnetic signal.

For each day of the time span July 1, 1998 (the start of the mission simulation) to December 31, 2002 we estimated the expansion coefficients ϵ_n^m (up to $n = 3$) and ι_n^m (up to n_{\max}) of equation 2.8 using a least-squared approach. The next steps are very similar to those described in the previous subsection 2.1.3.3: From the time series of ϵ_n^m and ι_n^m (which have a sampling rate of 1 day) we calculate time series of z_n^m and y_n^m , and of $Z(\theta, \phi)$ and $\mathcal{Y}(\theta, \phi)$ for points on a regular $5^\circ \times 5^\circ$ in colatitude θ and longitude ϕ consisting of $N_\theta \times (N_\phi - 1) = 37 \times 72 = 2664$ grid points. Finally, the C -response

$$C(\omega) = \frac{Z(\omega)}{\mathcal{Y}(\omega)} \quad (2.12)$$

is estimated using the section-averaging method of [Olsen \[1998a\]](#)) for periods between 3 and 77 days.

We used two different truncation levels for the spherical harmonic expansion of the internal, induced, field: $n_{\max} = 3$ and $n_{\max} = 9$. Maps of the obtained C -response for $n_{\max} = 3$ are shown in Figures 2.10 to 2.11; those for $n_{\max} = 9$ are shown in Figures 2.12 to 2.13.

2.2 Frequency-domain quasi 3-D inversion: methodology and tests

2.2.1 Inverse problem formulation

The quasi 3-D inversion is based on "site-by-site" 1-D inversions with an inter-site smoothing procedure [[Pankratov et al., 2006](#)]. As a result we obtain an initial 3-D conductivity model that will be used as starting (and probably also an a priori) model for the rigorous 3-D inversion. The overall scheme is as follows:

- Site-by-site 1-D inversions (with an excessive number of layers)
- Merging of the layers (at each site) in order to find the boundaries of the "true" section (focusing)
- Constructing a smoothed 3-D (a priori) model on the basis of results of step 1 and 2 (inter-site smoothing)
- Site-by-site 1-D inversions (with the 3-D model from step 3 as an a priori model)

2.2.2 Simple quasi 1-D inversion of ultimate ground-based data set

As a test to investigate whether we can obtain a reasonable image of the 3-D conductivity distribution using a quasi 3-D approach we started with simple "site-by-site" 1-D inversions (without focusing and inter-site smoothing). Another question we wanted to answer is whether we have to correct the C -responses for the ocean effect in the considered period range from 2 days to 2 months during quasi 3-D inversion.

As input data for our inversion we took the ultimate ground-based data set (Z:H C -responses; see details above). Using the quasi-Newton (QN) algorithm of [Byrd et al. \[1995\]](#) we derived spherical 1-D conductivity models beneath each site on a $2^\circ \times 2^\circ$ mesh. The calculation of 1-D responses and its gradients are explained in the appendix of [Kuvшинов и Olsen \[2006a\]](#). The spherical layer thicknesses increase with depth as an arithmetic series with step size 30 km, starting from a top layer thickness of 10 km. We terminate the model at a depth of 850 km. Thus 28 layers (with log(conductivities) as the

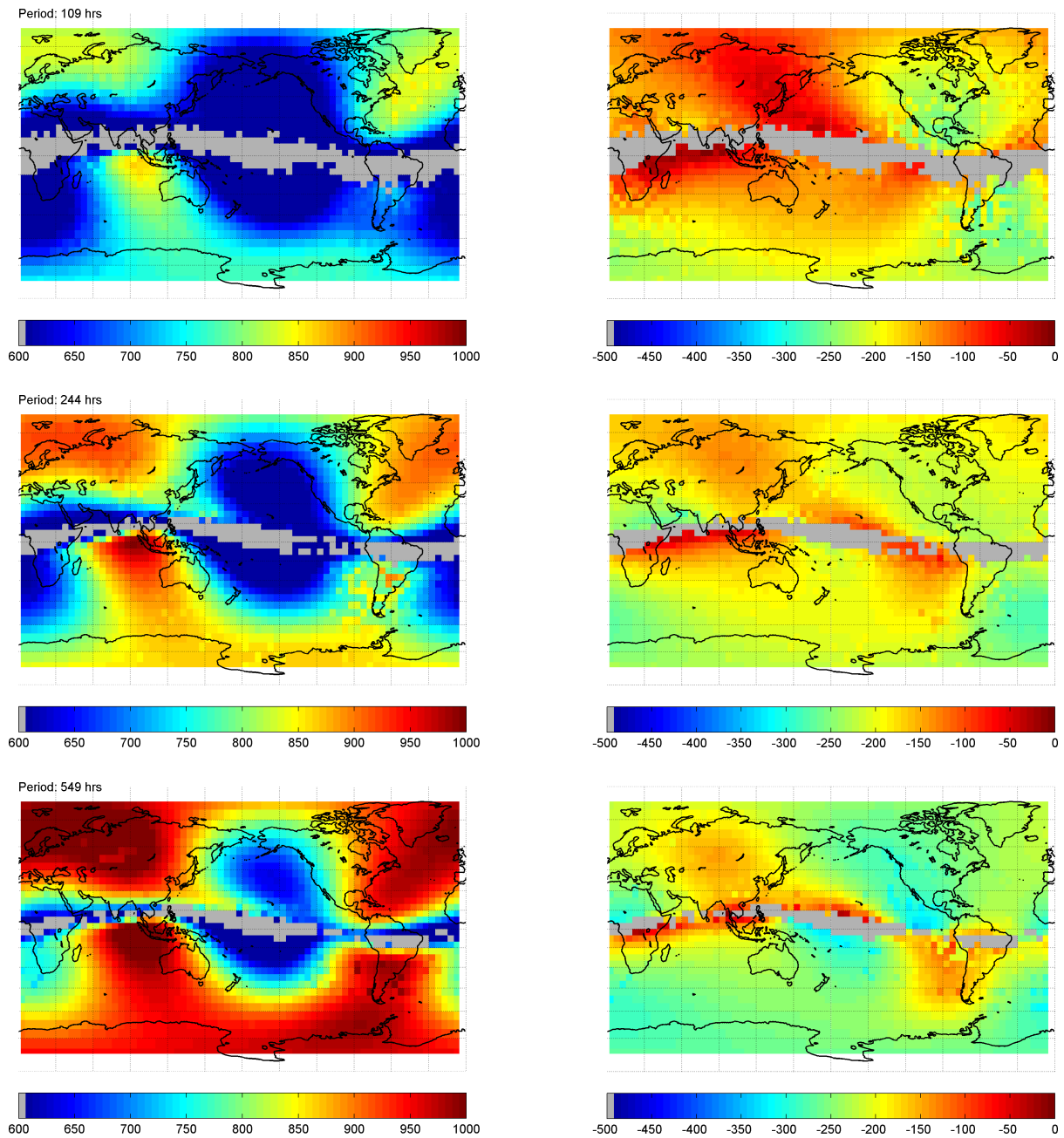


Figure 2.10: Map of real (left) and imaginary (right) part of the C -response (in km), determined from four years of *Swarm* constellation # 4 data and $n_{\max} = 3$. Regions with $\text{coh}^2 < 0.5$ are shown in grey.

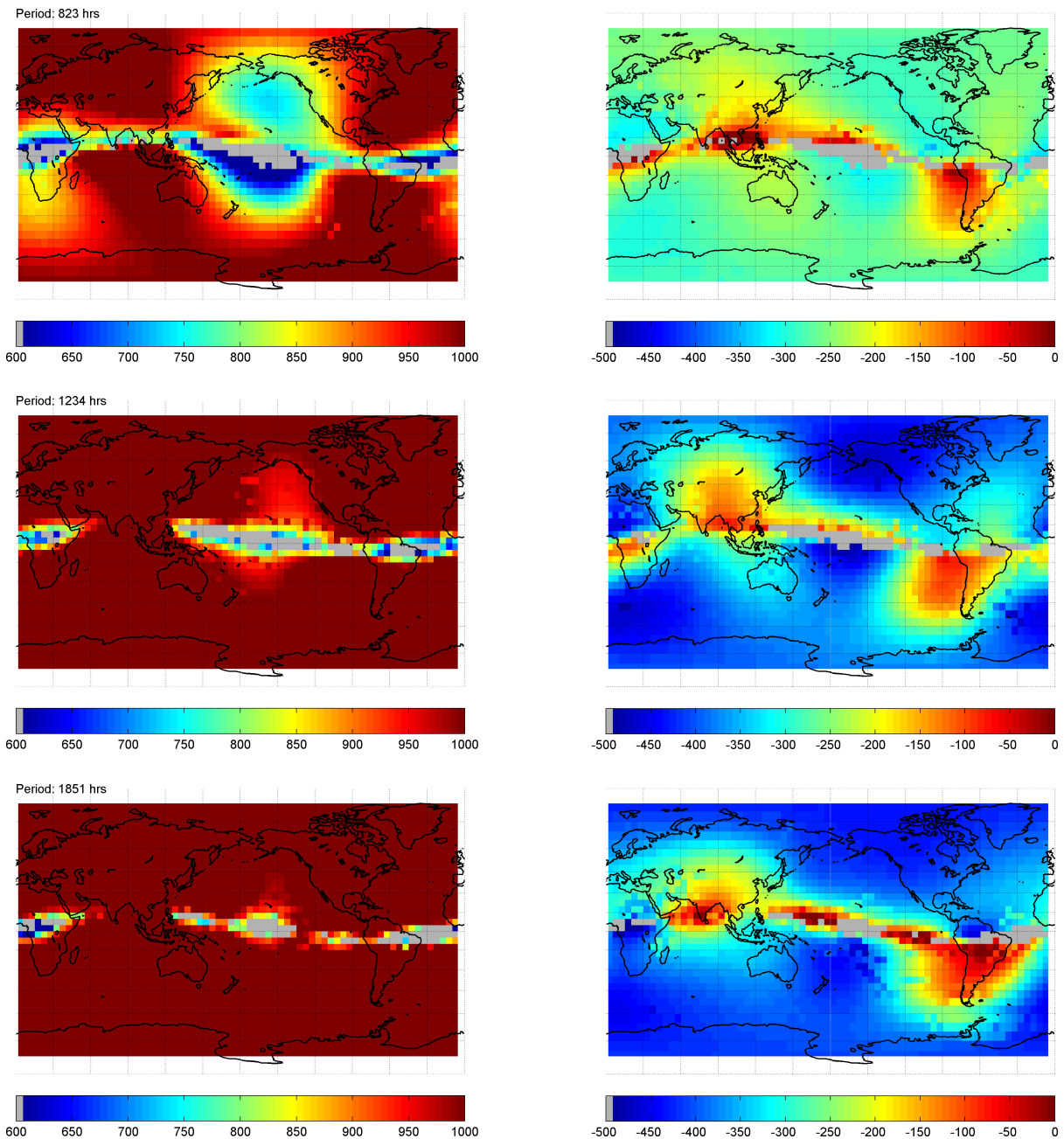


Figure 2.11: Map of real (left) and imaginary (right) part of the C -response (in km), determined from four years of *Swarm* constellation # 4 data and $n_{\max} = 3$. Regions with $\text{coh}^2 < 0.5$ are shown in grey.

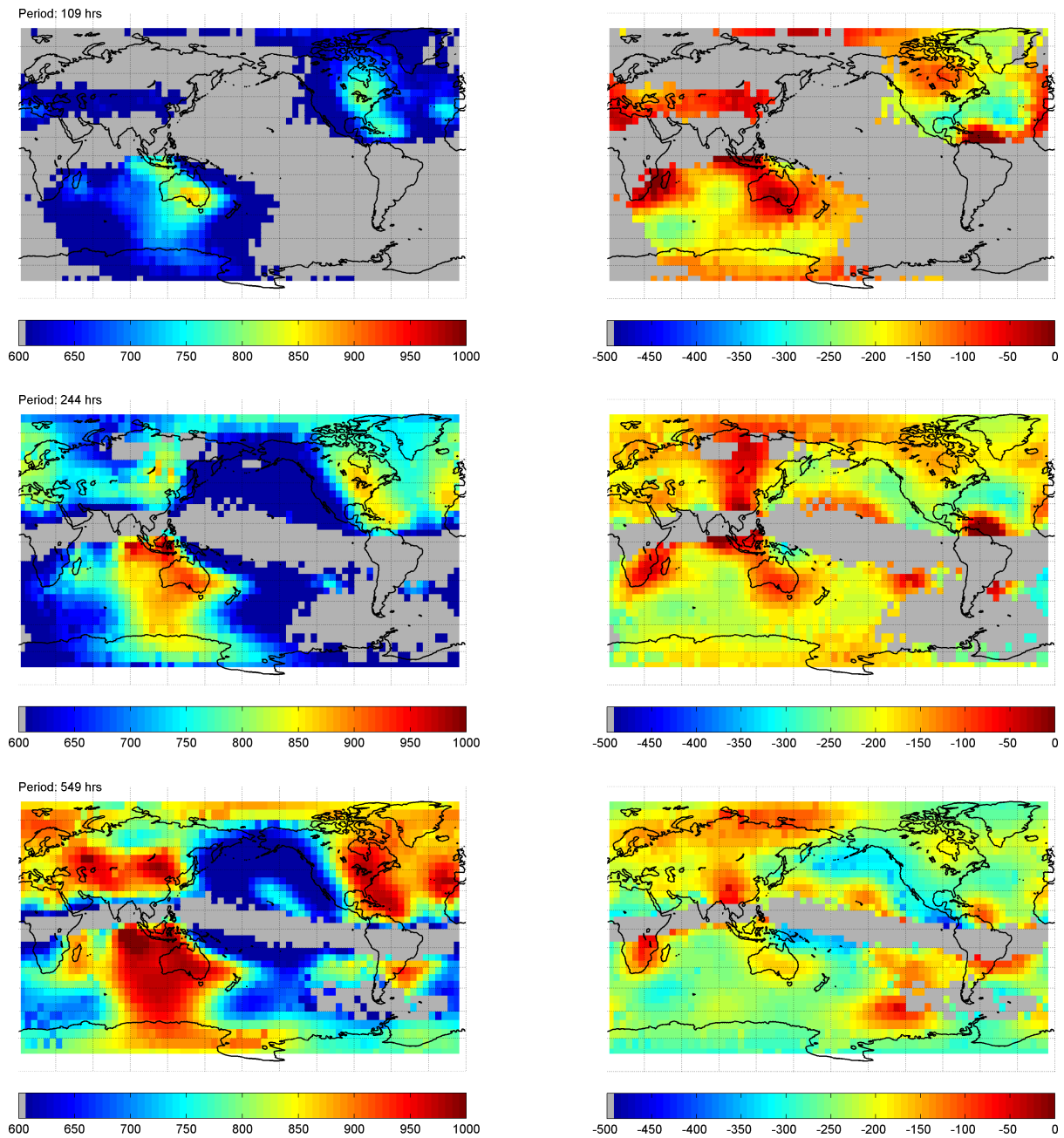


Figure 2.12: Map of real (left) and imaginary (right) part of the C -response (in km), determined from four years of *Swarm* constellation # 4 data and $n_{\max} = 9$. Regions with $\text{coh}^2 < 0.5$ are shown in grey.

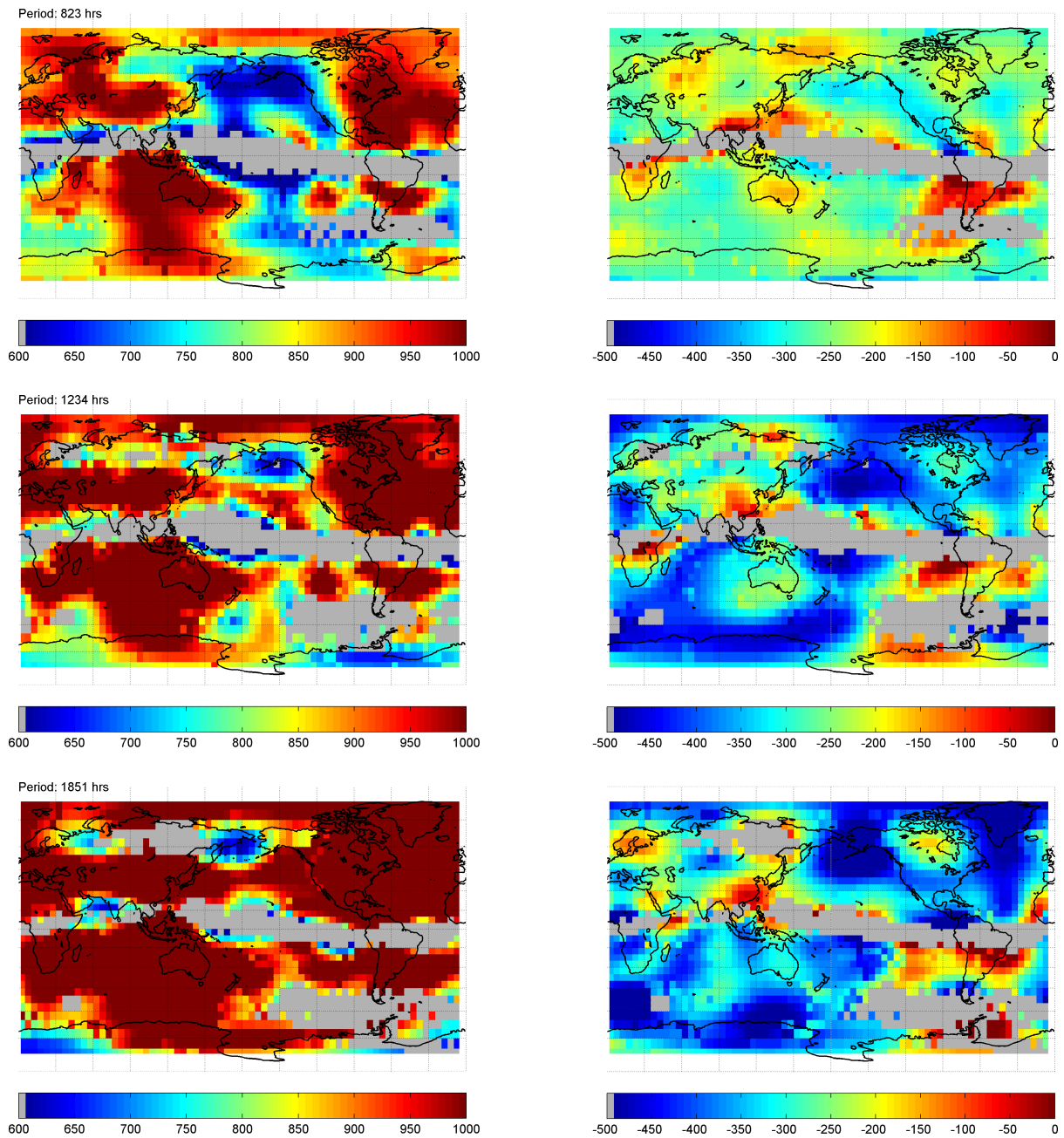


Figure 2.13: Map of real (left) and imaginary (right) part of the C -response (in km), determined from four years of *Swarm* constellation # 4 data and $n_{\text{max}} = 9$. Regions with $\text{coh}^2 < 0.5$ are shown in grey.

corresponding 28 model parameters) are considered. The solution is stabilized by requiring minimum first derivative of log(conductivity) with respect to depth. Fig. 2.14 shows the results of the conductivity recovery (on a logarithmic scale) at depths of 205 km (at the center of the uniform layer of 0.004 S/m conductivity), of 535 km (at the center of nonuniform layer), and of 775 km. For comparison, Fig. 2.15 presents the true conductivity distribution in the nonuniform target layer. Note that polar and equatorial regions are excluded in Fig. 2.14, to make the problem statement more realistic. The stabilizing parameter λ has been chosen to provide sufficient smoothness of the model and reasonably small misfit (in this case we used $\lambda = 100$). We obtain satisfactory but not perfect agreement.

We tried to improve the agreement by correcting the responses for the ocean effect. To do this we used

$$C^{corr,exp}(\mathbf{r}_i, \omega_j) = C^{exp}(\mathbf{r}_i, \omega_j) * C^{1D}(\mathbf{r}_i, \omega_j) / C^{1D+shell}(\mathbf{r}_i, \omega_j). \quad (2.13)$$

Here C^{exp} are responses calculated from the model with oceans and deep anomaly, C^{1D} are responses calculated from the 1-D model, and $C^{1D+shell}$ are responses calculated from the model with oceans and 1-D section underneath. Fig. 2.16 presents the result of an inversion of the corrected responses. It is clearly seen that the agreement between true and recovered conductivities is now much better. Note that for the correction we used the background section as the 1-D model.

2.3 Frequency-domain full 3-D inversion: methodology

2.3.1 Inverse problem formulation

We formulate the inverse problem of conductivity recovery as an optimization problem such that

$$\phi(\mathbf{m}, \lambda) \underbrace{\rightarrow}_{\sigma} \min, \quad (2.14)$$

with the penalty function

$$\phi(\mathbf{m}, \lambda) = \phi_d(\mathbf{m}) + \lambda \phi_s(\mathbf{m}). \quad (2.15)$$

Here $\phi_d(\mathbf{m})$ is the data misfit

$$\phi_d(\mathbf{m}) = \sum_{\omega \in \Omega} \sum_{a \in Sites} (C_a(\mathbf{m}, \omega) - C_a^{exp}(\omega))^* D_a(\omega) (C_a(\mathbf{m}, \omega) - C_a^{exp}(\omega)), \quad (2.16)$$

and λ and $\phi_s(\mathbf{m})$ are a regularization parameter and a stabilizer, respectively. $C_a(\mathbf{m}, \omega)$ and $C_a^{exp}(\omega)$ are the (complex-valued) predicted and observed response functions respectively at observation site a and frequency ω , $D_a(\omega) = \frac{1}{(\delta C_a^{exp}(\omega))^2}$ is the inverse of the squared uncertainties of the observed responses, and the asterisk stands for complex conjugate. $\mathbf{m} = (m_1, m_2, \dots, m_{N_{inv}})^T = (\ln(\sigma_1), \ln(\sigma_2), \dots \ln(\sigma_{N_{inv}}))^T$ is the vector of logarithms of the unknown conductivities in N_{inv} cells of the inversion domain V^{inv} that have to be determined. This, in particular, means that the conductivity distribution in the volume V^{inv} is represented as

$$\sigma(\mathbf{r}) = \sum_{l=1}^{N_{inv}} \sigma_l \chi_l(\mathbf{r}), \quad (2.17)$$

where

$$\chi_l(\mathbf{r}) = \begin{cases} 1, & \mathbf{r} \in V_l^{inv} \\ 0, & \mathbf{r} \notin V_l^{inv} \end{cases} \quad (2.18)$$

and where V_l^{inv} is the volume occupied by the l -th cell (note that $V^{inv} = \bigcup V_l^{inv}$). We assume that V^{inv} is a number of nonuniform spherical layers embedded in the Earth model that consists of a surface shell

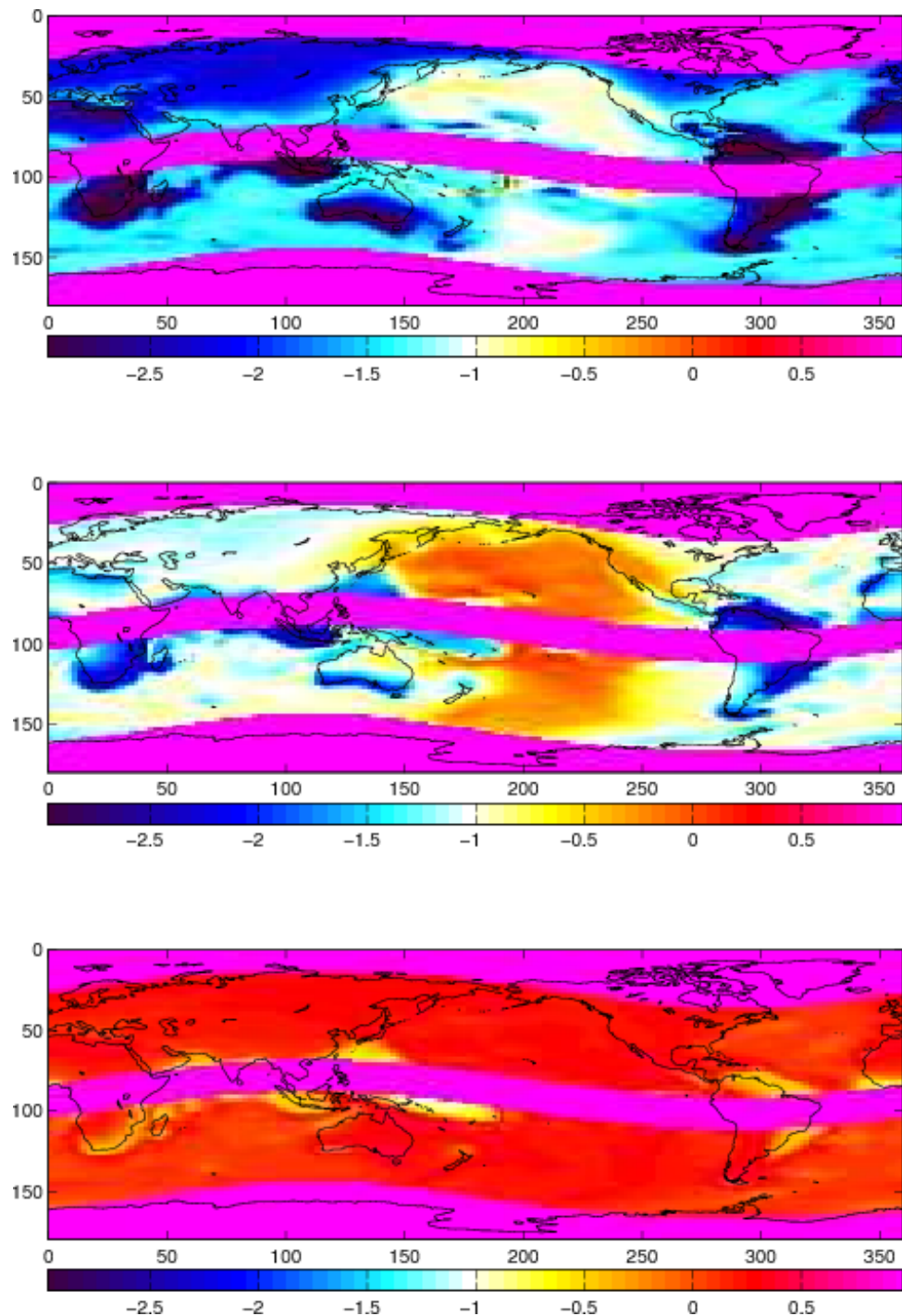


Figure 2.14: Log(conductivities) at depths of 205 km, 535 km and 775 km recovered by simple quasi 1-D inversion from the uncorrected C -responses.

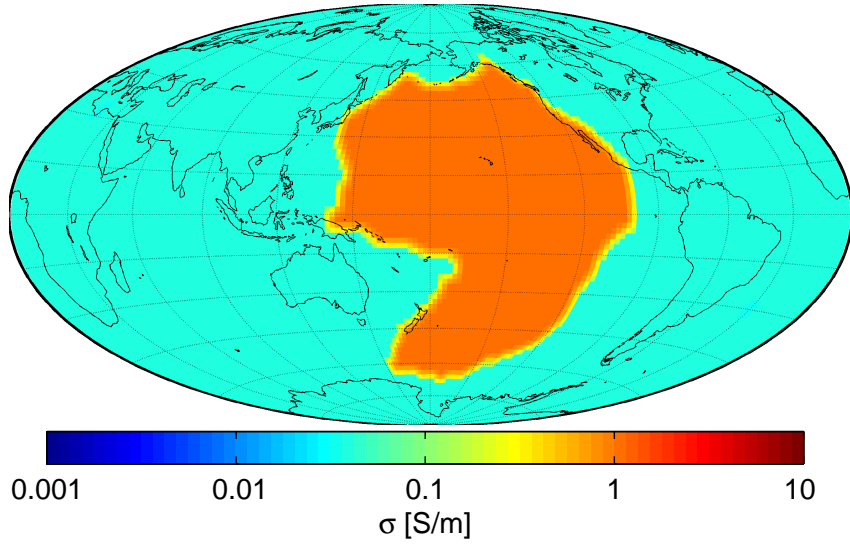


Figure 2.15: True log(conductivity) distribution in the target nonuniform layer located at depths between 310 km and 710 km.

of known laterally variable conductance and known background profile of conductivity (see Fig. 2.17). The dimension of the problem is rather large with N_{inv} and $N_{freq} \times N_{sites}$ both exceeding 10^4 . Note that the choice of logarithms of conductivities instead conductivities themselves as unknowns guarantees the positiveness of the conductivities during the inversion and provides a better scaling of the problem.

”Sites” define the locations of the observation sites:

$$Sites := \{(r_i, \vartheta_i, \varphi_i), i = 1, 2, \dots, N_{sites}\}, \quad (2.19)$$

and ” Ω ” define the frequencies in consideration:

$$\Omega := \{\omega_j, j = 1, 2, \dots, N_{freq}\}. \quad (2.20)$$

The stabilizer can be chosen in different ways but is often presented in the form

$$\phi_s(\mathbf{m}) = \{W\mathbf{m}\}^T \{W\mathbf{m}\}, \quad (2.21)$$

where the superscript T means transpose and W presents a regularization matrix which – together with the regularization parameter λ – controls the model smoothness. We will consider here as smoothing matrix the finite difference approximation to the gradient (∇) operator.

2.3.2 Choice of the optimization scheme

Due to the large scale of the inverse problem, gradient methods are probably the only methods of choice [cf. [Nocedal and Wright, 2006](#)]. Two competitive methods are often used for large scale inverse problems in geoelectromagnetism: the nonlinear conjugate gradient (NLCG), and the limited-memory quasi-Newton (LMQN) method [cf. [Newman and Alumbaugh, 2000](#), [Rodi and Mackie, 2000](#), [Newman and Boggs, 2004](#), [Haber, 2005](#), [Kelbert et al., 2007](#), [Avdeev and Avdeeva, 2009](#)]. In this section we will discuss shortly the essentials of these two methods and provide a test of their efficiency as applied to the simple 1-D global induction inversion problem.

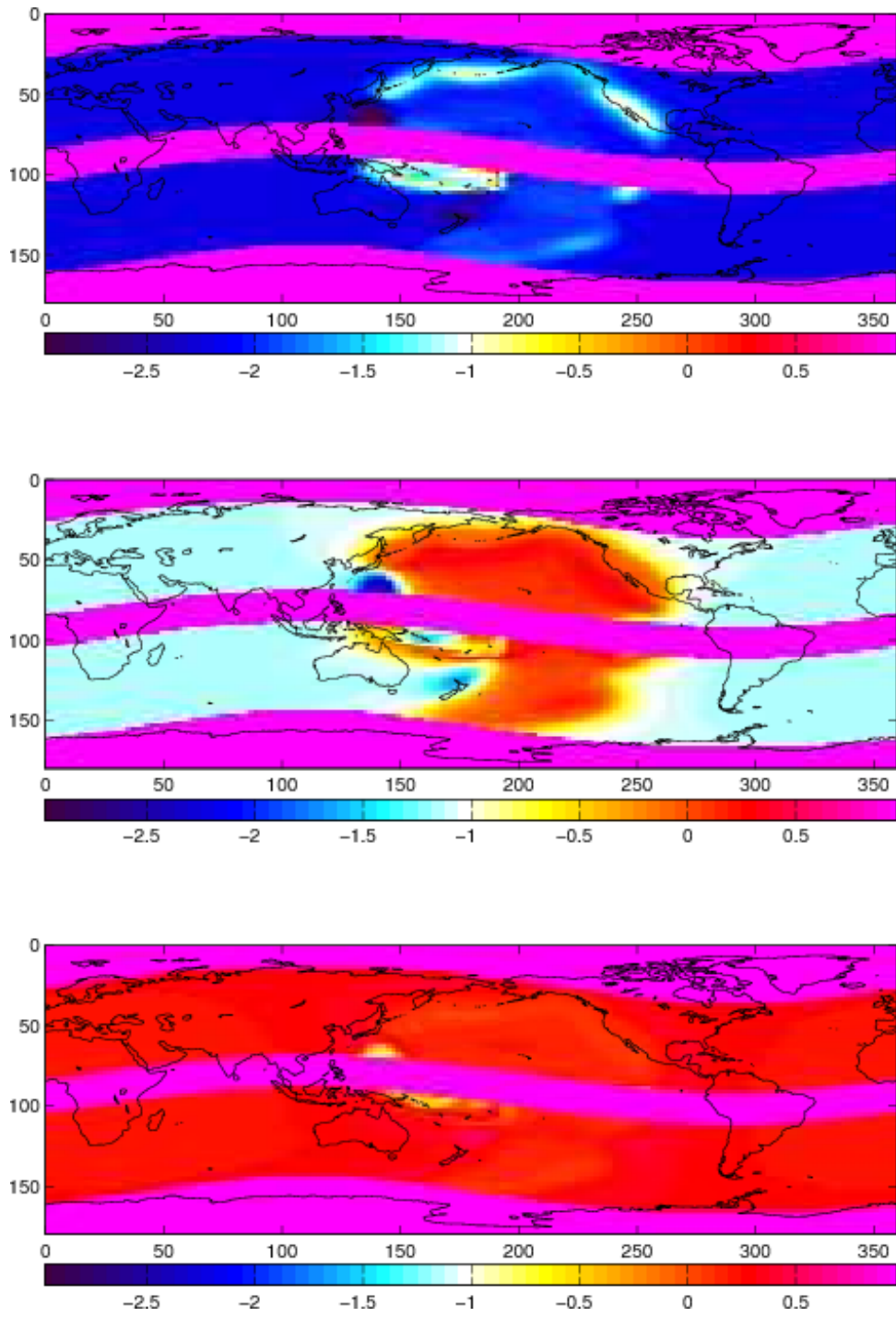


Figure 2.16: Log(conductivities) at depths of 205 km, 535 km and 775 km recovered by simple quasi 1-D inversion from the corrected C -responses.

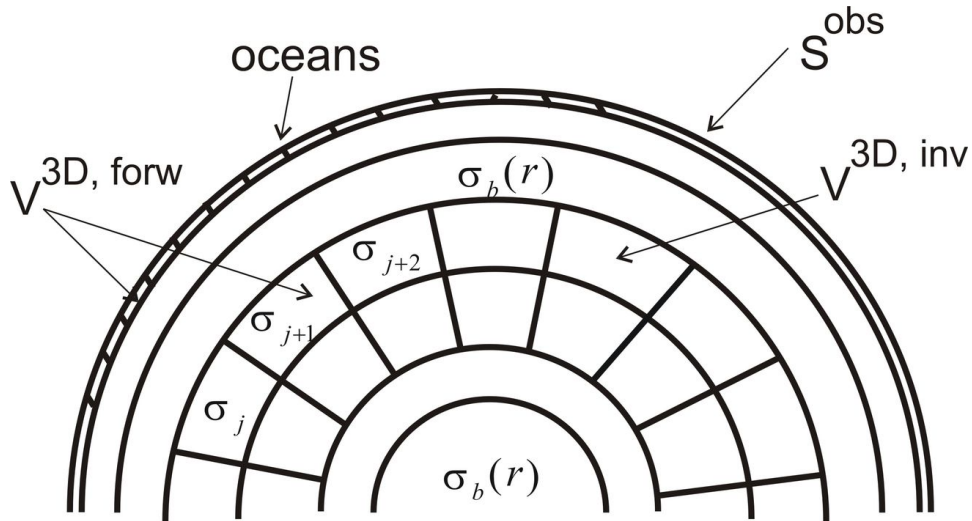


Figure 2.17: Sketch of 3-D conductivity model.

2.3.2.1 Limited memory quasi-Newton algorithm (LMQN)

The quasi-Newton (QN) method is based on the update formula

$$\mathbf{m}_{k+1} = \mathbf{m}_k + \alpha_k \mathbf{p}_k, \quad (2.22)$$

where \mathbf{p}_k is determined as

$$\mathbf{p}_k = -B_k^{-1} \nabla \phi_k. \quad (2.23)$$

Here $\nabla \phi_k = (\frac{\partial \phi_k}{\partial m_1}, \frac{\partial \phi_k}{\partial m_2}, \dots, \frac{\partial \phi_k}{\partial m_{N_{inv}}})^T$ is the gradient vector with respect to the current model parameters \mathbf{m}_k , α_k is the step length and B_k^{-1} is an approximation of the inverse Hessian matrix.

This updating procedure requires three basic operations:

1. Update of $\nabla \phi_k$;
2. Update of B_k^{-1} using, for example, Broyden-Fletcher-Goldfarb-Shanno (BFGS) formula;
3. Inexact line search to find appropriate α_k .

Since the inverse Hessian approximation is generally dense, the cost of storing and manipulating it is prohibitive when the number, N_{inv} , of variables is large. Indeed we need $O(N_{inv}^2)$ bytes and operations to respectively store B_k^{-1} and calculate $B_k^{-1} \nabla \phi_k$ at each iteration. For example, with the number of variables that we plan to use in our inversion

$$N_{inv} = N_r \times N_\vartheta \times N_\varphi = 6 \times 36 \times 72, \quad (2.24)$$

we need about 1 Gb of memory. To circumvent this problem, a limited-memory variant of QN was introduced which works with a modified version of B_k^{-1} and requires manipulations with m vector pairs $\{\mathbf{m}_i - \mathbf{m}_{i-1}, \nabla \phi_i - \nabla \phi_{i-1}\}$. Practical experience has shown that modest values of m (between 3 and 20, say) often produce satisfactory results. In this case we need $O(m N_{inv})$ bytes and operations to store B_k^{-1} and calculate $B_k^{-1} \nabla \phi_k$ in each iteration.

Note that the efficiency (rate of convergence to the solution) of the inversion strongly depends on the accuracy of the line search scheme. In both methods (LMQN and NLCG) we used a sophisticated scheme, following the reasonings presented in [Nocedal and Wright, 2006].



2.3.2.2 Nonlinear conjugate gradients (NLCG)

The nonlinear conjugate gradient method proposed by [Fletcher and Reeves \[1964\]](#) is based on the update formula

$$\mathbf{m}_{k+1} = \mathbf{m}_k + \alpha_k \mathbf{p}_k, \quad (2.25)$$

where \mathbf{p}_k is

$$\mathbf{p}_k = -\nabla \phi_{k-1} + \beta_k \mathbf{p}_{k-1}. \quad (2.26)$$

$$\beta_k = \frac{\nabla \phi_k^T \nabla \phi_k}{\nabla \phi_{k-1}^T \nabla \phi_{k-1}}, \quad (2.27)$$

There are many variants of the Fletcher-Reeves method that differ from each other mainly in the choice of the parameter β_k . An important variant, proposed by [Polyak and Ribiere \[1969\]](#), defines this parameter as

$$\beta_k = \frac{\nabla \phi_k^T (\nabla \phi_k - \nabla \phi_{k-1})}{\nabla \phi_{k-1}^T \nabla \phi_{k-1}}. \quad (2.28)$$

Other variants of the NLCG method have recently been proposed. Two choices for β_k that possess attractive theoretical and computational properties are

$$\beta_k = \frac{\nabla \phi_k^T \nabla \phi_k}{(\nabla \phi_k - \nabla \phi_{k-1})^T \mathbf{p}_k}, \quad (2.29)$$

(see [\[Dai and Yuan, 1999\]](#)) and

$$\beta_k = \left(\hat{\mathbf{y}}_k - 2\mathbf{p}_k \frac{\hat{\mathbf{y}}_k^T \hat{\mathbf{y}}_k}{\hat{\mathbf{y}}_k^T \mathbf{p}_k} \right), \quad (2.30)$$

with

$$\hat{\mathbf{y}}_k = \nabla \phi_k - \nabla \phi_{k-1}. \quad (2.31)$$

(see [\[Hager and Zhang, 2005\]](#)). It is seen from eqs. (2.25)- (2.31) that the NLCG update involves the calculation of $\nabla \phi_k$ and a line search, but does not require an update of the inverse Hessian matrix. Thus NLCG is appealing for large nonlinear optimization problems.

Both methods are terminated when $|\nabla \phi_k|$ becomes sufficiently small.

2.3.2.3 LMQN versus NLCG

We coded the two methods and tested their efficiency on a simple radially-symmetric (1-D) conductivity model, where the searching parameters are the log conductivities of four layers. The boundaries of these layers were fixed, no uncertainties were added, and no regularization was performed. Note that the calculation of the 1-D responses and its gradients are explained in the Appendix of [Kuvшинов и Olsen \[2006a\]](#). In the case of NLCG we tried all four variants for updating β_k described by eqs. (2.27) and (2.29)-(2.31) and obtained best results when using eqs. (2.30)-(2.31).

Fig. 2.18 presents the results of this test. The left and right panel shows the number of forward modeling calls and misfit, respectively, in dependence on the number of iterations. It is seen that LMQN requires 3 times fewer forward modelings compared to NLCG to achieve a misfit of 10^{-6} (which corresponds to 35 iterations). This result hints that LMQN is probably more appropriate than NLCG for our problem formulation.

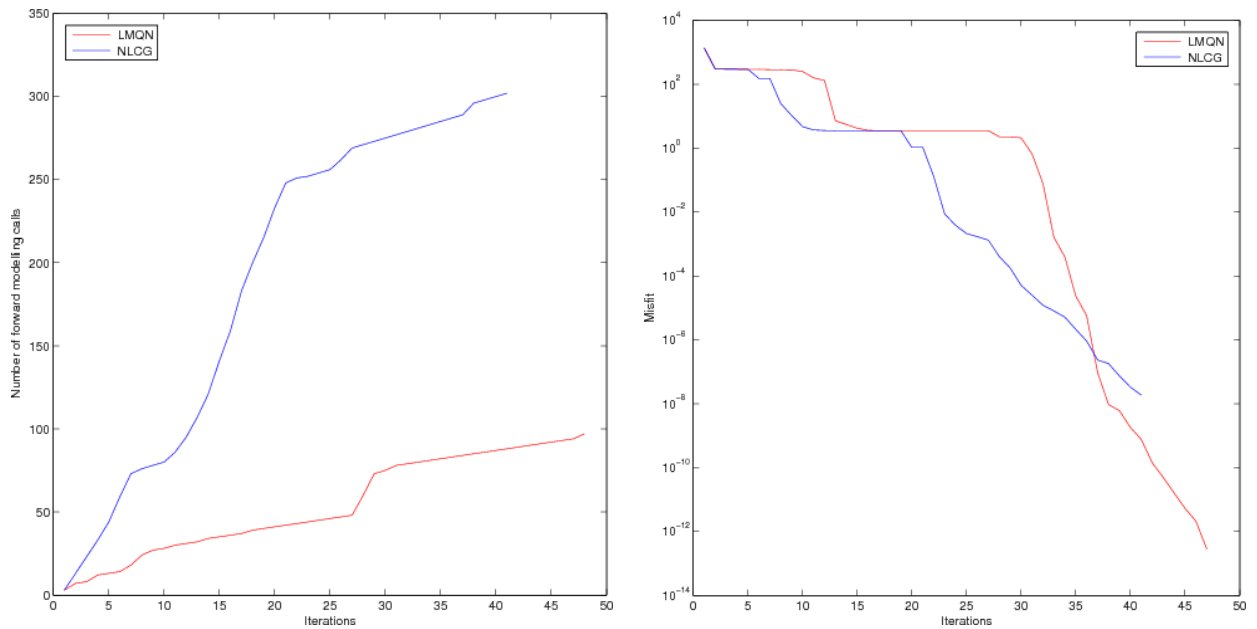


Figure 2.18: Number of the forward modeling calls (left) and misfit (right) with respect to number of iterations.

2.3.3 Test of different regularization schemes. 1-D case

An important problem in the inversion of electromagnetic data is the development of stable inverse problem solvers that are able to deliver sharp images of the conductivity inhomogeneities. To stabilize the inverse solution, conventional inverse schemes are based on a standard smoothness constraint, which, however, produces smoothed and blurry images. We investigated several alternative stabilizing procedures, which have been promoted recently to produce sharper images. These stabilizing procedures are Total Variance, Minimum Gradient Support, and Maximum Entropy Regularizations.

During our optimization we minimize the penalty function (2.15). Using different stabilizers and regularization parameters we obtained 1-D conductivity models of different smoothness. For comparative purposes, we introduce the widely used smoothness constraint, where $\phi_s(\mathbf{m})$ is the integral over the L_2 norm of the model gradient

$$\phi_s(\mathbf{m}) = \int_V \|\nabla \mathbf{m}\|^2 dv \quad (2.32)$$

where $\mathbf{m} = (m_1, m_2, \dots, m_{N_{inv}})^T = (\ln(\sigma_1), \ln(\sigma_2), \dots \ln(\sigma_{N_{inv}}))^T$. Here the contribution to the model increases with the square of the model gradient.

Alternatively, the L_1 -norm may be chosen [cf. Aster et al., 2005]

$$\phi_s(\mathbf{m}) = \int_V \|\nabla \mathbf{m}\| dv. \quad (2.33)$$

which increases only linearly with the model gradient and thus produces more blocky models than the L_2 -norm because the penalty for larger gradients is smaller. A problem is, however, the difficulty of calculating the gradient for the stabilizer. Therefore it is possible to use

$$\phi_s(\mathbf{m}) = \sqrt{\int_V \|\nabla \mathbf{m}\|^2 dv + \beta^2}. \quad (2.34)$$

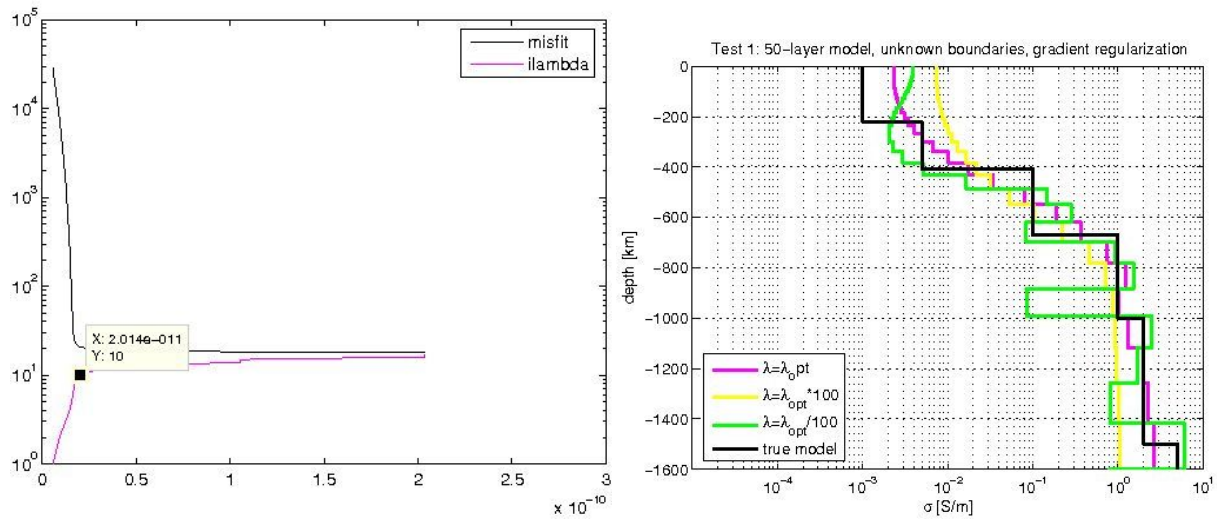


Figure 2.19: L-curve (black line, left) and comparison of conductivity profile between different λ (right) for the conventional regularization.

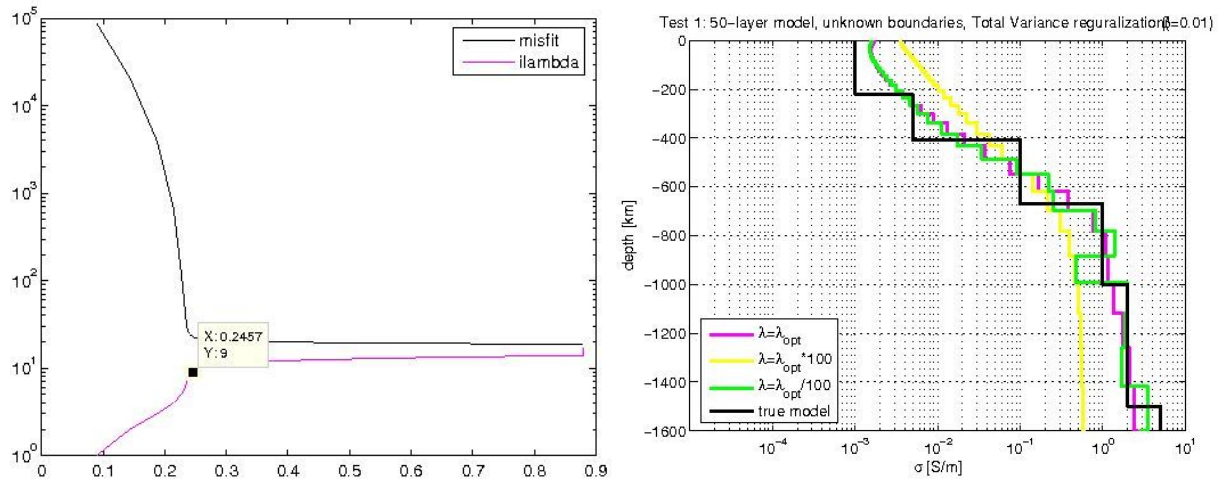


Figure 2.20: L-curve (black line, left) and comparison of conductivity profile between different λ (right) for the Total Variance regularization.

The Minimum Gradient Support functional [cf. [Blashek et al., 2008](#)] can be written as

$$\phi_s(\mathbf{m}) = \int_V \frac{\nabla m \cdot \nabla m}{\nabla m \cdot \nabla m + \beta^2} dv. \quad (2.35)$$

For small values of β , the functional behaves like a step function, as can be seen from

$$\lim_{\beta \rightarrow 0} \frac{\nabla m \cdot \nabla m}{\nabla m \cdot \nabla m + \beta^2} = \begin{cases} 1, & \text{for } \nabla m \neq 0 \\ 0, & \text{for } \nabla m = 0 \end{cases} \quad (2.36)$$

In the limit of large β , the function asymptotically converges toward a penalty proportional to the L_2 -norm:

$$\beta \gg \nabla m \Rightarrow \frac{\nabla m \cdot \nabla m}{\nabla m \cdot \nabla m + \beta^2} \approx \nabla m \cdot \nabla m \beta^2 \propto \nabla m \cdot \nabla m. \quad (2.37)$$

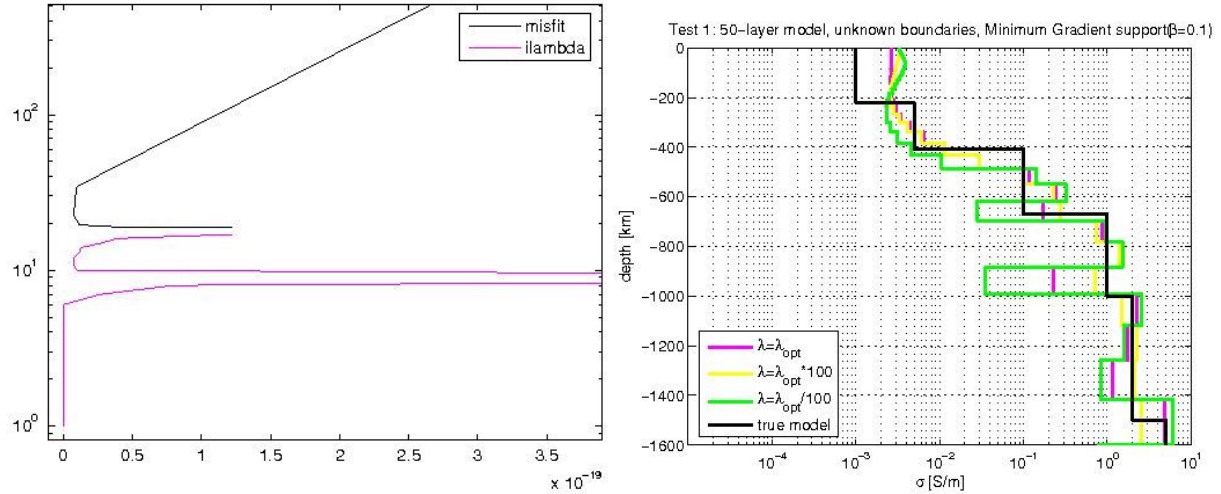


Figure 2.21: L-curve (black line, left) and comparison of conductivity profile between different λ (right) for the Minimum Gradient Support regularization.

We also consider the Maximum Entropy Regularization. The entropy norm, recently used in geomagnetic field modelling, provides models with better contrast, and involves a minimum of a priori information about field structure. According to Gillet et al. [2007], the entropy functional can be written as $\phi_s(\mathbf{m}) = (\sum_{i=1}^N \sigma_i - \sigma_{\text{apr}} - \sigma_i \log(\sigma_i/\sigma_{\text{apr}}))$. Here σ_i is the model-conductivity and σ_{apr} is the default model.

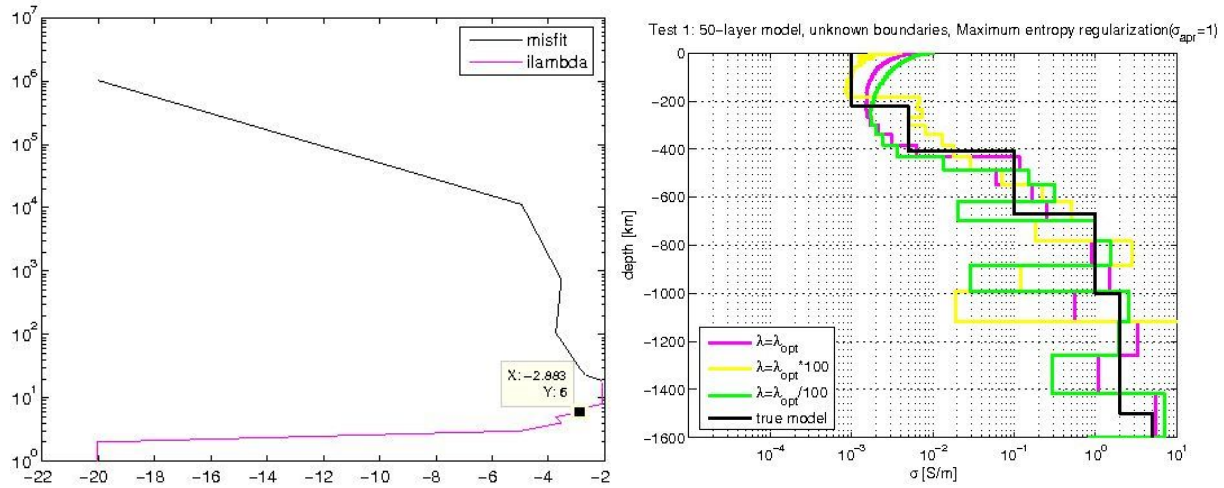


Figure 2.22: L-curve (black line, left) and comparison of conductivity profile between different λ (right) for the Maximum Entropy Regularization.

Figures 2.19-2.22 summarize our first experiments with different types of regularizations. We inverted synthetic C -responses from 1-D model (shown on the right panels of the Figures as fat solid line). Optimal λ is chosen following L-curve criterion [Hansen, 1992] in which the value of λ that gives the solution closest to the corner of the L-curve is selected. From the Figures it can be seen that the Maximum Entropy Regularization provides the most blocky profile. However, more work is required to support this conclusion.

2.4 Efficient calculation of the gradient of the misfit function

In the methods discussed above one has to calculate the gradient of the penalty function $\nabla\phi = \nabla\phi_d + \lambda\nabla\phi_s$. As for regularization term introduced by eq. (2.21), an evaluation of $\nabla\phi_s$ leads immediately to

$$\nabla\phi_s = 2W^T W \mathbf{m}. \quad (2.38)$$

For the computation of $\nabla\phi_d$ we adopt the adjoint approach [widely used, say, in electromagnetics, cf. Dorn et al., 1999, Newman and Alumbaugh, 2000, Rodi and Mackie, 2000, Kelbert et al., 2007, Avdeev and Avdeeva, 2009], which allows for calculating the gradient with only a few forward calculations. Following formalism presented in [Pankratov and Kuvшинов, 2010], we elaborate on applying this approach to the calculation of the gradient of our (specific) misfit function.

First we have to introduce the operators G_{3D}^{ej} , G_{3D}^{eh} and G_{3D}^{eg} that are needed to construct an efficient scheme for calculating the gradients.

2.4.1 Definition of the operators G_{3D}^{ej} , G_{3D}^{eh} , G_{3D}^{eg}

We consider Maxwell's equations

$$\begin{aligned} \nabla \times \mathbf{H} &= \sigma \mathbf{E} + \mathbf{j}^{ext}, \\ \nabla \times \mathbf{E} &= i\omega\mu_0 \mathbf{H}. \end{aligned} \quad (2.39)$$

and define the operator G_{3D}^{ej} as

$$\mathbf{E} = G_{3D}^{ej}(\mathbf{j}^{ext}) \Leftrightarrow \begin{cases} \nabla \times \mathbf{H} = \sigma \mathbf{E} + \mathbf{j}^{ext}, \\ \nabla \times \mathbf{E} = i\omega\mu_0 \mathbf{H}, \\ \mathbf{E}, \mathbf{H} \rightarrow 0 \text{ as } \mathbf{r} \rightarrow \infty \end{cases} \quad (2.40)$$

where

$$\mathbf{j}^{ext} = \mathbf{j}^{ext}(\omega, r, \vartheta, \varphi), \quad (2.41)$$

is the given exciting (imposed) current, and $\sigma = \sigma(r, \vartheta, \varphi)$ is the given three-dimensional (3-D) conductivity distribution in the Earth's model. The operator $G_{3D}^{ej}(\cdot)$ acts on the input distribution of electric current \mathbf{j}^{ext} and yields the electric field due to this current.

Further we define the operator G_{3D}^{eh}

$$\mathbf{E} = G_{3D}^{eh}(\mathbf{h}^{ext}) \Leftrightarrow \begin{cases} \nabla \times \mathbf{H} = \sigma \mathbf{E}, \\ \nabla \times \mathbf{E} = i\omega\mu_0 \mathbf{H} + \mathbf{h}^{ext}, \\ \mathbf{E}, \mathbf{H} \rightarrow 0 \text{ as } \mathbf{r} \rightarrow \infty. \end{cases} \quad (2.42)$$

which calculates the electric field $G_{3D}^{eh}(\mathbf{h}^{ext})$ provided that the input \mathbf{h}^{ext} has the spatial distribution

$$\mathbf{h}^{ext} = \mathbf{h}^{ext}(\omega, r, \vartheta, \varphi), \quad (2.43)$$

of the imposed magnetic dipoles. G_{3D}^{ej} and G_{3D}^{eh} are linked through

$$G_{3D}^{eh}(\mathbf{h}^{ext}) = G_{3D}^{ej} \left(\nabla \times \left(\frac{\mathbf{h}^{ext}}{i\omega\mu_0} \right) \right). \quad (2.44)$$

Finally we define the operator G_{3D}^{eg}

$$\mathbf{E} = G_{3D}^{eg}(F) \Leftrightarrow \begin{cases} \nabla \times \mathbf{H} = \sigma \mathbf{E}, \\ \nabla \times \mathbf{E} = i\omega\mu_0 \mathbf{H} + \nabla_\tau F, \\ \mathbf{E}, \mathbf{H} \rightarrow 0 \text{ as } \mathbf{r} \rightarrow \infty. \end{cases} \quad (2.45)$$



2.4.2 Derivatives of the Z:Y C -responses

Here we present the results for the Z:Y C -responses (those for Z:H C -responses will be discussed in Section 2.7).

We can write the C -response at the observation site a as

$$C_a(\omega) = C_a(\mathbf{H}(\omega)) = C(H_r, \nabla_\tau \cdot \mathbf{H})|_a = -\frac{H_r}{\nabla_\tau \cdot \mathbf{H}} \Big|_a. \quad (2.46)$$

In following we will omit (but imply) the dependence fn the quantities frequency on ω .

Let us derive the differential, $d(C_a(\omega))$, with respect to a variation of conductivity σ . By denoting

$$U = \nabla_\tau \cdot \mathbf{H}, \quad (2.47)$$

we have

$$dC_a = \left(\frac{\partial C}{\partial U} dU + \frac{\partial C}{\partial H_r} dH_r \right) \Big|_a = \left(\frac{H_r}{U^2} dU - \frac{1}{U} dH_r \right) \Big|_a. \quad (2.48)$$

Let us consider the calculation of $\frac{1}{U} dH_r$:

$$\begin{aligned} \left(\frac{1}{U} dH_r \right) \Big|_a &= \left(\frac{1}{U} d \frac{\nabla_r \times \mathbf{E}}{i\omega\mu_0} \right) \Big|_a = \left(\frac{1}{i\omega\mu_0} \frac{1}{U} \nabla_r \times d\mathbf{E} \right) \Big|_a = \\ &\left(\frac{1}{i\omega\mu_0} \frac{1}{U} \nabla_r \times (G_{3D}^{ej}(G_{3D}^{ej}(\mathbf{j}^{ext})d\sigma)) \right) \Big|_a = \\ &\left\langle \frac{1}{i\omega\mu_0} \frac{1}{U} \mathbf{e}_r \delta_a, \nabla \times (G_{3D}^{ej}(G_{3D}^{ej}(\mathbf{j}^{ext})d\sigma)) \right\rangle, \end{aligned} \quad (2.49)$$

where $\delta_a = \delta(\mathbf{r} - \mathbf{r}_a)$ is Dirac's delta function, and pair in angle brackets $\langle \cdot, \cdot \rangle$ denotes complex bilinear pairing

$$\langle \mathbf{a}, \mathbf{b} \rangle = \int_{R^3} (a_r(\mathbf{r})b_r(\mathbf{r}) + a_\vartheta(\mathbf{r})b_\vartheta(\mathbf{r}) + a_\varphi(\mathbf{r})b_\varphi(\mathbf{r}))r^2 \sin \vartheta d\vartheta d\varphi. \quad (2.50)$$

Note that in eq. (2.49) we used the following expression for differential of electric field with respect to variation of conductivity σ

$$d\mathbf{E} = G_{3D}^{ej}(G_{3D}^{ej}(\mathbf{j}^{ext})d\sigma). \quad (2.51)$$

Let us show how we derive this equation. We consider Maxwell's equations for $\sigma + \Delta\sigma$ and denote their solutions as $\mathbf{H} + \Delta\mathbf{H}$ and $\mathbf{E} + \Delta\mathbf{E}$

$$\begin{aligned} \nabla \times (\mathbf{H} + \Delta\mathbf{H}) &= (\sigma + \Delta\sigma)(\mathbf{E} + \Delta\mathbf{E}) + \mathbf{j}^{ext}, \\ \nabla \times (\mathbf{E} + \Delta\mathbf{E}) &= i\omega\mu_0(\mathbf{H} + \Delta\mathbf{H}). \end{aligned} \quad (2.52)$$

By subtracting eq. (2.39) from eq. (2.52) we get

$$\begin{aligned} \nabla \times \Delta\mathbf{H} &= (\sigma + \Delta\sigma)\Delta\mathbf{E} + \Delta\sigma\mathbf{E}, \\ \nabla \times \Delta\mathbf{E} &= i\omega\mu_0\Delta\mathbf{H}. \end{aligned} \quad (2.53)$$

But we notice, from eq. (2.40), that

$$\Delta\sigma\mathbf{E} = G_{3D}^{ej}(\mathbf{j}^{ext})\Delta\sigma. \quad (2.54)$$



By tending $\Delta\sigma$ to zero we arrive to the following equation

$$\begin{aligned}\nabla \times d\mathbf{H} &= \sigma d\mathbf{E} + G_{3D}^{ej}(\mathbf{j}^{ext})d\sigma, \\ \nabla \times d\mathbf{E} &= i\omega\mu_0 d\mathbf{H}.\end{aligned}\quad (2.55)$$

By comparing eq. (2.55) with eq. (2.40) we obtain the desired eq. (2.51).

Let us continue with eq. (2.49). Since the $\nabla \times$ is a self-adjoint operator, i.e.

$$\langle \nabla \times \mathbf{a}, \mathbf{b} \rangle = \langle \mathbf{a}, \nabla \times \mathbf{b} \rangle, \quad (2.56)$$

for any fields \mathbf{a} and \mathbf{b} , we obtain

$$\left(\frac{1}{U} dH_r \right) \Big|_a = \left\langle \nabla \times \left(\frac{1}{i\omega\mu_0} \frac{1}{U} \mathbf{e}_r \delta_a \right), G_{3D}^{ej}(G_{3D}^{ej}(\mathbf{j}^{ext})d\sigma) \right\rangle. \quad (2.57)$$

Since G_{3D}^{ej} is also self-adjoint operator (see the proof in the next section), we obtain

$$\left(\frac{1}{U} dH_r \right) \Big|_a = \left\langle G^{ej}(\nabla \times \left(\frac{1}{i\omega\mu_0} \frac{1}{U} \mathbf{e}_r \delta_a \right)), G_{3D}^{ej}(\mathbf{j}^{ext})d\sigma \right\rangle. \quad (2.58)$$

Using the link between G^{ej} and G^{eh} , described by eq. (2.44) we arrive to the final expression for $\left(\frac{1}{U} dH_r \right) \Big|_a$

$$\left(\frac{1}{U} dH_r \right) \Big|_a = \left\langle G_{3D}^{eh} \left(\frac{1}{U} \mathbf{e}_r \delta_a \right), G_{3D}^{ej}(\mathbf{j}^{ext})d\sigma \right\rangle. \quad (2.59)$$

Let us consider the calculation of the first term in right-hand side of eq. (2.48)

$$\begin{aligned}\left(\frac{H_r}{U^2} dU \right) \Big|_a &= \left(\frac{H_r}{U^2} d(\nabla_\tau \cdot \mathbf{H}) \right) \Big|_a = \left(\frac{H_r}{U^2} \nabla_\tau \cdot \left(d \left(\frac{\nabla \times \mathbf{E}}{i\omega\mu_0} \right) \right) \right) \Big|_a = \\ \left(\frac{H_r}{U^2} \nabla_\tau \cdot \left(\frac{\nabla \times d\mathbf{E}}{i\omega\mu_0} \right) \right) \Big|_a &= \left\langle \frac{1}{i\omega\mu_0} \frac{H_r}{U^2} \delta_a, \nabla_\tau \cdot (\nabla \times d\mathbf{E}) \right\rangle = \\ - \left\langle \nabla_\tau \left(\frac{1}{i\omega\mu_0} \frac{H_r}{U^2} \delta_a \right), \nabla \times d\mathbf{E} \right\rangle &= \\ - \left\langle \nabla \times \left(\frac{1}{i\omega\mu_0} \nabla_\tau \left(\frac{H_r}{U^2} \delta_a \right) \right), G_{3D}^{ej}(G_{3D}^{ej}(\mathbf{j}^{ext})d\sigma) \right\rangle &= \\ - \left\langle G_{3D}^{ej} \left(\nabla \times \left(\frac{1}{i\omega\mu_0} \nabla_\tau \left(\frac{H_r}{U^2} \delta_a \right) \right) \right), G_{3D}^{ej}(\mathbf{j}^{ext})d\sigma \right\rangle &= \\ - \left\langle G_{3D}^{eh} \left(\nabla_\tau \left(\frac{H_r}{U^2} \delta_a \right) \right), G_{3D}^{ej}(\mathbf{j}^{ext})d\sigma \right\rangle. &\end{aligned}\quad (2.60)$$

Among the reasonings discussed earlier we used in the latter equation the equality

$$\langle a, \nabla_\tau \cdot \mathbf{b} \rangle = -\langle \nabla_\tau a, \mathbf{b} \rangle. \quad (2.61)$$

From eq. (2.45) and eq. (2.59) we have

$$\left(\frac{H_r}{U^2} dU \right) \Big|_a = - \left\langle G_{3D}^{eg} \left(\frac{H_r}{U^2} \delta_a \right), G_{3D}^{ej}(\mathbf{j}^{ext})d\sigma \right\rangle. \quad (2.62)$$



Substituting eq. (2.59) and eq. (2.62) into eq. (2.48) we obtain the desired differential, $d(C_a(\omega))$, with respect to variation of σ

$$dC_a = - \left\langle G_{3D}^{eg}\left(\frac{H_r}{U^2}\delta_a\right), G_{3D}^{ej}(\mathbf{j}^{ext})d\sigma \right\rangle - \left\langle G_{3D}^{eh}\left(\frac{1}{U}\mathbf{e}_r\delta_a\right), G_{3D}^{ej}(\mathbf{j}^{ext})d\sigma \right\rangle. \quad (2.63)$$

2.4.3 Gradient of the data misfit (Z:Y case)

The differential of the misfit function defined by eq. (2.16) with respect to variation of σ can be written in the form

$$d\phi_d = 2 \operatorname{Re} \left\{ \sum_{\omega \in \Omega} \sum_{a \in \text{Sites}} (C_a(\mathbf{m}, \omega) - C_a^{\exp}(\omega))^* D_a(\omega) d(C_a(\mathbf{m}, \omega)) \right\}, \quad (2.64)$$

where the sign “*” stands for complex conjugation. Substituting eq. (2.63) into the latter equation and rearranging the terms we get

$$d\phi_d = 2 \operatorname{Re} \left\{ \sum_{\omega \in \Omega} (\langle G_{3D}^{eg}(J^G), G_{3D}^{ej}(\mathbf{j}^{ext})d\sigma \rangle + \langle G_{3D}^{eh}(\mathbf{J}^H), G_{3D}^{ej}(\mathbf{j}^{ext})d\sigma \rangle) \right\}, \quad (2.65)$$

where

$$\mathbf{J}^H = - \sum_{a \in \text{Sites}} (C_a(\mathbf{m}, \omega) - C_a^{\exp}(\omega))^* D_a \frac{1}{U_a} \mathbf{e}_r \delta_a, \quad (2.66)$$

and where

$$J^G = - \sum_{a \in \text{Sites}} (C_a(\mathbf{m}, \omega) - C_a^{\exp}(\omega))^* D_a \frac{H_r}{U^2} \Big|_a \delta_a. \quad (2.67)$$

Taking in mind our model parametrization we obtain the expressions for the partial derivatives $\frac{\partial \phi_d}{\partial m_l}$ in the form

$$\frac{\partial \phi_d}{\partial m_l} = \sigma_l \frac{\partial \phi_d}{\partial \sigma_l}, \quad (2.68)$$

where

$$\frac{\partial \phi_d}{\partial \sigma_l} = 2 \operatorname{Re} \left\{ \sum_{\omega \in \Omega} \left(\int_{V_l} G_{3D}^{eh}(\mathbf{J}^H) \cdot G_{3D}^{ej}(\mathbf{j}^{ext}) dv + \int_{V_l} G_{3D}^{eg}(J^G) \cdot G_{3D}^{ej}(\mathbf{j}^{ext}) dv \right) \right\}. \quad (2.69)$$

Here the sign “·” stands for the bilinear scalar product

$$\mathbf{a} \cdot \mathbf{b} = a_r b_r + a_\vartheta b_\vartheta + a_\varphi b_\varphi. \quad (2.70)$$

The formula (2.69) practically means that computational loads for calculating gradient $(\frac{\partial \phi}{\partial m_1}, \frac{\partial \phi}{\partial m_2}, \dots, \frac{\partial \phi}{\partial m_{N_{inv}}})^T$ are equivalent to those for the solution of N_{freq} forward problems $G_{3D}^{ej}(\mathbf{j}^{ext})$ and N_{freq} adjoint problems $G_{3D}^{eh}(\mathbf{J}^H)$ and $G_{3D}^{eg}(\mathbf{J}^G)$.

2.4.4 Reciprocity of operator G_{3D}^{ej}

In this subsection we show that

$$\langle G_{3D}^{ej}(\mathbf{a}), \mathbf{b} \rangle = \langle \mathbf{a}, G_{3D}^{ej}(\mathbf{b}) \rangle. \quad (2.71)$$

First let us obtain, from Maxwell's equations (2.39), the equation for electric field. By substituting the second equation of (2.39) into the first equation we have

$$\nabla \times \left(\frac{\nabla \times \mathbf{E}}{i\omega\mu_0} \right) - \sigma\mathbf{E} = \mathbf{j}^{ext}. \quad (2.72)$$

Let $\mathbf{A} = G_{3D}^{ej}(\mathbf{a})$ and $\mathbf{B} = G_{3D}^{ej}(\mathbf{b})$, i.e.

$$\nabla \times \left(\frac{\nabla \times \mathbf{A}}{i\omega\mu_0} \right) - \sigma\mathbf{A} = \mathbf{a}, \quad (2.73)$$

and

$$\nabla \times \left(\frac{\nabla \times \mathbf{B}}{i\omega\mu_0} \right) - \sigma\mathbf{B} = \mathbf{b}. \quad (2.74)$$

Using the reciprocity of $\nabla \times$ operator we obtain the following sequence of equalities

$$\begin{aligned} \langle G_{3D}^{ej}(\mathbf{a}), \mathbf{b} \rangle &= \langle \mathbf{A}, \nabla \times \left(\frac{\nabla \times \mathbf{B}}{i\omega\mu_0} \right) - \sigma\mathbf{B} \rangle = \langle \mathbf{A}, \nabla \times \left(\frac{\nabla \times \mathbf{B}}{i\omega\mu_0} \right) \rangle - \\ \langle \mathbf{A}, \sigma\mathbf{B} \rangle &= \langle \nabla \times \mathbf{A}, \frac{\nabla \times \mathbf{B}}{i\omega\mu_0} \rangle - \langle \sigma\mathbf{A}, \mathbf{B} \rangle = \langle \nabla \times \left(\frac{\nabla \times \mathbf{B}}{i\omega\mu_0} \right), \mathbf{B} \rangle - \\ \langle \sigma\mathbf{A}, \mathbf{B} \rangle &= \langle \nabla \times \left(\frac{\nabla \times \mathbf{A}}{i\omega\mu_0} \right) - \sigma\mathbf{A}, \mathbf{B} \rangle = \langle \mathbf{a}, G_{3D}^{ej}(\mathbf{b}) \rangle. \end{aligned} \quad (2.75)$$

2.5 Estimates of CPU time needed to perform a full cycle of 3-D inversion

We will call as a full cycle of 3-D inversion, a set of solutions of optimization problem (2.14) for N_λ trial values of regularization parameter λ , needed to achieve reasonable balance between sufficient decrease of misfit and desirable smoothness of the recovered 3-D model. We will call as a single inversion run, a solution of optimization problem (2.14) for one value of λ . Since the forward calculations take the largest proportion of the computational efforts during an inversion, the number of forward problems performed during one inversion run gives an impression regarding the overall computational load to perform a full cycle of inversions. We can estimate the number of forward modelings, N as

$$N = N_{iter} \times N_{calls} \times 3 \times N_{freq}, \quad (2.76)$$

where N_{iter} is the number of LMQN (or NLCG) iterations (updates), N_{calls} is the number of gradient estimates per iterate, N_{freq} is the number of frequencies on which C -responses are determined, 3 stands for a number of sources needed to calculate the gradients. By taking upper bounds for $N_{iter} = 100$, $N_{calls} = 5$, $N_{freq} = 10$ we obtain that $N = 15000$. In the forthcoming subsections we derive an estimate of the CPU time for a single (optimized) forward modeling. This number turns out to be 7 sec. Multiplying $N = 15000$ on 7 sec we obtain that one inverse run on a single processor takes 30 hours of CPU time. Parallelization with respect to frequencies diminishes the CPU time down to a few hours.

2.6 Forward modeling scheme: integral equation (IE) approach

2.6.1 Governing equations

To solve the forward problem (Maxwell's equations) either in the form (2.40) or (2.42), or (2.45) we have adopted the numerical solution which is described in Kuvshinov et al. [2002, 2005]) and which has been already successfully applied for a variety of global induction problems [cf. Maus and Kuvshinov, 2004, Kuvshinov and Olsen, 2005a,b, Kuvshinov et al., 2006, Manoj et al., 2006, Kuvshinov and Olsen, 2006b, Kuvshinov et al., 2007]. The solution is based on a volume integral equation approach, which combines the modified iterative dissipative method ([Singer, 1995]) with conjugate gradient iteration. The solution simulates electromagnetic (EM) fields excited by arbitrary sources in three-dimensional (3-D) spherical models of electric conductivity. These models consist of a number of anomalies of 3-D conductivity $\sigma(\mathbf{r})$, embedded in a host section of radially symmetric (1-D) conductivity $\sigma_0(r)$. Within the approach we first reduce the initial form of Maxwell's equations (with respect to total fields \mathbf{E} and \mathbf{H}) to Maxwell's equations with respect to scattered fields $\mathbf{E}^s = \mathbf{E} - \mathbf{E}^0$ and $\mathbf{H}^s = \mathbf{H} - \mathbf{H}^0$

$$\begin{aligned}\nabla \times \mathbf{H}^s &= \sigma \mathbf{E}^s + \mathbf{j}^s, \\ \nabla \times \mathbf{E}^s &= i\omega\mu_0 \mathbf{H}^s,\end{aligned}\quad (2.77)$$

where

$$\mathbf{j}^s = (\sigma - \sigma_0)\mathbf{E}^0. \quad (2.78)$$

Note that \mathbf{E}^0 is either the solution of

$$\begin{aligned}\nabla \times \mathbf{H}^0 &= \sigma_0 \mathbf{E}^0 + \mathbf{j}^{ext}, \\ \nabla \times \mathbf{E}^0 &= i\omega\mu_0 \mathbf{H}^0,\end{aligned}\quad (2.79)$$

or

$$\begin{aligned}\nabla \times \mathbf{H}^0 &= \sigma_0 \mathbf{E}^0, \\ \nabla \times \mathbf{E}^0 &= i\omega\mu_0 \mathbf{H}^0 + \mathbf{h}^{ext},\end{aligned}\quad (2.80)$$

or

$$\begin{aligned}\nabla \times \mathbf{H}^0 &= \sigma_0 \mathbf{E}^0, \\ \nabla \times \mathbf{E}^0 &= i\omega\mu_0 \mathbf{H}^0 + \nabla_\tau P.\end{aligned}\quad (2.81)$$

If we know Green's tensors (fundamental solutions) G_{1D}^{ej} , G_{1D}^{eh} and G_{1D}^{eg} of the respective equations (2.79), (2.80) and (2.81) then we can write either

$$\mathbf{E}^0(\mathbf{r}) = \int_{V^{ext}} G_{1D}^{ej}(\mathbf{r}, \mathbf{r}') \mathbf{j}^{ext}(\mathbf{r}') d\mathbf{v}', \quad \mathbf{r} \in V^{mod}, \quad (2.82)$$

or

$$\mathbf{E}^0(\mathbf{r}) = \int_{V^{ext}} G_{1D}^{eh}(\mathbf{r}, \mathbf{r}') \mathbf{h}^{ext}(\mathbf{r}') d\mathbf{v}', \quad \mathbf{r} \in V^{mod}, \quad (2.83)$$

or

$$\mathbf{E}^0(\mathbf{r}) = \int_{V^{ext}} G_{1D}^{eg}(\mathbf{r}, \mathbf{r}') P(\mathbf{r}') d\mathbf{v}', \quad \mathbf{r} \in V^{mod}, \quad (2.84)$$



where V^{ext} is the volume occupied by the imposed source \mathbf{j}^{ext} (or \mathbf{h}^{ext} or $\nabla_{\tau}P$), V^{mod} is a modeling region, where $\sigma - \sigma_0$ differs from 0. Explicit forms for G_{1D}^{ej} can be found in the Appendix of [Kuvshinov \[2008\]](#), whereas explicit forms for G_{1D}^{eh} and G_{1D}^{eg} are presented in forthcoming sections.

Further eq. (2.77) are reduced to a scattering equation of specific type [[Pankratov et al., 1997](#)]

$$\chi(\mathbf{r}) - \int_{V^{mod}} K(\mathbf{r}, \mathbf{r}') R(\mathbf{r}') \chi(\mathbf{r}') d\mathbf{v}' = \chi_o(\mathbf{r}), \quad \mathbf{r} \in V^{mod}, \quad (2.85)$$

which is solved by the generalized bi-conjugate gradient method [[Zhang, 1997](#)]. Here

$$R = \frac{\sigma - \sigma_0}{\sigma + \sigma_0}, \quad (2.86)$$

$$K(\mathbf{r}, \mathbf{r}') = \delta(\mathbf{r} - \mathbf{r}') I + 2\sqrt{\sigma_o(r)} G_{1D}^{ej}(\mathbf{r}, \mathbf{r}') \sqrt{\sigma_o(r')}, \quad (2.87)$$

$$\chi_o = \int_{V^{mod}} K(\mathbf{r}, \mathbf{r}') \frac{\sqrt{\sigma_o}}{\sigma + \sigma_o} \mathbf{j}^s(\mathbf{r}') d\mathbf{v}', \quad (2.88)$$

$$\chi = \frac{1}{2\sqrt{\sigma_o}} ((\sigma + \sigma_o) \mathbf{E}^s + \mathbf{j}^s), \quad (2.89)$$

Here $\delta(\mathbf{r} - \mathbf{r}')$ is Dirac's delta function, I is the identity operator,

Once χ is determined from the solution of the scattering equation (2.85), the magnetic field, \mathbf{H} , at the observation points, $\mathbf{r} \in Sites$ is calculated as

$$\mathbf{H} = \int_{V^{ext}} G_{1D}^{hj}(\mathbf{r}, \mathbf{r}') \mathbf{j}^{ext}(\mathbf{r}') d\mathbf{v}' + \int_{V^{mod}} G_{1D}^{hj}(\mathbf{r}, \mathbf{r}') \mathbf{j}^q(\mathbf{r}') d\mathbf{v}', \quad (2.90)$$

with

$$\mathbf{j}^q = (\sigma - \sigma_0)(\mathbf{E}^0 + \mathbf{E}^s), \quad (2.91)$$

$$\mathbf{E}^s = \frac{1}{\sigma + \sigma_0} (2\sqrt{\sigma_0} \chi - \mathbf{j}^s). \quad (2.92)$$

Explicit expressions for the elements of G_{1D}^{hj} are given in the Appendix of [Kuvshinov \[2008\]](#).

2.6.2 Optimization of the IE solution within 3-D inversion

The efficiency of 3-D inversion depends critically on the ability to perform fast and robust calculation of the responses (forward problem solution). Since our forward solver is based on an integral equation (IE) formulation we can take advantage of the IE solution and perform the time-consuming part of the simulations (calculations of tensor Greens functions) only once, prior to the inversion iterations. We have conducted model studies to investigate whether we indeed speed up the forward problem solution in the frame of inverse problem solution by calculating tensor Greens functions prior to inversion iterations. We calculated the responses within a 3-D conductivity model discretized by $N_r \times N_{\vartheta} \times N_{\varphi} = 6 \times 36 \times 72 = 15552$ cells (we plan to use this discretization during 3-D inversion). The CPU times for different modules of the forward solution at a specific frequency (on a single processor of ETH cluster Gonzales (which consists of 576 processors)) are

- Calculation of $G_{1D}^{ej}(\mathbf{r}, \mathbf{r}', \{\sigma_0(r)\}, \omega_i)$ (where $\mathbf{r} \in V_{mod}$, $\mathbf{r}' \in V_{mod}$) takes 120 sec
- Solution of scattering equation takes 5 sec
- Calculation of $G_{1D}^{hj}(\mathbf{r}, \mathbf{r}', \{\sigma_0(r)\}, \omega_i)$ (where $\mathbf{r} \in Sites$, $\mathbf{r}' \in V_{mod}$) takes 20 sec

These estimates in particular mean that isolating calculation of Green's functions gives $(120 \text{ sec} + 20 \text{ sec})/7 \text{ sec} = 20$ times acceleration of the forward problem calculations. We modified our solution to admit such kind of isolation.

Another dramatic saving of computational loads comes from parallelization of IE solution. Since forward calculations are completely independent with respect to frequencies we can perform the modelings at different frequencies in parallel on N_{freq} processors. It gives an additional N_{freq} times acceleration of the forward solution. of IE code that admits such a kind of parallelizations. Using N_{freq} processors we indeed succeeded in N_{freq} acceleration of the forward solution.

Finally, during a full cycle of inversion we have to conduct independent inversion runs for N_λ values of regularization parameter. Thus we can readily achieve additional N_λ times acceleration if we have enough number of processors.

2.6.3 Explicit forms for Green's tensor G_{1D}^{eh}

Let us consider Maxwell's equations

$$\begin{aligned} \nabla \times \mathbf{H} &= \sigma_0(r) \mathbf{E}, \\ \nabla \times \mathbf{E} &= i\omega\mu_0 \mathbf{H} + \mathbf{q}^{ext}. \end{aligned} \quad (2.93)$$

We then introduce vector spherical functions, which are determined via scalar functions $S_n^m(\vartheta, \varphi) = P_n^{|m|}(\cos \vartheta) e^{im\varphi}$ as

$$\begin{aligned} \mathbf{S}_{nm}^r &= S_m^n(\vartheta, \varphi) \mathbf{e}_r, \\ \mathbf{S}_{nm}^t &= \frac{1}{\sqrt{n(n+1)}} \mathbf{e}_r \times \nabla_{\perp} S_n^m(\vartheta, \varphi), \\ \mathbf{S}_{nm}^p &= \frac{1}{\sqrt{n(n+1)}} \nabla_{\perp} S_n^m(\vartheta, \varphi), \end{aligned} \quad (2.94)$$

where $P_n^{|m|}$ are associated Legendre polynomials of degree n ($n = 1, 2, \dots$) and of order m ($m = 0, \pm 1, \pm 2, \dots, \pm n$), ∇_{\perp} is the angular part of operator $\nabla = \mathbf{e}_r \frac{\partial}{\partial r} + \frac{1}{r} \nabla_{\perp}$, and "×" denotes vector product. We decompose the tangential component of the electric field as

$$\mathbf{E}_\tau(r, \vartheta, \varphi) = \frac{1}{r} \sum_{n,m} \{ \varepsilon_{nm}^t(r) \mathbf{S}_{nm}^t + \varepsilon_{nm}^p(r) \mathbf{S}_{nm}^p \}. \quad (2.95)$$

Hereinafter $\sum_{n,m}$ denotes summation $\sum_{n=1}^{\infty} \sum_{m=-n}^n$. Similarly tangential components of the magnetic field and current are decomposed as

$$\mathbf{e}_r \times \mathbf{H}_\tau(r, \vartheta, \varphi) = \frac{1}{r} \sum_{n,m} \{ h_{nm}^t(r) \mathbf{S}_{nm}^t + h_{nm}^p(r) \mathbf{S}_{nm}^p \}, \quad (2.96)$$

$$\mathbf{e}_r \times \mathbf{q}_\tau^{ext}(r, \vartheta, \varphi) = \frac{1}{r} \sum_{n,m} \{ q_{nm}^t(r) \mathbf{S}_{nm}^t + q_{nm}^p(r) \mathbf{S}_{nm}^p \}. \quad (2.97)$$



‡

$$\mathbf{H}_\tau(r, \vartheta, \varphi) = \frac{1}{r} \sum_{n,m} \{-h_{nm}^p(r)\mathbf{S}_{nm}^t + h_{nm}^t(r)\mathbf{S}_{nm}^p\}, \quad (2.98)$$

$$\mathbf{q}_\tau^{ext}(r, \vartheta, \varphi) = \frac{1}{r} \sum_{n,m} \{-q_{nm}^p(r)\mathbf{S}_{nm}^t + q_{nm}^t(r)\mathbf{S}_{nm}^p\}. \quad (2.99)$$

Radial components of the field and current we decompose as

$$E_r(r, \vartheta, \varphi)\mathbf{e}_r = \frac{1}{r} \sum_{n,m} \varepsilon_{nm}^r(r)\mathbf{S}_{nm}^r, \quad (2.100)$$

$$H_r(r, \vartheta, \varphi)\mathbf{e}_r = \frac{1}{r} \sum_{n,m} h_{nm}^r(r)\mathbf{S}_{nm}^r, \quad (2.101)$$

$$q_r^{ext}(r, \vartheta, \varphi)\mathbf{e}_r = \frac{1}{r} \sum_{n,m} q_{nm}^r(r)\mathbf{S}_{nm}^r. \quad (2.102)$$

Substituting (2.95)-(2.102) into Maxwell's equations (2.93) and gathering together terms involving functions \mathbf{S}_{nm}^t and \mathbf{S}_{nm}^p , we get the systems of equations

$$\begin{cases} \partial_r \varepsilon_{nm}^t = -i\omega\mu_0 h_{nm}^t - q_{nm}^t, \\ \partial_r h_{nm}^t = \varepsilon_{nm}^t (\sigma_0 - \frac{n(n+1)}{r^2 i\omega\mu_0}) - \frac{\sqrt{n(n+1)}}{ri\omega\mu_0} q_{nm}^r, \end{cases} \quad (2.103)$$

$$\begin{cases} \partial_r \varepsilon_{nm}^p = h_{nm}^p (\frac{n(n+1)}{r^2 \sigma_0} - i\omega\mu_0) - q_{nm}^p, \\ \partial_r h_{nm}^p = \sigma_0 \varepsilon_{nm}^p, \end{cases} \quad (2.104)$$

$$\begin{cases} \sigma_0 \varepsilon_{nm}^r = \frac{h_{nm}^p \sqrt{n(n+1)}}{r}, \\ i\omega\mu_0 h_{nm}^r = -\frac{\varepsilon_{nm}^t \sqrt{n(n+1)}}{r} - q_{nm}^r. \end{cases} \quad (2.105)$$

Systems (2.103) and (2.104) can be written in the following generic form

$$\begin{cases} \partial_r \varepsilon(r) = p(r)h(r) + f_h(r), \\ \partial_r h(r) = q(r)\varepsilon(r) + f_\varepsilon(r), \end{cases} \quad (2.106)$$

where

$$\begin{aligned} \varepsilon(r) &= \varepsilon_{nm}^t, & h(r) &= h_{nm}^t, \\ p(r) &= -i\omega\mu_0, & q(r) &= \sigma_0 - \frac{n(n+1)}{r^2 i\omega\mu_0}, \\ f_h(r) &= -q_{nm}^t, & f_\varepsilon(r) &= -\frac{\sqrt{n(n+1)}}{ri\omega\mu_0} q_{nm}^r, \end{aligned} \quad (2.107)$$

for system (2.103) and

$$\begin{aligned} \varepsilon(r) &= \varepsilon_{nm}^p, & h(r) &= h_{nm}^p, \\ p(r) &= \frac{n(n+1)}{r^2 \sigma_0} - i\omega\mu_0, & q(r) &= \sigma_0, \\ f_h(r) &= -q_{nm}^p, & f_\varepsilon(r) &= 0, \end{aligned} \quad (2.108)$$

for system (2.104). System (2.106) can be reduced to the second order equation

$$\partial_r \left(\frac{1}{p(r)} \partial_r \varepsilon(r) \right) - q(r)\varepsilon(r) = f(r), \quad (2.109)$$



where

$$f(r) = f_\varepsilon(r) + \partial_r \left(\frac{f_h(r)}{p(r)} \right). \quad (2.110)$$

The solution of (2.109) can be written as

$$\varepsilon(r) = \int_0^\infty G(n, r, r') f(r') dr', \quad (2.111)$$

where $G(n, r, r')$ is scalar Green's function of equation (2.109). We impose boundary conditions on the solution of (2.109) in the form $\varepsilon(r) \rightarrow 0$, when $r \rightarrow 0$ and $r \rightarrow \infty$.

Green's function

Definition: A Green's function, $G(x, s)$, of a linear differential operator $L = L(x)$ acting on distributions over a subset of the Euclidean space R^n , at a point s , is any solution of

$$LG(x, s) = \delta(x - s)$$

where δ is the Dirac delta function. If the kernel of L is nontrivial, then the Green's function is not unique. However, in practice, some combination of symmetry, boundary conditions and/or other externally imposed criteria will give a unique Green's function.

This property of a Green's function can be exploited to solve differential equations of the form

$$Lu(x) = f(x)$$

So, if such a function G can be found for the operator L , then if we multiply the first equation for the Green's function by $f(s)$, and then integrate in the s variable, we obtain:

$$\int LG(x, s) f(s) ds = \int \delta(x - s) f(s) ds = f(x) = Lu(x)$$

Because the operator $L = L(x)$ is linear and acts only on the variable x :

$$Lu(x) = L \left(\int G(x, s) f(s) ds \right) \Leftrightarrow u(x) = \int G(x, s) f(s) ds$$

Properties of the Green's function:

1. $G(n, r, r')$ is continuous, depending on r ;

2. $G(n, r, r') \rightarrow 0 \begin{cases} r \rightarrow \infty \\ r \rightarrow 0 \end{cases}$.

The first two properties arise from our definition of the Green's function.

3. $\left[\frac{1}{p(r)} \partial_r G(n, r, r') \right]_{r=r'-0}^{r=r'+0} = 1$

It comes from continuity of the Green's function, substituting in equation, defining it.

$$\int_{r'-\Delta}^{r'+\Delta} \partial_r \left(\frac{1}{p(r)} \partial_r G(n, r, r') \right) dr = \int_{r'-\Delta}^{r'+\Delta} q(r) G(n, r, r') dr + \int_{r'-\Delta}^{r'+\Delta} \delta(r - r') dr$$

Since $[q(r)G(n, r, r')]_{r=r'-0}^{r=r'+0}$ is finite the right part is equal to 1 and the left one to $\left[\frac{1}{p(r)} \partial_r G(n, r, r') \right]_{r=r'-0}^{r=r'+0}$

4. $G(n, r, r') = G(n, r', r)$

Proof:

$$\partial_r \left(\frac{1}{p(r)} \partial_r G(n, r, r') \right) = q(r) G(n, r, r') + \delta(r - r')$$



and another one

$$\partial_r \left(\frac{1}{p(r)} \partial_r G(n, r, r'') \right) = q(r) G(n, r, r'') + \delta(r - r'')$$

Let's multiply the first one by $G(n, r, r'')$ and the second one by $G(n, r, r')$. Afterwards subtract one from another and integrate over r :

$$\begin{aligned} & \int_0^\infty \partial_r \left(\frac{1}{p(r)} \partial_r G(n, r, r') \right) G(n, r, r'') dr - \int_0^\infty \partial_r \left(\frac{1}{p(r)} \partial_r G(n, r, r'') \right) G(n, r, r') dr = \\ &= \int_0^\infty G(n, r, r'') \delta(r - r') dr - \int_0^\infty G(n, r, r') \delta(r - r'') dr \end{aligned}$$

The left part leads to:

$$\frac{1}{p(r)} G(n, r, r'') \partial_r G(n, r, r') \Big|_0^\infty - \frac{1}{p(r)} G(n, r, r') \partial_r G(n, r, r'') \Big|_0^\infty = 0$$

because of the boundary conditions. And that means, that

$$G(n, r', r'') = G(n, r'', r')$$

Substituting (2.110) into (2.111) and integrating by parts, we get

$$\varepsilon(r) = \int_0^\infty G(n, r, r') f_\varepsilon(r') dr' - \int_0^\infty \beta G(n, r, r') f_h(r') dr', \quad (2.112)$$

where

$$\beta(n, r, r') = \frac{\partial_{r'} G(n, r, r')}{p(r') G(n, r, r')} \quad (2.113)$$

Then, substituting (2.112) into the first equation of the system (2.106), we get in a similar way

$$\begin{aligned} h(r) &= \frac{1}{p(r)} (\partial_r \varepsilon(r) - f_h(r)) = \\ &= \frac{\partial_r}{p(r)} \int G f_\varepsilon(r') dr' - \frac{\partial_r}{p(r)} \int \frac{\partial_{r'} G}{p(r')} f_h(r') dr' - \frac{1}{p(r)} f_h(r) \xrightarrow{(2.116)} \\ &\xrightarrow{(2.116)} \int \frac{\partial_r G}{p(r)} f_\varepsilon(r') dr' - \frac{1}{p(r)} \int \frac{\partial_r G}{p(r') G} \frac{\partial_{r'} G}{G} G f_h(r') dr' - \\ &- \frac{1}{p(r)} \int \partial_r \left(\frac{\partial_{r'} G}{p(r') G} \right) G f_h(r') dr' - \frac{1}{p(r)} f_h(r) \xrightarrow{(2.117)} \\ &\xrightarrow{(2.117)} \int \alpha G f_\varepsilon(r') dr' - \int \alpha \beta G f_h(r') dr' + \\ &+ \frac{1}{p(r)} \int \frac{\delta(r - r')}{G(n, r, r)} G(n, r, r') f_h(r') dr' - \frac{1}{p(r)} f_h(r) = \\ &= \int \alpha G f_\varepsilon(r') dr' - \int \alpha \beta G f_h(r') dr' \end{aligned} \quad (2.114)$$



where

$$\alpha(n, r, r') = \beta(n, r', r). \quad (2.115)$$

While deriving eq. (2.114) we used

$$\partial_r \left(\frac{\partial_{r'} G}{p(r')G} \right) = \frac{\partial_r}{p(r')} \left(\frac{\partial_{r'} G}{G} \right) = \frac{\partial_r \partial_{r'} G}{p(r')G} - \frac{\partial_r G \partial_{r'} G}{p(r')G^2}, \quad (2.116)$$

$$\partial_r \left(\frac{\partial_{r'} G}{p(r')G} \right) = \partial_r \beta(n, r, r') = -\frac{\delta(r - r')}{G(n, r, r)}. \quad (2.117)$$

This equality comes from discontinuity of β for $r = r'$ (see explanation below (2.129)).

Substituting further (2.107) and (2.108) into (2.112) and (2.114) we express coefficients $\varepsilon_{nm}^t, \varepsilon_{nm}^p, h_{nm}^t, h_{nm}^p$ via coefficients $q_{nm}^t, q_{nm}^p, q_{nm}^r$

$$\begin{aligned} \varepsilon_{nm}^t &= - \int_0^\infty G^t(n, r, r') \frac{\sqrt{n(n+1)}}{r' i \omega \mu_0} q_{nm}^r(r') dr' + \\ &\quad + \int_0^\infty \beta^t G^t(n, r, r') q_{nm}^t(r') dr', \end{aligned} \quad (2.118)$$

$$\varepsilon_{nm}^p = \int_0^\infty \beta^p G^p(n, r, r') q_{nm}^p(r') dr', \quad (2.119)$$

$$\begin{aligned} h_{nm}^t &= - \int_0^\infty \alpha^t G^t(n, r, r') \frac{\sqrt{n(n+1)}}{r' i \omega \mu_0} q_{nm}^r(r') dr' + \\ &\quad + \int_0^\infty \alpha^t \beta^t G^t(n, r, r') q_{nm}^t(r') dr', \end{aligned} \quad (2.120)$$

$$h_{nm}^p = \int_0^\infty \alpha^p \beta^p G^p(n, r, r') q_{nm}^p(r') dr'. \quad (2.121)$$

Then, using decompositions (2.97) and (2.102), the coefficients $q_{nm}^t(r')$, $q_{nm}^p(r')$ and $q_{nm}^r(r')$ are written as

$$q_{nm}^t(r') = \frac{r'}{\|S_n^m\|^2 \sqrt{n(n+1)}} \int_{\Omega} \nabla'_{\perp} \cdot (\mathbf{e}_{r'} \times \mathbf{e}_{r'} \times \mathbf{q}_{\tau}) \widetilde{S}_n^m d\Omega' = \quad (2.122)$$

$$= - \frac{r'}{\|S_n^m\|^2 \sqrt{n(n+1)}} \int_{\Omega} \nabla'_{\perp} \cdot \mathbf{q}_{\tau} \widetilde{S}_n^m d\Omega',$$

$$q_{nm}^p(r') = - \frac{r'}{\|S_n^m\|^2 \sqrt{n(n+1)}} \int_{\Omega} \nabla'_{\perp} \cdot (\mathbf{e}_{r'} \times \mathbf{q}_{\tau}) \widetilde{S}_n^m d\Omega', \quad (2.123)$$



$$q_{nm}^r(r') = \frac{r'}{\|S_n^m\|^2} \int_{\Omega} q_r \widetilde{S}_n^m d\Omega'. \quad (2.124)$$

Here Ω is complete solid angle, $d\Omega = d\vartheta' d\varphi' \sin \vartheta'$, $\widetilde{S}_n^m = \widetilde{S}_n^m(\vartheta', \varphi')$ denotes complex conjugation of S_n^m . Substituting (2.122)-(2.124) into (2.118)-(2.121) and further (2.94) and (2.118)-(2.121) into (2.95) and after some algebra we get

$$\begin{aligned} \mathbf{E}_\tau(r, \vartheta, \varphi) &= \frac{1}{r} \sum_{n,m} (\varepsilon_{nm}^t(r) \mathbf{S}_{nm}^t + \varepsilon_{nm}^p(r) \mathbf{S}_{nm}^p) = \\ &= \frac{1}{r} \sum_{n,m} \left(\left(\int_0^\infty G^t \frac{\beta^t}{\sqrt{n(n+1)}} q_{nm}^t(r') dr' - \right. \right. \\ &\quad \left. \left. - \int_0^\infty G^t \frac{\sqrt{n(n+1)}}{r' i \omega \mu_0} q_{nm}^r(r') dr' \right) \frac{1}{\sqrt{n(n+1)}} \mathbf{S}_{nm}^t + \right. \\ &\quad \left. + \int_0^\infty \beta^p G^p q_{nm}^p(r') dr' \frac{1}{\sqrt{n(n+1)}} \mathbf{S}_{nm}^p \right) = \\ &= \int_{\Omega} \int_0^\infty (\mathbf{e}_r \times \nabla_\perp) \left\{ \left[\nabla'_\perp \sum_{n,m} \frac{r' \beta^t G^t}{rn(n+1)} \frac{\widetilde{S}_n^m S_n^m}{\|S_n^m\|^2} \right] \cdot \mathbf{q}_\tau \right\} dr' d\Omega' - \\ &\quad - \int_{\Omega} \int_0^\infty (\mathbf{e}_r \times \nabla_\perp) \left\{ \left(\sum_{n,m} \frac{G^t}{rn(n+1)} \frac{\widetilde{S}_n^m S_n^m}{\|S_n^m\|^2} \right) q_r \right\} dr' d\Omega' - \\ &\quad - \int_{\Omega} \int_0^\infty \nabla_\perp \left\{ \left[(\mathbf{e}_{r'} \times \nabla'_\perp) \left(\sum_{n,m} \frac{r' \beta^p G^p}{ri \omega \mu_0} \frac{\widetilde{S}_n^m S_n^m}{\|S_n^m\|^2} \right) \right] \cdot \mathbf{q}_\tau \right\} dr' d\Omega' = \\ &= \int_{\Omega} \int_0^\infty (\mathbf{e}_r \times \nabla_\perp) \left\{ \nabla'_\perp P \left[\frac{r' \beta^t G^t}{rn(n+1)} \right] \cdot \mathbf{q}_\tau \right\} dr' d\Omega' - \\ &\quad - \int_{\Omega} \int_0^\infty (\mathbf{e}_r \times \nabla_\perp) \left\{ P \left[\frac{G^t}{ri \omega \mu_0} \right] q_r \right\} dr' d\Omega' - \\ &\quad - \int_{\Omega} \int_0^\infty \nabla_\perp \left\{ \left[(\mathbf{e}_{r'} \times \nabla'_\perp) P \left[\frac{r' \beta^p G^p}{rn(n+1)} \right] \right] \cdot \mathbf{q}_\tau \right\} dr' d\Omega', \end{aligned} \quad (2.125)$$

$$\begin{aligned} E_r(r, \vartheta, \varphi) &= \frac{1}{r} \sum_{n,m} \varepsilon_{nm}^r S_n^m = \frac{1}{r} \sum_{n,m} \frac{h_{nm}^p \sqrt{n(n+1)}}{\sigma_0 r} S_n^m = \\ &= -\frac{1}{r} \sum_{n,m} \frac{\sqrt{n(n+1)}}{\sigma_0 r} \int_0^\infty \alpha^p \beta^p G^p \frac{r'}{\|S_n^m\|^2 \sqrt{n(n+1)}} \int_{\Omega} \nabla'_\perp \cdot (\mathbf{e}_{r'} \times \mathbf{q}_\tau) \widetilde{S}_n^m dr' d\Omega' = \\ &= -\int_{\Omega} \int_0^\infty \left\{ (\mathbf{e}_{r'} \times \nabla'_\perp) P \left[\frac{\alpha^p \beta^p G^p r'}{\sigma_0 r^2} \right] \right\} \cdot \mathbf{q}_\tau dr' d\Omega'. \end{aligned} \quad (2.126)$$

Now from (2.125)-(2.126) we write the expressions for elements $g_{\vartheta\vartheta'}^{eh}, g_{\vartheta\varphi'}^{eh}, \dots$



$$\begin{aligned}
g_{\vartheta\vartheta'}^{eh} &= -\frac{1}{\sin \vartheta} \partial_\vartheta \partial_{\vartheta'} P\left[\frac{\beta^t G^t(n, r, r')}{rr'n(n+1)}\right] + \frac{1}{\sin \vartheta'} \partial_\vartheta \partial_{\vartheta'} P\left[\frac{\beta^p G^p(n, r, r')}{rr'n(n+1)}\right] \\
g_{\vartheta\varphi'}^{eh} &= -\frac{1}{\sin \vartheta} \frac{1}{\sin \vartheta'} \partial_\vartheta \partial_{\varphi'} P\left[\frac{\beta^t G^t(n, r, r')}{rr'n(n+1)}\right] - \partial_\vartheta \partial_{\vartheta'} P\left[\frac{\beta^p G^p(n, r, r')}{rr'n(n+1)}\right] \\
g_{\vartheta r'}^{eh} &= \frac{1}{\sin \vartheta} \partial_\varphi P\left[\frac{G^t(n, r, r')}{r'^2 ri\omega\mu_0}\right] \\
g_{\varphi\vartheta'}^{eh} &= \partial_\vartheta \partial_{\vartheta'} P\left[\frac{\beta^t G^t(n, r, r')}{rr'n(n+1)}\right] + \frac{1}{\sin \vartheta} \frac{1}{\sin \vartheta'} \partial_\varphi \partial_{\varphi'} P\left[\frac{\beta^p G^p(n, r, r')}{rr'n(n+1)}\right] \\
g_{\varphi\varphi'}^{eh} &= \frac{1}{\sin \vartheta'} \partial_\vartheta \partial_{\varphi'} P\left[\frac{\beta^t G^t(n, r, r')}{rr'n(n+1)}\right] - \frac{1}{\sin \vartheta} \partial_\varphi \partial_{\vartheta'} P\left[\frac{\beta^p G^p(n, r, r')}{rr'n(n+1)}\right] \quad (2.127) \\
g_{\varphi r'}^{eh} &= -\partial_\vartheta P\left[\frac{G^t(n, r, r')}{r'^2 ri\omega\mu_0}\right] \\
g_{r\vartheta'}^{eh} &= \frac{1}{\sin \vartheta'} \partial_\varphi P\left[\frac{\alpha^p \beta^p G^p(n, r, r')}{r^2 r' \sigma_0}\right] \\
g_{r\varphi'}^{eh} &= -\partial_{\vartheta'} P\left[\frac{\alpha^p \beta^p G^p(n, r, r')}{r^2 r' \sigma_0}\right] \\
g_{rr'}^{eh} &= 0.
\end{aligned}$$

Note, that all above components depend on $(r, r', \vartheta, \vartheta', \varphi - \varphi')$. Also, the transform

$$\mathcal{P}[f](\cos \gamma, r, r') = \sum_{n=1}^{\infty} \frac{2n+1}{4\pi} f(n, r, r') P_n(\cos \gamma), \quad (2.128)$$

converts a function of spectral number n into a function of $\cos \gamma$, where $\cos \gamma = \cos \vartheta \cos \vartheta' + \sin \vartheta \sin \vartheta' \cos(\varphi - \varphi')$ and P_n is the Legendre polynomial of degree n . The spectral functions α^t , α^p are determined via four admittances $Y^{l,t}$, $Y^{u,t}$, $Y^{l,p}$ and $Y^{u,p}$ as

$$\alpha(n, r, r') = \beta(n, r', r) = \begin{cases} -Y^u(n, r), & r > r' \\ Y^l(n, r), & r < r' \end{cases} \quad (2.129)$$

The scalar Green's functions $G(n, r, r')^{t(p)}$ are determined as

$$G(n, r, r') = -\frac{1}{Y^l(n, r') + Y^u(n, r')} \exp\left(\int_{r'}^r p(n, \xi) \alpha(n, \xi, r') d\xi\right), \quad (2.130)$$

where $p^t = -i\omega\mu_0$, $p^p = -i\omega\mu_0 + \frac{n(n+1)}{r^2 \sigma_o(r)}$.

Derivatives of the spectral functions

$$\partial_r \alpha(n, r, r') = (-Y^u(n, r') - Y^l(n, r')) \delta(r - r'),$$

because $\partial_{r'}\theta(r' - r_0) = \delta(r' - r_0)$, where θ is a Heaviside step function and δ is a Dirac function. And this leads to

$$\partial_{r'}\alpha(n, r, r') = \frac{1}{G(n, r', r)}\delta(r - r') = -\frac{1}{G(n, r', r)}\delta(r' - r),$$

and

$$\partial_r\beta(n, r, r') = \partial_r\alpha(n, r', r) = -\frac{1}{G(n, r, r)}\delta(r - r')$$

The four admittances $Y^{l,t}(n, r)$, $Y^{u,t}(n, r)$, $Y^{l,p}(n, r)$, $Y^{u,p}(n, r)$, and two factors $F^t(n, r, r') = \exp(\int_{r'}^r p^t(\xi)\alpha^t(n, \xi, r')d\xi)$, $F^p(n, r, r') = \exp(\int_{r'}^r p^p(n, \xi)\alpha^p(n, \xi, r')d\xi)$ are calculated by a unified procedure described below.

We assume that the radially symmetric reference section consists of N layers $\{r_{k+1} < r \leq r_k\}_{k=1,2,\dots,N}$. We construct the set $\{r_k\}_{k=1,2,\dots,N}$ in such a way that it includes all levels r_j , where we will calculate the admittances and the Green's scalar functions. We assume that within each layer the conductivity varies as

$$\sigma_o(r) = \sigma_k \left(\frac{r_k}{r} \right)^2, \quad r_{k+1} < r \leq r_k, \quad (2.131)$$

where $r_1 = r_e$ is the Earth's radius, $r_{N+1} = 0$, σ_k is an appropriate constant. Since N can be taken as large as necessary, the distribution (2.131) allows the approximation of any radially symmetric conductivity section. Distribution (2.131) is chosen to make the recurrence formulae as simple as possible. We express these formulae in the following form

$$Y_k^{l,t} = \frac{1}{q_k} \frac{q_{k+1} Y_{k+1}^{l,t} (b_k - 0.5\tau_k) + b_k^+ b_k^- \tau_k}{(b_k + 0.5\tau_k) + q_{k+1} \tau_k Y_{k+1}^{l,t}}, \quad k = N-1, N-2, \dots, 1, \quad Y_N^{l,t} = -\frac{b_N^+}{q_N}, \quad (2.132)$$

$$Y_{k+1}^{u,t} = \frac{1}{q_{k+1}} \frac{q_k Y_k^{u,t} (b_k + 0.5\tau_k) + b_k^+ b_k^- \tau_k}{(b_k - 0.5\tau_k) + q_k \tau_k Y_k^{u,t}}, \quad k = 1, 2, \dots, N-1, \quad Y_1^{u,t} = -\frac{n}{q_1}, \quad (2.133)$$

$$Y_{k+1}^{u,p} = g_k \eta_k \frac{Y_k^{u,p} (b_k + 0.5\tau_k) - g_k \tau_k}{g_k (b_k - 0.5\tau_k) - b_k^+ b_k^- \tau_k Y_k^{u,p}}, \quad k = 1, 2, \dots, N-1, \quad Y_1^{u,p} = 0, \quad (2.134)$$

$$Y_k^{l,p} = g_k \frac{Y_{k+1}^{l,p} (b_k - 0.5\tau_k) - g_k \eta_k \tau_k}{g_k \eta_k (b_k + 0.5\tau_k) - b_k^+ b_k^- \tau_k Y_{k+1}^{l,p}}, \quad k = N-1, N-2, \dots, 1, \quad Y_N^{l,p} = \frac{\sigma_N r_N}{b_N^-}, \quad (2.135)$$

where Y_k stands for $Y(n, r_k)$, the layer number k is the index of recurrence, n is the spectral number and

$$\eta_k = \frac{r_k}{r_{k+1}}, \quad \tau_k = \frac{1 - \zeta_k}{1 + \zeta_k}, \quad \zeta_k = \eta_k^{2b_k}, \quad g_k = \sigma_k r_k, \quad q_k = i\omega \mu_0 r_k.$$

$$b_k^- = b_k - \frac{1}{2}, \quad b_k^+ = b_k + \frac{1}{2}, \quad b_k = \left\{ (n + \frac{1}{2})^2 - i\omega \mu_0 \sigma_k r_k^2 \right\}^{\frac{1}{2}}.$$

Finally the recurrence formulae for the scalar Green's functions G^t, G^p are given by



$$\begin{aligned} G(r_i, r_j) &= -\frac{1}{Y_j^l + Y_j^u} \prod_{m=j}^{i-1} F_m, \quad r_i \leq r_j, \\ G(r_i, r_j) &= G(r_j, r_i), \quad r_i > r_j. \end{aligned} \quad (2.136)$$

where the factors F_m are

$$F_m^t = \frac{1}{1 + \zeta_m} \frac{2b_m \eta_m^{b_m^-}}{(b_m + 0.5\tau_m) + q_m \tau_m Y_{m+1}^{l,t}}. \quad (2.137)$$

for a toroidal mode and

$$F_m^p = \frac{1}{1 + \zeta_m} \frac{2g_m b_m \eta_m^{b_m^-}}{g_m \eta_m (b_m + 0.5\tau_m) - b_m^+ b_m^- \tau_m Y_{m+1}^{l,p}}. \quad (2.138)$$

for a poloidal mode. Note, that in eqs. (2.132)-(2.138) a dependence on the spectral number n is omitted but implied.

2.6.4 Explicit forms for Green's tensors G_{1D}^{eg}

Let us consider Maxwell's equation

$$\begin{aligned} \nabla \times \mathbf{H} &= \sigma_0(r) \mathbf{E}, \\ \nabla \times \mathbf{E} &= i\omega \mu_0 \mathbf{H} + \nabla_{\perp} F. \end{aligned} \quad (2.139)$$

We will decompose F as

$$F = \frac{1}{r} \sum_{n,m} p_{nm}(r) S_n^m(\vartheta, \varphi) \quad (2.140)$$

where

$$p_{nm}(r') = \frac{r'}{\|S_n^m\|^2} \int_{\Omega} P(r', \vartheta', \varphi') \widetilde{S}_n^m(\vartheta', \varphi') d\Omega'. \quad (2.141)$$

Further we can write

$$\nabla_{\perp} F = \frac{1}{r} \sum_{n,m} p_{nm}(r) \nabla_{\perp} S_n^m(\vartheta, \varphi) = \frac{1}{r} \sum_{n,m} p_{nm}(r) \sqrt{n(n+1)} \mathbf{S}_{nm}^p. \quad (2.142)$$

Substituting decomposition (2.142) and decompositions of the previous subsection into eqs. (2.139) we obtain

$$\begin{cases} \partial_r \varepsilon_{nm}^t = -i\omega \mu_0 h_{nm}^t - p_{nm} \sqrt{n(n+1)}, \\ \partial_r h_{nm}^t = \varepsilon_{nm}^t (\sigma_0 - \frac{n(n+1)}{r^2 i\omega \mu_0}), \end{cases} \quad (2.143)$$

$$\begin{cases} \partial_r \varepsilon_{nm}^p = h_{nm}^p (\frac{n(n+1)}{r^2 \sigma_0} - i\omega \mu_0), \\ \partial_r h_{nm}^p = \sigma_0 \varepsilon_{nm}^p, \end{cases} \quad (2.144)$$

$$\begin{cases} \sigma_0 \varepsilon_{nm}^r = \frac{h_{nm}^p \sqrt{n(n+1)}}{r}, \\ i\omega \mu_0 h_{nm}^r = -\frac{\varepsilon_{nm}^t \sqrt{n(n+1)}}{r}, \end{cases} \quad (2.145)$$



and

$$\begin{aligned} \varepsilon &= \varepsilon_{nm}^t & h &= h_{nm}^t, \\ p(r) &= -i\omega\mu_0 & q(r) &= \sigma_0 - \frac{n(n+1)}{r^2 i\omega\mu_0}, \\ f_h(r) &= -p_{nm}\sqrt{n(n+1)} & f_\varepsilon(r) &= 0, \end{aligned} \quad (2.146)$$

for a system (2.143) and

$$\begin{aligned} \varepsilon &= \varepsilon_{nm}^p & h &= h_{nm}^p, \\ p(r) &= \frac{n(n+1)}{r^2\sigma_0} - i\omega\mu_0 & q(r) &= \sigma_0, \\ f_h(r) &= 0 & f_\varepsilon(r) &= 0. \end{aligned} \quad (2.147)$$

for a system (2.144)

Proceeding further in a similar way as we did in the previous subsection we have

$$\varepsilon_{nm}^p = h_{nm}^p = 0, \quad (2.148)$$

$$\varepsilon_{nm}^t = \int_0^\infty \beta G^t(n, r, r') p_{nm}(r') \sqrt{n(n+1)} dr', \quad (2.149)$$

$$h_{nm}^t = \int_0^\infty \alpha \beta G^t(n, r, r') p_{nm}(r') \sqrt{n(n+1)} dr', \quad (2.150)$$

and finally

$$\mathbf{E}_\tau(r, \vartheta, \varphi) = \int_{\Omega} \int_0^\infty \left\{ (\mathbf{e}_r \times \nabla_{\perp}) P \left[\frac{r' \beta^t G^t}{r} \right] \right\} F(r', \vartheta', \varphi') dr' d\Omega', \quad (2.151)$$

$$E_r = 0. \quad (2.152)$$

Now from eq. (2.151) we write the expressions for elements g_ϑ^{eg} , g_φ^{eh} , g_r^{eh}

$$g_\vartheta^{eg} = -\frac{1}{\sin \vartheta} \partial_\varphi P \left[\frac{r' \beta^t G^t(n, r, r')}{r} \right], \quad (2.153)$$

$$g_\varphi^{eg} = \partial_\varphi P \left[\frac{r' \beta^t G^t(n, r, r')}{r} \right], \quad (2.154)$$

$$g_r^{eg} = 0. \quad (2.155)$$

2.7 Frequency-domain full 3-D inversion: proof of the concept

2.7.1 Derivatives of the Z:H C-responses

Let H_r , H_ϑ and H_ϕ be the components of the magnetic field in a geographic coordinate system. Then the Z:H C -responses can be written as

$$C_a(\omega) = \left(K \frac{H_r}{\cos \alpha H_\vartheta - \sin \alpha H_\phi} \right) \Big|_a. \quad (2.156)$$

Here $K = \frac{r}{2} \tan \vartheta_d$ and α is the angle between geographic and geomagnetic coordinate systems at site location a . By denoting

$$U = \cos \alpha H_\vartheta - \sin \alpha H_\phi, \quad (2.157)$$

we have

$$C_a(\omega) = \left(K \frac{H_r}{U} \right) \Big|_a. \quad (2.158)$$

Thus we can write

$$dC_a = \left(K \left(\frac{\partial C}{\partial U} dU + \frac{\partial C}{\partial H_r} dH_r \right) \right) \Big|_a = \left(K \left(-\frac{H_r}{U^2} dU + \frac{1}{U} dH_r \right) \right) \Big|_a. \quad (2.159)$$

Then using the reasoning presented in subsection 2.4.2 we arrive at the final formula for dC_a

$$dC_a = \left\langle G_{3D}^{eh} \left(\left(-\frac{KH_r}{U^2} (\cos \alpha \mathbf{e}_\vartheta - \sin \alpha \mathbf{e}_\phi) + \frac{K}{U} \right) \delta_a \right), G_{3D}^{ej}(\mathbf{j}^{ext}) d\sigma \right\rangle. \quad (2.160)$$

2.7.2 Gradients of the data misfit (Z:H case)

In a same manner as that performed in subsection 2.4.3 we obtain for each $\frac{\partial \phi}{\partial m_l}$ of $\nabla \phi_d = (\frac{\partial \phi_d}{\partial m_1}, \frac{\partial \phi_d}{\partial m_2}, \dots, \frac{\partial \phi_d}{\partial m_{N_{inv}}})^T$

$$\frac{\partial \phi_d}{\partial m_l} = \sigma_l \frac{\partial \phi_d}{\partial \sigma_l}, \quad (2.161)$$

where

$$\frac{\partial \phi_d}{\partial \sigma_l} = 2 \operatorname{Re} \left(\sum_{\omega \in \Omega} \left(\int_{V_l} G_{3D}^{eh}(\mathbf{J}^H) \cdot G_{3D}^{ej}(\mathbf{j}^{ext}) dv \right) \right), \quad (2.162)$$

and where

$$\mathbf{J}^H = \sum_{a \in \text{Sites}} (C_a(\mathbf{m}, \omega) - C_a^{exp}(\omega))^* D_a \left(-\frac{KH_r}{U^2} (\cos \alpha \mathbf{e}_\vartheta - \sin \alpha \mathbf{e}_\phi) + \frac{K}{U} \mathbf{e}_r \right) \delta_a. \quad (2.163)$$

2.7.3 Tests of calculation of Green's tensor G_{1D}^{eh}

For testing the calculation of elements of the Green's tensor G_{1D}^{eh} we consider a radially-symmetric Earth's model consisting of 400 km thick layer of 0.004 S/m, a 100 km thick transition layer of 0.04 S/m, and an inner uniform sphere of 2 S/m. Left plots of Fig. 2.23 present real (upper) and imaginary (lower) of southward component of electric field at depth of 450 km, induced by vertical magnetic dipole. The period of excitation is 1 day. The dipole is located at the equator on the surface of the Earth. For comparison, right hand side of the plots present the same component of electric field calculated by integral equation Cartesian code of Avdeev et al. [2002]. Note that we don't plot the eastward component since it has similar geometry (but rotated anticlockwise 90°) and similar amplitudes. Figs. 2.24 and 2.25 show in a similar manner the electric fields induced by southward and eastward directed magnetic dipoles. It is seen that the results for spherical and Cartesian cases as a whole agree very well, but some disagreement exists, most probably due to the different coordinate systems used.

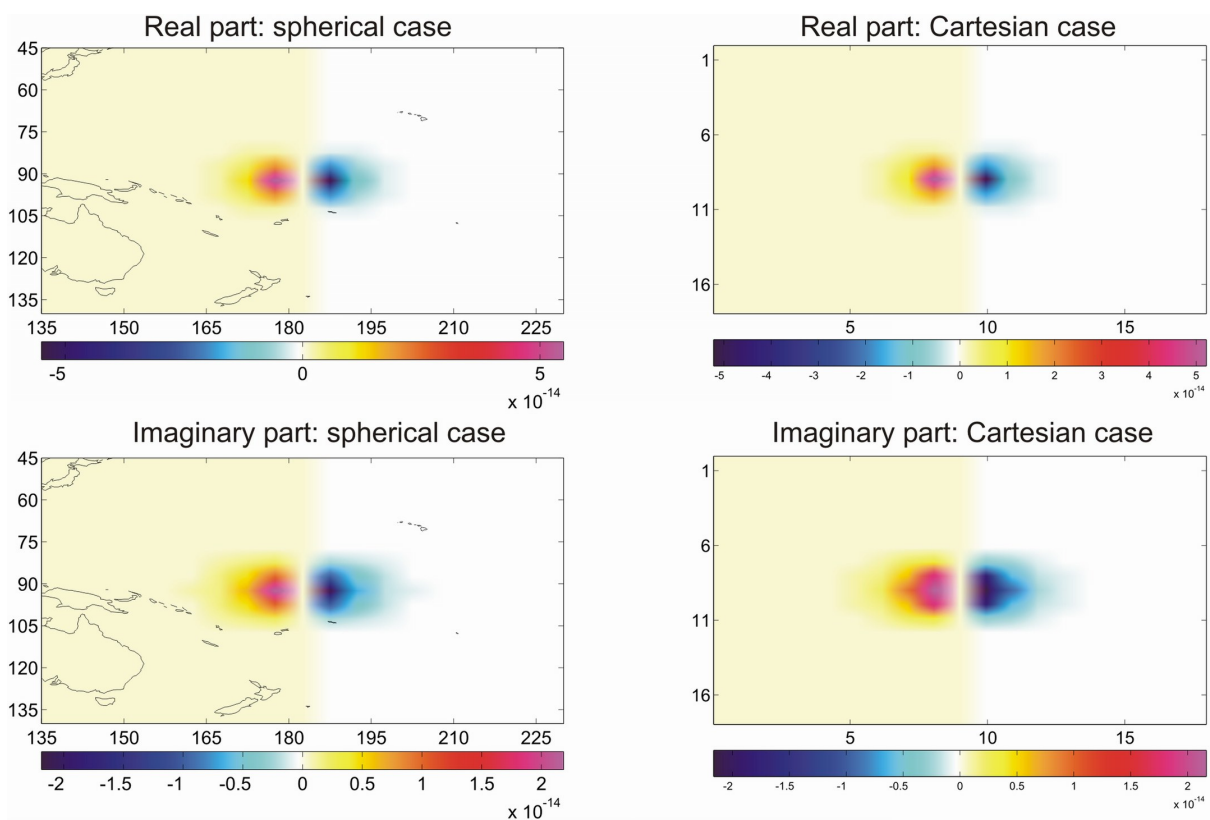


Figure 2.23: Comparison of results calculated in spherical (left plots) and Cartesian (right plots) geometries. Upper: real parts of southward component of electric field (V/m). Lower: imaginary parts (V/m). Excitation: radial magnetic dipole. See details in the text.

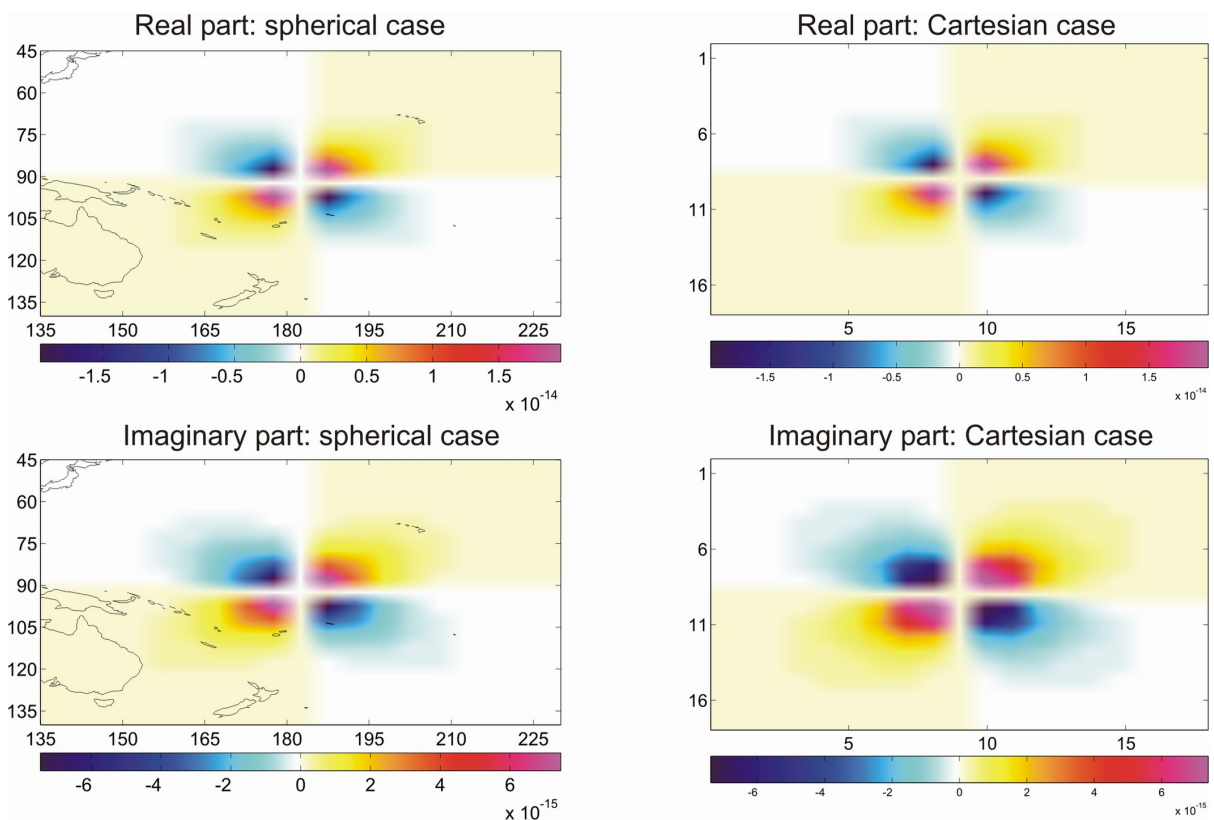


Figure 2.24: Comparison of results calculated in spherical (left plots) and Cartesian (right plots) geometries. Upper: real parts of southward component of electric field (V/m). Lower: imaginary parts (V/m). Excitation: southward magnetic dipole. See details in the text.

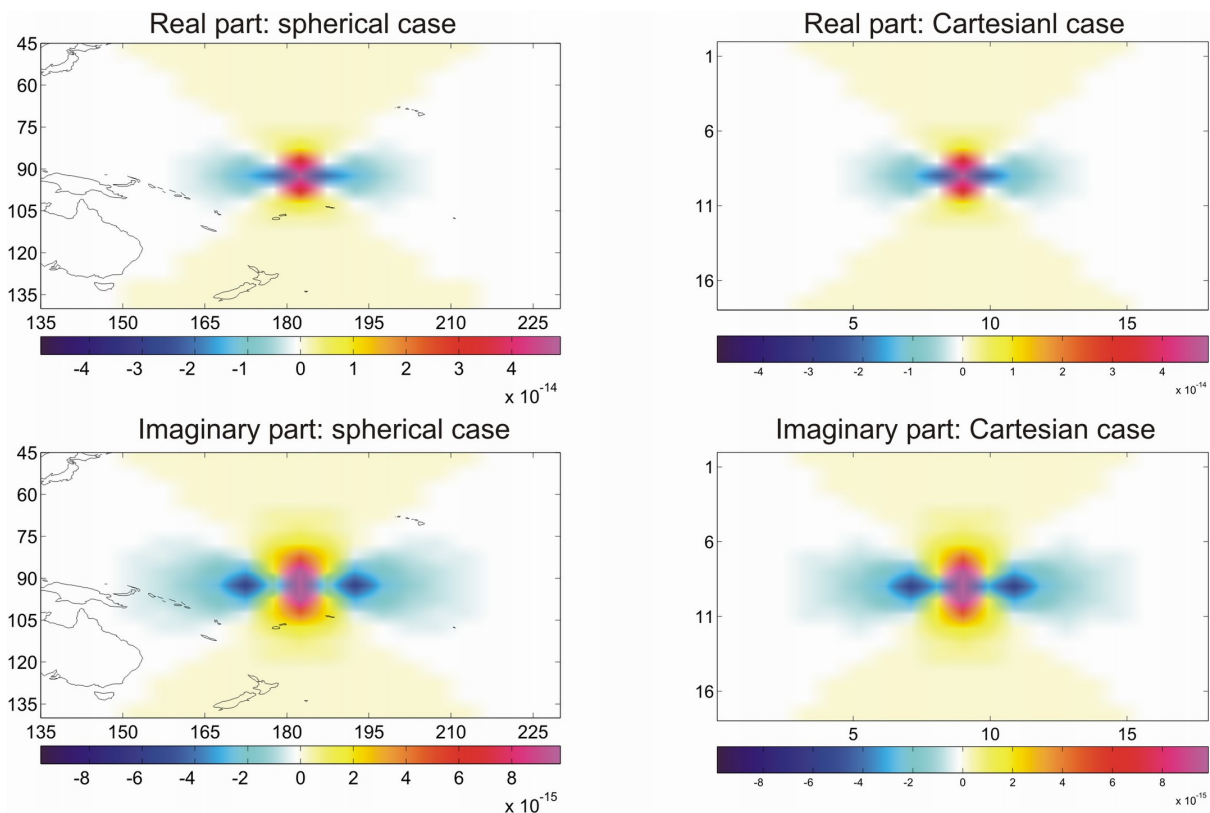


Figure 2.25: Comparison of results calculated in spherical (left plots) and Cartesian (right plots) geometries. Upper: real parts of southward component of electric field (V/m). Lower: imaginary parts (V/m). Excitation: eastward magnetic dipole. See details in the text.

2.7.4 Test of adjoint scheme to calculate gradient of the data misfit

For testing the efficient (adjoint) scheme to calculate gradient of the data misfit (Z:H case) we consider a 3-D model which consists of a deep-seated regional conductor of 1 S/m located between 400 km and 500 km depth. The conductor has the geometry of Pacific plate and is embedded in a radially-symmetric medium as described in the previous section. The model is splitted in the vertical direction into one inhomogeneous spherical layer of thickness 100 km located at 400 km depth; the layer is discretized in the horizontal direction in 72×36 cells of size $5^\circ \times 5^\circ$. The model is excited by a symmetric (in a geographic coordinate system) magnetospheric ring current. We calculate C -responses on the surface of the Earth on a mesh of $5^\circ \times 5^\circ$ at two periods: 2.66 and 3.77 days. We assume that $\mathbf{m} = (m_1, m_2, \dots, m_{N_{inv}})^T = (\ln(\sigma_1), \ln(\sigma_2), \dots, \ln(\sigma_{N_{inv}}))^T$ is the vector of logarithms of unknown electrical conductivities in $N_{inv} = 72 \times 36$ cells comprising the inhomogeneous layer. We calculate the gradient at a point where $\sigma_i = 0.04$ S/m for all i . The upper plot of Fig. 2.26 presents (in the form of global maps) the data misfit gradient calculated with the use of the efficient scheme described in section 2.7.2. The lower plot shows the data misfit gradient, $\nabla\phi_d = (\frac{\partial\phi_d}{\partial m_1}, \frac{\partial\phi_d}{\partial m_2}, \dots, \frac{\partial\phi_d}{\partial m_{N_{inv}}})^T$, calculated in a straightforward manner by a numerical differentiation

$$\frac{\partial\phi_d}{\partial m_i} \approx \frac{\phi_d(m_i + \delta m_i) - \phi_d(m_i)}{\delta m_i}, \quad i = 1, 2, \dots, N_{inv}. \quad (2.164)$$

Note that in our calculations we take $\frac{\delta m_i}{m_i} = 0.01$ for all i . It is seen from the Figure that the gradients calculated by the adjoint scheme and by straightforward numerical differentiation agree remarkably well. But straightforward differentiation required $2 \times N_{inv} = 2 \times 72 \times 36$ forward modellings whereas the adjoint procedure required only 2×2 forward modellings.

2.7.5 Inputs and outputs of 3-D inversion code

Based on the results of previous sections we coded the proposed 3-D inversion scheme. Fig. 2.27 presents a sketch describing input and output components of our 3-D inversion solution. An important feature of the code is the possibility to work on a parallel cluster of computers.

2.7.6 Tests of full FD 3-D inversion code

2.7.6.1 3-D model with 100-km thick deep layer

For the first test we consider the 3-D model described in section 2.7.4. The model is excited by a symmetric (in a geographic coordinate system) magnetospheric ring current. We calculate C -responses on the surface of the Earth on a mesh of $5^\circ \times 5^\circ$ at 10 periods from 2.66 to 60 days, with geometric step $\sqrt{2}$. Our aim is to recover from these data the conductivity distribution within the deep-seated inhomogeneous layer. The vector of parameters to be determined, \mathbf{m} , is the vector of logarithms of unknown electrical conductivities in $N_{inv} = 72 \times 36$ cells (of 100 km thickness) comprising the inhomogeneous layer. We start the inversion from a homogeneous layer of conductivity 0.2 S/m (let us remind ourselves that the true conductivity distribution within the inhomogeneous layer consists of a 1 S/m anomaly surrounded by a 0.04 S/m background medium). In this test we make the following assumptions: a) the background 1-D conductivity is known; b) the geometry of the source is known; c) the location (depth and thickness) of the inhomogeneous layer is known as well.

Figs. 2.28-2.30 summarize the results of our first test of the 3-D inversion. The left hand side plot of Fig. 2.28 shows the number of the forward modelling calls, whereas the right hand side plot presents the misfit and $|\nabla\phi_d|$ with respect to the number of iterations. It is seen that within 166 iterations the

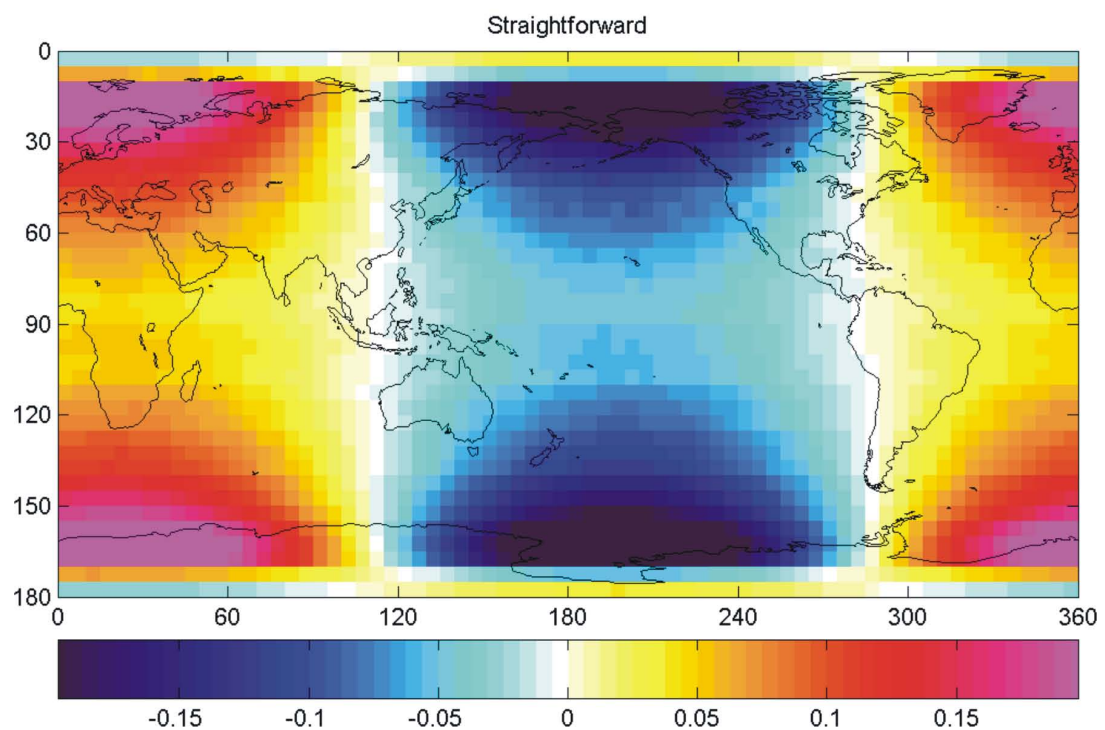
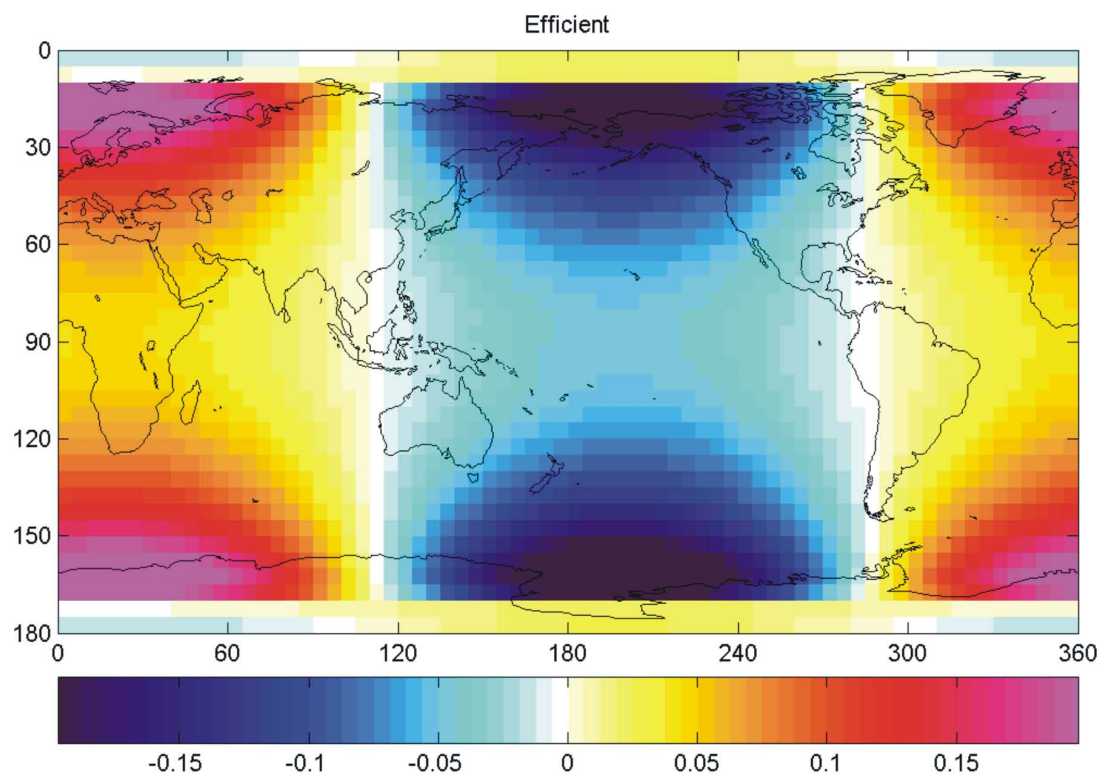


Figure 2.26: Comparison of data misfit gradients calculated by adjoint method (upper plot) and straight-forward numerical differentiation (lower plot).

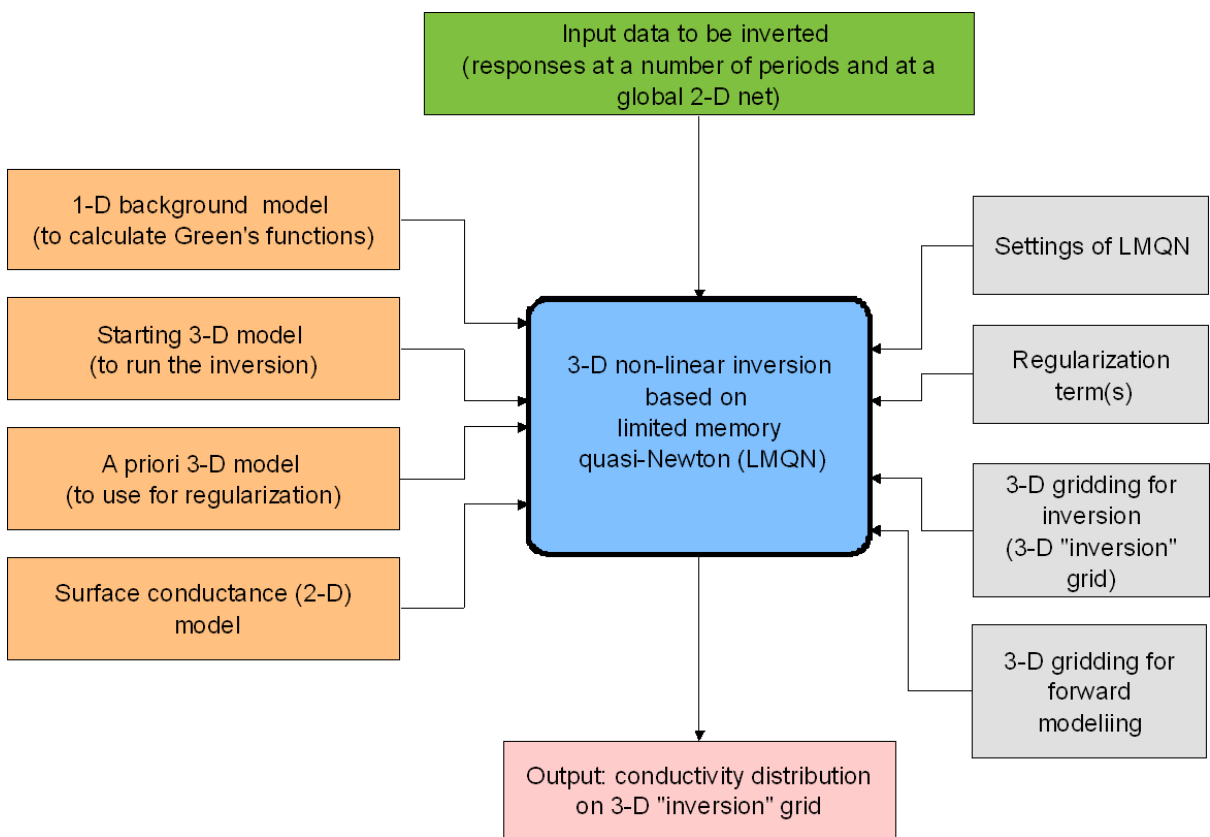


Figure 2.27: A sketch describing the input and output components of our frequency-domain 3-D inversion solution.

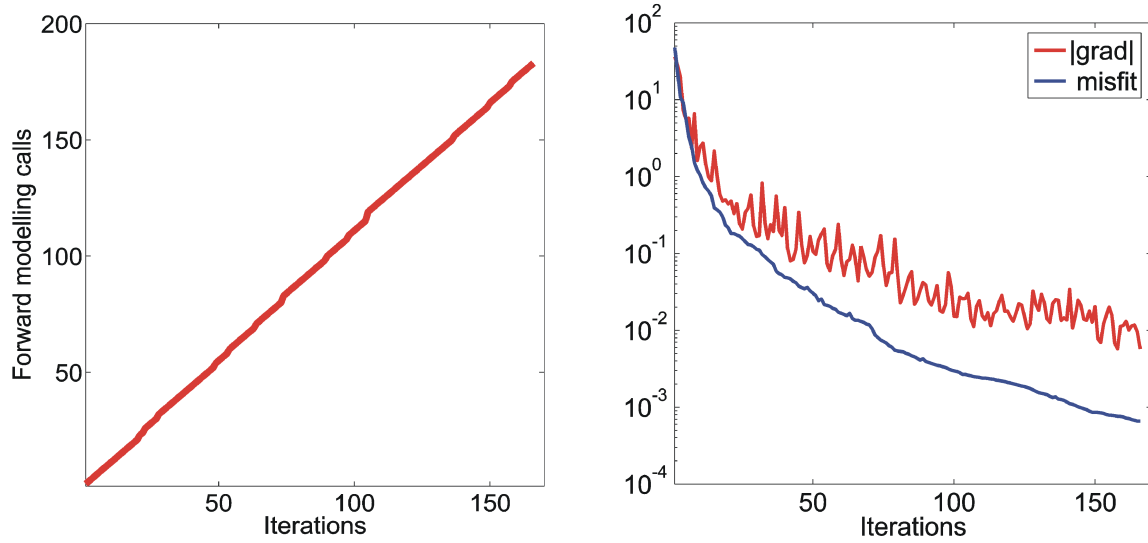


Figure 2.28: Number of the forward modelling calls (left plot), misfit and $|\nabla\phi_d|$ (right plot) with respect to iterations. The results are for the 3-D model with 100-km thick deep layer.

misfit and $|\nabla\phi_d|$ drop down from 35 and 79 to $6.5 \cdot 10^{-4}$ and $5.7 \cdot 10^{-3}$ respectively. Figs. 2.29-2.30 demonstrates the evolution of conductivity recovery with respect to inversion iterations. Fig. 2.29 presents the results of recovery at an initial stage of the inversion (at 0, 9, 19 and 30 iterations). It is seen that after 30 iterations the deep-seated anomaly is recovered fairly well. Then more than 100 iterations are spent to recover properly the background conductivity (see Fig. 2.30). The final image almost perfectly fits the true conductivity. It is important to note that our 3-D inversion works quite fast: this 3-D inversion run (ten periods, 1 inhomogeneous layer, and 72×36 parameters to be determined) took 15 min of clockwall time on 10 processors of ETH's Gonzales cluster.

Further we investigate whether we can speed up the 3-D inversion using as a starting model, the model recovered by quasi 3-D inversion, described in Chapter 2.2. Figs. 2.31-2.33 summarize the results of this inversion. Left hand side plot of Fig. 2.31 shows a number of the forward modelling calls, whereas right plot presents the misfit and $|\nabla\phi_d|$ with respect to the number of iterations. It is seen that the starting misfit and $|\nabla\phi_d|$ are less compared with the case when the inversion starts with a homogeneous layer (9.0 and 3.63 instead 35 and 79). However the misfit drops down $6.5 \cdot 10^{-4}$ only at 224 iteration (instead of 166 iteration for the case when inversion starts with homogeneous layer). Figs. 2.32-2.33 demonstrates the evolution of conductivity recovery with respect to inversion iterations. Fig. 2.32 presents the results of recovery at the initial stage of inversion (at 0, 9, 19 and 30 iterations). It is seen that after 30 iterations the starting image does not change much. Then more than 200 iterations are spent to suppress artefacts of the quasi 3-D inversion. But as expected the final image agrees very well with the true conductivity distribution. Note, however, that the starting model has been obtained from a simplified quasi 3-D inversion since the sophisticated quasi 3-D inversion is still under construction. Hopefully we will succeed to obtain "artefact-free" starting images from a new, sophisticated, version of quasi 3-D inversion.

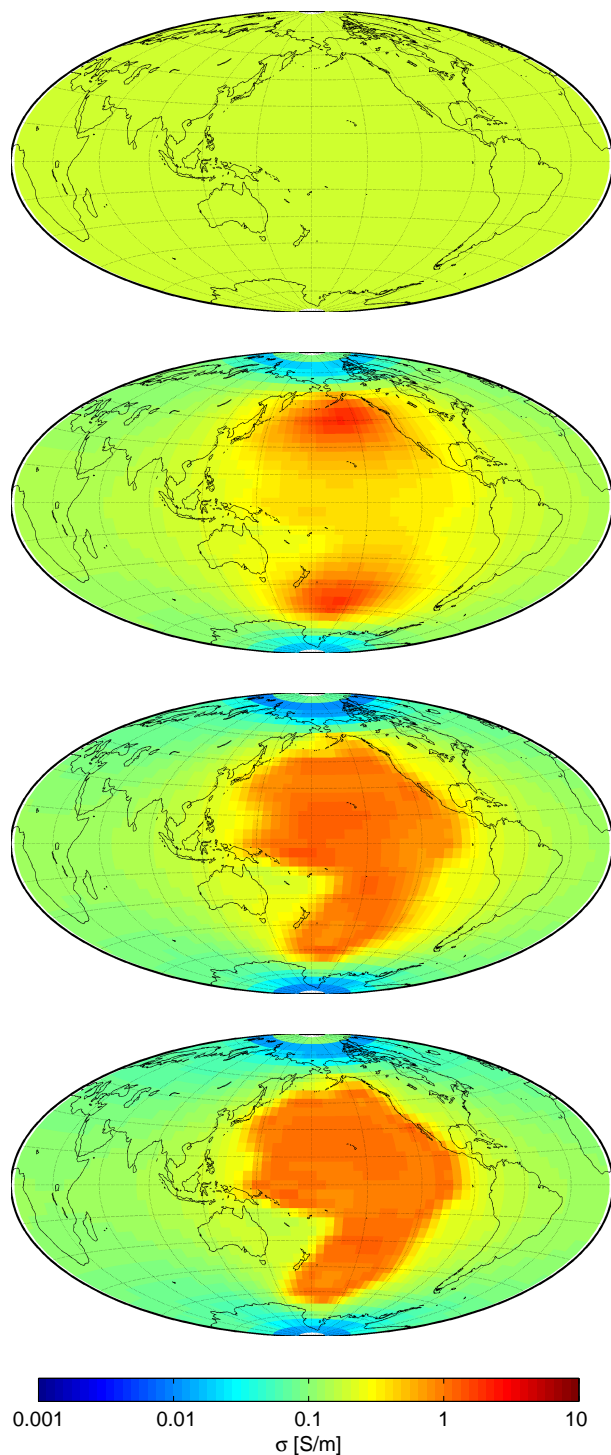


Figure 2.29: Results of conductivity recovery at initial stage of inversion (at 0, 9, 19 and 30 iterations). The results are for the 3-D model with 100-km thick deep layer.

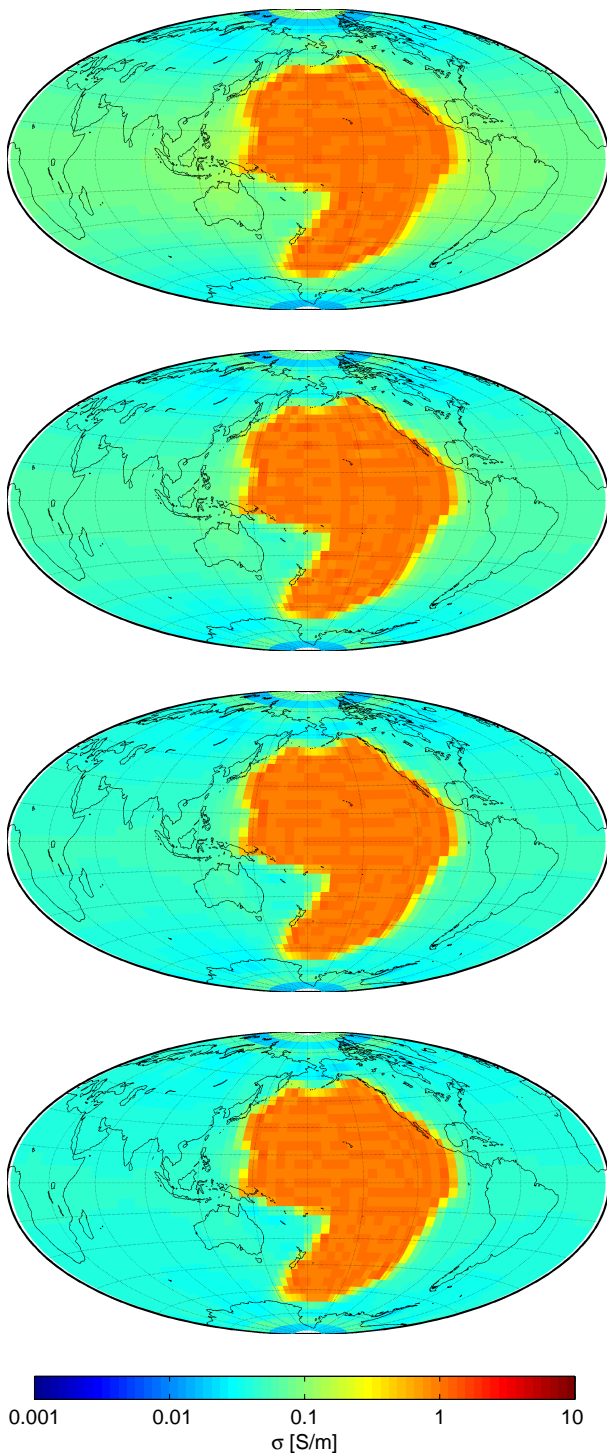


Figure 2.30: Results of conductivity recovery at intermediate and final stages of inversion (at 60, 90, 120 and 166 iterations). The results are for the 3-D model with 100-km thick deep layer.

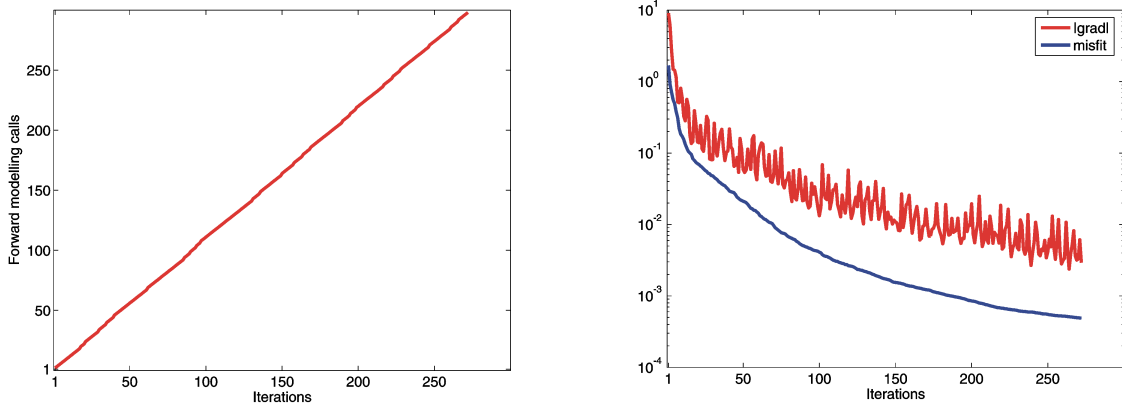


Figure 2.31: Number of the forward modelling calls (left plot), misfit and $|\nabla\phi_d|$ (right plot) with respect to iterations. The results are for the 3-D model with 100-km thick deep layer, when the starting model has been obtained from quasi 3-D inversion.

2.7.6.2 Ultimate 3-D model with nonuniform shell and 300-km thick deep layer

For this ultimate test we consider the most complicated 3-D model described in subsection 2.1.2.1 (third 3-D model). This model consists of a nonuniform surface shell of known conductance and a thick upper mantle nonuniform layer. Again the model is excited by a symmetric (in a geographic coordinate system) magnetospheric ring current. We calculate C -responses on the surface of the Earth on a mesh of $5^\circ \times 5^\circ$ at 10 periods from 2.66 to 60 days, with geometric step $\sqrt{2}$. Our aim is to recover from these data the conductivity distribution within the deep-seated inhomogeneous layer. The vector of parameters to be determined, \mathbf{m} , is the vector of logarithms of unknown electrical conductivities in $N_{inv} = 72 \times 36$ cells (of 300 km thickness) comprising inhomogeneous layer. Again we start the inversion from a homogeneous layer of conductivity 0.2 S/m. In this test we again make the following assumptions: a) the background 1-D conductivity is known; b) the geometry of the source is known; c) the location (depth and thickness) of the inhomogeneous layer is known as well.

Figs. 2.34-2.36 summarize the results of this test. The left hand side plot of Fig. 2.34 shows the number of the forward modelling calls, whereas right hand side plot presents the misfit and $|\nabla\phi_d|$ with respect to the number of iterations. It is seen that within 111 iterations the misfit and $|\nabla\phi_d|$ drop down from 2011 and 1264 to 0.0749 and 0.286 respectively (note that for this inversion run, further iterations did not improve the misfit). Figs. 2.35-2.36 demonstrate the evolution of conductivity recovery with respect to inversion iterations. Fig. 2.35 presents the results of recovery at initial stage of inversion (at 0, 9, 19 and 30 iterations). The Figures show that after 30 iterations the deep-seated anomaly is almost recovered. Then more than 80 iterations are spent to recover the background conductivity (see Fig. 2.36). The final image agrees rather well with the true conductivity. It is anticipated that the use of regularization will suppress visible artefacts near the boundaries of the anomaly.

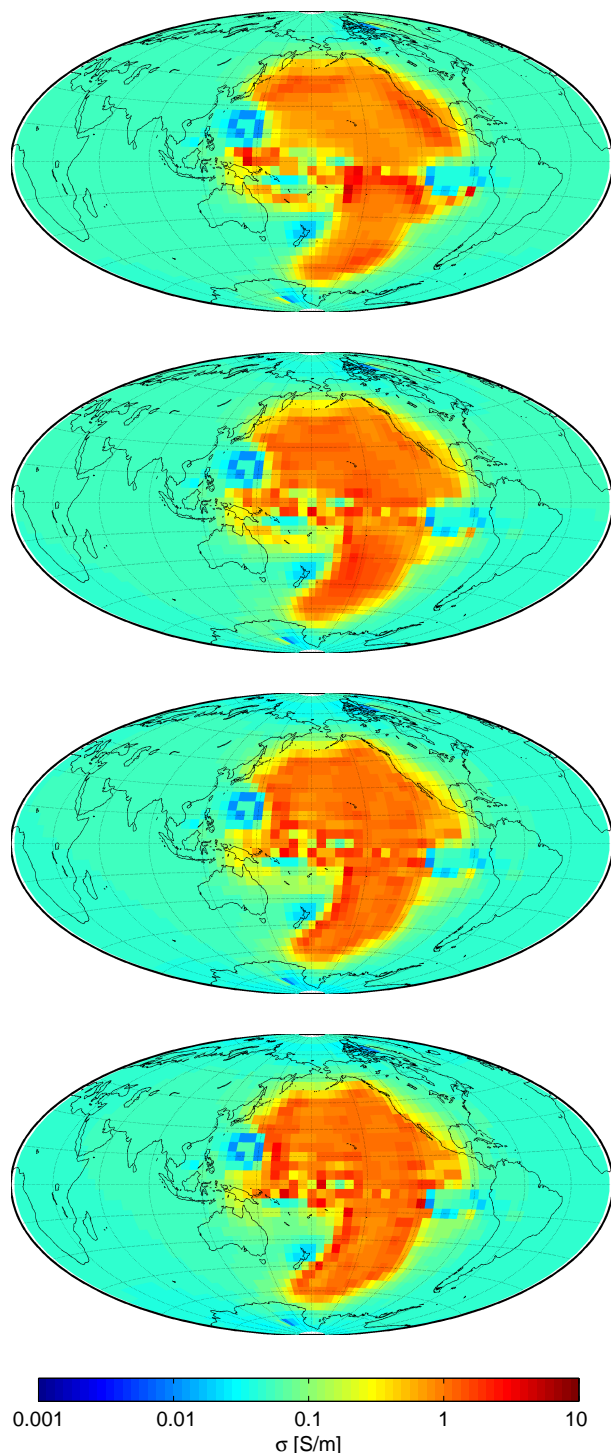


Figure 2.32: Results of conductivity recovery at initial stage of inversion (at 0, 9, 19 and 30 iterations). The results are for the 3-D model with 100-km thick deep layer, when the starting model has been obtained from quasi 3-D inversion.

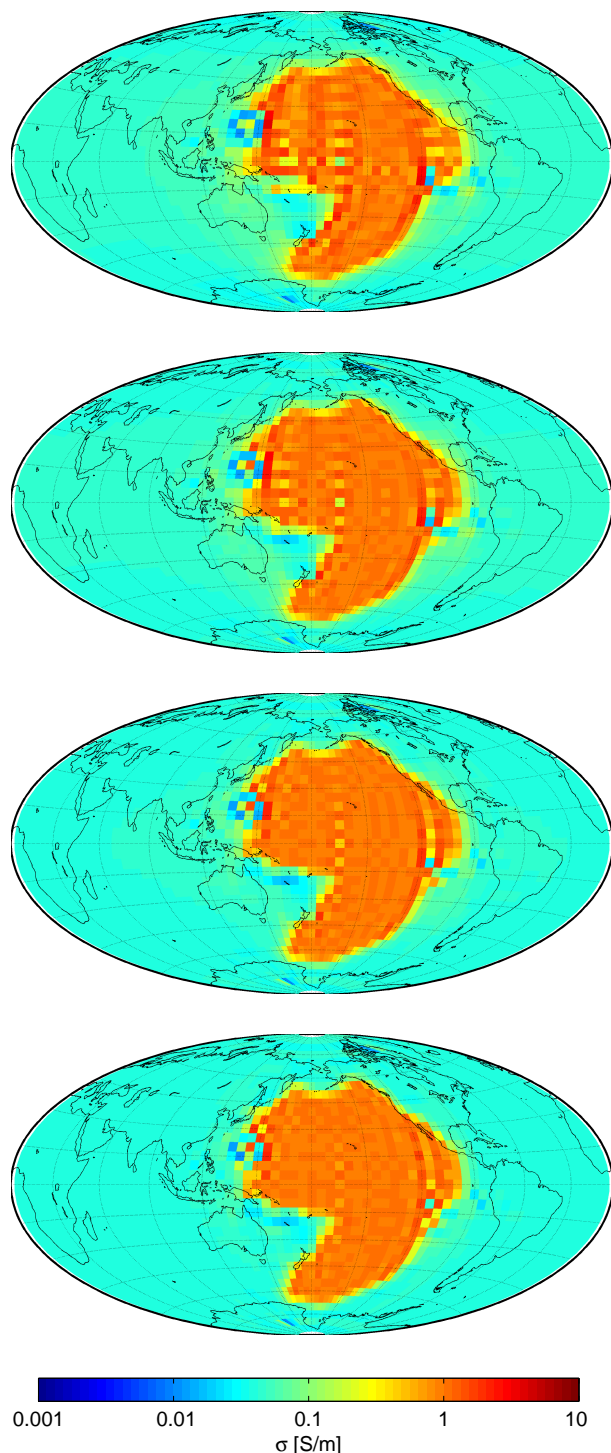


Figure 2.33: Results of conductivity recovery at intermediate and final stages of inversion (at 60, 120, 200 and 272 iterations). The results are for the 3-D model with 100-km thick deep layer, when the starting model has been obtained from quasi 3-D inversion.

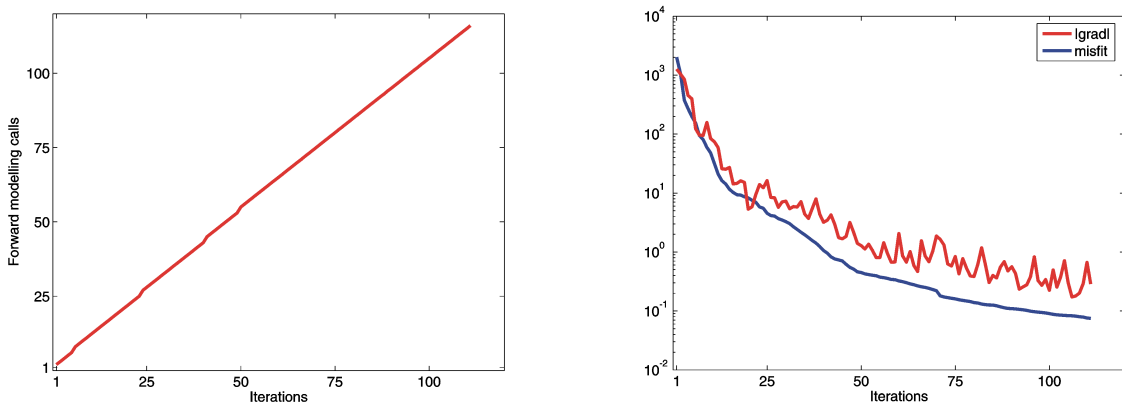


Figure 2.34: Number of the forward modelling calls (left plot), misfit and $|\nabla \phi_d|$ (right plot) with respect to iterations. The results are for the ultimate 3-D model with a nonuniform shell and a 300-km thick deep layer.

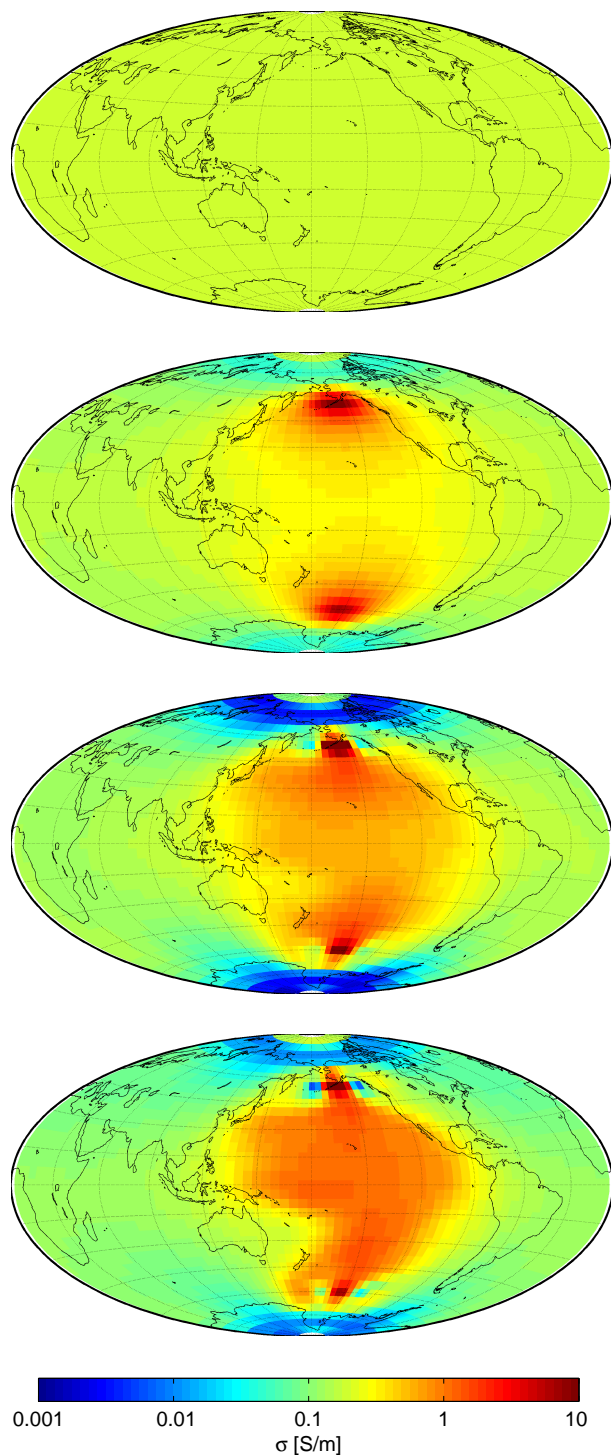


Figure 2.35: Results of conductivity recovery at initial stage of inversion (at 0, 9, 19 and 30 iterations). The results are for the ultimate 3-D model with a nonuniform shell and a 300-km thick deep layer.

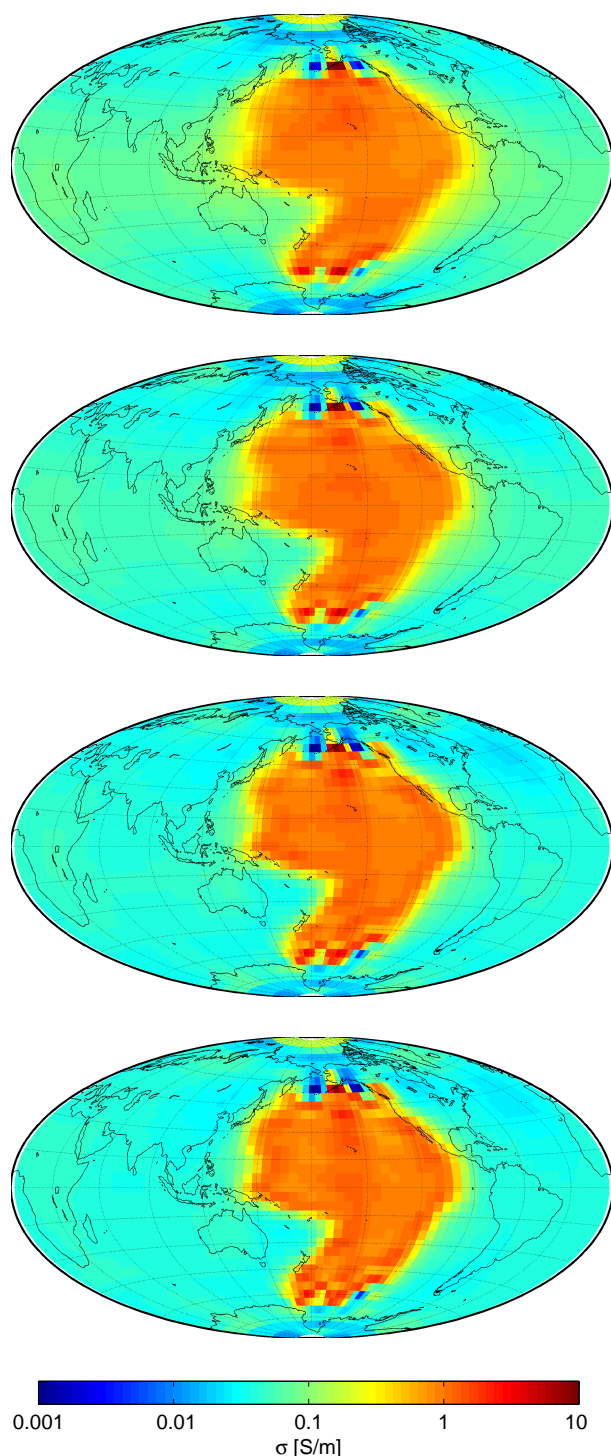


Figure 2.36: Results of conductivity recovery at initial stage of inversion (at 50, 70, 90 and 111 iterations). The results are for the ultimate 3-D model with a nonuniform shell and a 300-km thick deep layer.

Chapter 3

Time domain internal coefficient inversion

3.1 Formulation of the 3-D adjoint problem in time domain

3.1.1 Forward problems with Dirichlet, external and mixed boundary conditions

We start by recalling the formulations of the time-domain forward problem of EM induction in a 3-D heterogeneous Earth [Martinec, 1999, Velímský and Martinec, 2005]. From the quasi-stationary Maxwell equations, we directly derive the equation of EM induction for the magnetic field $\mathbf{B}(\mathbf{r}; t)$,

$$\operatorname{curl} (\rho \operatorname{curl} \mathbf{B}) + \mu_0 \frac{\partial \mathbf{B}}{\partial t} = \mathbf{0}, \quad (3.1)$$

which holds inside the sphere G with 3-D resistivity distribution $\rho(\mathbf{r})^1$ and constant magnetic permeability μ_0 . Outside the Earth, in the insulating atmosphere, the magnetic field can be described by a scalar magnetic potential $U(\mathbf{r}; t)$ which satisfies the Laplace equation and has an analytical solution in the form of an infinite series of scalar spherical harmonics,

$$\mathbf{B}(\mathbf{r}; t) = -\operatorname{grad} U(\mathbf{r}; t), \quad (3.2)$$

$$\nabla^2 U(\mathbf{r}; t) = 0, \quad (3.3)$$

$$U(\mathbf{r}; t) = a \sum_{j=1}^{\infty} \sum_{m=-j}^j \left[G_{jm}^{(e)}(t) \left(\frac{r}{a} \right)^j + G_{jm}^{(i)}(t) \left(\frac{a}{r} \right)^{j+1} \right] Y_{jm}(\Omega). \quad (3.4)$$

The magnetic field is continuous across the Earth's surface ∂G . Equation (3.1) is a vector equation, however it implicitly satisfies the divergence-free condition and therefore only two scalar boundary conditions have to be prescribed on ∂G to yield a unique solution. Let us expand the magnetic field in G into a series of vector spherical harmonics,

$$\mathbf{B}(\mathbf{r}; t) = \sum_{j=1}^{\infty} \sum_{m=-j}^j \sum_{\lambda=-1}^1 B_{jm}^{(\lambda)}(r; t) \mathbf{S}_{jm}^{(\lambda)}(\Omega), \quad (3.5)$$

where the terms $\mathbf{S}_{jm}^{(0)}(\Omega)$, $\mathbf{S}_{jm}^{(-1)}(\Omega)$, and $\mathbf{S}_{jm}^{(1)}(\Omega)$ correspond to the toroidal field, poloidal vertical field,

¹While resistivity is used through the derivation of the time-domain method, electrical conductivity $\sigma = 1/\rho$ is presented in most images consistently with other chapters.



and poloidal horizontal field, respectively. Continuity of \mathbf{B} across ∂G yields,

$$B_{jm}^{(0)}(a; t) = 0, \quad (3.6)$$

$$B_{jm}^{(-1)}(a; t) = -[j G_{jm}^{(e)}(t) - (j+1) G_{jm}^{(i)}(t)] = -Z_{jm}(t), \quad (3.7)$$

$$B_{jm}^{(1)}(a; t) = -[G_{jm}^{(e)}(t) + G_{jm}^{(i)}(t)] = -X_{jm}(t). \quad (3.8)$$

In addition, we can also introduce the vector of electric field $\mathbf{E}(\mathbf{r}; t)$, which is related to \mathbf{B} by the Ampère and Faraday laws,

$$\rho \operatorname{curl} \mathbf{B} = \mu_0 \mathbf{E}, \quad (3.9)$$

$$\operatorname{curl} \mathbf{E} = -\frac{\partial \mathbf{B}}{\partial t}. \quad (3.10)$$

In particular, expanding the electric field into the vector spherical harmonics, we can write for the vertical component of the Faraday law,

$$\frac{\Pi_j}{r} E_{jm}^{(0)}(r; t) = \frac{\partial B_{jm}^{(-1)}}{\partial t}(r; t), \quad (3.11)$$

where $\Pi_j = j(j+1)$.

Now we arrive at three possible choices of boundary conditions complementing the EM induction equation (3.1). The first boundary condition on the toroidal magnetic field is common for all cases,

$$B_{jm}^{(0)}(a; t) = 0. \quad (3.12)$$

The second scalar boundary condition can be given as:

External BC We prescribe a known model of the external magnetic field at the surface,

$$B_{jm}^{(-1)}(a; t) + (j+1) B_{jm}^{(1)}(a; t) = -(2j+1) G_{jm}^{(e, \text{obs})}(t), \quad (3.13a)$$

and predict the coefficients $G_{jm}^{(i)}(t)$ corresponding to the internal, induced magnetic field at the surface and compare them to observation-derived values $G_{jm}^{(i, \text{obs})}(t)$. This approach is suitable for modeling with a-priori given geometry of external ionospheric and/or magnetospheric currents [Velímský and Martinec, 2005].

Dirichlet BC We prescribe the total horizontal poloidal magnetic field at the surface,

$$B_{jm}^{(1)}(a; t) = -X_{jm}^{(\text{obs})}(t), \quad (3.13b)$$

and predict the coefficients $Z_{jm}(t)$ corresponding to the total vertical magnetic field at the surface and compare them to observation-derived values $Z_{jm}^{(\text{obs})}(t)$. In this approach, one can avoid the separation of external and internal field in the data and process each vector component independently [Martinec and McCreadie, 2004].

Mixed BC We prescribe the toroidal electric field at the surface,

$$E_{jm}^{(0)}(a; t) = -\frac{a}{\Pi_j} \frac{\partial Z_{jm}^{(\text{obs})}}{\partial t}(t), \quad (3.13c)$$

and predict the coefficients $X_{jm}(t)$ corresponding to the horizontal magnetic field at the surface and compare them to observation-derived values $X_{jm}^{(\text{obs})}(t)$. This approach requires either direct electric measurements at the Earth's surface, e.g., from underwater cables, or time derivative of the vertical magnetic field [Martinec, 1999].



Finally, we specify an initial condition at time $t = 0$,

$$\mathbf{B}(\mathbf{r}; 0) = \mathbf{B}_0. \quad (3.14)$$

Let us summarize all three forward problem formulations:

For given resistivity model $\rho(\mathbf{r})$, find the magnetic field $\mathbf{B}(\mathbf{r}; t)$, such that

$$\operatorname{curl} (\rho \operatorname{curl} \mathbf{B}) + \mu_0 \frac{\partial \mathbf{B}}{\partial t} = \mathbf{0}, \quad (3.15)$$

in a sphere G , with boundary condition

$$B_{jm}^{(0)}(a; t) = 0, \quad (3.16)$$

and one of boundary conditions

$$B_{jm}^{(-1)}(a; t) + (j+1) B_{jm}^{(1)}(a; t) = -(2j+1) G_{jm}^{(\text{e,obs})}(t), \quad (3.17\text{a})$$

$$B_{jm}^{(1)}(a; t) = -X_{jm}^{(\text{obs})}(t), \quad (3.17\text{b})$$

$$E_{jm}^{(0)}(a; t) = -\frac{a}{\Pi_j} \frac{\partial Z_{jm}^{(\text{obs})}}{\partial t}(t), \quad (3.17\text{c})$$

on the surface ∂G ($r = a$), and with initial condition

$$\mathbf{B}(\mathbf{r}; 0) = \mathbf{B}_0. \quad (3.18)$$

3.1.2 Misfit and misfit derivative in the model space

Let the resistivity ρ be described by M real parameters,

$$\mathbf{m} = (m_1, m_2, \dots, m_M), \quad (3.19)$$

$$\rho = \rho(\mathbf{m}; \mathbf{r}). \quad (3.20)$$

Typically, these correspond to the expansion coefficients of resistivity into some system of base functions, either with global support (such as spherical harmonics) or local support (such as piecewise constant functions).

We introduce the dimensionless L_2 misfit function

$$\chi^2(\mathbf{m}) = \frac{1}{2} \frac{1}{4\pi a^2(t_1 - t_0)} \int_{t_0}^{t_1} \int_{\partial G} \left(\frac{\mathbf{B}(\mathbf{m}) - \mathbf{B}^{(\text{obs})}}{\sigma_B} \right)^2 dS dt, \quad (3.21)$$

which measures the fit of magnetic field $\mathbf{B}(\mathbf{m})$ obtained from forward modeling against observed field $\mathbf{B}^{(\text{obs})}$ at the surface. We use $\sigma_B(\Omega; t)$ to denote the mean quadratic error of observations. For simplicity and depending on context, we assume either the angular dependence of $\sigma_B(\Omega; t)$, or the dependence on spherical harmonic degree and order, $\sigma_{B,jm}(t)$, without explicit description in the following derivations. Note that only data after $t_0 \geq 0$ are included in the evaluation of the misfit, since the time-domain solution can be biased for times $t < t_0$ by the switch-on effect of the initial condition.



Using the spherical harmonic representation, we obtain for the external, Dirichlet, and mixed boundary conditions,

$$\chi^2 = \frac{1}{2} \sum_{jm} \frac{(j+1)(2j+1)}{4\pi(t_1-t_0)} \int_{t_0}^{t_1} \left(\frac{G_{jm}^{(i)}(t) - G_{jm}^{(i,obs)}(t)}{\sigma_B} \right)^2 dt, \quad (3.22a)$$

$$\chi^2 = \frac{1}{2} \sum_{jm} \frac{1}{4\pi(t_1-t_0)} \int_{t_0}^{t_1} \left(\frac{Z_{jm}(t) - Z_{jm}^{(obs)}(t)}{\sigma_B} \right)^2 dt, \quad (3.22b)$$

$$\chi^2 = \frac{1}{2} \sum_{jm} \frac{\Pi_j}{4\pi(t_1-t_0)} \int_{t_0}^{t_1} \left(\frac{X_{jm}(t) - X_{jm}^{(obs)}(t)}{\sigma_B} \right)^2 dt, \quad (3.22c)$$

respectively.

To solve the inverse problem, we have to find a model \mathbf{m} that minimizes the penalty function

$$F(\mathbf{m}) = \chi^2(\mathbf{m}) + \lambda R^2(\mathbf{m}), \quad (3.23)$$

where $\lambda R^2(\mathbf{m})$ is the regularization, which will be specified later.

Many effective multidimensional minimization algorithms, such as conjugate gradients or variable metrics method [Press et al., 1992, Chapters 10.6–7], are based on the knowledge of gradient of the penalty function F in the space of model parameters,

$$\mathbf{D}_\mathbf{m} F = \mathbf{D}_\mathbf{m} \chi^2 + \mathbf{D}_\mathbf{m} R^2 \quad (3.24)$$

where the gradient operator is given as

$$\mathbf{D}_\mathbf{m} = (D_1, D_2, \dots, D_M)^T, \quad D_\alpha = \frac{\partial}{\partial m_\alpha}. \quad (3.25)$$

To evaluate the gradient of the penalty function, we need in particular the partial derivatives of the L_2 misfit (3.21), which read as

$$D_\alpha \chi^2 = \frac{1}{4\pi a^2(t_1-t_0)} \int_0^{t_1} \int_{\partial G} \frac{(\mathbf{B} - \mathbf{B}^{(obs)}) \cdot D_\alpha \mathbf{B}}{\sigma_B^2} H(t-t_0) dS dt, \quad (3.26)$$

since $D_\alpha \mathbf{B}^{(obs)} = 0$. Here $H(t)$ denotes the Heaviside step function.

The straightforward approach would be to solve M forward problems for small perturbations of the model \mathbf{m} into each direction in the model space. Then, by numerical differentiation, we could obtain an approximation of each $D_\alpha \chi^2$.

The adjoint method [Fichtner et al., 2006, Newman and Commer, 2005, Tarantola, 2005, Chapter 6] allows us to evaluate $D_\alpha \chi^2$ without explicit knowledge of $D_\alpha \mathbf{B}$. It reduces the computational burden to the solution of one adjoint problem, which is equivalent to the forward problem excited by the field residua.

3.1.3 Adjoint method

Let us introduce the adjoint time $\hat{t} = t_1 - t$, $\frac{\partial}{\partial t} = -\frac{\partial}{\partial \hat{t}}$. By multiplying the EM induction equation (3.15) by an arbitrary, sufficiently smooth function $\hat{\mathbf{B}}(\mathbf{r}; \hat{t})$, integrating over sphere G and time interval



$(0, t_1)$, normalizing, applying the vector calculus identity [Martinec, 1999],

$$\int_G \operatorname{curl} (h \operatorname{curl} \mathbf{f}) \cdot \mathbf{g} \, dV = \int_G h \operatorname{curl} \mathbf{f} \cdot \operatorname{curl} \mathbf{g} \, dV - \int_{\partial G} h \operatorname{curl} \mathbf{f} \cdot (\mathbf{n} \times \mathbf{g}) \, dS, \quad (3.27)$$

and per partes integration in time, we obtain

$$\begin{aligned} & \frac{1}{4\pi a^3 \mu_0} \left\{ \int_0^{t_1} \left[\int_G \left(\rho \operatorname{curl} \hat{\mathbf{B}} \cdot \operatorname{curl} \mathbf{B} + \mu_0 \frac{\partial \hat{\mathbf{B}}}{\partial \hat{t}} \cdot \mathbf{B} \right) \, dV \right. \right. \\ & \left. \left. - \int_{\partial G} \mu_0 (\mathbf{n} \times \hat{\mathbf{B}}) \cdot \mathbf{E} \, dS \right] \, dt + \int_G \mu_0 [\hat{\mathbf{B}}(0) \cdot \mathbf{B}(t_1) - \hat{\mathbf{B}}(t_1) \cdot \mathbf{B}(0)] \, dV \right\} = 0. \end{aligned} \quad (3.28)$$

We will call $\hat{\mathbf{B}}$ the adjoint magnetic field and assume, that it is given in reciprocal units of \mathbf{B} so that their product is a dimensionless number.

Let us compute the derivative of equation (3.28) in the model space and add it to the misfit derivative (3.26). We obtain

$$\begin{aligned} D_\alpha \chi^2 &= \frac{1}{4\pi a^3 \mu_0} \int_0^{t_1} \int_G D_\alpha \rho \operatorname{curl} \hat{\mathbf{B}} \cdot \operatorname{curl} \mathbf{B} \, dV \, dt \\ &+ \frac{1}{4\pi a^3 \mu_0} \int_0^{t_1} \int_G \left(\rho \operatorname{curl} \hat{\mathbf{B}} \cdot \operatorname{curl} D_\alpha \mathbf{B} + \mu_0 \frac{\partial \hat{\mathbf{B}}}{\partial \hat{t}} \cdot D_\alpha \mathbf{B} \right) \, dV \, dt \\ &+ \frac{1}{4\pi a^3 \mu_0} \int_G \mu_0 [\hat{\mathbf{B}}(0) \cdot D_\alpha \mathbf{B}(t_1) - \hat{\mathbf{B}}(t_1) \cdot D_\alpha \mathbf{B}(0)] \, dV \\ &- \frac{1}{4\pi a^3 \mu_0} \int_0^{t_1} \int_{\partial G} \mu_0 (\mathbf{n} \times \hat{\mathbf{B}}) \cdot D_\alpha \mathbf{E} \, dS \, dt \\ &+ \frac{1}{4\pi a^2 (t_1 - t_0)} \int_0^{t_1} \int_{\partial G} \frac{(\mathbf{B} - \mathbf{B}^{(\text{obs})}) \cdot D_\alpha \mathbf{B}}{\sigma_B^2} H(t - t_0) \, dS \, dt. \end{aligned} \quad (3.29)$$

One more application of identity (3.27) on the second integral in the previous equation yields

$$\begin{aligned}
 D_\alpha \chi^2 &= \frac{1}{4\pi a^3 \mu_0} \int_0^{t_1} \int_G D_\alpha \rho \operatorname{curl} \hat{\mathbf{B}} \cdot \operatorname{curl} \mathbf{B} dV dt \\
 &+ \frac{1}{4\pi a^3 \mu_0} \int_0^{t_1} \int_G \left[\operatorname{curl} (\rho \operatorname{curl} \hat{\mathbf{B}}) + \mu_0 \frac{\partial \hat{\mathbf{B}}}{\partial \hat{t}} \right] \cdot D_\alpha \mathbf{B} dV dt \\
 &+ \frac{1}{4\pi a^3 \mu_0} \int_G \mu_0 \hat{\mathbf{B}}(0) \cdot D_\alpha \mathbf{B}(t_1) dV \\
 &+ \frac{1}{4\pi a^3 \mu_0} \int_0^{t_1} \int_{\partial G} \mu_0 \left[(\mathbf{n} \times D_\alpha \mathbf{B}) \cdot \hat{\mathbf{E}} - (\mathbf{n} \times \hat{\mathbf{B}}) \cdot D_\alpha \mathbf{E} \right] dS dt \\
 &+ \frac{1}{4\pi a^2 (t_1 - t_0)} \int_0^{t_1} \int_{\partial G} \frac{(\mathbf{B} - \mathbf{B}^{(\text{obs})}) \cdot D_\alpha \mathbf{B}}{\sigma_B^2} H(t - t_0) dS dt. \tag{3.30}
 \end{aligned}$$

Here we assumed that $D_\alpha \mathbf{B}(0) = \mathbf{0}$, i.e., the initial condition does not depend on the resistivity model. We also introduced the adjoint electric field $\hat{\mathbf{E}}$ using the adjoint form of the Ampère and Faraday laws, $\mu_0 \hat{\mathbf{E}} = \rho \operatorname{curl} \hat{\mathbf{B}}$, $\operatorname{curl} \hat{\mathbf{E}} = -\frac{\partial \hat{\mathbf{B}}}{\partial \hat{t}}$.

Up to now, $\hat{\mathbf{B}}$ was arbitrary. Now we aim to constrain it in such a way that all integrals in equation (3.30) except for the first one disappear. The second integral will be zero if $\hat{\mathbf{B}}$ solves the adjoint EM induction equation. The next integral enforces the zero initial condition on $\hat{\mathbf{B}}$ at adjoint time $\hat{t} = 0$ (in other words, a terminal condition at regular time $t = t_1$). Finally, zeroing the sum of the surface integrals while taking into account the boundary conditions (3.16–3.17) yields the boundary conditions imposed on $\hat{\mathbf{B}}$.

Derivation of these adjoint boundary conditions requires, that we express the surface integrals from



equation (3.30) in the spherical-harmonic parametrization,

$$-\frac{1}{4\pi a^3} \int_0^{t_1} \int_{\partial G} (\mathbf{n} \times \hat{\mathbf{B}}) \cdot D_\alpha \mathbf{E} dS dt = \frac{1}{4\pi a} \sum_{jm} \Pi_j \int_0^{t_1} \left(\hat{B}_{jm}^{(0)} D_\alpha E_{jm}^{(1)} - \hat{B}_{jm}^{(1)} D_\alpha E_{jm}^{(0)} \right) dt, \quad (3.31)$$

$$-\frac{1}{4\pi a^3} \int_0^{t_1} \int_{\partial G} (\mathbf{n} \times D_\alpha \mathbf{B}) \cdot \hat{\mathbf{E}} dS dt = \frac{1}{4\pi a} \sum_{jm} \Pi_j \int_0^{t_1} \left(D_\alpha B_{jm}^{(0)} \hat{E}_{jm}^{(1)} - D_\alpha B_{jm}^{(1)} \hat{E}_{jm}^{(0)} \right) dt, \quad (3.32)$$

$$\frac{1}{4\pi a^2 (t_1 - t_0)} \int_0^{t_1} \int_{\partial G} \frac{\Delta \mathbf{B} \cdot D_\alpha \mathbf{B}}{\sigma_B^2} H(t - t_0) dS dt = \frac{1}{4\pi (t_1 - t_0)} \sum_{jm} \int_0^{t_1} \frac{D_\alpha B_{jm}^{(-1)} \Delta B_{jm}^{(-1)} + \Pi_j D_\alpha B_{jm}^{(1)} \Delta B_{jm}^{(1)}}{\sigma_B^2} H(t - t_0) dt, \quad (3.33)$$

where $\Delta \mathbf{B} = \mathbf{B} - \mathbf{B}^{(\text{obs})}$, $\Delta B_{jm}^{(\lambda)} = B_{jm}^{(\lambda)} - B_{jm}^{(\lambda, \text{obs})}$. Now we apply the derivative to the boundary conditions (3.16–3.17),

$$D_\alpha B_{jm}^{(0)}(a; t) = 0, \quad (3.34)$$

$$D_\alpha B_{jm}^{(-1)}(a; t) + (j+1) D_\alpha B_{jm}^{(1)}(a; t) = (-2j+1) D_\alpha G_{jm}^{(\text{e, obs})}(t) = 0, \quad (3.35a)$$

$$D_\alpha B_{jm}^{(1)}(a; t) = -D_\alpha X_{jm}^{(\text{obs})}(t) = 0, \quad (3.35b)$$

$$D_\alpha E_{jm}^{(0)}(a; t) = -\frac{a}{\Pi_j} \frac{\partial D_\alpha Z_{jm}^{(\text{obs})}}{\partial t}(t) = 0. \quad (3.35c)$$

Zeroing of the sum of surface integrals in equation (3.30) then yields,

$$0 = \sum_{jm} \Pi_j \int_0^{t_1} \left[\hat{B}_{jm}^{(0)} D_\alpha E_{jm}^{(1)} - \hat{B}_{jm}^{(1)} D_\alpha E_{jm}^{(0)} - D_\alpha B_{jm}^{(0)} \hat{E}_{jm}^{(1)} + D_\alpha B_{jm}^{(1)} \hat{E}_{jm}^{(0)} + \frac{a}{\Pi_j (t_1 - t_0)} \frac{D_\alpha B_{jm}^{(-1)} \Delta B_{jm}^{(-1)} + \Pi_j D_\alpha B_{jm}^{(1)} \Delta B_{jm}^{(1)}}{\sigma_B^2} H(t - t_0) \right] dt, \quad (3.36)$$

In the case of an external BC, we substitute (3.34) and (3.35a) into (3.36), and make use of the Faraday

law (3.11), its adjoint equivalent, and per partes time integration,

$$\begin{aligned}
0 &= \sum_{jm} \int_0^{t_1} \left[\Pi_j \hat{B}_{jm}^{(0)} D_\alpha E_{jm}^{(1)} - a \hat{B}_{jm}^{(1)} \frac{\partial D_\alpha B_{jm}^{(-1)}}{\partial t} + a D_\alpha B_{jm}^{(1)} \frac{\partial \hat{B}_{jm}^{(-1)}}{\partial \hat{t}} + \right. \\
&\quad \left. + \frac{a}{(t_1 - t_0)} \frac{-(j+1) D_\alpha B_{jm}^{(1)} \Delta B_{jm}^{(-1)} + \Pi_j D_\alpha B_{jm}^{(1)} \Delta B_{jm}^{(1)}}{\sigma_B^2} H(t - t_0) \right] dt = \\
&= \sum_{jm} \int_0^{t_1} \left[\Pi_j \hat{B}_{jm}^{(0)} D_\alpha E_{jm}^{(1)} + a(j+1) \hat{B}_{jm}^{(1)} \frac{\partial D_\alpha B_{jm}^{(1)}}{\partial t} + a D_\alpha B_{jm}^{(1)} \frac{\partial \hat{B}_{jm}^{(-1)}}{\partial \hat{t}} + \right. \\
&\quad \left. + \frac{a}{(t_1 - t_0)} \frac{-(j+1) D_\alpha B_{jm}^{(1)} \Delta B_{jm}^{(-1)} + \Pi_j D_\alpha B_{jm}^{(1)} \Delta B_{jm}^{(1)}}{\sigma_B^2} H(t - t_0) \right] dt = \\
&= \sum_{jm} \int_0^{t_1} \left[\Pi_j \hat{B}_{jm}^{(0)} D_\alpha E_{jm}^{(1)} + a \left((j+1) \frac{\partial \hat{B}_{jm}^{(1)}}{\partial \hat{t}} + \frac{\partial \hat{B}_{jm}^{(-1)}}{\partial \hat{t}} + \right. \right. \\
&\quad \left. \left. + \frac{1}{(t_1 - t_0)} \frac{-(j+1)(2j+1) \Delta G_{jm}^{(i)}}{\sigma_B^2} H(t - t_0) \right) D_\alpha B_{jm}^{(1)} \right] dt. \tag{3.37}
\end{aligned}$$

The first term implies zero adjoint toroidal magnetic field,

$$\hat{B}_{jm}^{(0)}(a; \hat{t}) = 0. \tag{3.38}$$

The second term, after rearranging and time integration yields

$$\hat{B}_{jm}^{(-1)}(a; \hat{t}) + (j+1) \hat{B}_{jm}^{(1)}(a; \hat{t}) = -(2j+1) \hat{G}_{jm}^{(e)}(\hat{t}), \tag{3.39}$$

$$\hat{G}_{jm}^{(e)}(\hat{t}) = -\frac{(j+1)}{t_1 - t_0} \int_{\max(t_0, t_1 - \hat{t})}^{t_1} \frac{G_{jm}^{(i)}(\tau) - G_{jm}^{(i, \text{obs})}(\tau)}{\sigma_B^2} d\tau. \tag{3.40}$$

The external adjoint field is given by time-integrated residua of the internal field obtained from the forward solution.

In the case of Dirichlet BC, similar use of (3.11), (3.34), and (3.35b) in (3.36) leads to

$$0 = \sum_{jm} \int_0^{t_1} \left[\Pi_j \hat{B}_{jm}^{(0)} D_\alpha E_{jm}^{(1)} + a \left(-\frac{\partial \hat{B}_{jm}^{(1)}}{\partial \hat{t}} + \frac{\Delta B_{jm}^{(-1)}}{(t_1 - t_0) \sigma_B^2} H(t - t_0) \right) D_\alpha B_{jm}^{(-1)} \right] dt.$$

Again, the first term implies zero adjoint toroidal field (3.38), and the second term, after some rearrangements,

$$\hat{B}_{jm}^{(1)}(a; \hat{t}) = -\hat{X}_{jm}(\hat{t}), \tag{3.41}$$

$$\hat{X}_{jm}(\hat{t}) = -\frac{1}{t_1 - t_0} \int_{\max(t_0, t_1 - \hat{t})}^{t_1} \frac{Z_{jm}(\tau) - Z_{jm}^{(\text{obs})}(\tau)}{\sigma_B^2} d\tau. \tag{3.42}$$

The adjoint problem also has Dirichlet BC with the poloidal horizontal field given by the time-integrated residua of vertical field from the forward solution.



Finally, in the case of mixed BC, equation (3.36) can be rewritten as

$$0 = \sum_{jm} \Pi_j \int_0^{t_1} \left[\hat{B}_{jm}^{(0)} D_\alpha E_{jm}^{(1)} + \left(\hat{E}_{jm}^{(0)} + \frac{a \Delta B_{jm}^{(1)}}{(t_1 - t_0) \sigma_B^2} H(t - t_0) \right) D_\alpha B_{jm}^{(1)} \right] dt, \quad (3.43)$$

leading to (3.38) and

$$\hat{E}_{jm}^{(0)}(a; \hat{t}) = -\frac{a}{\Pi_j} \frac{\partial \hat{Z}_{jm}}{\partial \hat{t}}(\hat{t}), \quad (3.44)$$

$$\hat{Z}_{jm}(\hat{t}) = \frac{\Pi_j}{t_1 - t_0} \int_{\max(t_0, t_1 - \hat{t})}^{t_1} \frac{X_{jm}(\tau) - X_{jm}^{(\text{obs})}(\tau)}{\sigma_B^2} d\tau. \quad (3.45)$$

Note that in this case the time derivative and integration are introduced only formally for consistency with boundary condition (3.17c); the adjoint toroidal electric field is given directly by residua of the horizontal component of the forward solution.

Hence we arrive at the complete formulation of the adjoint problem.

Given the resistivity $\rho(\mathbf{r})$, the forward solution $\mathbf{B}(\mathbf{r}; t)$, and observations $\mathbf{B}^{(\text{obs})}$ with errors σ_B , we find the solution $\hat{\mathbf{B}}(\mathbf{r}; \hat{t})$ of the adjoint problem

$$\text{curl} \left(\rho \text{curl} \hat{\mathbf{B}} \right) + \mu_0 \frac{\partial \hat{\mathbf{B}}}{\partial \hat{t}} = \mathbf{0}, \quad (3.46)$$

in G , with boundary condition

$$\hat{B}_{jm}^{(0)}(a; t) = 0, \quad (3.47)$$

and one of boundary conditions

$$\hat{B}_{jm}^{(-1)}(a; \hat{t}) + (j+1) \hat{B}_{jm}^{(1)}(a; \hat{t}) = -(2j+1) \hat{G}_{jm}^{(\text{e})}(\hat{t}), \quad (3.48a)$$

$$\hat{B}_{jm}^{(1)}(a; \hat{t}) = -\hat{X}_{jm}(\hat{t}), \quad (3.48b)$$

$$\hat{E}_{jm}^{(0)}(a; \hat{t}) = -\frac{a}{\Pi_j} \frac{\partial \hat{Z}_{jm}}{\partial \hat{t}}(\hat{t}), \quad (3.48c)$$

where

$$\hat{G}_{jm}^{(\text{e})}(\hat{t}) = -\frac{(j+1)}{t_1 - t_0} \int_{\max(t_0, t_1 - \hat{t})}^{t_1} \frac{G_{jm}^{(\text{i})}(\tau) - G_{jm}^{(\text{i,obs})}(\tau)}{\sigma_B^2} d\tau, \quad (3.49a)$$

$$\hat{X}_{jm}(\hat{t}) = -\frac{1}{t_1 - t_0} \int_{\max(t_0, t_1 - \hat{t})}^{t_1} \frac{Z_{jm}(\tau) - Z_{jm}^{(\text{obs})}(\tau)}{\sigma_B^2} d\tau, \quad (3.49b)$$

$$\hat{Z}_{jm}(\hat{t}) = \frac{\Pi_j}{t_1 - t_0} \int_{\max(t_0, t_1 - \hat{t})}^{t_1} \frac{X_{jm}(\tau) - X_{jm}^{(\text{obs})}(\tau)}{\sigma_B^2} d\tau, \quad (3.49c)$$

on the surface ∂G ($r = a$), and with initial condition at $\hat{t} = 0$,

$$\hat{\mathbf{B}}(\mathbf{r}; 0) = \mathbf{0}. \quad (3.50)$$



For any minimization algorithm, that is based on the knowledge of the gradient of penalty function in the model parameter space, we can write the general scheme, as follows:

1. For a given point \mathbf{m} in the model space, find the forward solution $\mathbf{B}(\mathbf{r}; t)$;
2. from the residua, obtain the adjoint excitation $\hat{G}_{jm}^{(e)}(\hat{t})$, $\hat{X}_{jm}(\hat{t})$, or $\hat{Z}_{jm}(\hat{t})$;
3. find the adjoint solution $\hat{\mathbf{B}}(\mathbf{r}; \hat{t})$;
4. compute the misfit using appropriate equation (3.22);
5. for each model parameter m_α compute the derivative,

$$D_\alpha \chi^2(\mathbf{m}) = \frac{1}{4\pi a^3 \mu_0} \int_0^{t_1} \int_G D_\alpha \rho(\mathbf{m}) \operatorname{curl} \hat{\mathbf{B}} \cdot \operatorname{curl} \mathbf{B} dV dt; \quad (3.51)$$

6. add regularization terms to $\chi^2(\mathbf{m})$ and $D_\alpha \chi^2(\mathbf{m})$ to obtain the penalty function $F(\mathbf{m})$ and its gradient;
7. use the minimization algorithm to advance to next \mathbf{m} .

3.2 3-D time-domain forward solver

3.2.1 Semi-implicit scheme

From now on, we will concentrate only on the formulation of the forward and adjoint problems with the external boundary condition. The forward solver described in details in [Velímský and Martinec \[2005\]](#) can be directly applied also to the adjoint problem (3.46–3.47, 3.48a, 3.49a, 3.50). It is based on the spherical harmonic-finite element parametrization of the weak formulation of the problem. This leads to a set of ordinary differential equations,

$$\mathcal{M} \cdot \frac{\partial \vec{X}}{\partial t}(t) + \mathcal{A}(\rho) \cdot \vec{X}(t) = \vec{Y}(t), \quad (3.52)$$

which are solved at each time step. Here \vec{X} is a vector containing the spherical harmonic coefficients $B_{jm}^{(\lambda)}$ for each layer, the matrices \mathcal{M} and \mathcal{A} correspond to the L_2 product $\mu_0 (\cdot, \cdot)_{L_2}$, and sesquilinear form $(\rho \operatorname{curl} \cdot, \operatorname{curl} \cdot)_{L_2}$, respectively, and \vec{Y} contains the boundary conditions in the form of coefficients $G_{jm}^{(e)}$. The semi-implicit scheme is based on splitting of the matrix \mathcal{A} according to spherically symmetric 1-D resistivity model ρ_0 and 3-D variations ρ_1 ,

$$\left(\frac{1}{\Delta t} \mathcal{M} + \mathcal{A}_0(\rho_0) \right) \cdot \vec{X}_{i+1} = \vec{Y}_{i+1} + \left(\frac{1}{\Delta t} \mathcal{M} - \mathcal{A}_1(\rho_1) \right) \cdot \vec{X}_i, \quad (3.53)$$

where Δt is constant time step, $\vec{X}_i = \vec{X}(t_i)$, $\vec{Y}_i = \vec{Y}(t_i)$. The left-hand side matrix $(\frac{1}{\Delta t} \mathcal{M} + \mathcal{A}_0)$ has only 9 non-zero bands around the diagonal and can be effectively factorized. The right-hand side matrix is much more dense. However, the product $\mathcal{A}_1 \cdot \vec{X}$ can be computed efficiently using the FFT technique.



3.2.2 Crank-Nicolson scheme and iterative approach

As can be expected, the numerical tests of the semi-implicit scheme show some time lag of 3-D effects [Velímský and Martinec, 2005]. This improves with shortening the time-step, but the implicit treatment of these effects still implies accumulated errors over long time series. Therefore, we introduce a modification of our forward solver based on an iterative approach to the Crank-Nicolson time-integration scheme, which is second-order accurate in time [Press et al., 1992, Chapter 19.2].

First, we write the Crank-Nicolson scheme centered around time $t_{i+\frac{1}{2}}$,

$$\mathcal{M} \cdot \frac{\vec{X}_{i+1} - \vec{X}_i}{\Delta t} + \mathcal{A}(\rho) \cdot \frac{\vec{X}_{i+1} + \vec{X}_i}{2} = \frac{\vec{Y}_{i+1} + \vec{Y}_i}{2}. \quad (3.54)$$

Then we split the solution into the 1-D part and 3-D corrections,

$$\vec{X}_{i+1} = \vec{X}_{i+1}^{(0)} + \vec{x}_{i+1}^{(k)}. \quad (3.55)$$

where $\vec{X}_{i+1}^{(0)}$ solves

$$\left(\frac{2}{\Delta t} \mathcal{M} + \mathcal{A}_0(\rho_0) \right) \cdot \vec{X}_{i+1}^{(0)} = \vec{Y}_{i+1} + \vec{Y}_i + \left(\frac{2}{\Delta t} \mathcal{M} - \mathcal{A}_0(\rho_0) \right) \cdot \vec{X}_i. \quad (3.56)$$

The 3-D corrections $\vec{x}_{i+1}^{(k)}$ are then found by an iterative scheme,

$$\left(\frac{2}{\Delta t} \mathcal{M} + \mathcal{A}_0(\rho_0) \right) \cdot \vec{x}_{i+1}^{(k)} = -\mathcal{A}_1(\rho_1) \cdot \left(\vec{X}_i + \vec{X}_{i+1}^{(0)} + \vec{x}_{i+1}^{(k-1)} \right), \quad (3.57)$$

which makes use of the factorization of matrix $(\frac{2}{\Delta t} \mathcal{M} + \mathcal{A}_0)$ and fast multiplication by matrix \mathcal{A}_1 , and which terminates when

$$\frac{|\vec{x}_{i+1}^{(k+1)} - \vec{x}_{i+1}^{(k)}|^2}{|\vec{x}_{i+1}^{(k+1)}|^2} < \varepsilon. \quad (3.58)$$

Depending on the required accuracy ε and on the amplitude of 3-D anomalies, it usually takes between 10^0 to 10^2 iterations to make one time-integration step. This forward solver has been used in the initial tests of the inversion code using checkerboard resistivity models and smooth analytical model of the external field.

3.2.3 Crank-Nicolson scheme with factorization of full matrix

For long time series, the cost of the iterative approach to the Crank-Nicolson scheme becomes prohibitive. Therefore, a third implementation of the forward solver was recently developed. The Crank-Nicolson scheme (3.54) is rewritten as

$$\left(\frac{2}{\Delta t} \mathcal{M} + \mathcal{A} \right) \cdot \vec{X}_{i+\frac{1}{2}} = \frac{\vec{Y}_{i+1} + \vec{Y}_i}{2} + \frac{2}{\Delta t} \mathcal{M} \cdot \vec{X}_i, \quad (3.59)$$

where

$$\vec{X}_{i+\frac{1}{2}} = \frac{\vec{X}_{i+1} + \vec{X}_i}{2}. \quad (3.60)$$

Fast spherical transformation routines are used to assemble the matrix \mathcal{A} . Complete LU decomposition of wide-banded (band width $\approx j_{\max}^2$) matrix $(\frac{2}{\Delta t} \mathcal{M} + \mathcal{A})$ is computed and stored at the start of time integration, and then repeatedly used for fast solution of linear system (3.59) at each time step. Equation

k	r_k	r_{k+1}	$\rho_{00,k}$
1	0 km	3480 km	-4
2	3480 km	5171 km	-2
3	5171 km	5571 km	0
4	5571 km	5971 km	1
5	5971 km	6371 km	2

Table 3.1: Layer radii and 1-D resistivity model.

(3.60) is then used to compute \vec{X}_{i+1} . Storage, and multiplication by the matrix \mathcal{A} during the time integration is thus avoided.

While CPU and especially memory requirements of the LU factorization are large, off the shelf parallelized subroutines can be used for increased effectiveness. Currently, shared-memory (OpenMP) parallel code based on the LAPACK library is mature and can be used for runs with lateral resolution up to $j_{\max} \leq 10$ on a modern workstation. This code has been used in the test inversions based on the E2E resistivity and external field models.

A distributed-memory (MPI) version of the code based on the MUMPS library is still in development, with a possible future switch to the SCALAPACK library.

3.3 Checkerboard tests of the inversion

3.3.1 Checkerboard model

Here we present the results of a simple, but fully 3-D checkerboard synthetic test. We parametrize the logarithm of resistivity by spherical harmonics in lateral coordinates and piecewise constant functions in radius,

$$\log(\rho(r, \Omega) \text{ in } \Omega \cdot \text{m}) = \sqrt{4\pi} \sum_{k=1}^K \sum_{j=0}^J \sum_{m=-j}^j \rho_{jm,k} Y_{jm}(\Omega) \xi_k(r). \quad (3.61)$$

Since ρ is real, the complex coefficients $\rho_{jm,k}$ are constrained by relation

$$\rho_{j-m,k} = (-1)^m \rho_{jm,k}. \quad (3.62)$$

Treating only the real parts for $m \geq 0$, and imaginary parts for $m > 0$ as independent real parameters, yields the dimension of the model space

$$M = K(J+1)^2. \quad (3.63)$$

The radial part of the model, i.e., the spherical harmonic coefficients $\rho_{00,k}$ are fixed at their respective values (see Table 3.1) and excluded from the inversion. The target model, that is the model that we will try to recover by inversion, has the coefficients $\rho_{32,k}$ set to ± 0.1 in three 400 km thick layers. Other coefficients in these layers are zero. The inversion attempts to recover all coefficients $\rho_{jm,k}$, $(j, m) \neq (0, 0)$, in the 3-D layers up to degree 3. The two lowermost layers have no lateral variations.

3.3.2 Synthetic excitation model

The resistivity model is loaded by a 10 days long synthetic model of a geomagnetic storm with dipolar geometry and analytical time-dependence, (Fig. 3.1)

$$G_{10}^{(e)} = 0.003 \text{ nT/s} t \exp\left(\frac{-t}{24 \text{ h}}\right). \quad (3.64)$$

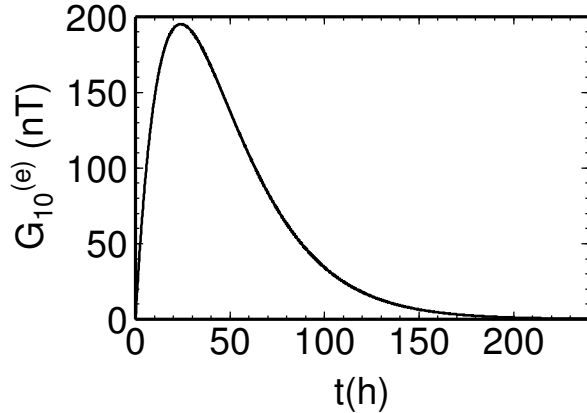


Figure 3.1: Synthetic model of external field.

All forward problems are started from a zero initial condition and therefore $t_0 = 0$ can be assumed in the misfit evaluation (3.29).

3.3.3 Accuracy of time-integration schemes

First, we compare the accuracy of the semi-implicit and Crank-Nicolson time-integration schemes. For each method we start from the target model and evaluate the misfit and its derivative along lines in three directions in the model space, corresponding to the real parts of parameters $\rho_{32,k}$, $k = 3, 4, 5$, respectively. The results are summarized in Figure 3.2. In the left column, we can see that both methods yield similar results for small 3-D variations ($|\rho_{32,k}| < 0.3$). As the effect of 3-D resistivity increases, the results obtained by both methods start to differ. Similar behavior is observed in the middle column, where the derivative of the misfit with respect to $\rho_{32,k}$ is shown. Finally, we compute the misfit derivative by numerical differentiation and compare it to the value obtained from the adjoint method. The result is shown in the right column. We can observe, that as the amplitude of 3-D variations increases, the difference between the misfit derivative obtained by the adjoint method and by the numerical differentiation increases considerably faster when using the semi-implicit algorithm than in the case of Crank-Nicolson scheme. In other words, the value of the misfit and its derivative as given by the semi-implicit method are not consistent. In this sense, the results of the Crank-Nicolson scheme are significantly more accurate, albeit at a significant computational cost.

3.3.4 Conjugate gradient inversion

Here we show the solution of full 3-D time-domain inversion. We employ the conjugate gradient (CG) minimization with bracketing and line search using Brent's method with derivative [Press et al., 1992, Chapters 9.1, 10.2, 10.6]. No explicit regularization in the model space is implemented, i.e., $R(\mathbf{m}) = 0$, although the choice of the spherical harmonics represents an implicit regularization. The forward problem is solved with spherical-harmonic truncation degree $j_{\max} = 10$, $k_{\max} = 40$ unequally spaced layers, and with time step $\Delta t = 0.1$ h. The Crank-Nicolson scheme is used with accuracy criterion introduced in Equation (3.58) set to $\varepsilon = 10^{-4}$. The minimization is started from a random point in the model space.

The results of inversion are summarized in Figures 3.3–3.6. In Figure 3.3 we show from top to bottom the 3-D target resistivity model, the initial random model, a model obtained after 10 CG iterations, and the final model reached after 42 CG iterations. Note that the CG algorithm recovers the resistivity

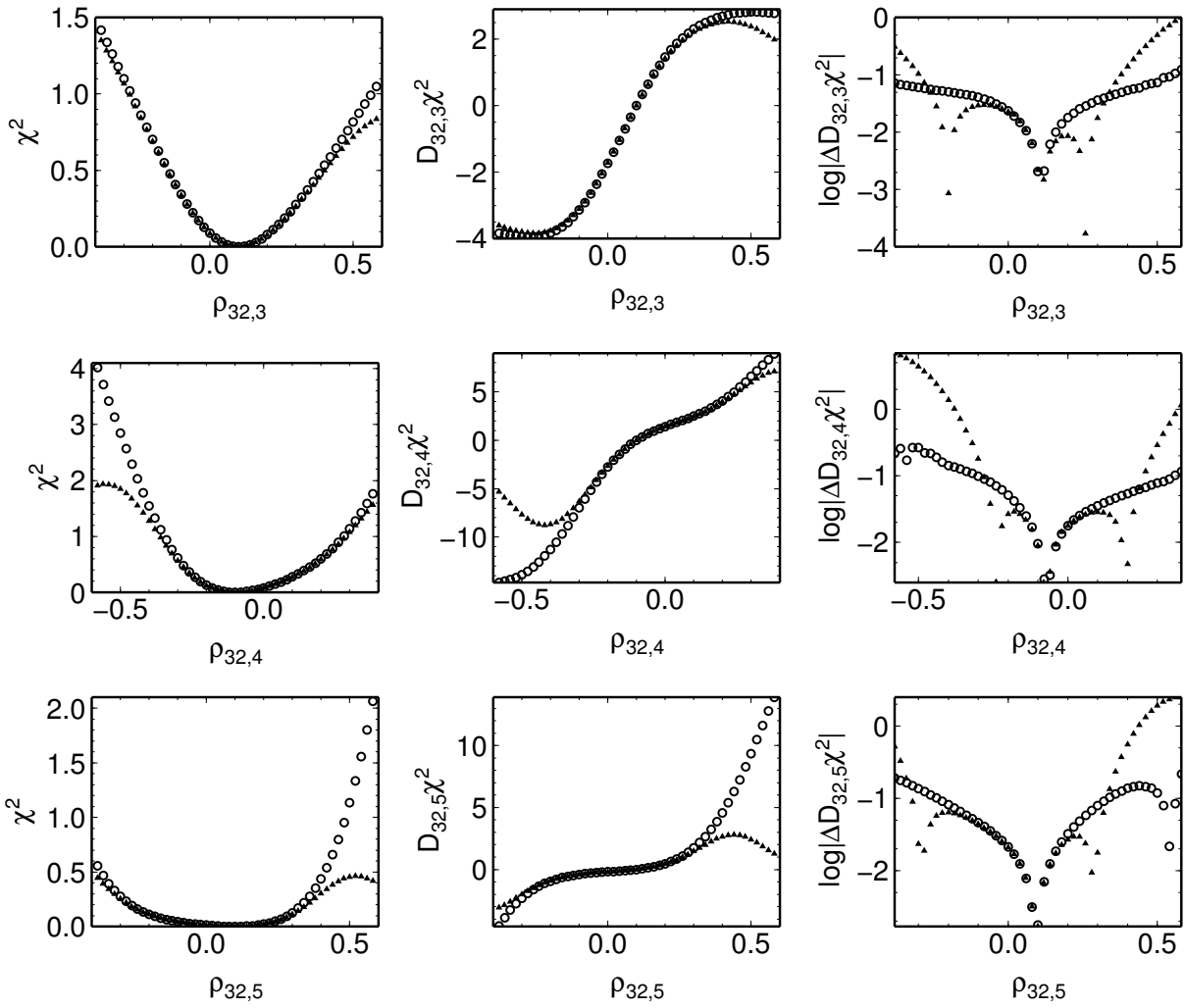


Figure 3.2: Comparison of Crank-Nicolson (open circles) and semi-implicit (full triangles) time-integration scheme. All figures show one-dimensional cross-sections through the target model along the model parameter $\rho_{32,k}$; $k = 3$ (bottom), $k = 4$ (middle), $k = 5$ (top). Left column compares the misfits, central column shows the misfit derivatives obtained by the adjoint method, and the right column shows differences between these derivatives and those obtained by direct numerical differentiation of the misfit.

in the lowermost model almost perfectly already after 10 iterations, and manages to recover most of the middle layer structure as well. It takes about 30 more iterations to recover also the uppermost layer.

In Figure 3.4 we display the sensitivity, which we define as

$$Q(\mathbf{r}) = \int_{t_0}^{t_1} \operatorname{curl} \hat{\mathbf{B}}(\mathbf{r}; \hat{t}) \cdot \operatorname{curl} \mathbf{B}(\mathbf{r}; t) dt. \quad (3.65)$$

By conferring Equation (3.65), we see that this quantity tells us what effect the spatial distribution of the gradient of resistivity has on the gradient of misfit. Note that the sensitivity in the lowermost layer is 2–3 orders of magnitude larger than in the uppermost layer and that the overall sensitivity decreases as we approach to the misfit minimum.

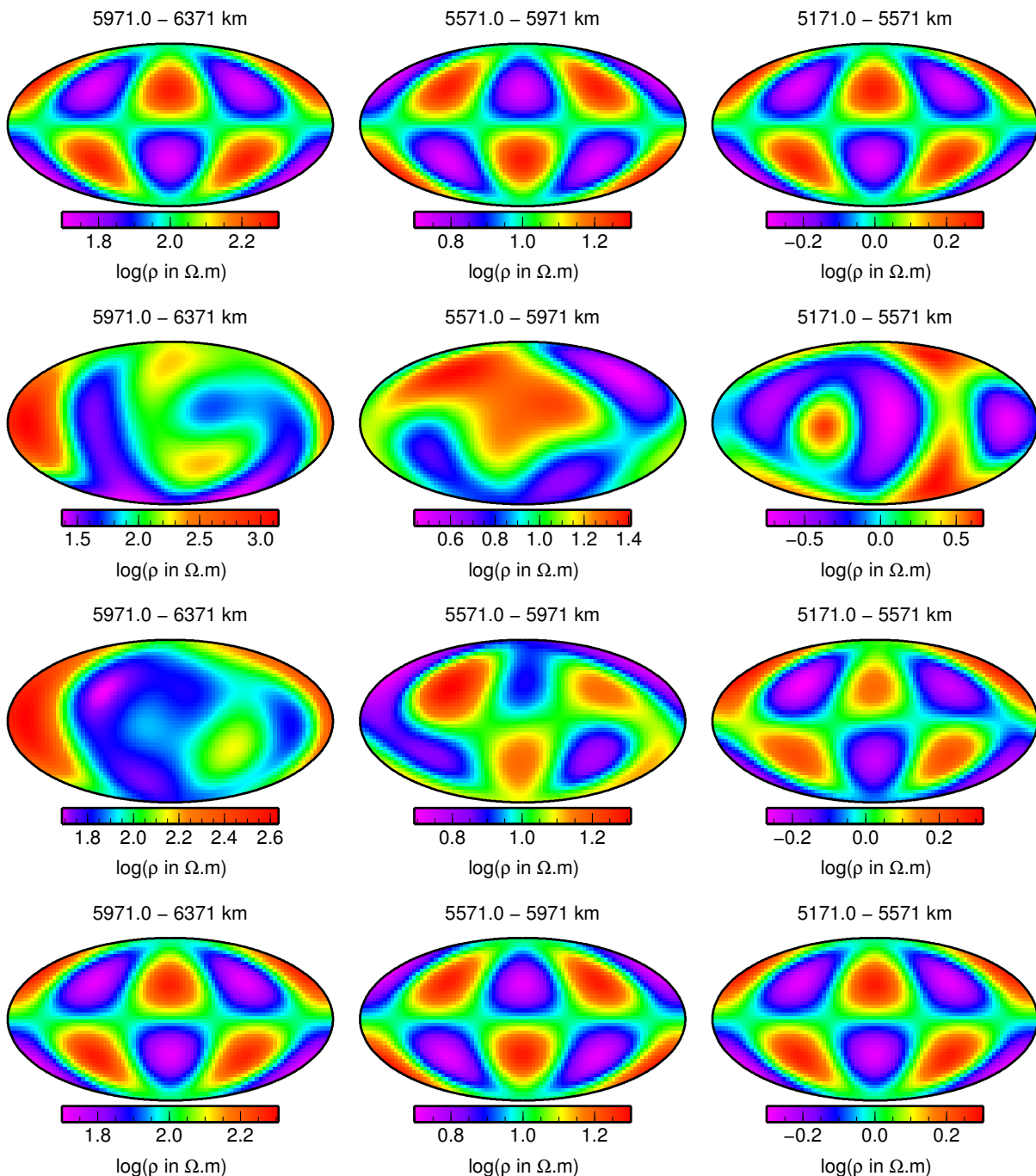


Figure 3.3: CG minimization: The top row shows the target resistivity model in the three 3-D layers. Second row shows the initial random model. The third row shows the resistivity model after 10 CG iterations and the fourth row the final model obtained after 42 CG iterations.

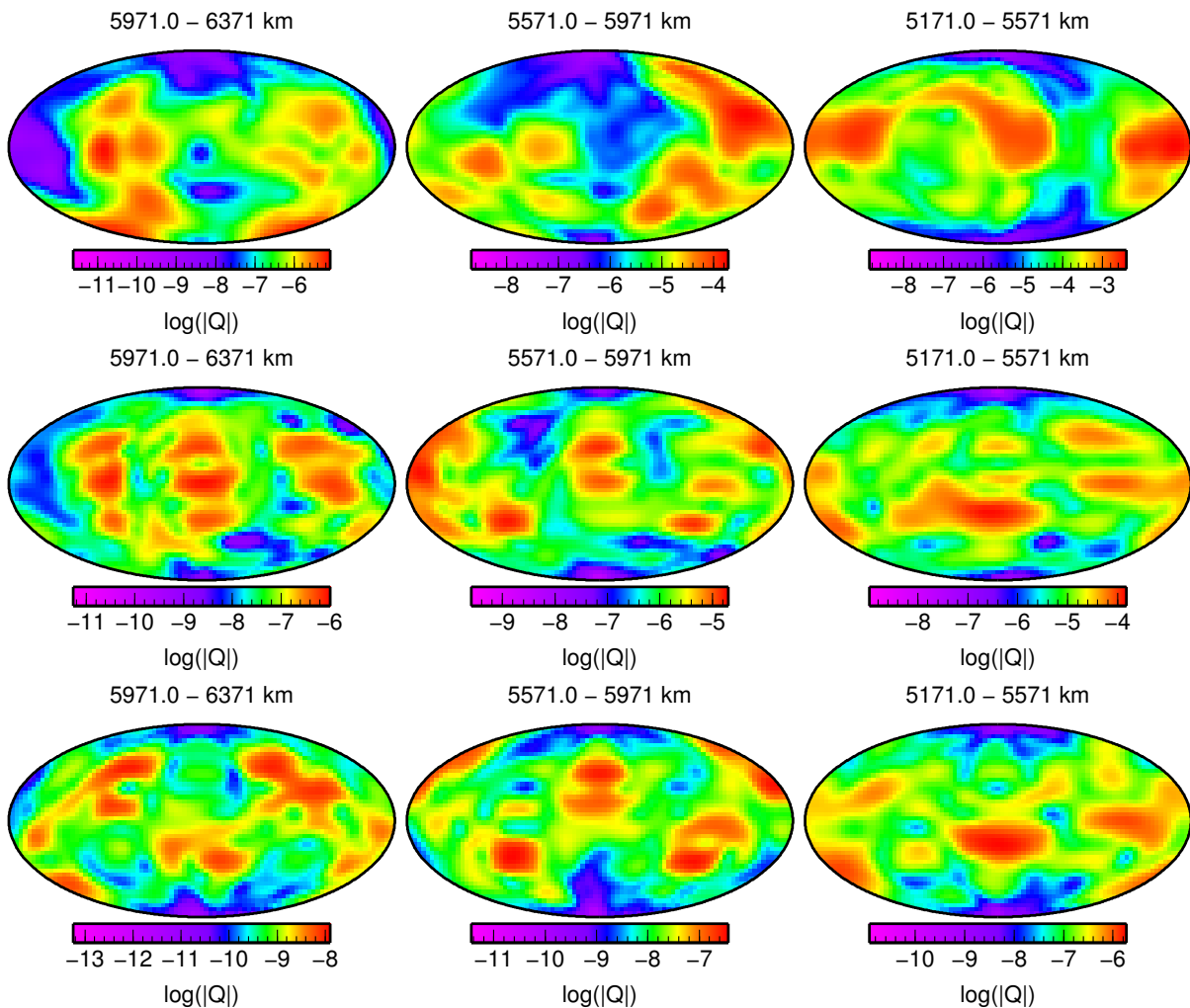


Figure 3.4: Sensitivity Q , as given by equation (3.65) for the initial random model (top row), after 10 iterations (middle row) and after 42 iterations (bottom row).

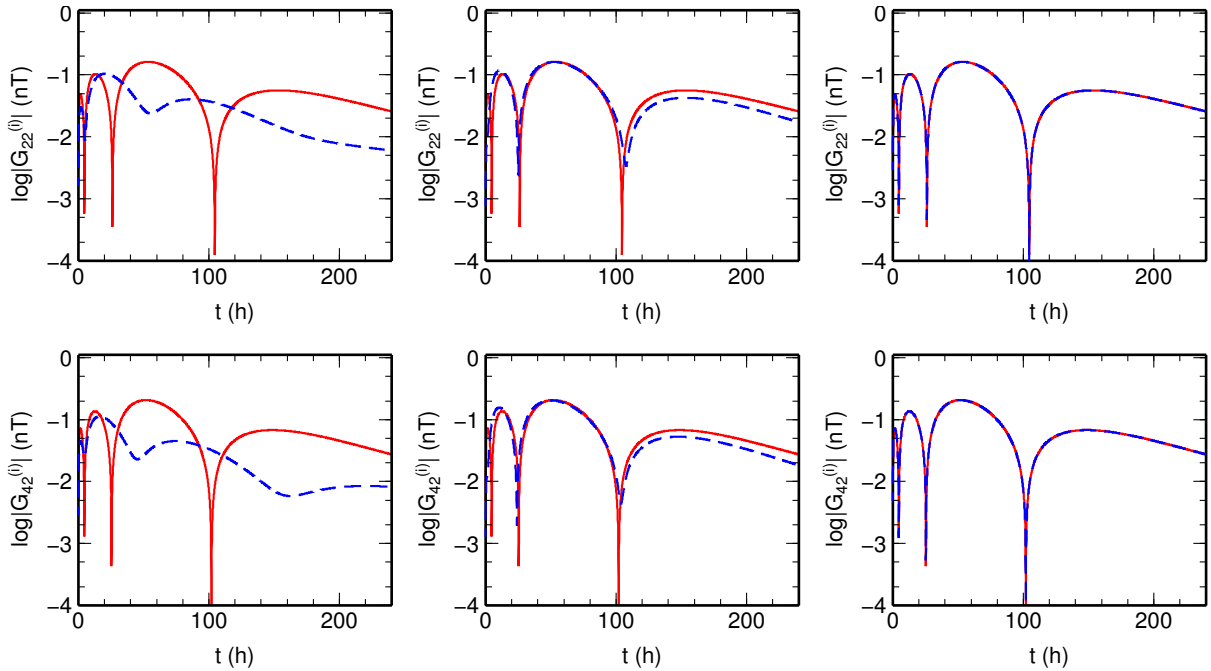


Figure 3.5: Magnitudes of the internal field coefficients $G_{22}^{(i)}(t)$ (top row) and $G_{42}^{(i)}(t)$ (bottom row). The solid red lines show the response of the target model in all plots. The blue dashed lines correspond to the responses of the initial random model (left column), after 10 CG iterations (middle column), and after 42 iterations (right column).

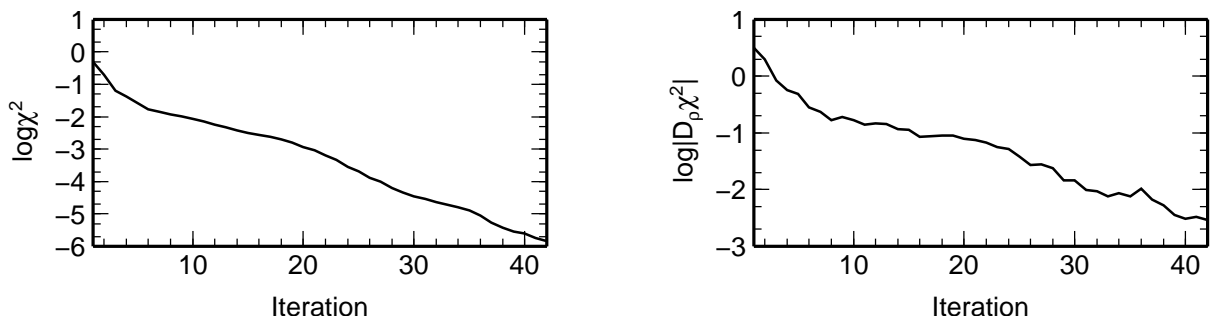


Figure 3.6: Evolution of misfit (left) and magnitude of its gradient (right) with CG iterations.

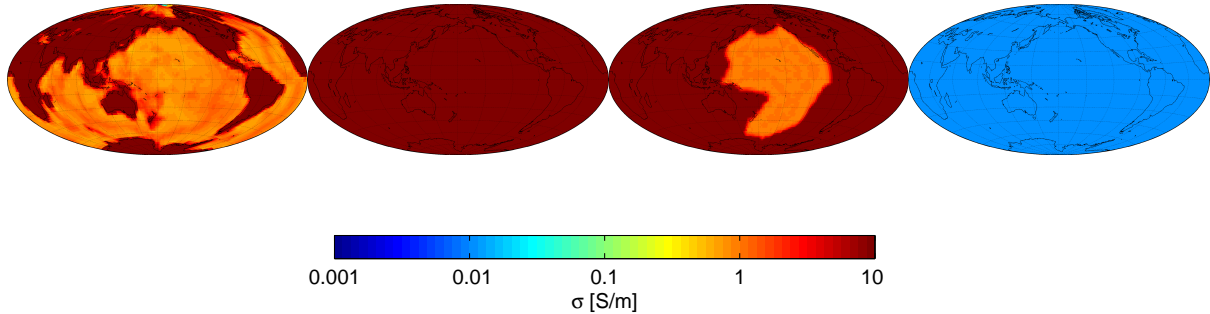


Figure 3.7: E2E conductivity model.

We also display how the internal field coefficients $G_{22}^{(i)}(t)$ and $G_{42}^{(i)}(t)$ approach the responses of the target model as the CG iterations progress (Figure 3.5). The effect of P_{32} resistivity structure is most prominent at these harmonics, as they are offset by one spherical harmonic degree, which corresponds to the source P_{10} geometry. Note that both the amplitudes and the positions of zero crossings are adjusted by the inversion, reminiscent of seismogram fitting in seismological problems.

Finally, Figure 3.6 shows the monotonous decrease of misfit and the decrease of the magnitude of its gradient. One can see, that with the relatively simple model and with exact synthetic data without noise, the target model is recovered after 42 time steps almost perfectly.

3.4 E2E-based tests of the inversion

3.4.1 E2E resistivity model

The End-To-End (E2E) simulation of Olsen et al. [2006] introduced a 3-D resistivity model that we summarize in Figure 3.7. It consists of a highly heterogeneous thin layer representing the surface conductance, a 400 km thick homogeneous upper mantle with 3 small-scale conductive heterogeneities placed below Baikal, Hawaii and Chilean subduction, a 300 km thick transition zone with a large-scale heterogeneity below Pacific, and a homogeneous lower mantle.

Similarly to the checkerboard test, we parametrize the resistivity model by spherical harmonic expansion of its logarithm (3.61) up to degree 5 in 6 layers 200 km thick. The 1-D model, consisting of the parameters $\rho_{00,k}$, is initially found by 1-D inversion and then used as a starting model for full 3-D inversion runs. The near surface heterogeneous layer is prescribed on a grid and assumed to be a-priori known. The target E2E model that we aim to recover lies outside this parameter space, because it is given on a grid with higher lateral resolution and some of the layer interfaces do not coincide with those prescribed in the model space discretization.

3.4.2 E2E external field model

We use the E2E model [Olsen et al., 2006] that describes the external field up to degree and order 6 (Figure 3.8). A 100 day time series is used to compute the internal field generated by the E2E resistivity model. In the presented examples, we add random noise to the SH coefficients of external and/or internal

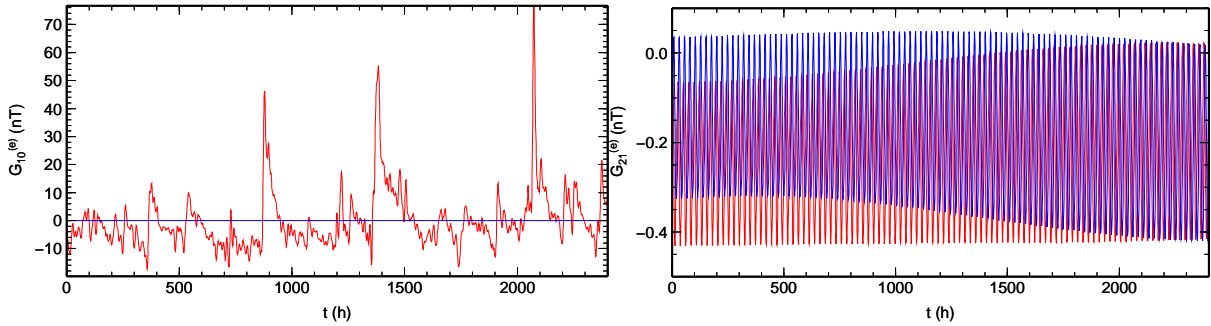


Figure 3.8: E2E external field model. Left column shows the $G_{10}^{(e)}$ coefficient, right column shows the real and imaginary parts of $G_{21}^{(e)}$ by red and blue lines, respectively.

Case	external field		internal field		
	target model	inversion		j_{\max}	f
		j_{\max}	j_{\max}		
I	6	6	0 %	7	5 %
II	6	1	0 %	7	5 %
III	1	1	5 %	7	5 %
IV	6	1	5 %	7	5 %

Table 3.2: Parameters of the E2E inversions.

field, scaled by the average amplitude,

$$A_{jm}^{(e|i)} = \frac{1}{t_1} \int_0^{t_1} |G_{jm}^{(e|i)}(t)| dt, \quad (3.66)$$

$$\tilde{G}_{jm}^{(e|i)}(t) = G_{jm}^{(e|i)}(t) + f A_{jm}^{(e|i)} N_{0,1}(t), \quad (3.67)$$

where $f = 0$ or 5% and $N_{0,1}(t)$ is real (for $m = 0$) or complex (for $m \neq 0$) normal distribution. Parameters of the inversions are summarized in Table 3.2. In Case I, we assume exact knowledge of the spatio-temporal structure of the external field in the inversion. In Case II, the inversion uses spatially inaccurate excitation, in Case III, the excitation includes noise in time, and Case IV combines both effects into spatially and temporally inaccurate description of the external field.

3.4.3 Regularization and LMQN inversion

We have implemented a regularization term that constrains the smoothness of the resistivity model by minimizing the spherical Laplacian of logarithm of resistivity,

$$R^2(\mathbf{m}) = \frac{1}{2} \frac{a^4}{V} \int_G [\nabla^2 \log \rho(\mathbf{m})]^2 dV,$$

$$D_\alpha R^2(\mathbf{m}) = \frac{a^4 \log e}{V} \int_G \nabla^2 \log \rho(\mathbf{m}) \nabla^2 \frac{D_\alpha \rho(\mathbf{m})}{\rho(\mathbf{m})} dV$$

The inverse problem is solved for several regularization parameters λ , the optimal value is then chosen near the maximum curvature point of the L-curve plotting data misfit $\chi^2(\mathbf{m})$ vs. the regularization $R^2(\mathbf{m})$.

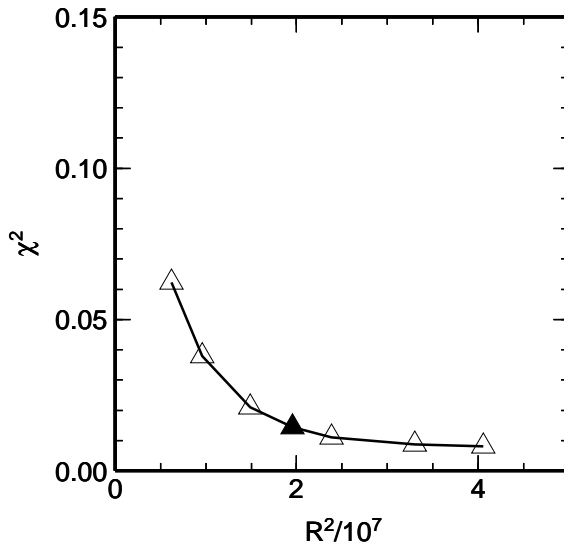


Figure 3.9: Case I. L-curve showing trade-off between data misfit and regularization, with optimal regularization marked by black triangle.

The inverse problem is solved by limited-memory quasi-Newton (LMQN, also known as variable metrics) minimization [Press et al., 1992, Chapter 10.7],

$$\mathbf{m}_{i+1} - \mathbf{m}_i = H_{i+1} \cdot D\mathbf{m} [F(\mathbf{m}_{i+1}) - F(\mathbf{m}_i)], \quad (3.68)$$

using the Broyden-Fletcher-Goldfarb-Shanno formula for updating the symmetric, positive-definite approximation of Hessian H_{i+1} and Brent's method for line minimization. This method requires a lower number of forward solver calls, than the conjugate-gradient method used previously.

Results for Cases I–IV are summarized in Figures 3.10–3.16. In all cases, the large-scale heterogeneity in the transition zone was successfully recovered. Naturally, spatially inaccurate external field model and/or adding noise to the time-series increases the data misfit considerably. At this resolution, there is little hope to resolve any of the small-scale features in the upper mantle. There is also significant leaking of the effect of the large heterogeneity to layers above and below it. This effect can be caused by overregularization in the radial direction as can be seen by comparing Figure 3.16 obtained with optimal regularization with Figure 3.17 showing results of the inversion with extremely small regularization parameter λ . While the 1-D background values are better resolved in the underregularized model, lateral resolution of the heterogeneity is poor. That suggests, that anisotropic regularization, stronger in the lateral direction while more relaxed in the radial direction, could be used.

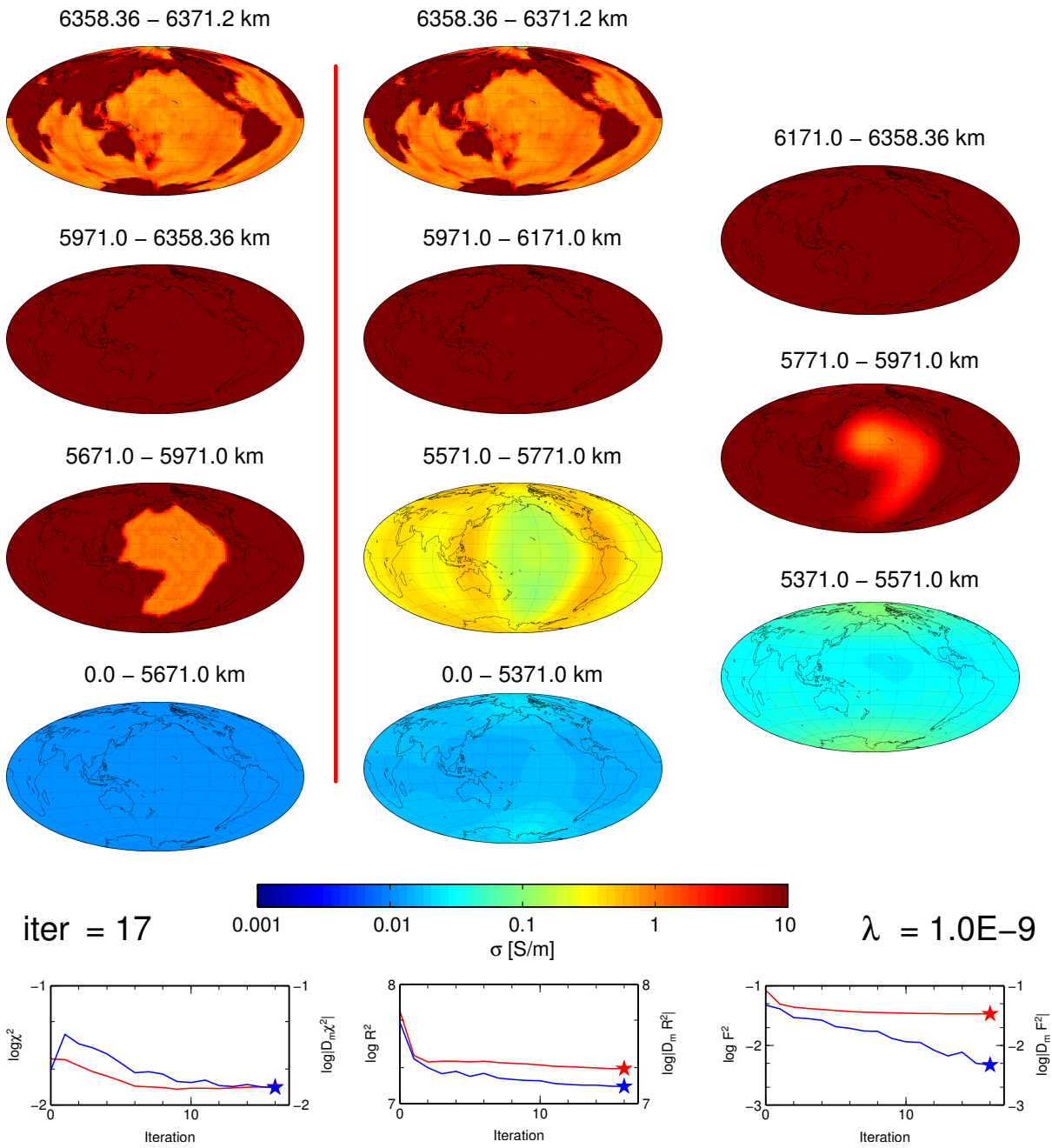


Figure 3.10: Case I. Left column: Target E2E model shown for comparison. Right staggered columns: Conductivity model recovered by inversion. The radial position of each layer is marked above the map. Bottom row, left to right: data misfit, regularization and total penalty functions (red) and their gradients (blue) as functions of number of LMQN iterations.

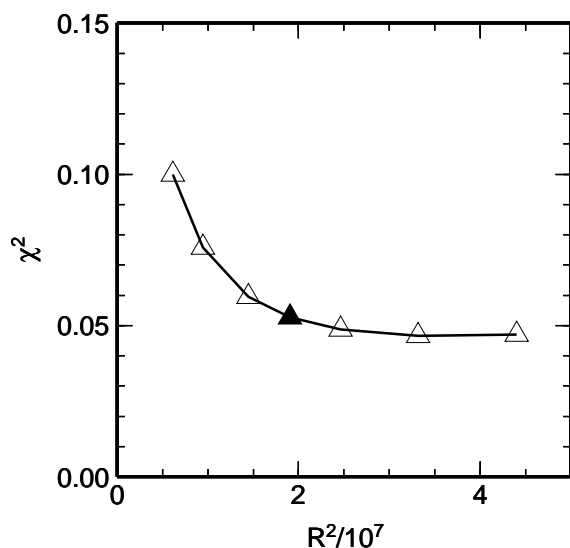


Figure 3.11: Case II.

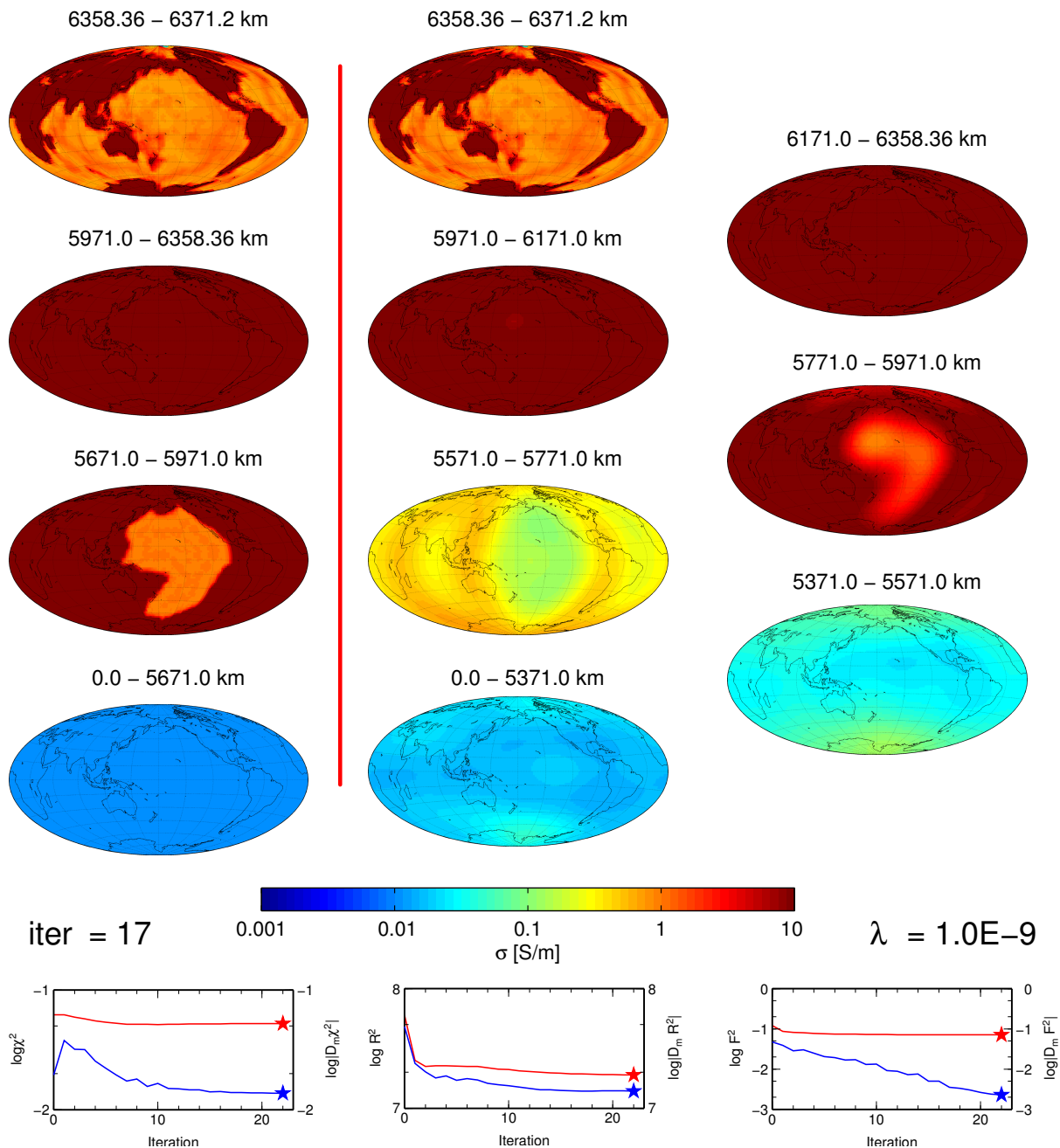


Figure 3.12: Case II.

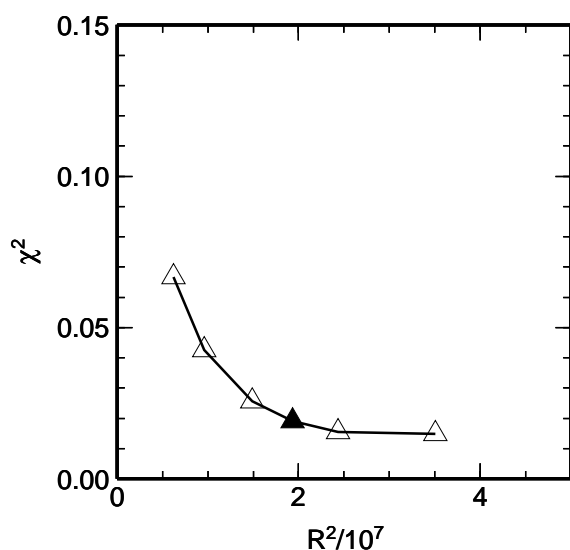


Figure 3.13: Case III.

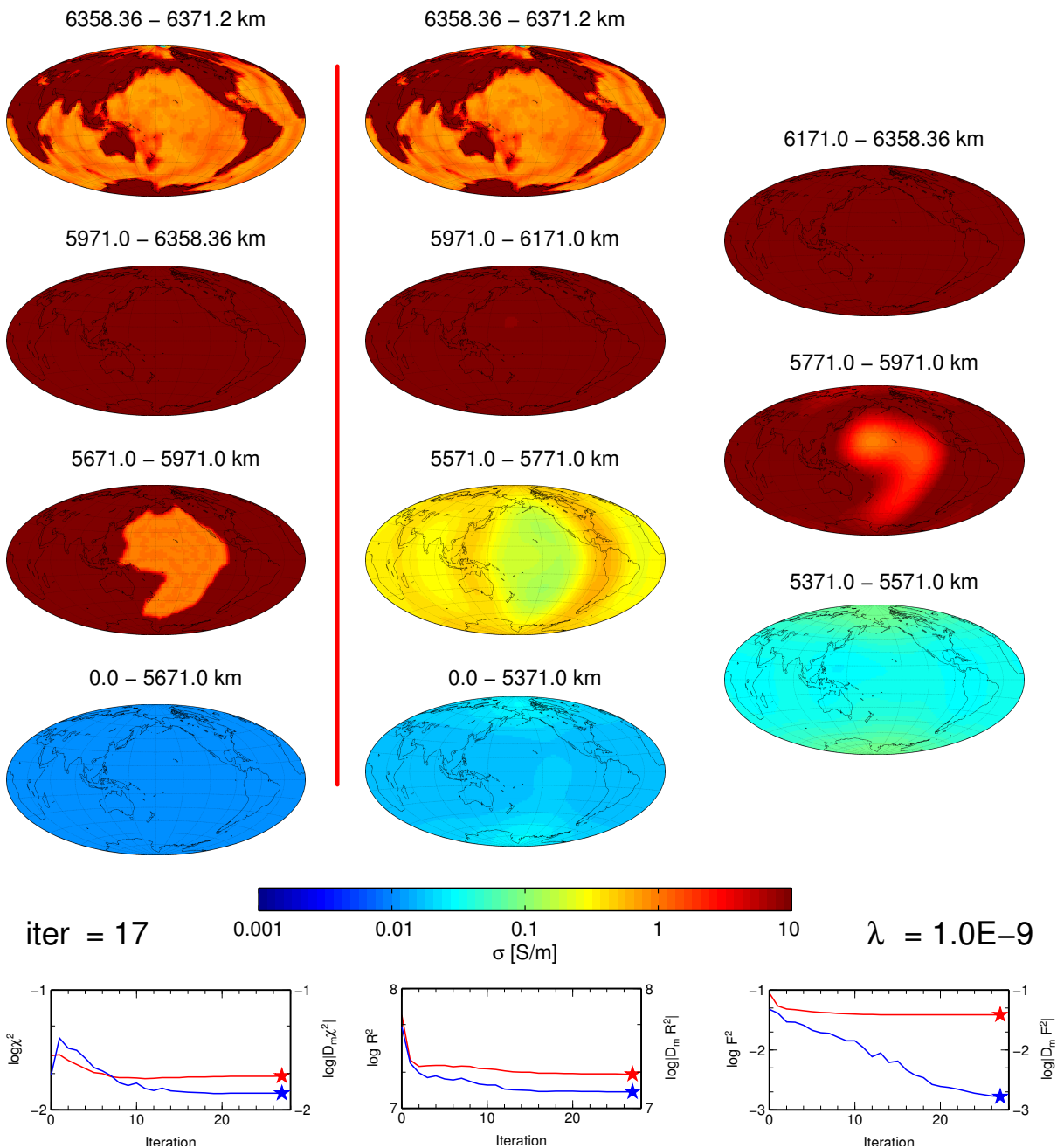


Figure 3.14: Case III.

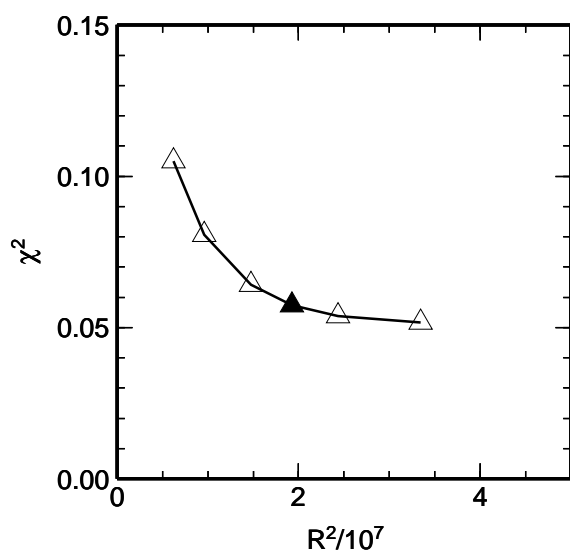


Figure 3.15: Case IV.

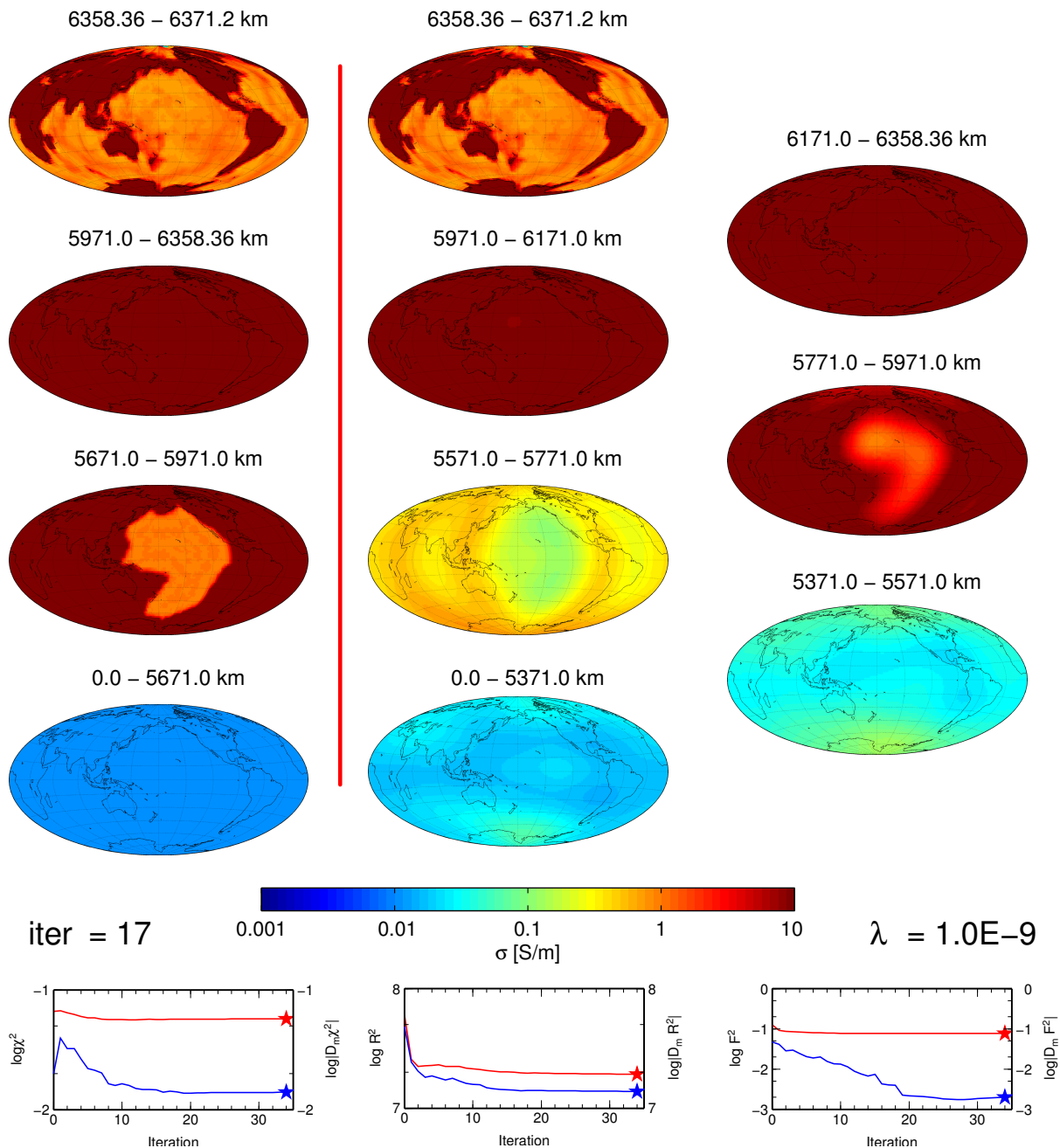


Figure 3.16: Case IV.

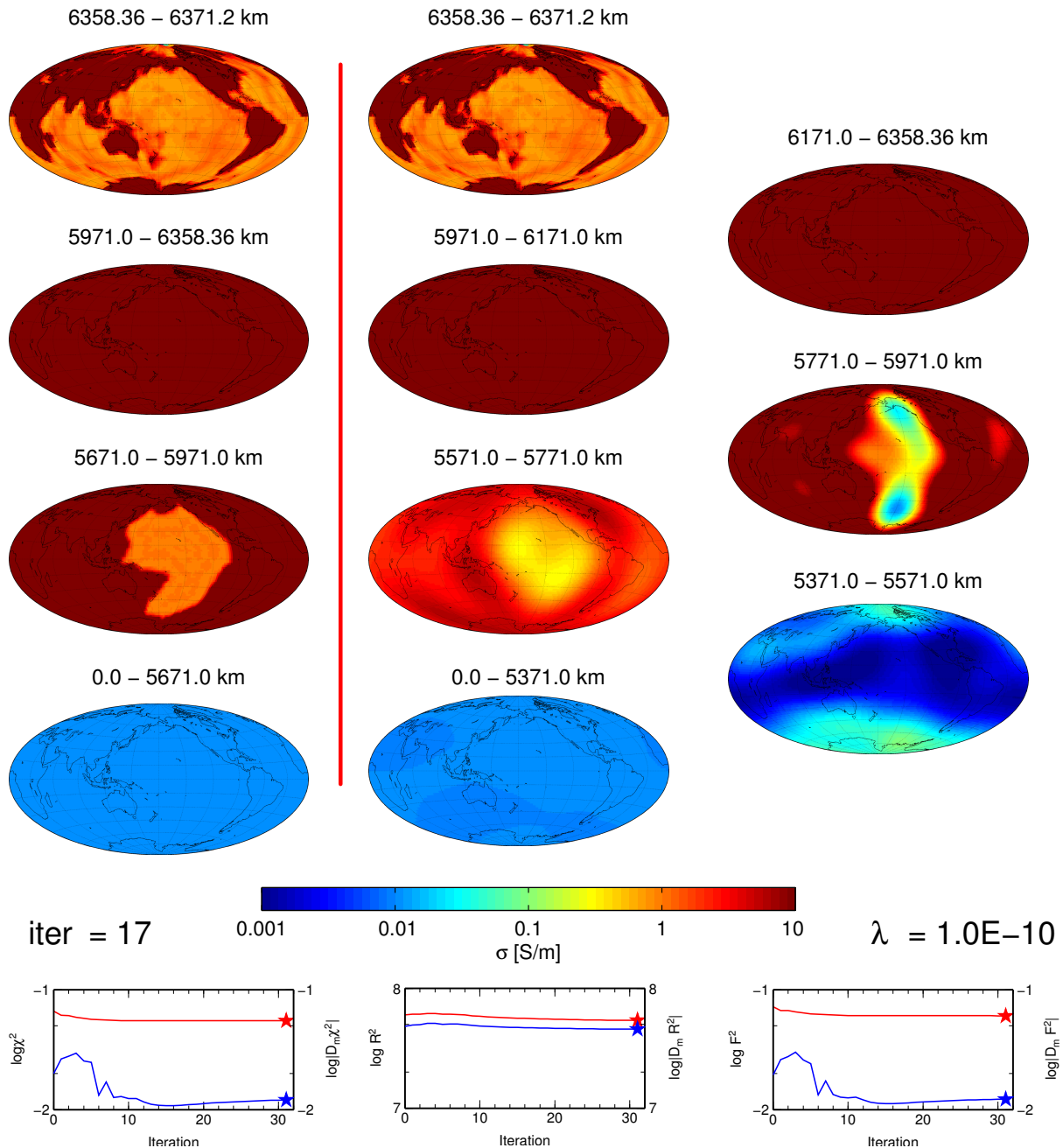


Figure 3.17: Case IV. Underregularized model.

Chapter 4

Frequency domain internal coefficient inversion

4.1 Some general remarks

The purpose of the study presented in this Chapter is to demonstrate the feasibility of 3-D conductivity inversion using satellite magnetic data. With the forthcoming *Swarm* constellation project for magnetic studies, a new era for global induction studies is opening with new ways to infer the electrical conductivity in the Earth.

The situation is very unusual for induction studies as the transient magnetic field is sampled simultaneously both in time and space. It is however sampled at a high rate and continuously over the Earth. Several studies have demonstrated the feasibility of induction studies from space for simple source geometries and one dimensional (1-D) conductivity models (e.g. [Olsen, 1999]). The main objective of space induction is to obtain data to image the 3-D mantle conductivity. Studies to date suggest that a 3-D induction signal is present in the satellite data [Tarits, 2000, Constable and Constable, 2004]. Here, a full solution to this problem is tested. The first step consists of data processing to obtain observables suitable for conductivity modelling. The second step is modelling these observables to recover the 3-D conductivity structure. The approach is tested on synthetic magnetic data from [Kuvshinov et al., 2006].

4.2 The numerical model

The mantle is divided into spherical shells. The conductivity in each shell may be uniform or it may vary horizontally, but it may not vary radially. The stack of shells starts from a homogeneous core of finite conductivity and ends at an upper boundary above which the medium is insulating. A generic Earth model is shown in Fig. 4.1. Under the quasi-static approximation, the governing equations in the core are:

$$\begin{aligned}\nabla \bullet \mathbf{B}(\mathbf{r}, t) &= 0 \\ \nabla \times \mathbf{E}(\mathbf{r}, t) &= -\frac{\partial}{\partial t} \mathbf{B}(\mathbf{r}, t) \\ \nabla \times \mathbf{B}(\mathbf{r}, t) &= \mu\sigma_c \mathbf{E}(\mathbf{r}, t)\end{aligned}\tag{4.1}$$

where μ is the magnetic permeability in vacuum, σ_c is the constant core conductivity, and \mathbf{B} and \mathbf{E} are the total magnetic and electric fields. In the mantle the electromagnetic field satisfies:

$$\begin{aligned}\nabla \bullet \mathbf{B}(\mathbf{r}, t) &= 0 \\ \nabla \times \mathbf{E}(\mathbf{r}, t) &= -\frac{\partial}{\partial t} \mathbf{B}(\mathbf{r}, t) \\ \nabla \times \mathbf{B}(\mathbf{r}, t) &= \mu\sigma_m(\mathbf{r}) \mathbf{E}(\mathbf{r}, t)\end{aligned}\tag{4.2}$$

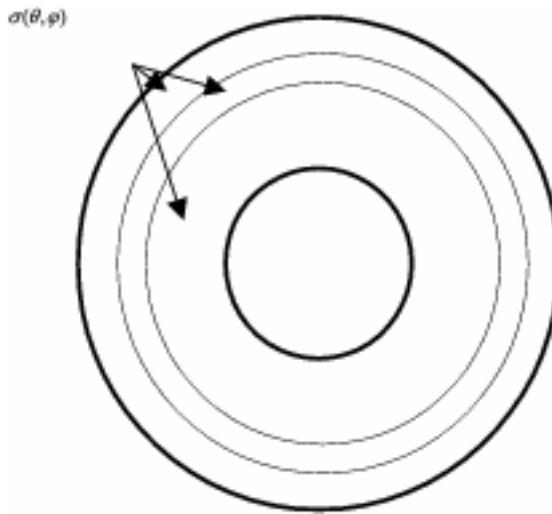


Figure 4.1: Spherical model.

where the mantle conductivity $\sigma_m(\mathbf{r})$ depends on the position vector \mathbf{r} . Continuity conditions (see below) at the core mantle boundary (CMB) relate \mathbf{E} and \mathbf{B} in the mantle just above the CMB to \mathbf{E} and \mathbf{B} in the core just below the CMB.

The time-varying part of the electric and magnetic (EM) fields are defined as $\mathbf{e}(\mathbf{r}, t)$ and $\mathbf{b}(\mathbf{r}, t)$ respectively, so that $\mathbf{B}(\mathbf{r}, t) = \mathbf{B}_s(\mathbf{r}) + \mathbf{b}(\mathbf{r}, t)$ and $\mathbf{E}(\mathbf{r}, t) = \mathbf{E}_s(\mathbf{r}) + \mathbf{e}(\mathbf{r}, t)$. The subscript s stands for static. The fields $\mathbf{e}(\mathbf{r}, t)$ and $\mathbf{b}(\mathbf{r}, t)$ satisfy:

$$\begin{aligned}\nabla \times \mathbf{e}(\mathbf{r}, t) &= -\frac{\partial}{\partial t} \mathbf{b}(\mathbf{r}, t) \\ \nabla \times \mathbf{b}(\mathbf{r}, t) &= \mu \sigma_c \mathbf{e}(\mathbf{r}, t)\end{aligned}\quad (4.3)$$

below CMB while above, they satisfy:

$$\begin{aligned}\nabla \times \mathbf{e}(\mathbf{r}, t) &= -\frac{\partial}{\partial t} \mathbf{b}(\mathbf{r}, t) \\ \nabla \times \mathbf{b}(\mathbf{r}, t) &= \mu \sigma_m(\mathbf{r}) \mathbf{e}(\mathbf{r}, t)\end{aligned}\quad (4.4)$$

Above the upper boundary of the conductivity layer, where the medium is assumed to be insulating, eq (4.4) is still valid with $\sigma_m = 0$.

The second equation in both eq (4.3) and eq (4.4) (Faraday's Law) implies that $\partial(\nabla \bullet \mathbf{b})/\partial t = 0$. Since \mathbf{b} is the time-dependent part of the field, this can be integrated to give $\nabla \bullet \mathbf{b} = 0$. Thus, the first equation in eq (4.1) and eq (4.2) is redundant and was not repeated in eq (4.3) and eq (4.4).

The boundary conditions are that all components of \mathbf{b} , the tangential components of \mathbf{e} , and the radial component of the current $\mathbf{J} = \sigma \mathbf{e}$, are continuous across the IMB, across the upper boundary of the conductivity layer in the mantle, and across every internal boundary separating two adjacent shells in the conductive mantle. One consequence of these boundary conditions is that the radial component of \mathbf{e} must vanish at the upper boundary of the conductivity layer since $\sigma = 0$ above that boundary.

The solution to equations (4.3) and (4.4) is written as:

$$\begin{aligned}\mathbf{e}(\mathbf{r}, t) &= \mathbf{e}_n(\mathbf{r}, t) + \mathbf{e}_a(\mathbf{r}, t) \\ \mathbf{b}(\mathbf{r}, t) &= \mathbf{e}_n(\mathbf{r}, t) + \mathbf{e}_a(\mathbf{r}, t)\end{aligned}\quad (4.5)$$

where the normal field, $(\mathbf{e}_n, \mathbf{b}_n)$, is the solution for a homogeneous core ($\sigma = \sigma_c$) and an insulating mantle ($\sigma = 0$). The anomalous field, $(\mathbf{e}_a, \mathbf{b}_a)$ represents the effects of mantle conductivity. The



equations which govern the normal field $\mathbf{e}_n(r, t)$ and $\mathbf{b}_n(r, t)$ are:

$$\left. \begin{aligned} \nabla \times \mathbf{e}_n(\mathbf{r}, t) &= -\frac{\partial}{\partial t} \mathbf{b}_n(\mathbf{r}, t) \\ \nabla \times \mathbf{b}_n(\mathbf{r}, t) &= \mu\sigma_c \mathbf{e}_n(\mathbf{r}, t) \end{aligned} \right\} \text{in the core} \quad (4.6)$$

$$\left. \begin{aligned} \nabla \times \mathbf{e}_n(\mathbf{r}, t) &= -\frac{\partial}{\partial t} \mathbf{b}_n(\mathbf{r}, t) \\ \nabla \times \mathbf{b}_n(\mathbf{r}, t) &= 0 \end{aligned} \right\} \text{above the core} \quad (4.7)$$

The field \mathbf{b}_n , the horizontal components of \mathbf{e}_n , and the radial component of the electric current $\mathbf{J}_n = \sigma \mathbf{e}_n$ are all continuous across the IMB. Hence $\sigma_c e_{nr} = J_{nr} = 0$ at the core side of the IMB, since for the normal field the medium above the IMB is assumed to be insulating. As a consequence, e_{nr} at the IMB (core side) is null. Subtracting eq. (4.6) from (4.1) and (4.7) from (4.2), we obtain the set of equations for the anomalous field:

$$\left. \begin{aligned} \nabla \times \mathbf{e}_a(\mathbf{r}, t) &= -\frac{\partial}{\partial t} \mathbf{b}_a(\mathbf{r}, t) \\ \nabla \times \mathbf{b}_a(\mathbf{r}, t) &= \mu\sigma_c \mathbf{e}_a(\mathbf{r}, t) \end{aligned} \right\} \text{in the core} \quad (4.8)$$

$$\left. \begin{aligned} \nabla \times \mathbf{e}_a(\mathbf{r}, t) &= -\frac{\partial}{\partial t} \mathbf{b}_a(\mathbf{r}, t) \\ \nabla \times \mathbf{b}_a(\mathbf{r}, t) - \mu\sigma_m(\mathbf{r}) \mathbf{e}_a(\mathbf{r}, t) &= \mu\sigma_m(\mathbf{r}) \mathbf{e}_n(\mathbf{r}, t) \end{aligned} \right\} \text{in the mantle} \quad (4.9)$$

The magnetic field \mathbf{b}_a and the horizontal components of the electric field \mathbf{e}_a are continuous across all boundaries. The boundary condition on the radial component of the anomalous current, $\mathbf{J}_a = \sigma \mathbf{e}_a$, is more complicated, and is determined by the requirement that the total, time-variable, radial current, $\sigma(\mathbf{e}_n + \mathbf{e}_a)$ be continuous across each boundary. At any boundary in the mantle, the conditions is:

$$\sigma(\mathbf{r}^-) e_{ar}(\mathbf{r}^-, t) - \sigma(\mathbf{r}^+) e_{ar}(\mathbf{r}^+, t) = \sigma(\mathbf{r}^+) e_{nr}(\mathbf{r}^+, t) - \sigma(\mathbf{r}^-) e_{nr}(\mathbf{r}^-, t) \quad (4.10)$$

where the superscripts + and - refer to just above and just below the boundary. Equation (4.10) also describes the continuity of e_{ar} at the IMB (where $e_{nr}(\mathbf{r}^-, t) = 0$); and at the upper boundary of the conductive region in the mantle (where $\sigma = 0$).

This separation of the field into normal and anomalous components allows us to solve the problem in two steps. First, eqs (4.6-4.7) are solved to obtain the normal field. We then use this normal field as the source term for generating the anomalous field, using the \mathbf{e}_n terms in eqs (4.9-4.10). We define the current source in terms of the electric and magnetic fields it would produce in an Earth with a spherical homogeneous core and an insulating mantle. Hence we simply assume the normal field is known throughout the mantle, and we use that field in eqs (4.9-4.10). We do ensure that this known normal field is consistent with eq. (4.7) in the mantle.

The fact that the boundaries in our Earth model are all spherical surfaces, means that our equations can be solved most easily in spherical coordinates, (r, θ, φ) , where θ and φ are the colatitude and eastward longitude respectively. Although the laterally-varying conductivity removes spherical symmetry, it is useful to employ spherical harmonic expansions when solving the equations. Accordingly, the electric and magnetic fields are expanded into a generalized spherical harmonics (GSH) series Y_l^{Nm} (see the Appendix) using the canonical basis $(\hat{\mathbf{e}}^+, \hat{\mathbf{e}}^0, \hat{\mathbf{e}}^-)$. In this basis, a vector \mathbf{F} has the form:

$$\mathbf{F}(r, \theta, \varphi) = \sum^N F^N(r, \theta, \varphi) \hat{\mathbf{e}}^N = \sum_{N,l,m} F_l^{Nm}(r) Y_l^{Nm}(\theta, \varphi) \hat{\mathbf{e}}^N \quad N=-1,0,+1 \quad (4.11)$$

The $N = 0$ terms in eq. (4.11) describe the radial component of \mathbf{F} . The horizontal components F_l^{+1m} and F_l^{-1m} are combined into toroidal and spheroidal (or poloidal) component, F_l^{Tm} and F_l^{Pm} respectively (see the Appendix).

The GSH expansions of the e and b fields in eqs (4.6-4.10) are used to obtain differential equations for the GSH coefficients in these expansions. Those equations are shown in the Appendix. The equations are solved in the frequency domain, assuming a time dependence of $e^{i\omega t}$ for e and b where ω is the angular frequency. The resulting equations are first order ordinary differential equations in the radial coordinate r .

4.2.1 Solution for the normal field

The normal field can be completely determined in the mantle by specifying the values of the spherical harmonic components of the radial magnetic and electric field at the IMB (mantle side, $r = c^+$), $b_{nl}^{0m}(c^+)$ and $e_{nl}^{0m}(c^+)$, for every spherical harmonic degree and order (l, m) . The continuation of these IMB values up through the insulating mantle can be determined from the GSH expansion of eq (4.6-4.7) (see Appendix A2). For the b_{nl}^{0m} case the solution for the normal EM field in the insulating mantle is:

$$\begin{bmatrix} b_{nl}^{Pm}(r) \\ b_{nl}^{0m}(r) \end{bmatrix} = b_{nl}^{0m}(c^+) \left(\frac{c}{r}\right)^{l+2} \begin{bmatrix} -l \\ 1 \end{bmatrix} \quad (4.12)$$

$$e_{nl}^{Tm}(r) = \omega r b_{nl}^{0m}(c^+) \left(\frac{c}{r}\right)^{l+2}$$

$$e_{nl}^{Pm}(r) = e_{nl}^{0m}(r) = b_{nl}^{Tm}(r) = 0$$

For the e_{nl}^{0m} case, the solution is:

$$\begin{bmatrix} e_{nl}^{Pm}(r) \\ e_{nl}^{0m}(r) \end{bmatrix} = e_{nl}^{0m}(c^+) \left(\frac{c}{r}\right)^{l+2} \begin{bmatrix} -l \\ 1 \end{bmatrix} \quad (4.13)$$

$$e_{nl}^{Tm}(r) = b_{nl}^{0m}(r) = b_{nl}^{Pm}(r) = b_{nl}^{Tm}(r) = 0$$

4.2.2 Solution for the anomalous field

In the mantle, eqs (4.2) are expanded into GSH (Appendix A2). The resulting equations for the anomalous field are obtained from the GSH expansion of eq. (4.9) by subtracting eqs (4.45-4.46) from (4.44). For each degree and order (l, m) , the following first order system of differential equations is obtained:

$$\frac{d}{dr} \begin{bmatrix} b_{al}^{Pm} \\ b_{al}^{0m} \\ e_{al}^{Pm} \\ J_{al}^{0m} \end{bmatrix} - \begin{bmatrix} -\frac{1}{r} & \frac{2\Omega_l}{r} & 0 & 0 \\ \frac{1}{r} & -\frac{2}{r} & 0 & 0 \\ 0 & 0 & -\frac{1}{r} & i\omega\mu r \\ 0 & 0 & 0 & -\frac{2}{r} \end{bmatrix} \begin{bmatrix} b_{al}^{Pm} \\ b_{al}^{0m} \\ e_{al}^{Pm} \\ J_{al}^{0m} \end{bmatrix} - \begin{bmatrix} i\mu J_{al}^{Tm} \\ 0 \\ \frac{2\Omega_l^2}{r} e_{al}^{0m} \\ \frac{1}{r} J_{al}^{Pm} \end{bmatrix} = \begin{bmatrix} i\mu J_{nl}^{Tm} \\ 0 \\ i\omega\mu r J_{nl}^{0m} \\ -\frac{2}{r} J_{nl}^{0m} - \frac{d}{dr} J_{nl}^{0m} + \frac{1}{r} J_{nl}^{Pm} \end{bmatrix} \quad (4.14)$$

where J_{nl}^{0m} , J_{nl}^{Pm} , J_{nl}^{Tm} are the radial, poloidal, and toroidal (l, m) GSH components of the electric current $\sigma(\mathbf{r})\mathbf{e}_n(\mathbf{r}, \omega)$; and J_{al}^{0m} , J_{al}^{Pm} , J_{al}^{Tm} are the radial, poloidal, and toroidal (l, m) GSH components of the electric current $\sigma(\mathbf{r})\mathbf{e}_a(\mathbf{r}, \omega)$.

The system (4.14) is described as follows: the anomalous e and b fields are represented by the four functions of radius $[b_{al}^{Pma}(r), b_{al}^{0m}(r), e_{al}^{Pm}(r), J_{al}^{0m}(r)]$ for each (l, m) . The anomalous current J_{al}^{0m} is used instead of e_{al}^{0m} because it simplifies the mathematics. These four functions are represented with the symbol:

$$Z^{lm}(r) = [b_{al}^{Pm}(r), b_{al}^{0m}(r), e_{al}^{Pm}(r), J_{al}^{0m}(r)] \quad (4.15)$$

To completely describe the e and b fields, the toroidal components b_{al}^{Tm} and e_{al}^{Tm} need to be specified. But those components are related to the other four variables through simple algebraic relations (see 4.44) that do not involve radial differentiation. The system (4.14) thus, can be considered as a forced ordinary differential equation for the anomalous e and b fields, with the unknown scalars on the left-hand side and the forcing from the known normal field on the right-hand side.

The last term on the left-hand-side of (4.14) includes the scalars J_{al}^{Tm} , e_{al}^{0m} and J_{al}^{Pm} which are not among the four components used to describe the anomalous fields. These three scalars, however, can be directly related to our four components. For example, e_{al}^{0m} is the (l, m) component in the Y_l^{Nm} expansion of:

$$J_a^0(r, \theta, \varphi)/\sigma(r, \theta, \varphi) = \left[\sum_{l', m'} J_{al'}^{0m'}(r) Y_{l'}^{0m'}(\theta, \varphi) \right] / \sigma(r, \theta, \varphi) \quad (4.16)$$

In this way $e_{al}^{0m}(r)$ can be related to the $\{J_{al'}^{0m'}(r)\}$. For laterally-varying conductivity, e_{al}^{0m} will, in general, depend on all the $J_{al'}^{0m'}$ (i.e. on $J_{al'}^{0m'}$ with $l, m \neq l', m'$). Similar results hold for $J_{al}^{Tm}(r)$ and $J_{al}^{Pm}(r)$. Thus, the last term on the left-hand-side of (4.14) is viewed as a direct, though complicated, linear function of the $\{Z^{l'm'}\}$.

The boundary conditions on our four components are that b_{al}^{Pm} , b_{al}^{0m} and e_{al}^{Pm} are continuous across any boundary in the mantle:

$$J_{al}^{0m}(r^+) - J_{al}^{0m}(r^-) = J_{nl}^{0m}(r^-) - J_{nl}^{0m}(r^+) \quad (4.17)$$

Equation (4.17) follows from eq. (4.10).

There are two boundary conditions at the top of the conducting region of the mantle ($r = a$). One comes from the requirement that there is no net electric current flowing into the insulator, so that at the upper boundary:

$$J_{al}^{0m}(a) = -J_{nl}^{0m}(a) \quad (4.18)$$

The other is the relationship between the spectral components of the anomalous magnetic field at the upper boundary:

$$b_{al}^{Pm}(a) + l b_{al}^{0m}(a) = 0 \quad (4.19)$$

This condition is obtained from the radial dependence of the field in an insulator, as given by eq. (4.12) (eqs (4.12-4.13) were introduced to describe the radial dependence of the normal field; but they serve equally well to illustrate the radial dependence of the anomalous field in an insulator). The last term on the left-hand side of system (4.14) couples together Z^{lm} with different values of (l, m) , through lateral variations in conductivity. Thus, eqs (4.14) and (4.17-4.19) must be solved to find all (l, m) terms simultaneously. These equations are solved for GSH components up to some arbitrary degree l_{max} .

The terms on the right-hand sides of eqs (4.14) and (4.17-4.18) depend on the normal field. These inhomogeneous terms provide the forcing for the system of equations, and they can be inferred from eqs (4.12-4.13) once we have specified the values of $b_{nl}^{0m}(c^+)$ and $e_{nl}^{0m}(c^+)$. If the normal field has been specified, a solution for the anomalous field can be obtained by finding a particular solution of the eqs (4.14) and (4.17): i.e. any solution we can find that satisfies eqs (4.14) and (4.17), but without requiring that it also satisfy the continuity conditions, (4.18-4.19), at the upper boundary of the conductive region. To find a particular solution we start with an arbitrary anomalous electromagnetic field at $r = c^+$ that is propagated up to $r = a$. Our method of propagation is described below. For our arbitrary anomalous field at $r = c^+$ we choose all components to be zero: i.e. $b_a^{P\alpha} = b_a^{0\alpha} = e_a^{P\alpha} = J_a^{0\alpha} = 0$ for every (l, m) . We denote the (l, m) component of the particular solution as $\overline{Z^\alpha}(r)$ (with $\alpha = l, m$).

Because our particular solution will almost certainly not satisfy eqs (4.18-4.19) at the upper boundary, we must add to it solutions of the homogeneous differential equations (i.e.(4.14) and (4.17) with their right-hand sides set to 0 so that the sum does satisfy equations 4.18-4.19). This requires finding a complete set of homogeneous solutions. A homogeneous solution is found by choosing starting values at $r = c^+$, and propagating those values to $r = a$ using the homogeneous equations and internal boundary conditions. To find a complete set of solutions, this propagation must be done for each linearly independent set of starting values. Those starting values are of two types: (1) $e_{al}^{0m}(c^+) = 1$ and

$b_{al}^{0m}(c^+) = 0$; and (2) $e_{al}^{0m}(c^+) = 0$ and $b_{al}^{0m}(c^+) = 1$. There are starting values of types (1) and (2) for each (l, m) pair, where $l = 1$ to l_{max} , and $m = -l$ to l . These starting values are labeled with the indices (j, l, m) , where $j = 1$ or 2 depending on whether the starting values are of type (1) or (2). Thus, there are $2 \times l_{max} \times (l_{max} + 2)$ starting values, and so there are $2 \times l_{max} \times (l_{max} + 2)$ homogeneous solutions. The (l, m) component of the solution that is generated by the (j, l', m') starting value is noted as $Z_{j,\alpha'}^\alpha(r)$ (with $\alpha = l, m$).

The final solution of the system (4.14) and (4.17-4.19) is the sum of the particular solution and of a linear combination of all the solutions of the homogeneous system:

$$Z^\alpha(r) = \bar{Z}^\alpha(r) + \sum_{j,\alpha'} A_{j,\alpha'} \cdot Z_{j,\alpha'}^\alpha(r) \quad (4.20)$$

The coefficients $A_{j,\alpha'}$ are determined from the boundary conditions (4.18-4.19) at $r = a$. To find those coefficients, the $b_a^{P\alpha}$ and $J_a^{0\alpha}$ components of the expansion (4.20) are extracted, evaluated at $r = a$, and used in eqs (4.18-4.19). This manipulation leads to a linear system of equations of the form

$$\sum_{j,\alpha'} M_{k,\alpha}^{j,\alpha'} A_{j,\alpha'} = C_{k,\alpha} \quad (4.21)$$

for each (l, m) , and for $k = 1, 2$ corresponding to the boundary conditions (4.18-4.19) respectively. The $C_{k,\alpha}$ in eq. (4.21) represent the contributions of the normal field to the right-hand-sides of eqs (4.18-4.19). The eq. (4.21) is solved to get the coefficients $A_{j,\alpha}$, from which the components of the electromagnetic field can be obtained using eq. (4.20).

The entire approach described above is also valid for both an external (exospheric) source field and an internal (core) source and thus provides a general solution to the three-dimensional induction problem in a spherical Earth. The only difference is in the definition of the normal field.

4.2.3 Numerical considerations

In an heterogeneous shell (Fig. 4.1), the system (4.14) is integrated upward from the bottom of the shell to its top with a fourth-order Runge Kutta integration technique though when a shell is homogeneous, we use instead an analytical solution to eqs (4.14). To improve the accuracy, the shell may be subdivided into thinner shells according to a criteria based upon the minimum penetration depth in the shell. The maximum thickness across which the system of eqs (4.14) and (4.17-4.19) is numerically integrated should not exceed a fraction of the minimum penetration depth (penetration depth = $\sqrt{2/\omega\mu\sigma_{max}}$). We found that a fraction equal to 0.4 was a good compromise between the numerical accuracy for the integration and the necessity to limit the number of subdivisions to minimise the computation time.

Our method of radially integrating up through a shell requires some description. The differential eq. (4.14) is of the form $dZ^\alpha/dr = f(r, Z^\alpha)$. Any numerical integrator, including Runge Kutta, requires evaluation of $f(r, Z^\alpha)$ for specified values of r and Z^α . The function f includes terms dependent on $e_a^{0\alpha}$, $J_a^{T\alpha}$ and $J_a^{P\alpha}$, which, as described above, can be linearly related to the $\{Z^{\alpha'}\}$. But those relations are complicated, and involve the GSH expansion of the product of the laterally-varying conductivity with the $Z^{\alpha'}$ scalars. Depending on the spatial pattern of the conductivity, these terms are likely to couple together the electromagnetic GSH components of all degrees and orders. The evaluation of these terms could be done by expanding the conductivity into GSH's, multiplying that expansion by the appropriate components of $Z^\alpha(r)$, and then taking the GSH components of the product. This approach would involve the use of Wigner 3-J symbols. Instead, we use an approach that is more efficient for large l_{max} . The GSH components of $Z^\alpha(r)$ are summed to obtain the appropriate e_a and b_a components in the spatial domain. The electric field components are multiplied by the conductivity in the spatial domain and the product is then expanded back into GSH's. The results are used to find $f(r, Z^\alpha)$. These forward

and inverse transformations between the spectral and spatial domains are carried out with an efficient generalized Legendre transform algorithm.

Propagation across boundaries is done in a similar manner. The fields just below the boundary between two adjacent shells are converted back to the spatial domain, and multiplied by the conductivity when appropriate. The fields just above are obtained using the boundary conditions and then are expanded again into GSH and propagated through the next shell.

4.3 Data analysis

In the free space, at any time t , the vector magnetic field \mathbf{B} may be described by a Fourier and a spherical harmonic expansion (FSHE) model of the form (see Appendix A3 for the definition of the SHE used here):

$$B^N(r, \theta, \varphi) = \sum_{l,m} \sum_{\omega} G_{l,\omega}^{Nm}(E, I) F_{l,\omega}^{Nm}(\theta, \varphi) \quad (4.22)$$

The term (r, θ, φ) is the position vector. The coefficients E and I are the external and internal potentials at the degree and order l, m and frequency ω . For the sake of simplicity from now on l, m and ω are implicit in E and I values unless otherwise specified. Eq. (4.22) is a linear system of the form $\mathbf{y} = \mathbf{Ax}$. The vector \mathbf{y} contains the 3 components of the vector field \mathbf{B} at all times t and all satellites. The vector \mathbf{x} is the vector of the potential coefficients E and I at all l, m and ω . The matrix \mathbf{A} contains the FSH functions. The least-square solution of Eq. (4.22) is:

$$\mathbf{x} = (\mathbf{A}^* \cdot \mathbf{A})^{-1} \mathbf{A}^* \mathbf{y} \quad (4.23)$$

The matrix \mathbf{A}^* is the Hermitian transposed of \mathbf{A} . The term $\mathbf{A}^* \mathbf{y}$ may be seen as a discrete estimate of the general Fourier solution of Eq. (4.22) (Appendix A4). The matrix $\mathbf{R} = (\mathbf{A}^* \cdot \mathbf{A})^{-1}$ would reduce to a diagonal matrix if the field was sampled independently in space and time (Appendix A4). Because the satellite samples simultaneously the spatial and time variation of the magnetic vector \mathbf{B} , the matrix contains off-diagonal terms expressing the coupling between the Fourier and SH coefficients. An example of the structure of the matrix \mathbf{R} is presented in Fig. 4.2.

In this example, we used a SHE up to $l = 3$ for the external field and up to $l = 7$ for the internal field. The satellite rotation period and the Earth rotation induce a strong aliasing effect at periods day. The aliasing couples both space and time functions. The coupling is weaker at periods $\gtrsim 1$ day. There is a numerical difficulty to analyse fully the structure of \mathbf{R} . Even with a simplified source field structure, the task to describe fully the matrix \mathbf{R} becomes increasingly formidable as frequencies, degrees and orders are added to Eq. (4.22).

On Earth, the external source field is roughly the result of 3 contributions, the magnetospheric ring current, the ionospheric solar variation and the field-aligned currents. The ionospheric source is internal with respect to the satellite. [Kuvshinov et al. \[2006\]](#) produced a series of simulation of the source field and its induction effect to study how to detect deep-seated regional conductivity anomalies. Three years of synthetic magnetic data were calculated for the future swarm constellation. The conductivity models of type I are a one-dimensional (1-D) mantle topped by the ocean/continent distribution. The type II conductivity models include additionally deep-seated ad-hoc conductive bodies. The inducing sources may be magnetospheric only or may contain a ionospheric source as well. The description of the data sets is found in [\[Kuvshinov et al., 2006\]](#) and will not be detailed here.

The synthetic satellite data used in this study are produced for a magnetospheric source only (with a SHE up to $l = 1$ or $l = 1 - 3$) and a conductivity model of type I. Such data cannot describe the full

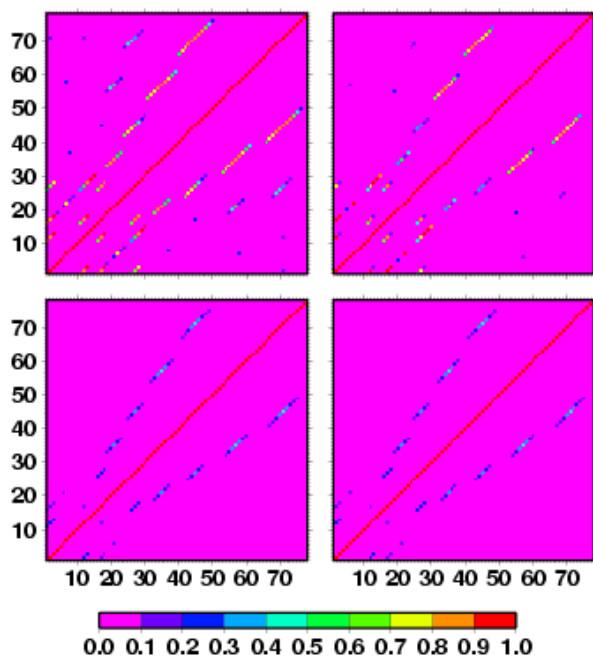


Figure 4.2: The matrix R for 4 periods: 12hrs (top left), 24hrs (top right), 2 days (bottom left) and 5 days (bottom right). The coefficients $\|R_{ij}\|$ are normalized by $\sqrt{R_{ii}R_{jj}}$ to vary between 0-1. The external coefficients E , are between $l = l - 3$ and $m = -l, l$. They are numbered from $n = 1 - 15$ ($n = l * l + l + m$). The internal coefficients I are between $l = 1 - 7$ and $m = -l, l$. They are numbered from $n = 16 - 78$ ($n = 15 + l * l + l + m$).

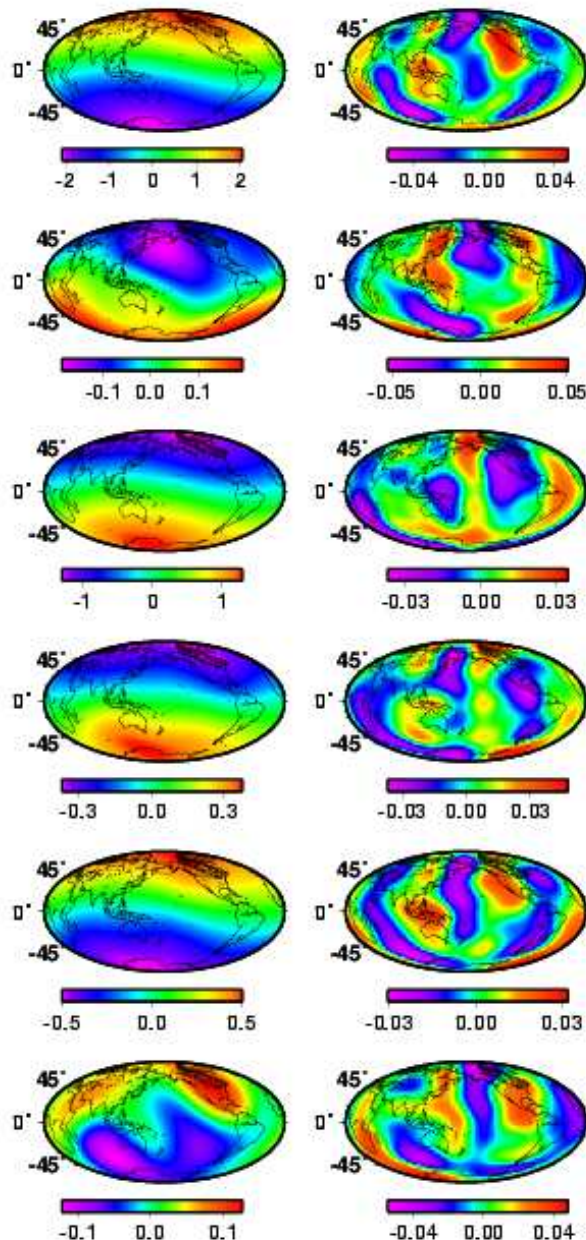


Figure 4.3: The E (left) and I (right) potentials are displayed in the space domain at four periods. For each period; the upper maps are the real part of the E and I potentials while the lower maps are the imaginary part

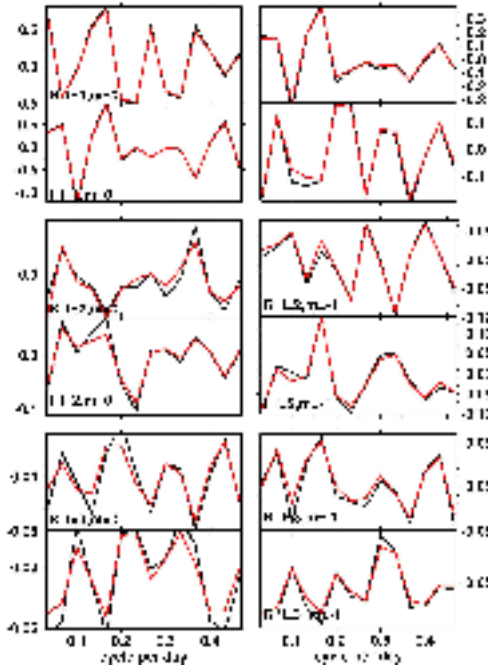


Figure 4.4: SH coefficients E as a function of the frequency in cycle per day ($1 \text{ cpd} = 11.57 \text{ mHz}$): in blue a the original coefficients used to produce the synthetic data.; in red, the coefficients obtained from the data analysis of the synthetic satellite data. The term R stands for real part and I for imaginary part.

complexity of real data but this simplifies the data analysis to obtain the E and I terms of the SHE. They are extremely useful to test the approach proposed to derive the E and I potentials.

One example is treated. The number of frequencies as well as the number of degrees and orders l, m was limited to a small number. The SHE was limited to $l = 1 - 3, m = -l, l$ for the FSHE coefficients $E, l = 7, m = -l, l$ for the FSHE coefficients I . The Fourier spectrum was obtained at 15 periods from 2-15 days. The data were analysed for successive 30 days long time series over one year. The results presented in this report are for the first set of 30 days of data.

The resulting E and I potentials are presented in Fig. 4.3 at a selection of 3 periods (15, 4 and 2.3 days). At each period, the SHE coefficients E and I are recombined into the E and I potentials in the space domain. The E potential is the SHE sum from $l = 1 - 3, m = -l, l$ while the I potential is the SHE sum from $l = 2 - 7, m = -l, l$. The external field is correctly recovered at all periods for the real part (Fig. 4.2). The imaginary part is less stable than the real part at some periods where its amplitude is small. The internal potential I is calculated from $l = 2$ to visualize the spatial geometry of the potential otherwise masked by the dominant $l = 1$ term. The geometry of the internal anomalous (i.e. induced by the conductivity heterogeneity) is complex but clearly controlled by the main conductivity contrasts (Fig. 4.3). In Fig. 4.4, some of the SH coefficients recovered was compared to the original coefficients used to generate the synthetic data [Kuvshinov et al., 2006]. The processing of the synthetic satellite magnetic data provided in general fairly good estimates of the FSH coefficients. The best result was obtained for the dominant source field at $l = 1$ and $m = 0$ (Fig. 4.4).

The time series of the internal coefficients of the magnetospheric field at degrees and orders larger than those of the source field are difficult to recover because of their small amplitude. Here, the coefficients are recovered with some noise level related to aliasing problems and possibly numerical precision which makes the synthetic example a good proxy for real data analysis.

The inversion is based on the minimisation of a misfit function between observables and a model. The E and I coefficients could be used as such. However, they contain noise and some statistical estimates should be determined. In order to optimize the signal over noise ratio, the following procedure is proposed. Time windows of given lengths (say 30 or 60 days) are selected and the E and I coefficients are obtained for each time window. For $l_{0\max}(l_{0\max} + 2)$ external source coefficients, each internal coefficients of degree and order l, m is given by:

$$I_l^{0m}(\omega, n) = \sum_{l_0, m_0} Q_{lm}^{l_0 m_0}(\omega) E_{l_0}^{0m_0}(\omega, n) \quad (4.24)$$

where n is the window number and Q the induced response function of degree and order l, m forced by a unit source term of degree and order l_0, m_0 . We defined the internal vs external co- and cross-spectra as:

$$\begin{aligned} S_{ee}^{lm, l_0 m_0}(\omega) &= \frac{1}{NW} \sum_n E_l^{0m}(\omega, n) (E_{l_0}^{0m_0}(\omega, n))^* \\ S_{ie}^{lm, l_0 m_0}(\omega) &= \frac{1}{NW} \sum_n I_l^{0m}(\omega, n) (E_{l_0}^{0m_0}(\omega, n))^* \end{aligned} \quad (4.25)$$

where NW is the number of time windows. Various trials were carried out using 1-3 satellites, 1-3 years of data and 30 or 60 days windows. The maximum degree for the external field was 3 and 7-9 for the internal field. The periods in days range from 2 to TW days where TW is the window length.

4.4 Inversion

The 3-D modelling of the electrical conductivity in the Earth at the global scale implies the use of a 3-D spherical solver. [Kuvshinov et al. \[2006\]](#) generated the synthetic satellite data using the forward code proposed by [Kuvshinov et al. \[2002\]](#). In order to perform an inversion of these data, it is best to use a forward solver entirely different. The one used here [[Tarits et al., 1998](#), [Grammatica and Tarits, 2002](#)] is based on the space/spectral approach described above. The forcing field is given by its SH coefficients and is applied at the Earth surface. Since the E and I coefficients are obtained at the Earth surface, there is no need to continue the computed field upward to satellite altitude. The approach proposed here to invert the satellite data is based on the modelling of the potential coefficients recovered from the data analysis presented above. The coefficients have been accurately recovered (Fig. 4.4). Nevertheless the data analysis may only provide a limited number of SH coefficients at a limited number of periods. The question therefore is whether or not such restricted number of coefficients carries enough information to recover the conductivity structure with a reasonable degree of accuracy.

The strategy proposed here is to run the inversion to find a model that fit the S_{ie} values given the S_{ee} . In standard magnetotelluric or global induction analysis, 1-2 source terms are considered and the Q values (or functions of the Q values) are uniquely obtained from eq. 4.25 or equivalent relationships. Here, the approach is more general. There may be an unknown number of time-independent source terms. They may have different geometries and similar time dependency. As a result, the Q values cannot be uniquely obtained (although the $l = 1, m = 0$ term is always dominant and well characterized).

The first step is to calculate the Q values (eq. 4.24) for all l_0, m_0 values of the source field. Then the theoretical co-spectrum $S_{ie}(\text{cal})$ is obtained from the combination of the calculated Q values and the observed external E coefficients using eqs. 4.24-4.25. The misfit function used in the inversion procedure is defined as follow:

$$\chi^2 = \sum_{\omega, l, m, l_0 m_0} \left[S_{ie}^{lml_0 m_0}(\omega)_{\text{obs}} - S_{ie}^{lml_0 m_0}(\omega)_{\text{cal}} \right]^2 W^{lml_0 m_0}(\omega) + \lambda \sum_{i,j}^{\sigma} [\log(\sigma_i / \sigma_j)]^2 \quad (4.26)$$

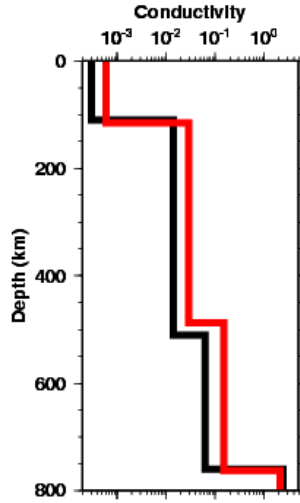


Figure 4.5: Best fitting 1-D model (in red) for the minimum misfit function between the FSHE internal coefficients I . The original 1-D structure beneath the heterogeneous upper shell used to synthesize the data is in black.

The misfit is weighted with the coefficient W . The second term on the right hand side of eq. 4.26 is the smoothness term which minimizes the log-conductivity differences between all meshes in a layer and the mean log-conductivity value between layers.

In the inverse procedure, the starting model is 1-D and is the best 1-D fitting model obtained using the coefficients E and I up to $l = 3$. The 3-D solver was used for the inversion but with homogeneous layers. Fig. 4.5 shows the best fitting 1-D model compared to the mantle structure used in conductivity models of type I to generate the data.

Before running the full 3-D inversion to recover the mantle structure, it is necessary to deal with the uppermost crustal structures, namely the distribution of oceanic masses and large sedimentary basins responsible for large distortion of the induced geomagnetic field.

4.4.1 Accounting for the coast effect

The coast effect is the generic name to describe the electromagnetic distortion caused by the large conductivity contrast between oceanic or sedimentary basins and the electrically resistive bedrock. Here we proposed to generalize the approach proposed by [Nolasco et al. \[1998\]](#) to include the coast effect in the inversion procedure.

Following [Kuvshinov et al. \[2006\]](#), we define a model comprised of the 1-D conductivity structure topped by an heterogeneous sheet of conductance $\tau = \tau_n + \tau_a$ where τ_n is the conductance of the ocean. We define a new normal model which is the 1-D conductivity structure topped by a uniform sheet of conductance τ_n . The corresponding total horizontal normal field at the Earth surface is \mathbf{E}_{ns} . The total horizontal electric field \mathbf{E}_s at a given position \mathbf{r}_0 at the Earth surface is solution of an integral equation of the type:

$$\mathbf{E}_s(\mathbf{r}_0) = \mathbf{E}_{ns}(\mathbf{r}_0) + \int_{\partial V_a} \tau_a(\mathbf{r}) \mathbf{G}_s(\mathbf{r}_0, \mathbf{r}) \mathbf{E}_s(\mathbf{r}) d\mathbf{s} \quad (4.27)$$

where \mathbf{G}_s is the surface Green dyadic and ∂V_a the anomalous domain (compared to the normal model with the top layer of conductance τ_n). Now we introduce an anomalous body in the mantle of conductivity $\sigma = \sigma_n + \sigma_a$. The surface electric field becomes:

$$\mathbf{E}_s(\mathbf{r}_0) = \mathbf{E}_{ns}(\mathbf{r}_0) + \int_{\partial V_a} \tau_a(\mathbf{r}) \mathbf{G}_{s1}(\mathbf{r}_0, \mathbf{r}) \mathbf{E}_{s1}(\mathbf{r}) ds + \int_{V_a} \sigma_a(\mathbf{r}) \mathbf{G}_{s2}(\mathbf{r}_0, \mathbf{r}) \mathbf{E}_2(\mathbf{r}) dv \quad (4.28)$$

where the subscripts 1 and 2 correspond to the top sheet and the mantle anomalous body respectively. We note \mathbf{E}_{Ms} the surface electric field for a model with a normal surface sheet (of conductance τ_n and the anomalous mantle body. This field is solution of:

$$\mathbf{E}_{Ms}(\mathbf{r}_0) = \mathbf{E}_{ns}(\mathbf{r}_0) + \int_{V_a} \sigma_a(\mathbf{r}) \mathbf{G}_{s2}(\mathbf{r}_0, \mathbf{r}) \mathbf{E}_2(\mathbf{r}) dv \quad (4.29)$$

The general solution of eq. 4.27 is of the form:

$$\mathbf{E}_s(\mathbf{r}_0) = \mathbf{E}_{ns}(\mathbf{r}_0) + \int_{\partial V_a} \mathbf{K}_s(\mathbf{r}_0, \mathbf{r}) \mathbf{E}_{ns}(\mathbf{r}) ds \quad (4.30)$$

where \mathbf{K} is a kernel function of both the normal model and the anomalous domain. At the long period considered here (more than 1 day), the mutual induction of the anomalous electric currents distorted by the surface and deep heterogeneities is weak and may be neglected [Nolasco et al., 1998, Tarits and Menvielle, 1983]. Within the approximation that mutual coupling between anomalous currents flowing in domains (1) and (2) is negligible, the solution of eq. 4.28 at Earth surface is of the form:

$$\mathbf{E}_s(\mathbf{r}_0) = \mathbf{E}_{Ms}(\mathbf{r}_0) + \int_{\partial V_a} \mathbf{K}_s(\mathbf{r}_0, \mathbf{r}) \mathbf{E}_{Ms}(\mathbf{r}) ds \quad (4.31)$$

The mantle field \mathbf{E}_M plays the role of the normal field with the same distortion kernel \mathbf{K} as in eq. 4.30. Hence, the kernel \mathbf{K} may be calculated for the normal model from eq. 4.30 and included into eq. 4.31 to account for the distortion of the mantle field \mathbf{E}_M by the surface heterogeneous layer.

4.4.2 Calculation of the distortion kernels

It is convenient to consider the SHE of eq. 4.30 in order to determine the distortion coefficients of the kernel \mathbf{K} . Using the generalized SH approach (Appendix 1), we define the toroidal electric field at the Earth surface $E_{l'}^{Tm'}$ of the distorted field and E_{nl}^{Tm} of the normal field. After some algebra, the SHE of eq. 4.31 is obtained and may be written as:

$$E_{l'}^{Tm'} = E_{nl}^{Tm'} \delta_{lm}^{l'm'} + K_{lm}^{l'm'} E_{nl}^{Tm} \quad (4.32)$$

where δ is the Kronecker symbol and the K values are the SHE coefficients of the distortion.

The forward calculation for the normal model topped by the heterogeneous sheet for all possible forcing terms l', m' provides all necessary K values. In order to accurately calculate these coefficients, the surface structure must be well described. Here we used a maximum SHE degree of 27. In order to obtain the distortion coefficients for all SHE values of the mantle field (of maximum degree l_M , the forward calculation must be carried out $l_M(l_M + 2)$ times for each period which may be a lot. However it is done once.

The distorted mantle field observed at the Earth surface is a function of the internal and external coefficients (see Appendices 1-3). Once, E_{MT} is calculated as follow:

$$E_{l'}^{Tm'} = E_{Ml'}^{Tm'} \delta_{lm}^{l'm'} + K_{lm}^{l'm'} E_{Ml}^{Tm} \quad (4.33)$$

it is straightforward to obtain (using A15) the internal potential Q_M of degree and order l, m for a unit external forcing of degree and order l_0, m_0 . These values for all necessary internal and external degrees and orders are combined with the observed external field in eq. 4.25 to obtain the calculated cross-spectrum $S_{ie}(cal)$ in eq. 4.26.

4.4.3 Results of the 3-D inversion

The inversion started with the 1-D model in Figure 4.5. The non-linear minimisation of the misfit function (4.26) varies successively the conductivity in all meshes in the layers ascribed to be heterogeneous (namely layers 2 and 3). The top layer is homogeneous and of conductivity 3.2 S/m. At each iteration, the mantle Q coefficients are calculated and corrected for coast effect using eq. 4.33 from which we derive the distorted Q values. The misfit is then calculated according to eq. 4.26.

The minimisation procedure starts with no or very little smoothness. Then the smoothness is added. The coefficient λ in eq. 4.26 is adjusted so that the smoothness is of same order as the misfit. The minimisation is stopped when the misfit starts to increase while the smoothness is decreasing.

In figure 4.6, we present the inversion result using the exact time series I and E coefficients used by Kuvshinov et al. [2006] to generate the E2E magnetospheric (external+induced) data. In this example, the maximum degree of the internal SHE is 9. The time series of the coefficients were Fourier transformed by time windows of 30 days over 1 year. The Fourier coefficients were combined to form the co- and cross-spectra values S_{ie} and S_{ee} used to build the misfit function (4.26). The grid is divided into 12x24 cells. The structure is correctly recovered. The various tests carried out showed the importance of a priori information about the radial layering, here provided by the prior 1-D analysis. The smoothness criteria proved to be efficient to remove spurious effect in layer 2 but removed also any features related to the structures in that layer, however too small to be retrieve with the spatial resolution used here.

4.5 Conclusion

A general approach was proposed to process and invert satellite geomagnetic data to infer the 3-D conductivity of the Earth. Both data analysis and inversion scheme were proved satisfactory to process synthetic data. While the approach presented here seems to work reasonably well, it is only a partial answer to the question of magnetic data inversion for induction studies. A simple case with a pure magnetospheric source was considered. The inverse solution was found for satellite data synthesized with conductivity models with the mantle structures. At the resolution used here (18x18 or 12x12 degrees grid), only the major features were recovered.

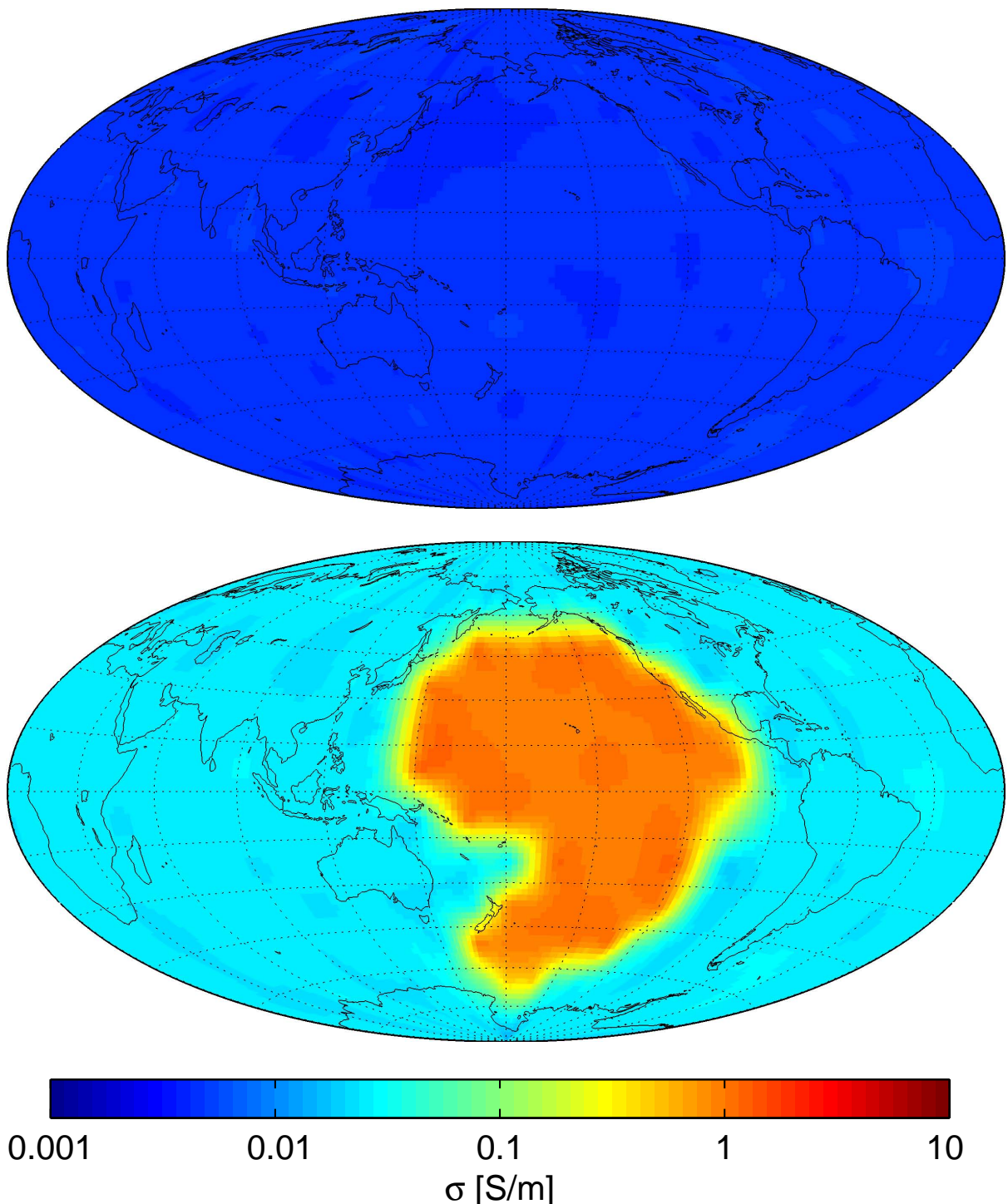


Figure 4.6: Result of the 3-D inversion obtained from the synthetic E and I coefficients [Kuvшинов et al., 2006]. The color scale is the log of the electrical conductivity.



4.6 Appendices

4.6.1 Appendix A1: expansion of a vector into generalized spherical harmonics (GSH)

Let $\mathbf{F}(r, \theta, \varphi)$ with components $(F_r, F_\theta, F_\varphi)$ be a vector function of position in the spherical coordinate system $(\hat{\mathbf{e}}_r, \hat{\mathbf{e}}_\theta, \hat{\mathbf{e}}_\varphi)$, r is the radius, θ the colatitude and φ the longitude. The GHS vector canonical basis is:

$$\begin{bmatrix} \hat{\mathbf{e}}^+ \\ \hat{\mathbf{e}}^0 \\ \hat{\mathbf{e}}^- \end{bmatrix} = \begin{bmatrix} \frac{1}{\sqrt{2}}(\hat{\mathbf{e}}_\theta - i\hat{\mathbf{e}}_\varphi) \\ \hat{\mathbf{e}}_r \\ \frac{-1}{\sqrt{2}}(\hat{\mathbf{e}}_\theta + i\hat{\mathbf{e}}_\varphi) \end{bmatrix} \quad (4.34)$$

In this basis, the vector \mathbf{F} has the form:

$$\mathbf{F}(r, \theta, \varphi) = \sum_{-1,0,1}^N F^N(r, \theta, \varphi) \hat{\mathbf{e}}^N \quad (4.35)$$

and its generalized spherical harmonic (GSH) expansion is, using the greek letter α to refer to the degree and order (l, m) :

$$\mathbf{F}(r, \theta, \varphi) = \sum_{-1,0,1}^N \sum_{l=0}^{\infty} \sum_{m=-l}^l F^{N\alpha}(r) Y_l^{Nm}(\theta, \varphi) \hat{\mathbf{e}}^N \quad (4.36)$$

Here $Y_l^{Nm}(\theta, \varphi) = P^{N\alpha}(\cos \theta) e^{im\varphi}$ are generalized spherical harmonics (GSHs), normalized so that:

$$\int_0^{2\pi} \int_0^\pi Y_l^{Nm} (Y_l^{Nm})^* \sin \theta d\theta d\varphi = \frac{4\pi}{2l+1} \quad (4.37)$$

$(Y_l^{Nm})^*$ is the complex conjugate of Y_l^{Nm} . Note that the $F^{0\alpha}$ are the GSH coefficients of the radial component of the vector \mathbf{F} . We introduce the following definition for the non radial GSH components of the vector \mathbf{F} :

$$\begin{aligned} F^{P\alpha} &= \Omega_l (F^{+\alpha} + F^{-\alpha}) \\ F^{T\alpha} &= \Omega_l (F^{+\alpha} - F^{-\alpha}) \end{aligned} \quad (4.38)$$

where $\Omega_l = \sqrt{l(l+1)/2}$. $F^{P\alpha}$ and $F^{T\alpha}$ are the GSH the spheroidal (or poloidal) and toroidal components of the vector \mathbf{F} . With this definition, the GSH radial, spheroidal and toroidal components of the differential operations ∇f , $\nabla \cdot \mathbf{F}$, $\nabla \times \mathbf{F}$ are:

$$\left\{ \begin{array}{lcl} (\nabla f)^{P\alpha} & = & \frac{2\Omega_l^2}{r} f^{0\alpha} \\ (\nabla f)^{T\alpha} & = & 0 \\ (\nabla f)^{0\alpha} & = & \frac{d}{dr} f^{0\alpha} \\ (\nabla \cdot \mathbf{F})^{0\alpha} & = & \frac{1}{r^2} \frac{d}{dr} F^{0\alpha} - \frac{1}{r} F^{P\alpha} \\ (\nabla \times \mathbf{F})^{P\alpha} & = & \frac{-i}{r} \frac{d}{dr} r F^{T\alpha} \\ (\nabla \times \mathbf{F})^{T\alpha} & = & \frac{-i}{r} \left(\frac{d}{dr} r F^{P\alpha} - 2\Omega_l^2 F^{0\alpha} \right) \\ (\nabla \times \mathbf{F})^{0\alpha} & = & \frac{-i}{r} F^{T\alpha} \end{array} \right. \quad (4.39)$$

When the vector field \mathbf{F} is solenoidal on the sphere, it may be split into a toroidal field and a poloidal field:

$$\mathbf{F} = \nabla \times \nabla \times \hat{\mathbf{e}}_r P + \nabla \times \hat{\mathbf{e}}_r T \quad (4.40)$$

P and T are the poloidal and the toroidal scalars respectively. It is straightforward to verify that the GSH components F^T , F^P and F^0 of \mathbf{F} are closely related to the GSH expansion of the scalars P and

T :

$$\begin{aligned} F^{P\alpha} &= \frac{2\Omega_l^2}{r} \frac{d}{dr} r P^{0\alpha} \\ F^{T\alpha} &= \frac{2i\Omega_l^2}{r} T^{0\alpha} \\ F^{0\alpha} &= \frac{2\Omega_l^2}{r} P^{0\alpha} \end{aligned} \quad (4.41)$$

In this paper and for simplicity, we denote F^T as the toroidal field and F^P as the poloidal field for any vector \mathbf{F} expanded into GSH. Note however that the term poloidal is usually reserved for solenoidal fields.

4.6.2 Appendix A2: expansion of the Maxwell's equations into GSH

Equations (4.1-4.2) may be expanded into GSH with the use of the definitions (4.34-4.39) Let l and m be the degree and order of the expansion. The spectral components of (4.1-4.2) reduce to:

Everywhere:

$$\begin{aligned} \frac{-i}{r} \left(\frac{d}{dr} r E^{P\alpha} - 2\Omega_l^2 E^{0\alpha} \right) &= -\frac{\partial}{\partial t} B^{T\alpha} \\ \frac{-i}{r} \frac{d}{dr} r E^{T\alpha} &= -\frac{\partial}{\partial t} B^{P\alpha} \\ \frac{-i}{r} E^{T\alpha} &= -\frac{\partial}{\partial t} B^{0\alpha} \end{aligned} \quad (4.42)$$

In the core:

$$\begin{aligned} \frac{-i}{r} \frac{d}{dr} r B^{T\alpha} &= \mu \sigma_c E^{P\alpha} \\ \frac{-i}{r} \left(\frac{d}{dr} r B^{P\alpha} - 2\Omega_l^2 B^{0\alpha} \right) &= \mu \sigma_c E^{T\alpha} \\ \frac{-i}{r} B^{T\alpha} &= \mu \sigma_c E^{0\alpha} \end{aligned} \quad (4.43)$$

In the mantle

$$\begin{aligned} \frac{-i}{r} \frac{d}{dr} r B^{T\alpha} &= \mu [\sigma(\mathbf{r}) E(\mathbf{r}, t)]_l^{Pm} \\ \frac{-i}{r} \left(\frac{d}{dr} r B^{P\alpha} - 2\Omega_l^2 B^{0\alpha} \right) &= \mu [\sigma(\mathbf{r}) E(\mathbf{r}, t)]_l^{Tm} \\ \frac{-i}{r} B^{T\alpha} &= \mu [\sigma(\mathbf{r}) E(\mathbf{r}, t)]_l^{0m} \end{aligned} \quad (4.44)$$

When the mantle is an insulator, the normal EM field in the mantle satisfies:

$$\begin{aligned} \frac{-i}{r} \left(\frac{d}{dr} r E_n^{P\alpha} - 2\Omega_l^2 E_n^{0\alpha} \right) &= -\frac{\partial}{\partial t} B_n^{T\alpha} \\ \frac{-i}{r} \frac{d}{dr} r E_n^{T\alpha} &= -\frac{\partial}{\partial t} B_n^{P\alpha} \\ \frac{-i}{r} E_n^{T\alpha} &= -\frac{\partial}{\partial t} B_n^{0\alpha} \end{aligned} \quad (4.45)$$

$$\begin{aligned} \frac{-i}{r} \frac{d}{dr} r B_n^{T\alpha} &= 0 \\ \frac{-i}{r} \left(\frac{d}{dr} r B_n^{P\alpha} - 2\Omega_l^2 B_n^{0\alpha} \right) &= 0 \\ \frac{-i}{r} B_n^{T\alpha} &= 0 \end{aligned} \quad (4.46)$$

4.6.3 Appendix A3: SHE of external and internal coefficients

The spherical harmonic expansion (SHE) definition used throughout the paper is based on vectorial spherical harmonics. The vector magnetic field is defined by \mathbf{B} (B^+ , B^0 , B^-):

$$\begin{aligned} B^+ &= (B_\theta + i B_\varphi)/\sqrt{2} \\ B^0 &= B_r \\ B^- &= (-B_\theta + i B_\varphi)/\sqrt{2} \end{aligned} \quad (4.47)$$

The terms B_r , B_θ , B_φ are the usual spherical components of \mathbf{B} . The terms in eq. (4.22) are:

$$\begin{aligned} G_{l,\omega}^{Nm}(E, I) &= \epsilon_l^N(r_t) E_l^{0m}(\omega) + \eta_l^N(r_t) I_l^{0m}(\omega) \\ F_{l,\omega}^{Nm}(\theta_t, \varphi_t) &= Y_l^{Nm}(\theta_t, \varphi_t) e^{i\omega t} \end{aligned} \quad (4.48)$$



with $N = -1, 0, 1$. The Y_l^{Nm} terms are the SHE functions and:

$$\begin{aligned} (\epsilon^{-1}, \epsilon^0, \epsilon^{+1}) &= (r/a)^{l-1}(-\Omega, l, -\Omega) \\ (\eta^{-1}, \eta^0, \eta^{+1}) &= (a/r)^{l+2}(-\Omega, -l - 1, -\Omega) \\ \Omega &= \sqrt{l(l+1)/2} \end{aligned} \quad (4.49)$$

The value a is the Earth's radius. As a result of eq.(4.49), the FSHE coefficients E and I , solution of eqs. (4.22-4.23), are obtained at the Earth's surface.

4.6.4 Appendix A4: solution for satellite data

The FSHE coefficients E and I may be formally obtained from the Fourier and Legendre inverse of eq. (4.22):

$$(E_l^{0m}, I_l^{0m}) = \int_S \int_t \sum_N (K_E^N, K_I^N) B^N ds dt \quad (4.50)$$

where K_E and K_I are the kernels for E and I . The integral are over the Earth surface S and time. When the space and time are sampled at regular interval over S and a time length T , eq. (4.50) is estimated with:

$$(E_l^{0m}, I_l^{0m}) = \sum_S \sum_T \sum_N (K_E^N, K_I^N) B^N \quad (4.51)$$

For satellite data, the surface is sampled over time and the right-hand side of eq.(4.51) becomes:

$$\sum_{t, S(t)} \sum_N (K_E^N, K_I^N) B^N \quad (4.52)$$

Chapter 5

Frequency-domain Q -responses inversion

5.1 Concept

We present a three-dimensional (3-D) frequency domain inversion scheme to recover 3-D mantle conductivity from satellite data. A necessary prerequisite for such a retrieval is the determination of time series of external (inducing) and internal (induced) coefficients of the magnetic potential. These time series are assumed to be available as *Swarm* Level 2 data product. Two inverse problem formulations are discussed. The first formulation deals with an inversion of transfer functions (elements of Q -matrix) which connect external and internal potential coefficients. The second formulation is based on an inversion of time spectra of internal coefficients. Due to the large scale of our 3-D nonlinear inversion a gradient-type (quasi-Newton) optimization method is chosen to solve the inverse problem. In order to make the inversion tractable we elaborate an adjoint approach for the fast and robust calculation of the data misfit gradients. We verify our inversion scheme with synthetic time spectra of internal coefficients calculated using a realistic 3-D conductivity model of the Earth.

To illustrate the concept let us recall the solution of the global EM induction forward problem. This involves prediction of the EM fields induced by a given time-varying magnetospheric source in a given conductivity model of the spherical Earth. Assuming that the considered source can be converted into the frequency domain by a Fourier transform, the time spectra of the electric and magnetic fields, \mathbf{E} and \mathbf{B} obey Maxwell's equations

$$\begin{aligned} \frac{1}{\mu_0} \nabla \times \mathbf{B} &= \sigma \mathbf{E} + \mathbf{j}^{ext}, \\ \nabla \times \mathbf{E} &= i\omega \mathbf{B}, \end{aligned} \quad . \quad (5.1)$$

where \mathbf{j}^{ext} is an impressed (given) current, $i = \sqrt{-1}$, $\sigma = \sigma(r, \vartheta, \varphi)$ is the spatial conductivity distribution in the Earth, and μ_0 is the magnetic permeability of free space. We adopt the Fourier convention $f(t) = \frac{1}{2\pi} \int_{-\infty}^{+\infty} f(\omega) e^{-i\omega t} d\omega$.

Above the conducting Earth ($r > a$, where $a=6371.2$ km is the mean Earth's radius) but below the magnetospheric source, the magnetic field, $\mathbf{B}(\omega) = -\text{grad } U(\omega)$ can be derived from a scalar magnetic potential, U , which can be represented by a spherical harmonic expansion of its external and internal parts

$$U = U^{ext} + U^{int}, \quad (5.2)$$

where



$$U^{ext}(r, \vartheta, \varphi, \omega) = a \sum_{n,m} \varepsilon_n^m(\omega) \left(\frac{r}{a}\right)^n S_n^m(\vartheta, \varphi), \quad (5.3)$$

and

$$U^{int}(r, \vartheta, \varphi, \omega) = a \sum_{k,l} \iota_l^k(\omega) \left(\frac{a}{r}\right)^{k+1} S_k^l(\vartheta, \varphi). \quad (5.4)$$

In particular, the radial component of the magnetic field follows from this potential expansion as

$$B_r(r, \vartheta, \varphi, \omega) = - \sum_{n,m} n \varepsilon_n^m(\omega) \left(\frac{r}{a}\right)^{n-1} S_n^m(\vartheta, \varphi) + \sum_{k,l} (k+1) \iota_l^k(\omega) \left(\frac{a}{r}\right)^{k+2} S_k^l(\vartheta, \varphi), \quad (5.5)$$

At this stage it is important to remember that the general solution of eq. 5.1 implies that the 3-D conductivity is excited by volume/surface impressed current of arbitrary geometry. However, if the fields and responses generated by the magnetospheric ring current are investigated, the inducing currents can be considered in the form of a spherical harmonic expansion of equivalent sheet currents. These are assumed to flow in a shell at $r = a$ (embedded in an insulator) and produce exactly the external magnetic field $\mathbf{B}^{ext} = -\text{grad } U^{ext}$, at the Earth's surface $r = a$. In this case \mathbf{j}^{ext} reduces to equivalent sheet current, that is written in the form

$$\mathbf{J}^{ext} = \frac{\delta(r-a)}{\mu_0} \sum_{n,m} \frac{2n+1}{n+1} \varepsilon_n^m(\omega) \mathbf{e}_r \times \nabla_\tau S_n^m(\vartheta, \varphi). \quad (5.6)$$

Note that EM fields from actual magnetospheric source and equivalent sheet current exactly coincide in the region beneath the sheet current. Let us assume that the 3-D conductivity model is excited by a source that only involves one spherical harmonic expansion term $\varepsilon_n^m(\omega) = 1$

$$\mathbf{J}_n^m = \frac{\delta(r-a)}{\mu_0} \frac{2n+1}{n+1} \mathbf{e}_r \times \nabla_\tau S_n^m(\vartheta, \varphi). \quad (5.7)$$

Solving eq. 5.1 we can then decompose the internal part of potential (above the Earth's surface) as

$$U_n^{m,int}(r, \vartheta, \varphi, \omega) = a \sum_{k,l} Q_{nk}^{ml}(\omega) \left(\frac{a}{r}\right)^{k+1} S_k^l(\vartheta, \varphi). \quad (5.8)$$

Since Maxwell's equations 5.1 are linear with respect to the source, this allows us to write the total potential in a 3-D case for \mathbf{J}^{ext} as

$$U(r, \vartheta, \varphi, \omega) = a \sum_{n,m} \varepsilon_n^m(\omega) \left[\left(\frac{r}{a}\right)^n S_n^m(\vartheta, \varphi) + \sum_{k,l} Q_{nk}^{ml}(\omega) \left(\frac{a}{r}\right)^{k+1} S_k^l(\vartheta, \varphi) \right]. \quad (5.9)$$

Note that in practice the summation in eq. 5.9 are finite.

Observed values of the transfer functions $Q_{nk}^{ml,exp}$ may be obtained in the following way. We assume that the data we deal with are time series of external

$$q_n^{m,exp}(t), s_n^{m,exp}(t) \quad n = 1, 2, \dots, N_\varepsilon, \quad m = 0, 1, \dots, n, \quad (5.10)$$

and internal coefficients

$$g_k^{l,exp}(t), h_k^{l,exp}(t) \quad k = 1, 2, \dots, N_\iota, \quad l = 0, 1, \dots, k, \quad (5.11)$$

which are provided for instance using Comprehensive Inversion [Olsen et al., 2007] of the geomagnetic signals collected by *Swarm* constellation. (Since we are interested in detecting 3-D conductivity anomalies we assume that $N_t > N_\varepsilon$.) Using a multivariate analysis [Bendat and Piersol, 1968] we recover $Q_{nk}^{ml,exp}$ from the relation

$$\iota_k^l(\omega) = \sum_{n,m} Q_{nk}^{ml,exp}(\omega) \varepsilon_n^m(\omega), \quad (5.12)$$

which follows from equations 5.3-5.4 and 5.9. Here complex-valued coefficients $\varepsilon_n^m(\omega)$ correspond to the time series of $q_n^{m,exp}(t)$ and $s_n^{m,exp}(t)$, whereas $\iota_k^l(\omega)$ – to the time series of $g_k^{l,exp}(t)$ and $h_k^{l,exp}(t)$. Note that if the electrical conductivity is one-dimensional, each external coefficient ε_n^m induces only one internal coefficient ι_n^m of the degree n and order m , and their ratio is independent on m

$$\iota_n^m(\omega) = Q_n(\omega) \varepsilon_n^m(\omega). \quad (5.13)$$

Now we formulate the inverse problem of the conductivity recovery as an optimization problem, so that

$$\phi(\mathbf{m}, \lambda) \underbrace{\rightarrow}_{\sigma} \min, \quad (5.14)$$

with a penalty function ϕ given as

$$\phi(\mathbf{m}, \lambda) = \phi_d(\mathbf{m}) + \lambda \phi_s(\mathbf{m}), \quad (5.15)$$

where λ and $\phi_s(\mathbf{m})$ are a regularization parameter and a stabilizer, respectively, and $\phi_d(\mathbf{m})$ is the data misfit

$$\phi_d(\mathbf{m}) = \sum_{\omega \in \Omega} \sum_{n,m} \sum_{k,l} D_{nk}^{ml}(\omega) \left| Q_{nk}^{ml,pred}(\mathbf{m}, \omega) - Q_{nk}^{ml,exp}(\omega) \right|^2 \quad (5.16)$$

with $D_{nk}^{ml}(\omega)$ as the inverse of the squared uncertainties of the elements of Q -matrix, $Q_{nk}^{ml,exp}$. Here $\Omega := \{\omega_j\}_{j=1}^{N_\Omega}$ defines set of frequencies, the vector \mathbf{m} defines the model parametrization. In our implementation we consider a smoothing stabilizer in a form

$$\phi_s(\mathbf{m}) = \{W\mathbf{m}\}^T \{W\mathbf{m}\}, \quad (5.17)$$

where W represents a finite-difference approximation to the gradient operator.

The advantage of working with Q -matrix is that the inversion setting does not depend on the source. However, this merit is counterbalanced by the necessity to perform a multivariate signal analysis which is not trivial, especially bearing in mind that the magnetospheric source is dominated by the $n = 1, m = 0$ term. To avoid this difficulty we consider also an alternative inverse problem setting where the time spectra of the internal coefficients are analyzed. In this case the data misfit term is

$$\phi_d(\mathbf{m}) = \sum_{\omega \in \Omega} \sum_{k,l} D_k^l(\omega) \left| \iota_k^{l,pred}(\mathbf{m}, \omega) - \iota_k^{l,exp}(\omega) \right|^2 \quad (5.18)$$

with $D_k^l(\omega)$ as the inverse of the squared uncertainties of $\iota_k^{l,exp}$. Due to the large scale of the 3-D EM inverse problems (large number of model parameters N_M), iterative gradient-type methods [Nocedal and Wright, 2006] are typically the methods of choice. In these methods one has to calculate the gradient of the penalty function



$$\nabla \phi_k = \left(\frac{\partial \phi_k}{\partial m_1}, \frac{\partial \phi_k}{\partial m_2}, \dots, \frac{\partial \phi_k}{\partial m_{N_M}} \right)^T, \quad (5.19)$$

with respect to the model parameters. Usually the evaluation of gradient of the regularization term can be done analytically. But the calculation of the data misfit gradient is not easy. The straightforward option – numerical differentiation – requires extremely high computational loads. A much more efficient and elegant way to calculate the gradient of the misfit is provided by the so-called "adjoint" approach, see e.g. [Dorn et al., 1999]. It allows the calculation of the misfit gradient for the price of only a few additional forward calculations (i. e. numerical solutions of Maxwell's equations) excited by a specific (adjoint) source. Each inverse problem setting requires the finding of explicit formulas for the adjoint source. In the next section we provide these formulas for our two inverse problem formulations.

5.2 Adjoint approach to calculate data misfit gradients

First, we explain how the predicted $Q_{nk}^{ml,pred} = Q_{nk}^{ml}$ are calculated. Let $B_{n,r}^m$ be the calculated radial magnetic component from a given elementary source \mathbf{J}_n^m , described by eq. 5.7. On the surface of the Earth $B_{n,r}^m$ can be written as

$$B_{n,r}^m(r = a, \vartheta, \varphi, \omega, \{\sigma\}) = B_{n,r}^{m,ext} + B_{n,r}^{m,int}, \quad (5.20)$$

with

$$B_{n,r}^{m,ext}(r = a, \vartheta, \varphi) = -nS_n^m(\vartheta, \varphi), \quad (5.21)$$

and

$$B_{n,r}^{m,int}(r = a, \vartheta, \varphi, \omega, \{\sigma\}) = \sum_{k,l} (k+1)Q_{nk}^{ml}(\omega, \{\sigma\})S_k^l(\vartheta, \varphi). \quad (5.22)$$

Here the inclusion of $\{\sigma\}$ stresses the fact that $B_{n,r}^m$, $B_{n,r}^{m,int}$ and Q_{nk}^{ml} depend on the conductivity distribution. From eq. 5.22 the quantity Q_{nk}^{ml} is calculated as

$$Q_{nk}^{ml} = \frac{1}{(k+1)\|S_k^l\|^2} \int_S (B_{n,r}^m(\mathbf{r}') - B_{n,r}^{m,ext}(\mathbf{r}')) \widetilde{S}_k^l(\vartheta', \varphi') ds', \quad (5.23)$$

where $\mathbf{r}' = (r = a, \vartheta', \varphi')$. Let us derive now the differential dQ_{nk}^{ml} with respect to variation of σ . By denoting $c_{kl} = \frac{1}{(k+1)\|S_k^l\|^2}$ and using formalism described in [Pankratov and Kuvшинов, 2010] we obtain, after some algebra

$$\begin{aligned} dQ_{nk}^{ml} &= c_{kl} d \left(\int_S (B_{n,r}^m(\mathbf{r}') - B_{n,r}^{m,ext}(\mathbf{r}')) \widetilde{S}_k^l(\vartheta', \varphi') ds' \right) = c_{kl} \int_S dB_{n,r}^m(\mathbf{r}') \widetilde{S}_k^l(\vartheta', \varphi') ds' = \dots \\ &\dots = \langle G^{eh}(\mathbf{h}_k^l), d\sigma G^{ej}(\mathbf{J}_n^m) \rangle, \end{aligned} \quad (5.24)$$

where

$$\mathbf{h}_k^l(\mathbf{r}) = c_{kl} \int_S \widetilde{S}_k^l(\vartheta', \varphi') \mathbf{e}_r(\mathbf{r}) \delta(\mathbf{r} - \mathbf{r}') ds' \quad (5.25)$$



is a fictitious source, consisting of radial magnetic dipoles, distributed along the Earth's surface with weights that are equal to $c_{kl} \widetilde{S}_k^l$. Also in eq. 5.24 $\mathbf{E}^{\mathbf{J}_n^m} = G^{ej}(\mathbf{J}_n^m)$ is the "electric field solution" of eq. 5.1, whereas $\mathbf{E}^{\mathbf{h}_k^l} = G^{eh}(\mathbf{h}_k^l)$ is the electric field solution of

$$\frac{1}{\mu_0} \nabla \times \mathbf{B} = \sigma \mathbf{E}, \\ \nabla \times \mathbf{E} = i\omega \mathbf{B} + \mathbf{h}^{ext}, \quad (5.26)$$

with the "magnetic" source $\mathbf{h}^{ext} = \mathbf{h}_k^l$. Now we are equipped to calculate the differential of the misfit (described by eq. 5.16) with respect to variation of σ . This differential can be written as

$$d\phi_d(\mathbf{m}) = 2Re \left\{ \sum_{\omega \in \Omega} \sum_{n,m} \sum_{k,l} \left(Q_{nk}^{ml}(\mathbf{m}, \omega) - Q_{nk}^{ml,exp}(\omega) \right)^* D_{nk}^{ml}(\omega) dQ_{nk}^{ml}(\mathbf{m}, \omega) \right\}, \quad (5.27)$$

where the upper asterisk stands for complex conjugate. Substituting eq. 5.24 into eq. 5.27 and rearranging the terms we obtain

$$d\phi_d(\mathbf{m}) = 2Re \left\{ \sum_{\omega \in \Omega} \sum_{n,m} \left\langle G^{eh}(\mathbf{u}_n^m), d\sigma G^{ej}(\mathbf{J}_n^m) \right\rangle \right\}, \quad (5.28)$$

where

$$\mathbf{u}_n^m(\mathbf{r}) = \sum_{k,l} \left\{ c_{kl} \left(Q_{nk}^{ml}(\mathbf{m}, \omega) - Q_{nk}^{ml,exp}(\omega) \right)^* D_{nk}^{ml} \int_S \widetilde{S}_k^l(\vartheta', \varphi') \mathbf{e}_r(\mathbf{r}) \delta(\mathbf{r} - \mathbf{r}') ds' \right\}. \quad (5.29)$$

What is left to do is to determine the model parameterization. Let V^{inv} be the volume for which we want to determine the conductivity distribution. V^{inv} consists of a set of elementary volumes V_i , where $V^{inv} = \bigcup_{i=1}^{N_M} V_i$, and within each volume V_i the conductivity is constant, $\sigma(\mathbf{r}) = \sigma_i$, for $\mathbf{r} \in V_i$. We then define \mathbf{m} as $\mathbf{m} = (\ln \sigma_1, \ln \sigma_2, \dots, \ln \sigma_{N_M})^T$. Bearing in mind this model parameterization we obtain for the elements of the misfit gradient

$$\frac{\partial \phi_d}{\partial m_i} = \sigma_i 2Re \sum_{\omega \in \Omega} \sum_{n,m} \int_{V_i} \left(E_r^{\mathbf{u}_n^m} E_r^{\mathbf{J}_n^m} + E_\vartheta^{\mathbf{u}_n^m} E_\vartheta^{\mathbf{J}_n^m} + E_\varphi^{\mathbf{u}_n^m} E_\varphi^{\mathbf{J}_n^m} \right), \quad i = 1, 2, \dots, N_M, \quad (5.30)$$

where $\mathbf{E}^{\mathbf{u}_n^m} = G^{eh}(\mathbf{u}_n^m)$. This equation demonstrates the essence of the adjoint approach: in order to calculate the gradient of the data misfit one needs to perform one (per frequency and elementary source \mathbf{J}_n^m) additional forward modeling with the excitation by the adjoint source, \mathbf{u}_n^m , which is determined via residuals of elements of the Q -matrix, see eq. 5.29.

If the misfit is described by eq. 5.18 the elements of misfit gradient are modified as

$$\frac{\partial \phi_d}{\partial m_i} = \sigma_i 2Re \sum_{\omega \in \Omega} \sum_{n,m} \int_{V_i} \left(E_r^{\mathbf{u}} E_r^{\mathbf{J}^{ext}} + E_\vartheta^{\mathbf{u}} E_\vartheta^{\mathbf{J}^{ext}} + E_\varphi^{\mathbf{u}} E_\varphi^{\mathbf{J}^{ext}} \right) \quad i = 1, 2, \dots, N_M, \quad (5.31)$$

with $\mathbf{E}^{\mathbf{u}} = G^{eh}(\mathbf{u})$, $\mathbf{E}^{\mathbf{J}^{ext}} = G^{eh}(\mathbf{J}^{ext})$, where \mathbf{u} is

$$\mathbf{u}(\mathbf{r}) = \sum_{k,l} \left\{ c_{kl} \left(\iota_k^l(\mathbf{m}, \omega) - \iota_k^{l,exp}(\omega) \right)^* D_k^l \int_S \widetilde{S}_k^l(\vartheta', \varphi') \mathbf{e}_r(\mathbf{r}) \delta(\mathbf{r} - \mathbf{r}') ds' \right\}. \quad (5.32)$$

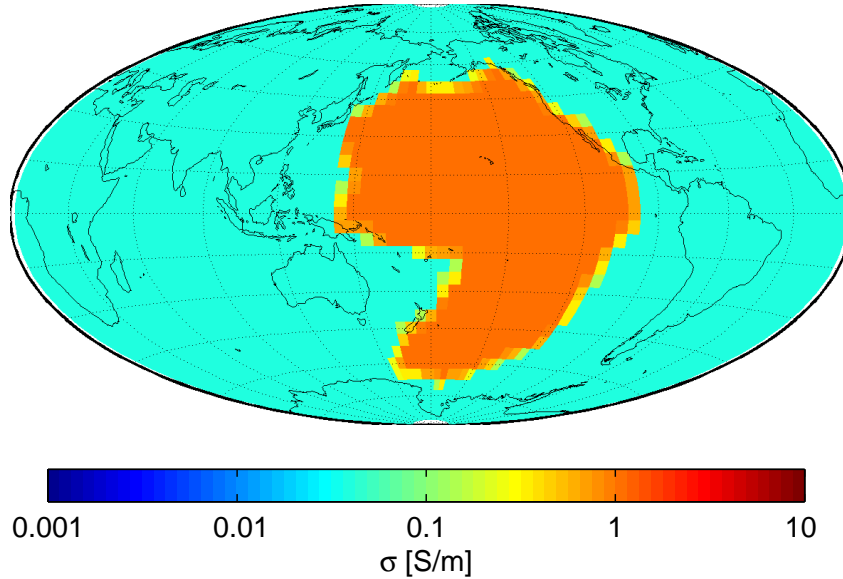


Figure 5.1: Conductivity distribution in mid mantle layer

The predictions, $\iota_k^l(\mathbf{m}, \omega)$ involved in eq. 5.18 and 5.32 are calculated as

$$\iota_k^l = \frac{1}{(k+1)\|S_k^l\|^2} \int_S (B_r(\mathbf{r}') - B_r^{ext}(\mathbf{r}')) \widetilde{S}_k^l(\vartheta', \varphi') ds', \quad (5.33)$$

where

$$B_r^{ext}(r = a, \vartheta, \varphi) = - \sum_{n,m} n \varepsilon_n^m(\omega) S_n^m(\vartheta, \varphi), \quad (5.34)$$

and B_r are external and total magnetic fields (on the surface of the Earth) induced by the source \mathbf{J}^{ext} , see eq. 5.6. Note that the overall numerical machinery is very similar for these two inverse problem settings. However the latter approach has an evident advantage: it avoids independent forward problem calculations for each source term, \mathbf{J}_n^m . This gives $N_\varepsilon(N_\varepsilon + 1)$ saving compared with the "Q-matrix" case; if, for example, $N_\varepsilon = 3$ the gain is more than one order of magnitude. The next section describes first tests of an inversion based on the analysis of internal coefficients $\iota_k^{l,exp}$.

5.3 Inverse problem scheme and its numerical verification

To minimize the penalty function we apply the limited-memory quasi-Newton method (LMQN) with Broyden-Fletcher-Goldfarb-Shanno (BFGS) scheme to update approximation to the inverse Hessian matrix. The details of LMQN-BFGS optimization scheme is discussed in Chapter 2. As forward modeling engine to calculate the data misfit gradient as well as the predictions themselves we use the integral equation solver, see Chapter 2 and [Kuvшинов, 2008].

To verify our inverse scheme we consider the similar model as in the last section of Chapter 2. This model consists of two spherical inhomogeneous layers embedded in background 1-D conductivity model. The surface thin layer of known variable conductance approximates the distribution of land masses and oceans. The deep-seated layer (of 300 km thickness) describes a (hypothetical) anomaly in the mid mantle beneath Pacific Ocean plate. Fig. 5.1 shows the conductivity distribution in mid mantle

layer. In the forward/inverse modeling both layers are discretized in horizontal direction by 72×36 cells of size $5^\circ \times 5^\circ$. The model is induced by a source described by the $n = 1, m = 1$ term in the geographic coordinate system. We calculate internal coefficients at 10 periods from 2.66 to 60 days, with geometric step of $\sqrt{2}$ between successive periods. Our aim is to recover from these data the conductivity distribution in 72×36 cells (of 300 km thickness) comprising the deep-seated inhomogeneous layer. In this test we assume that: a) the background 1-D conductivity; b) the geometry and the amplitude of the source; and c) the location (depth and thickness) of the deep-seated inhomogeneous layer are known. No noise is added to the data, and no regularization is applied. Thus this test can be considered as a proof of concept, to verify whether our implementation of the LMQN-BFGS optimization method along with the adjoint approach works correctly. We start the inversion from a homogeneous layer of conductivity 0.2 S/m which is far away from both the conductivity of anomaly (1 S/m) and of the background (0.04 S/m). Fig. 5.2 shows the results of the inversion for three data sets which differ by the number of the inverted coefficients. The upper, middle and lower panels show the recovered conductivities when respectively 35 ($N_i = 5$), 63 ($N_i = 7$) and 99 ($N_i = 9$) internal coefficients are used as input. As expected the recovery quality increases with the amount of data (maximum spherical harmonic degree). However, even for $N_i = 5$ the anomaly is recovered satisfactory well. Another observation is that already 63 internal coefficients ($N_i = 7$) capture this large-scale anomaly with acceptable resolution and accuracy. Note that the number of LMQN iterations do not exceed 120 in all three cases. Each inversion run took less than one hour of clock wall time at 10 processors (a number of processors is equal to a number of periods considered) of ETH high-performance Linux cluster "Brutus" (consisting of 8548 processors cores in 1006 compute nodes (with a peak performance of about 75 TF)).

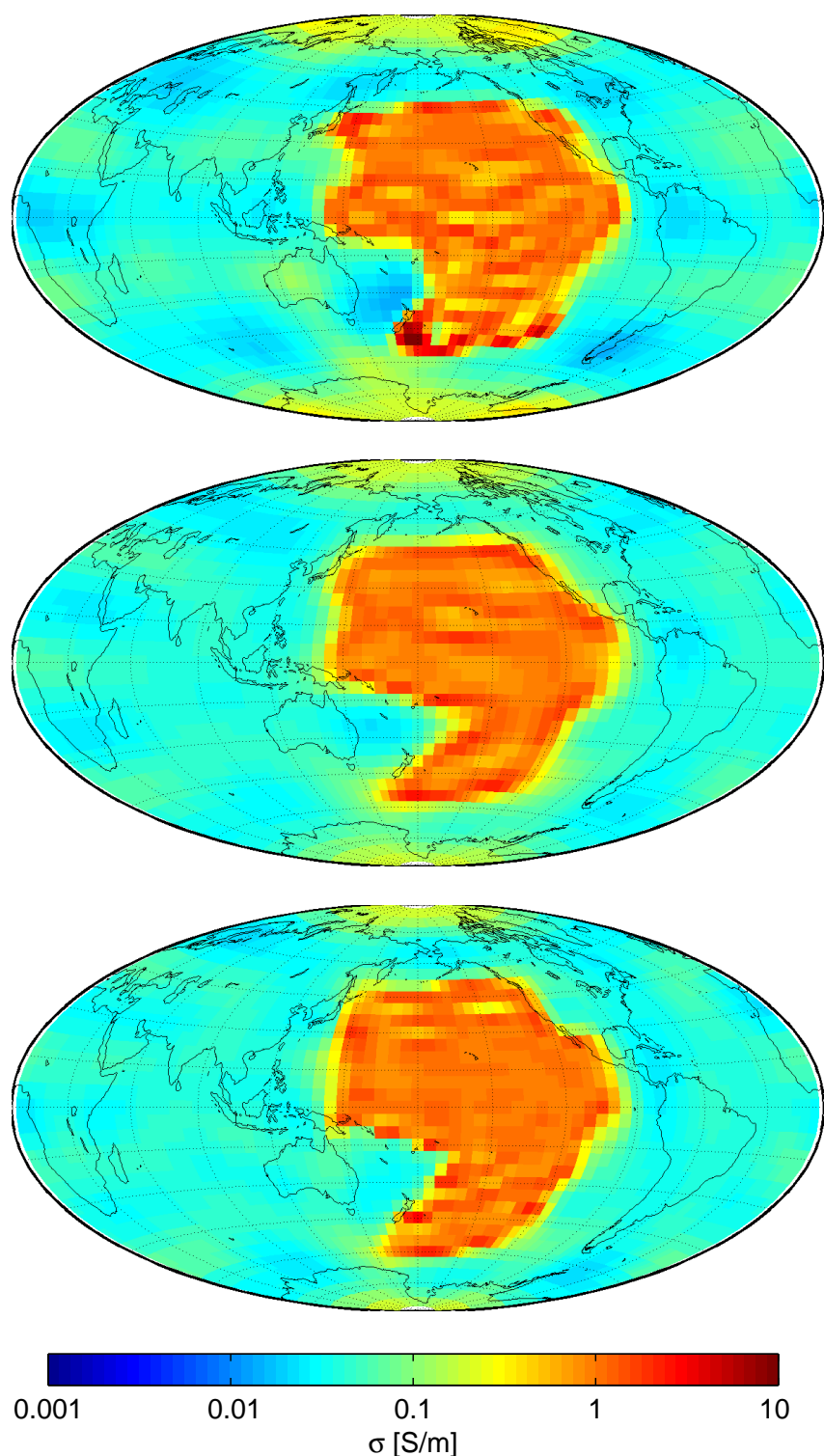


Figure 5.2: The results of inversion when 35 (a), 63 (b) and 99 (c) internal coefficients are inverted. See details in the text

Chapter 6

Preparation of 3-D synthetic data sets

In this Chapter we describe three synthetic data sets that we prepared to perform benchmarking of different inversion approaches (the results of benchmarking studies are presented in Chapters 7 and 8). Figure 6.1 provides a brief explanation of these test data sets which are assumed to be the time series of external (inducing) and internal (induced) coefficients of the magnetic potential. The idealistic data set is prepared using smooth, checkerboard, 3-D mantle conductivity model. The details of the preparation of this data set are summarised in Section 6.1. The realistic data I set is prepared using blocky 3-D mantle conductivity model. The details of the preparation of this data set are presented in Section 6.2. Finally the realistic data II set is the result of the recovery of realistic data I set from the End-to-End simulations. The recovery is performed using Comprehensive Inversion (CI) approach. Thus this ultimate data set mimics as much as possible the actual data set to be expected from the *Swarm* mission. The results of this recovery are described in Section 6.3.

6.1 Calculation of induced time series of spherical harmonic expansion coefficients using smooth 3-D mantle conductivity model (idealistic data)

The *smooth* model is designed to test the resolution of 1-D and 3-D inversion techniques assuming radially and laterally smoothly varying conductivity, as opposed to more rugged conductivity model used in the *realistic* simulations.

It is defined analytically as follows:

1. Homogeneous, highly conductive core (radius $r \leq 3480$ km, or depth $h \geq 2891$ km), $\sigma =$

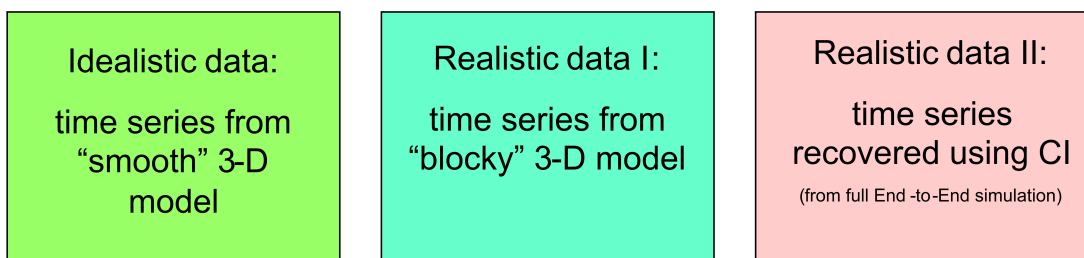


Figure 6.1: The sketch of three synthetic data sets prepared for benchmarking studies, see details in the text.

10^5 S/m .

2. Heterogeneous mantle ($3480 \text{ km} < r \leq 6361 \text{ km}$, or $10 \text{ km} \leq h < 2891 \text{ km}$) with background 1-D conductivity $\sigma_0(r)$, and overlaying 3-D variations $\sigma_1(r, \vartheta, \varphi)$, given as

$$\log \sigma(r, \vartheta, \varphi) = \log \sigma_0(r) + \log \sigma_1(r, \vartheta, \varphi), \quad (6.1)$$

where $\log \sigma_0(r)$ is defined as interpolation by natural cubic splines through three nodes $[r_i, \log \sigma_0(r_i)] = [3480, 1], [5371, 0], [6361, -2]$. The 3-D structure resembles a smoothed checkerboard pattern with 6, 6, and 3 lobes in radius, longitude, and colatitude, respectively,

$$\log \sigma_1(r, \vartheta, \varphi) = -0.4 \sqrt{4\pi} P_{53}(\cos \vartheta) \cos(3\varphi) \sin\left(2\pi \frac{3r}{6361 - 3480 \text{ km}}\right). \quad (6.2)$$

Here $P_{53}(x)$ denotes a fully normalized associated Legendre polynomial of degree 5 and order 3.

3. Surface layer ($r > 6361 \text{ km}$, or $h < 10 \text{ km}$) with surface conductance map based on the distribution of igneous rocks, continental and oceanic sediments, and seawater. The conductance map is scaled to conductivity assuming homogeneous thickness of 10 km.

Figure 6.2 shows the background 1-D model as function of radius. Figure 6.3 gives an insight at the full 3-D model, visualising the checkerboard structure by isosurfaces.

The idealistic conductivity model is excited by the external field model provided by E2E+ simulation ([Tøffner-Clausen et al. \[2010\]](#)). It spans 6 years with time step 1 hr and is truncated at spherical harmonic degree and order 6.

The response of the conductivity model is computed using the forward time-domain technique with truncation degree 14, radial discretization 30 km in the mantle and 160 km in the core, and time-step 1 hr. At this lateral resolution, it is sufficient to use the surface conductance map downsampled do 64×32 grid, as shown in the upper left image of Figure 6.3.

Time series of internal field coefficients up to degree 14 are provided both in fully normalized complex notation, and Schmidt semi-normalized real notation.

6.2 Calculation of induced time series of spherical harmonic expansion coefficients using blocky 3-D mantle conductivity model (realistic data I)

The *blocky* 3-D model is described in Section 2.1.3.1. The model is excited by a source which is described by a given time series of hourly mean values of external (inducing) coefficients $q_n^m(t)$ and $s_n^m(t)$ ($n = 1 - 3, m = 0 - 1$) of the magnetic potential (details of how the inducing coefficients have been derived are given in [Olsen et al. \[2006\]](#)). The induced time series of spherical harmonic expansion coefficients (up to degree $n = 45$) have been calculated using the methodology presented in Section 2.1.3.2. Note that these inducing and induced time series have been used to simulate realistic *Swarm* constellation data (that also includes contributions from the core, lithosphere, ionosphere, etc.)

6.3 Recovery of magnetospheric and induced time series of spherical harmonic expansion coefficients from realistic *Swarm* constellation data ((realistic data II))

The recovery of the time series of the spherical harmonic coefficients representing the magnetic field of the magnetospheric currents and their induced counter part from the simulated *Swarm* constellation

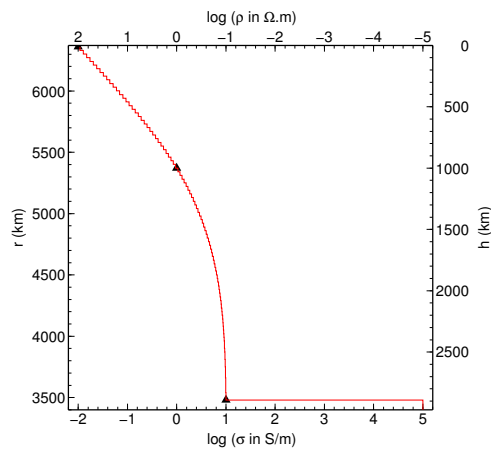


Figure 6.2: The 1-D background conductivity $\sigma_0(r)$ of the idealistic model. Spline knots are marked by triangles.

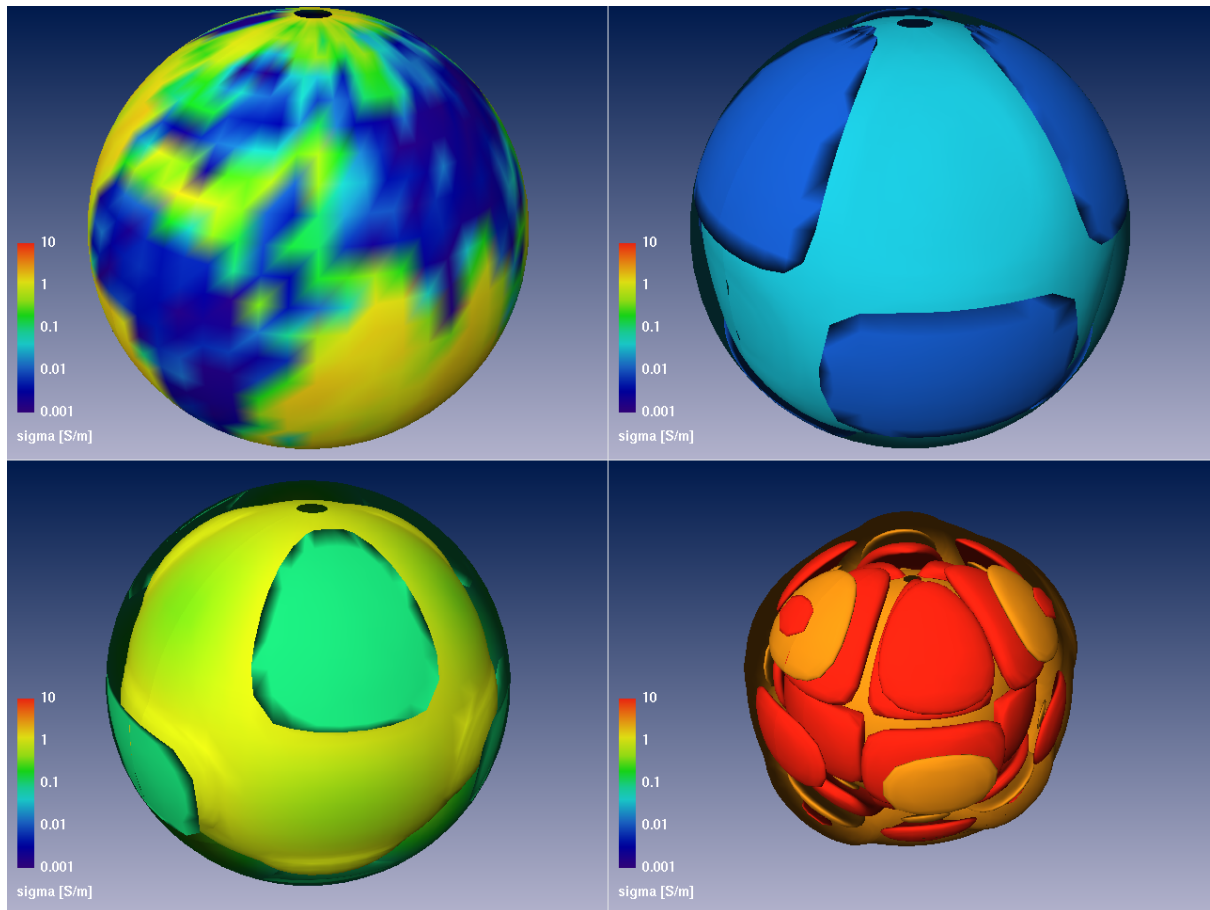


Figure 6.3: The idealistic 3-D mantle conductivity model. Isosurfaces at 0.01, 0.03, 0.1, 1, 3, and 10 S/m, respectively, are plotted through the mantle. Conductivity of the uppermost layer is shown in a 64×32 grid.

data is done using a three-step process:

1. Perform a full *Comprehensive Inversion* of selected quite-time data. See Section 6.3.1
2. Synthesize the estimated model from Step 1 – **excluding** magnetospheric and its induced parts – for the entire mission and subtract this from the data to generate *data residuals* corresponding to the magnetospheric and induced fields only. See Section 6.3.2
3. Perform an inversion of magnetospheric and induced fields for the entire mission using data residuals computed in Step 2. See Section 6.3.3

Note: Contrary to Steps 1 and 2, which are performed only once for a chosen satellite constellation, Step 3 is performed separately for each of the various model parametrizations of the magnetosphere and its induced counter-part listed in Table 6.2.

6.3.1 Comprehensive Inversion

The simulated data were inverted using the Comprehensive Inversion scheme described in [Sabaka and Olsen \[2006\]](#) with slightly modified parameters as specified in Table 6.1 below. No regularization was imposed on the solution.

Source	Representation	n_{Max}	m_{Max}	Temporal Representation
Core	Spherical harmonics	20	20	Cubic B-spline, 1 internal knot
Lithosphere	Spherical harmonics	150	150	Static
Ionosphere	Quasi dipole	45	6	Seasonal and daily periodicity
Toroidal	Quasi dipole	45	6	Seasonal and daily periodicity
Magnetosphere	Spherical harmonics	3	1	1 hour bins
Induced, magnetosphere	Spherical harmonics	3	3	1 hour bins
Instrument alignment	Euler angles	–	–	30 day bins

Table 6.1: Comprehensive Inversion – Parametrization

The estimated models showed good agreement with the reference models except for slight deviations in the low degree ($n = 15-20$) core/crustal field, see Figure 6.4. Recent work has shown that this deviation can be reduced by imposing regularization of the secular variation, see [Tøffner-Clausen et al. \[2010\]](#).

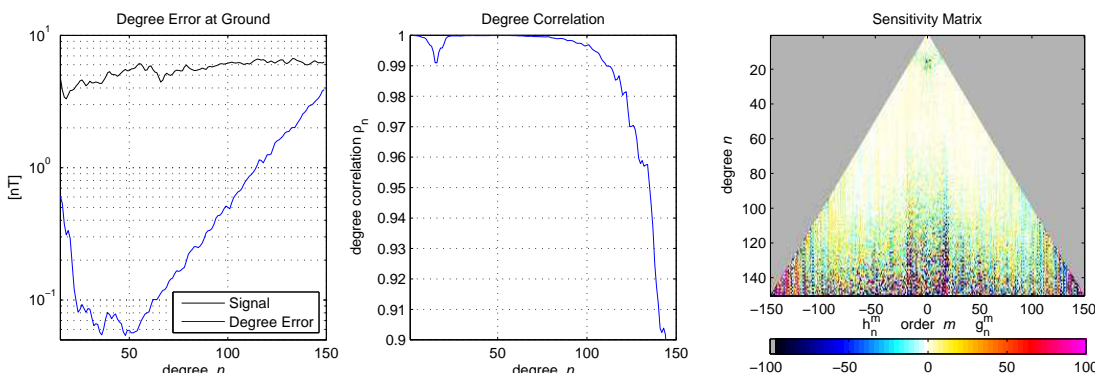


Figure 6.4: Assessment of crustal field recovery

To assess the recovery of the time series of magnetospheric, respectively induced, expansion coefficients we calculate the squared coherency (coh^2) between original (input) and recovered (output) time series using the robust section averaging method of Olsen [1998a]. Results for the magnetospheric expansion coefficients are shown in Figure 6.5. Data from the first year (red curves) shows poorer recovery than the other years due to the unfavourable orbit constellation particularly for the degree and order one coefficients (q_1^1 and s_1^1) which also affects coh^2 of the entire mission (black curves).

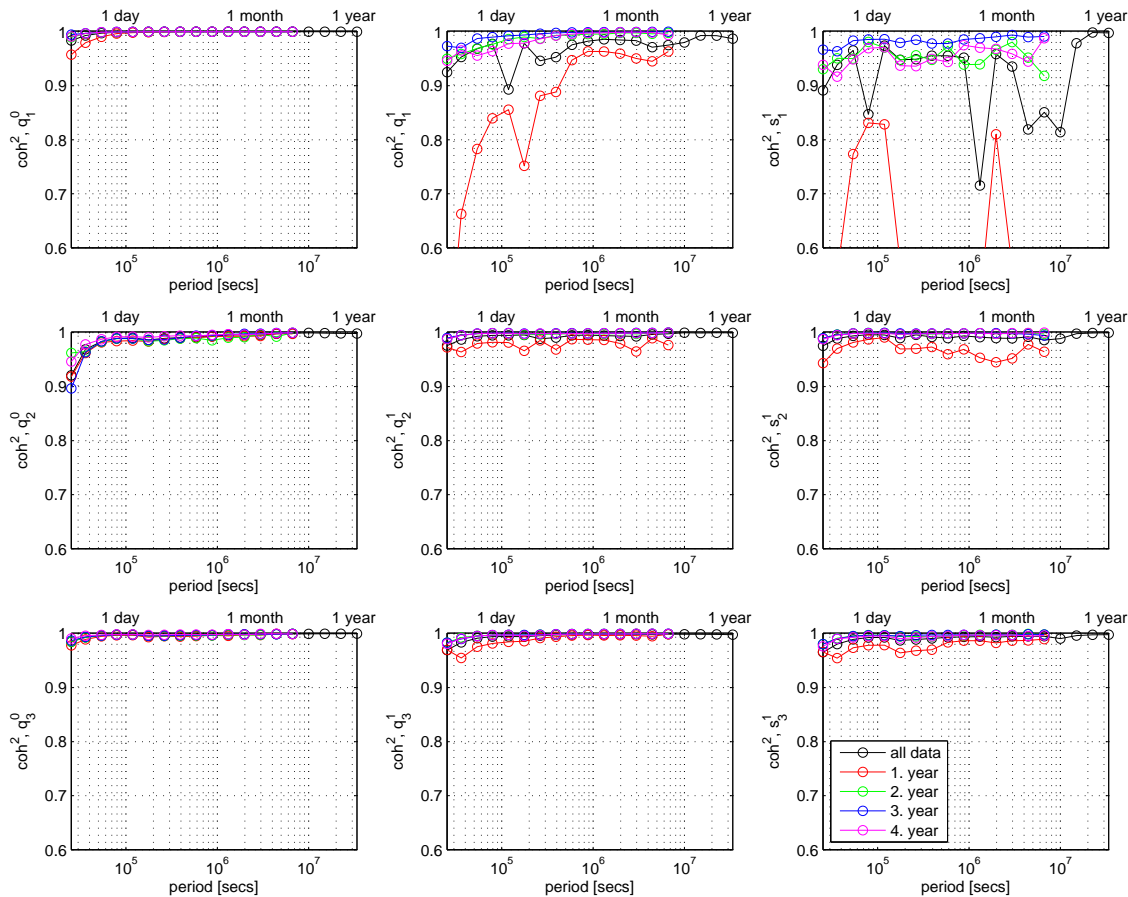


Figure 6.5: Recovery of magnetospheric spherical harmonic coefficients, coherency-squared. Plot row corresponds to degree. Order increases to the right. Each year is plotted in different color; black curves correspond to entire mission.

6.3.2 Computation of “magnetospheric” residuals from recovered model

The model recovered in the preceding section – **excluding** the terms for the magnetosphere and its induced counter-part – were synthesized for the entire mission and these model values were subtracted from the original, simulated, data to produce “magnetospheric residuals”, which contain the contribution from the magnetosphere, induced currents, and residual model errors.

6.3.3 Estimations of magnetospheric and induced fields for various model parametrizations

The “magnetospheric residuals” computed in Section 6.3.2 were used as observations in a series of modelings of the magnetosphere and its induced counter-part for various combinations of degrees, orders, and time bins. The following list of models (cases) have been estimated, **External** refers to magnetospheric contribution, **Internal** to its induced counter-part.

Case	External		Internal		Time bins [hour]
	Degree	Order	Degree	Order	
A	3	1	3	3	1
B	3	1	5	5	6
C	3	3	5	5	6
D	3	3	3	3	6
E	3	3	5	5	12

Table 6.2: Magnetospheric + Induced Models

Note: Case A has same parametrization as the full Comprehensive Inversion

The recovery of the magnetospheric field model parameters is generally fine ($\text{coh}^2 > 0.9$) and does not vary much between the models. Figure 6.6 shows the coherency-squared for Case C – compare with Figure 6.5.

For the coefficients of the induced contribution, the recovery is much less coherent when looking at the individual spherical harmonic expansion coefficients, cf. Figures 6.7 through 6.11 on pages 132–136. However, this does not mean that recovery is weak in all regions on the Earth; maps of coherency between the original and recovered part of the induced B_r show that correlation is well above 0.8 everywhere except close to the dipole equator, as shown in Fig. 6.12. This is caused by the dominance of the P_1^0 coefficient, which is the expansion coefficients with largest amplitude. The radial magnetic field of a P_1^0 source vanishes at the equator, which is the reason for the weak low-latitude coherence.

Excluding the P_1^0 coefficient, i.e. looking at the coherence of time series synthesized from all other coefficients, results in coherence maps (shown in Fig. 6.13) that are dominated by the pattern next largest expansion coefficient, which turns out to be the equatorial dipole coefficients ($n = 1, m = 1$). Of special importance here is the fact that this results in rather high coherence at some low-latitude longitudinal regions, where coherence was weak if all coefficients are included.

These results indicate that it is not sufficient to look at the coherence of individual expansion coefficients alone – even if coherence is weak for some coefficients it is possible to extract information on lateral variations of the induced signal from certain combinations of the spherical harmonic expansion coefficients. This is confirmed by the results presented in section 8.3.2.

The present results were obtained from *Swarm* satellite data alone. Inclusion of ground-based observatory data in the modeling is expected to improve the recovery of the internal, induced coefficients, and thereby enhance the capability to detect lateral conductivity variations.

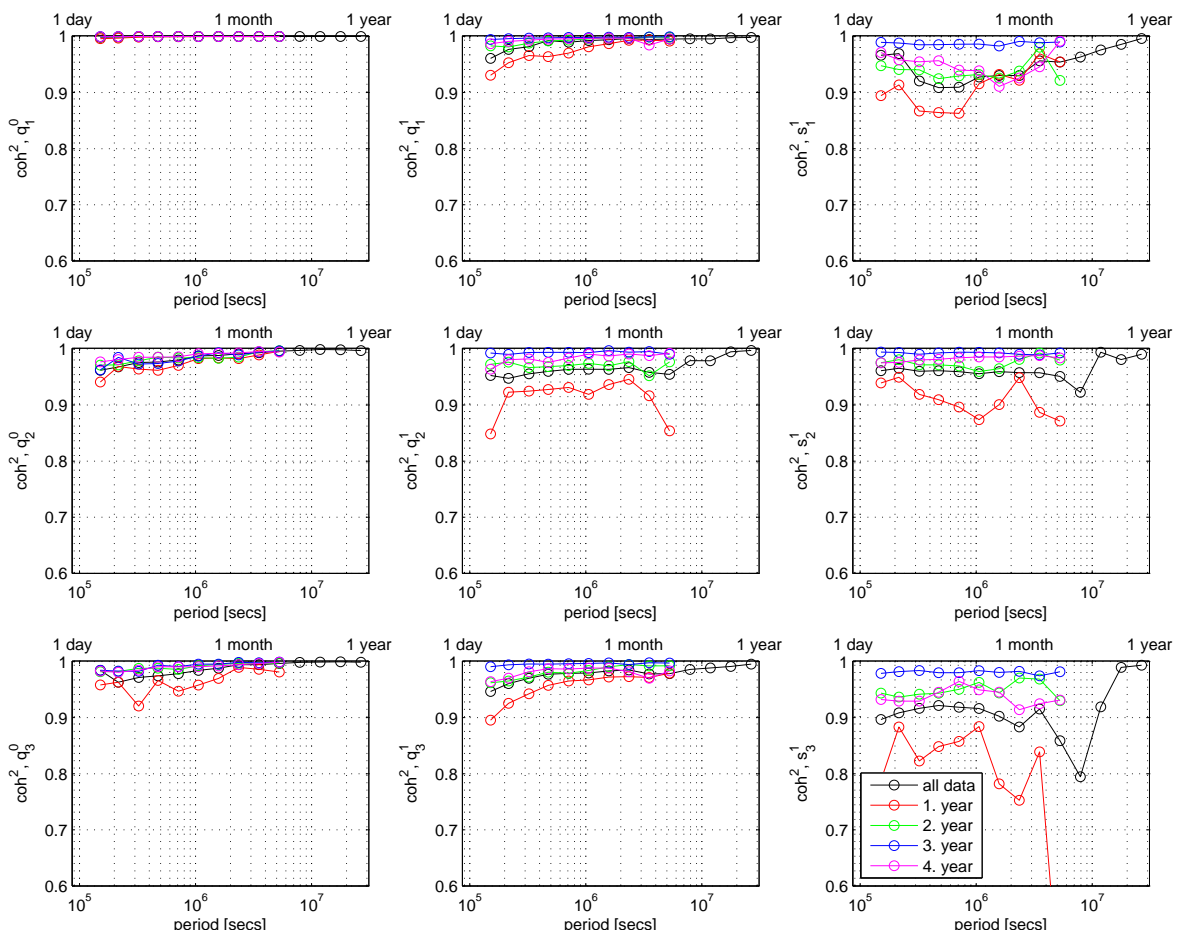


Figure 6.6: Coherency of recovered magnetospheric spherical harmonic coefficients, Case C.

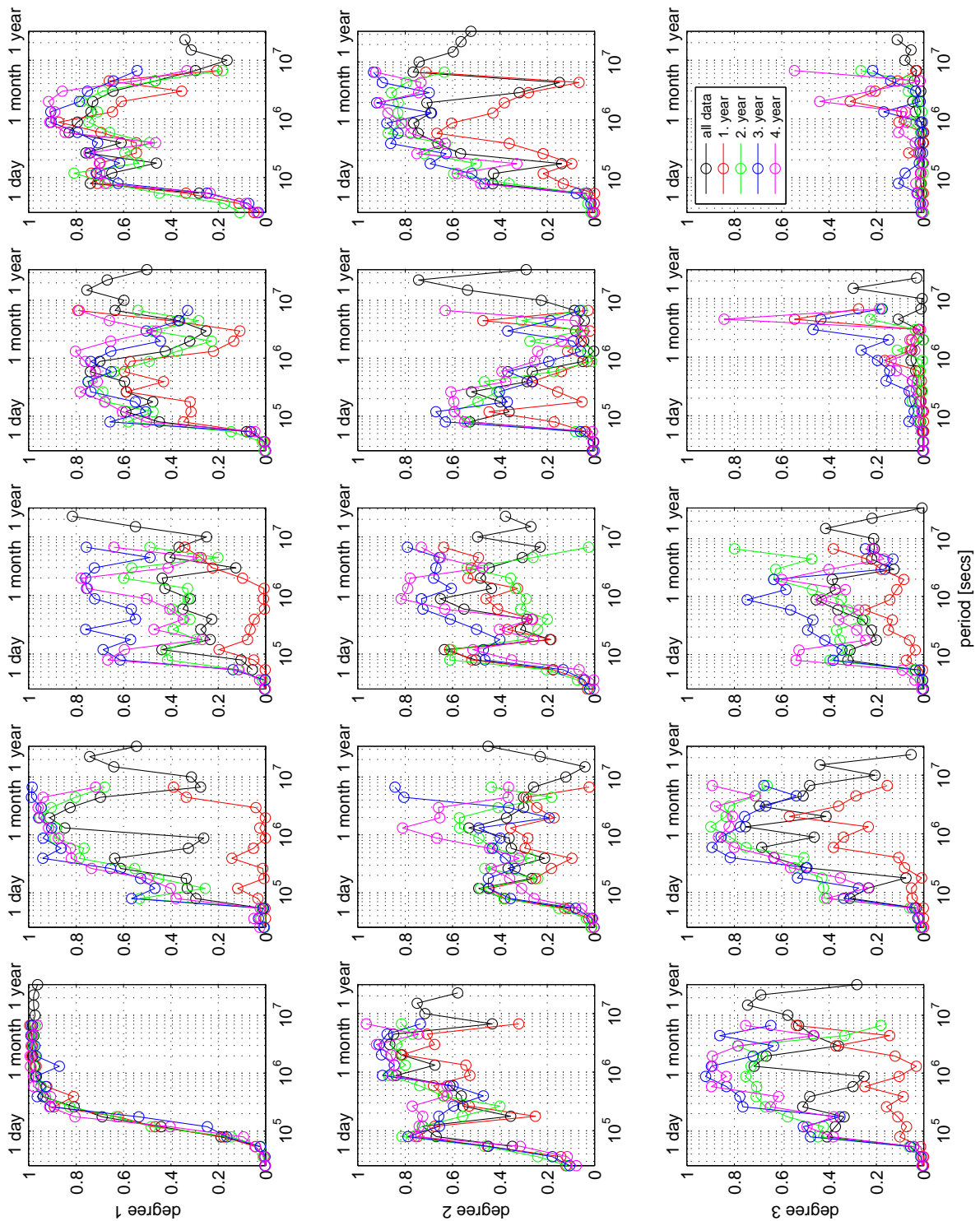


Figure 6.7: Coherency of recovered induced spherical harmonic coefficients, Case A.

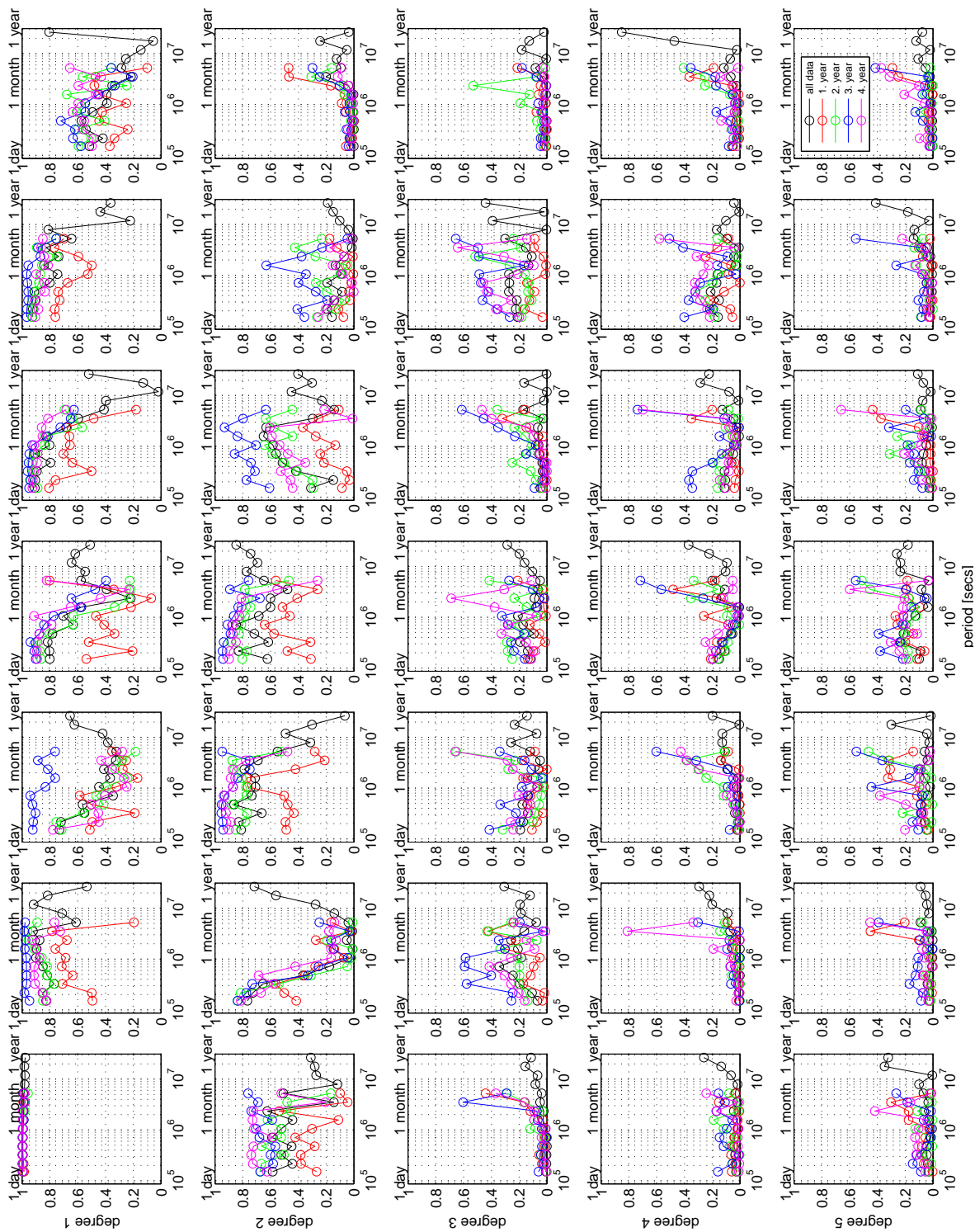


Figure 6.8: Coherency of recovered induced spherical harmonic coefficients, Case B.

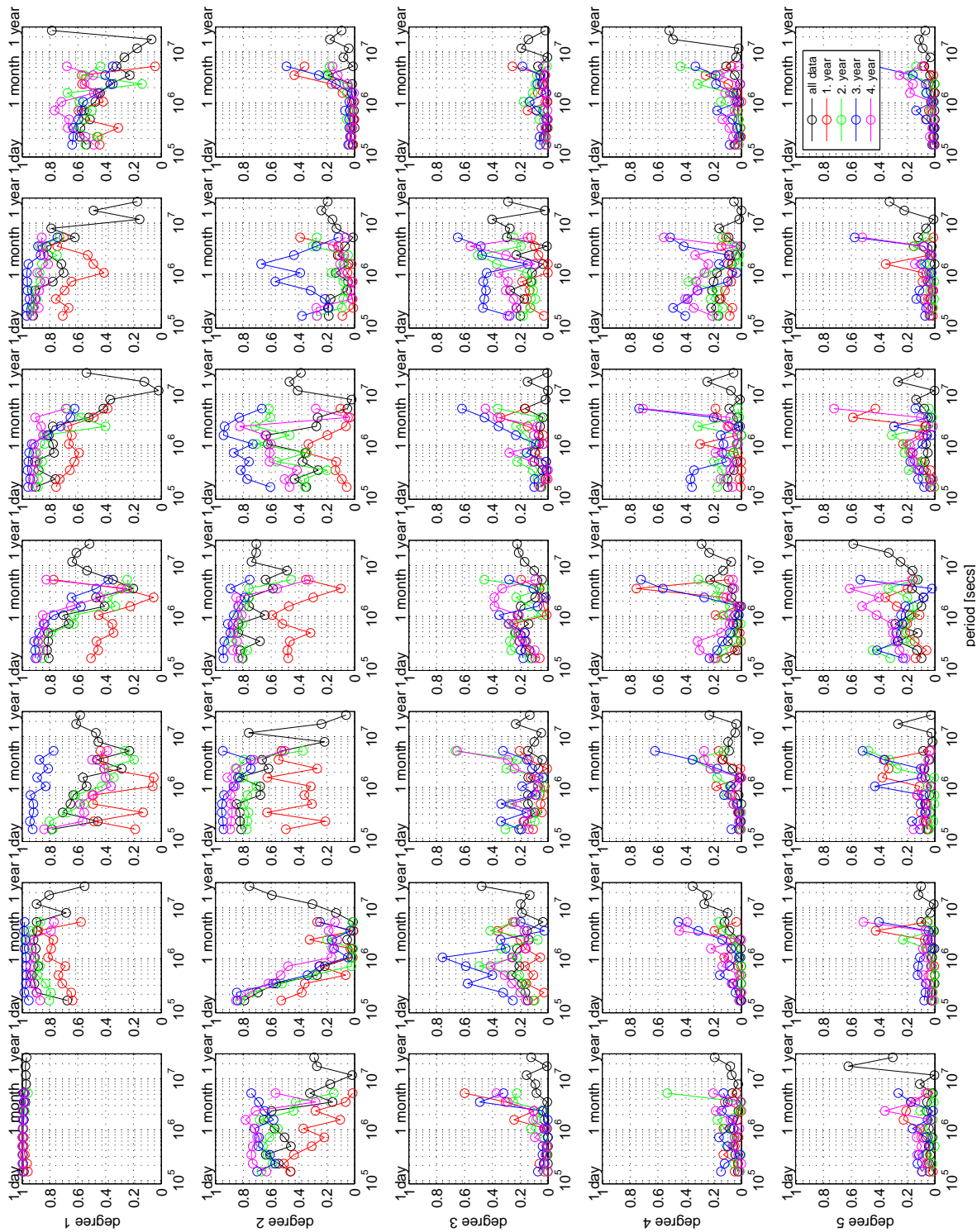


Figure 6.9: Coherency of recovered induced spherical harmonic coefficients, Case C.

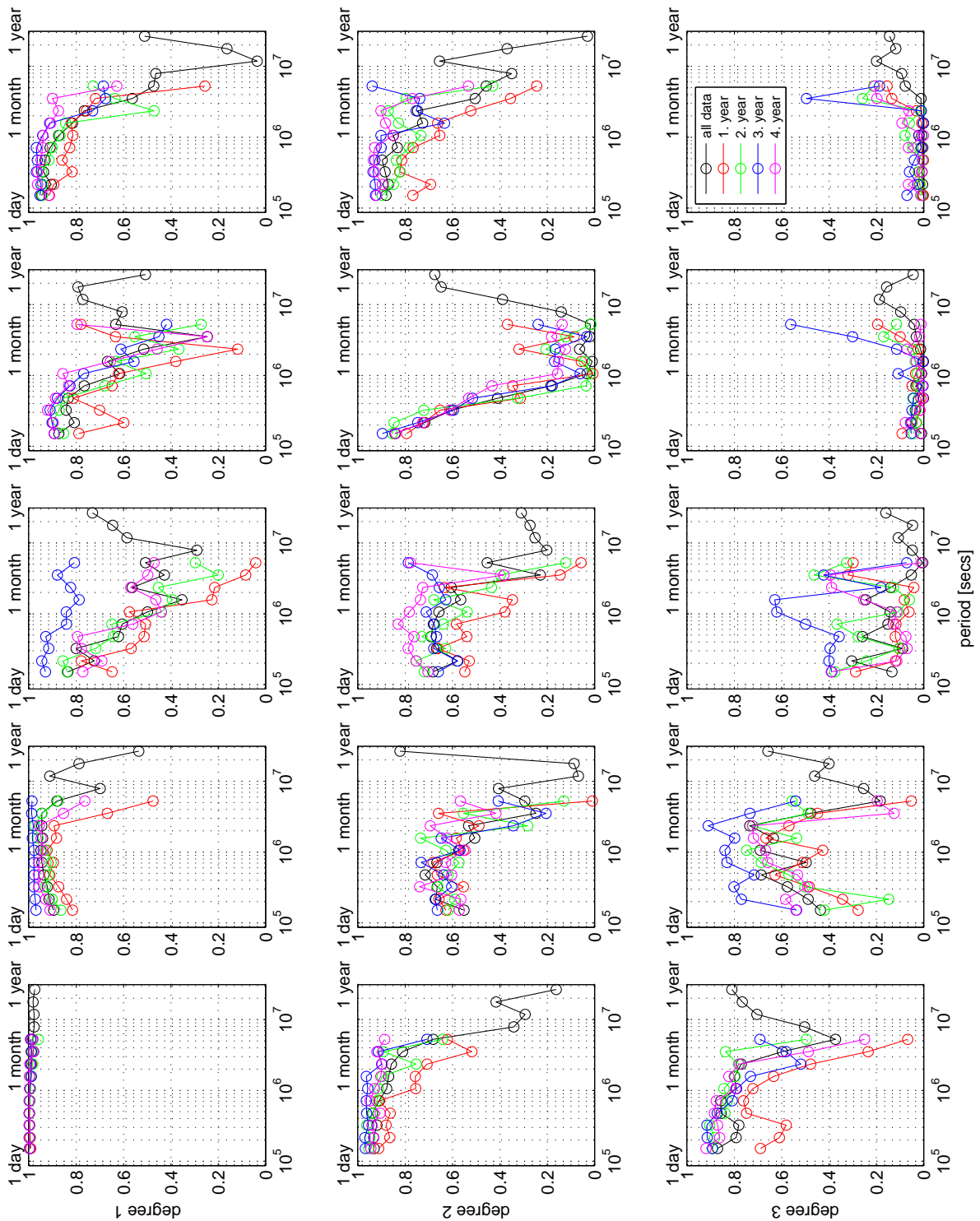


Figure 6.10: Coherency of recovered induced spherical harmonic coefficients, Case D.

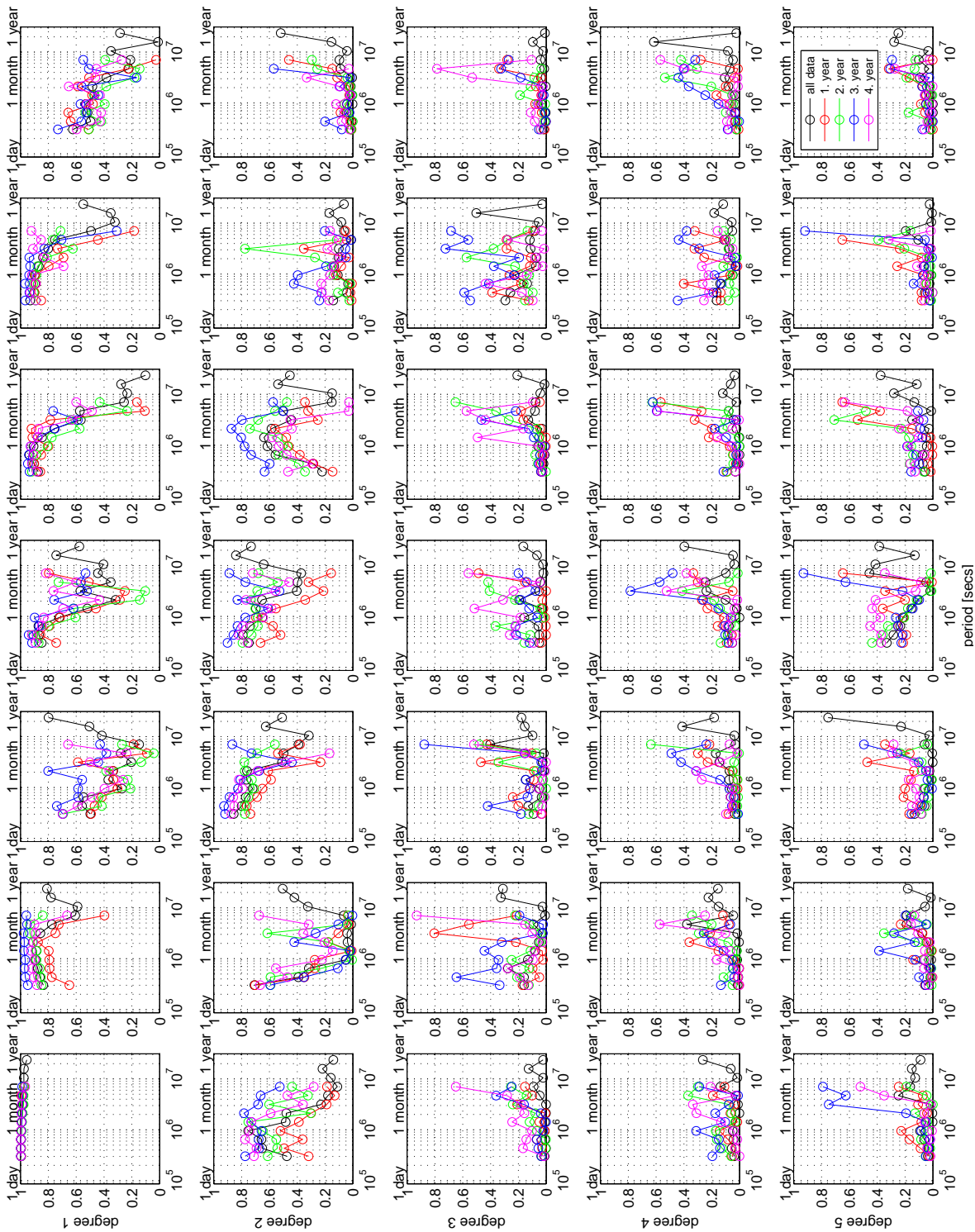


Figure 6.11: Coherency of recovered induced spherical harmonic coefficients, Case E.

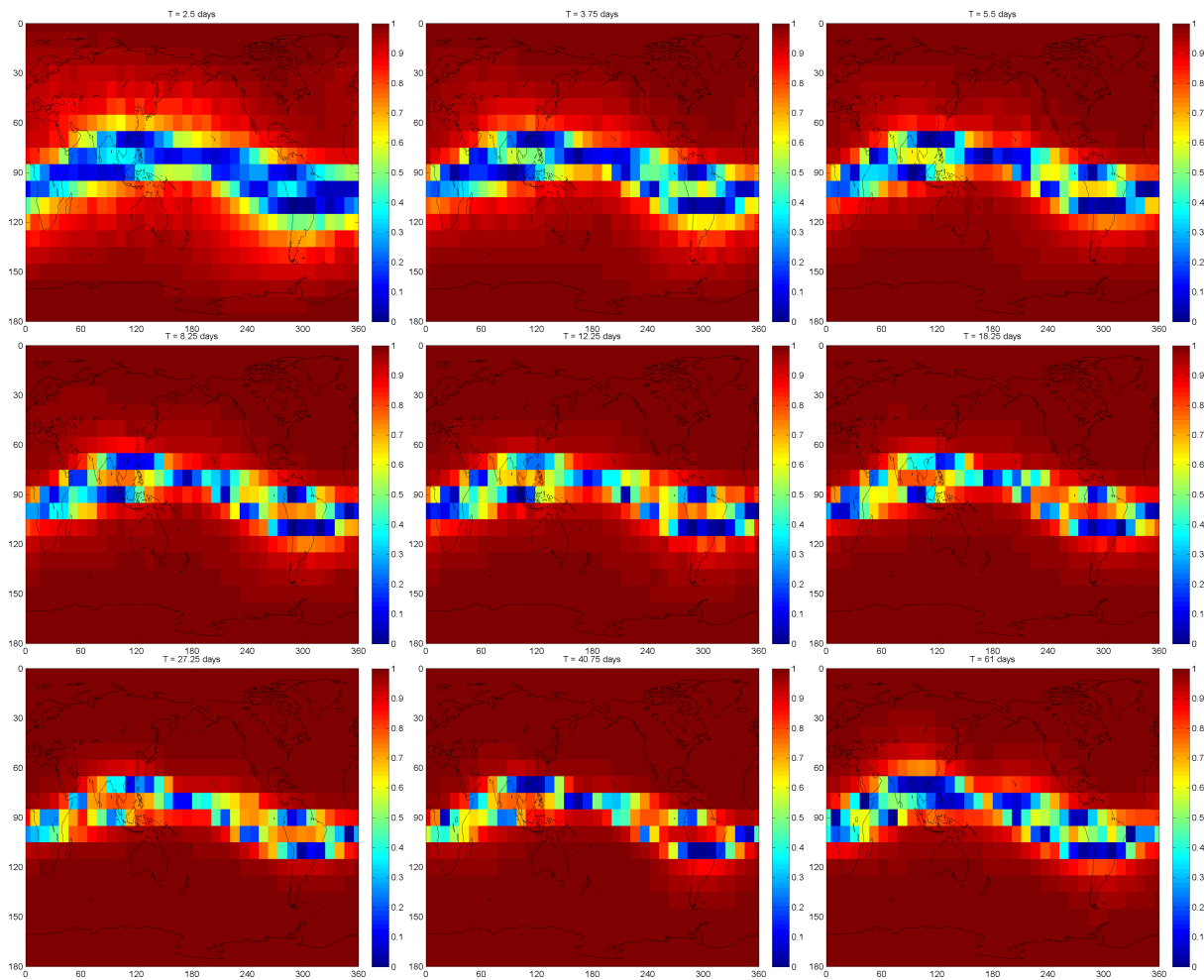


Figure 6.12: Maps of coherence of the induced B_r , case C, for periods between 2.5 days (top left) to 61 days (bottom right).

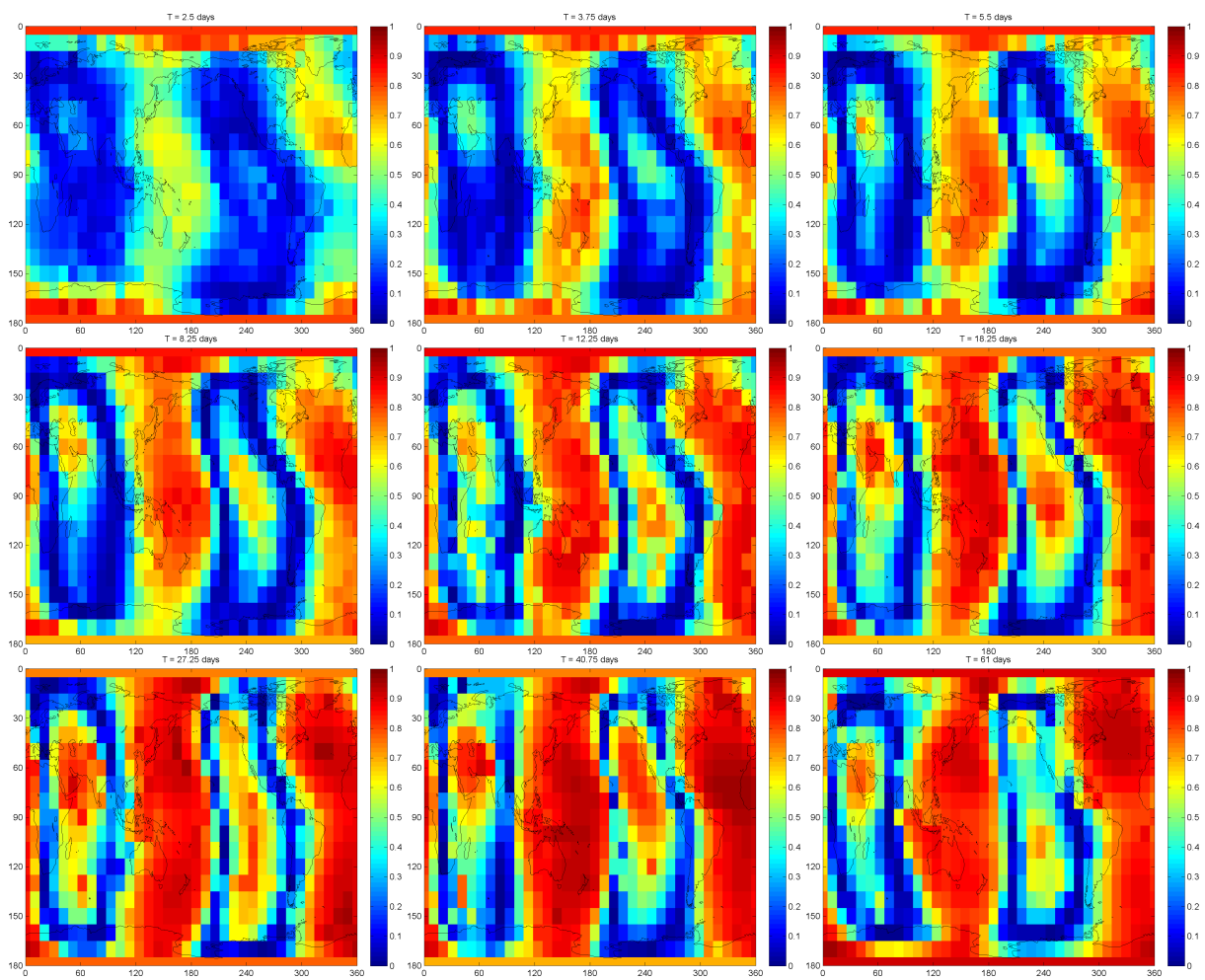


Figure 6.13: Similar to Fig. 6.12, but excluding the dominant P_1^0 term.

Chapter 7

Benchmarking of 1-D inversion approaches

7.1 1-D inversion of 1-D synthetic data

In this section we present results of the first simple test of various 1-D inversion schemes. In this test a “secret” 1-D conductivity model was excited by a dipolar source $\varepsilon_1^0(t)$ with time-dependence based on D_{st} index (Figure 7.1). The synthetic response described by internal field coefficient $\iota_1^0(t)$ was passed to participants along with known layer boundaries of the conductivity model. Note that this data set

Results for four different inversion approaches are summarized in Figure 7.2. All methods accurately resolved the conductivity in the mid-mantle. The results in the upper mantle differ by less than half order of magnitude from the target model.

This test also showed, that it is absolutely essential to remove the mean values from the time-series

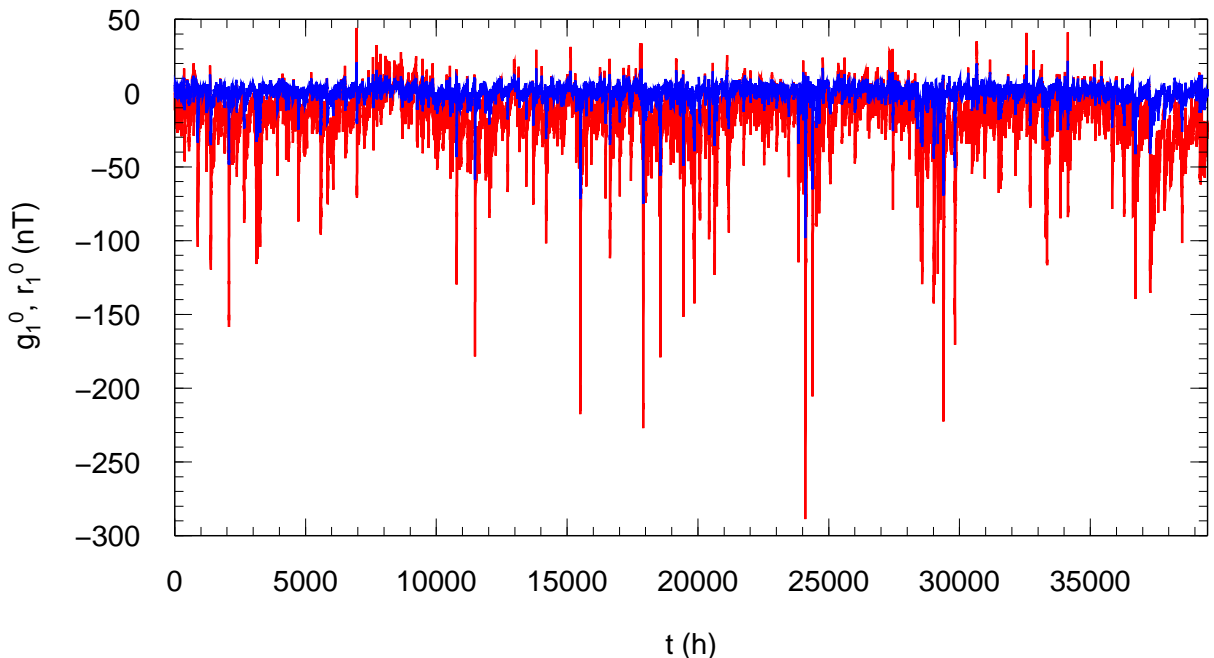


Figure 7.1: D_{st} -based dipolar excitation $\varepsilon_1^0(t)$ (red) and corresponding induced field $\iota_1^0(t)$ (blue) for a 1-D conductivity model.

of external and internal field coefficients in the time-domain inversions. Otherwise, both time-domain methods yield results strongly biased by the DC terms.

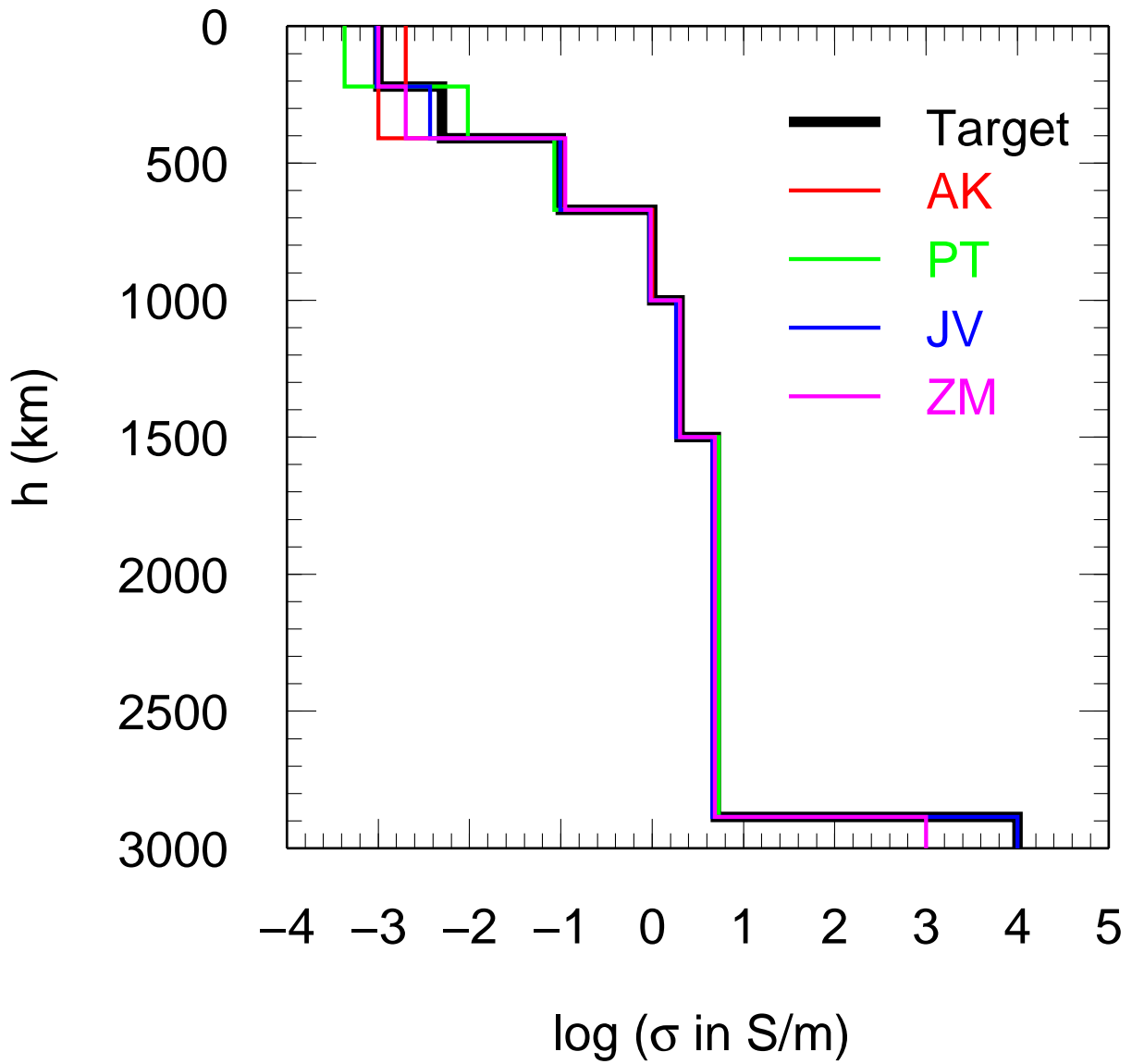


Figure 7.2: Secret target model (black) and results of 1-D inversion using frequency-domain approaches by A. Kuvshinov (red), P. Tarits (green), and time-domain approaches by J. Velímský (blue), and Z. Martinec (magenta).

7.2 1-D inversion of idealistic data

In this test we use time series of dominant external (inducing) and internal (induced) coefficients, $\epsilon_1^0(t)$ and $\nu_1^0(t)$, from idealistic 3-D data discussed in section 6.1 of Chapter 6.

7.2.1 Frequency domain approach

In frequency domain formulation we first calculate frequency dependent transfer function $Q_1(\omega)$ between the Fourier transformed time series ϵ_1^0 and ι_1^0

$$\iota_1^0(\omega) = Q_1(\omega)\epsilon_1^0(\omega), \quad (7.1)$$

We used the modified version of section averaging approach [cf. [Olsen, 1998b](#)] to estimate $Q_1(\omega)$ (the errors δQ_1 were estimated using a standard statistical approach [cf. [Jenkins and Watts, 1968](#)] with a chosen error probability of $\beta=0.10$). $Q_1(\omega)$ is then transformed to the C -response [cf. [Weidelt, 1972](#)] by means of

$$C(\omega) = \frac{a}{2} \frac{1 - 2Q_1(\omega)}{1 + Q_1(\omega)}. \quad (7.2)$$

with corresponding errors [cf. [Schmucker, 1999](#)]

$$\delta C(\omega) = \frac{3a}{2} \frac{1}{|1 + Q_1(\omega)|^2} \delta Q_1(\omega) \quad (7.3)$$

Figure 7.3 shows "observed" C -responses (circles with error bars) and the C -responses calculated from the recovered 1-D structure. It is seen that the error bars tend to be larger at longer periods. This is because our data section length depends on the period (shorter sections for shorter periods), and hence the number of sections (and thus the number of degrees of freedom) is smaller for longer periods compared to shorter periods. Since the statistical error is inversely proportional to the number of degrees of freedom (and coh^2 does not change much with period), this results in larger errors at longer periods.

Using the quasi-Newton (QN) algorithm of [Byrd et al. \[1995\]](#) we derived 1-D conductivity model from the "observed" C -response estimates. The model is discretized by 96 spherical layers of uniform thickness of 30 km and terminates with a highly conducting core at a depth of 2890 km. The solution is stabilized (regularized) by requiring minimum first derivative of log(conductivity) with respect to depth. The proper regularization parameter α is found by visual detecting the "knee" of the L -curve, shown on Figure 7.4.

Figure 7.5 presents the recovered and true 1-D conductivity distributions. They agree very well, however some small "wiggles" are seen, most probably, due to the fact that our 1-D inversion is applied to 3-D data.

7.2.2 Time domain approach

The synthetic 6 years-long time series of internal (induced) spherical harmonic coefficient $G_{10}^{(i)}(t)$ sampled at 1 hr step was directly inverted by the TD approach. The external (inducing) spherical harmonic coefficient $G_{10}^{(e)}(t)$ was assumed to be perfectly known, identical to the one used in the computation of synthetic data as described in Section (6.1). The model was parameterized by 89 layers with uniform thicknesses of 20 and 50 km in the upper and lower mantle, respectively. The conductivity of the uppermost 10 km was fixed at 1.58 S/m — the average value of the surface conductance map scaled to 10 km thickness. The conductivity of the core was fixed at 10^5 S/m. Regularization was applied in terms of minimization of $R^2 = \int_{r_{\text{CMB}}+\delta}^{a-10 \text{ km}-\delta} \nabla_r^2 \log \sigma(r) r^2 dr$, i.e., excluding penalization of jumps across CMB and near the surface. The inverse problem was solved by Quasi-Newton (QN) iterations, starting from an initial model of homogeneous mantle of $\sigma = 1$ S/m.

Figure 7.6 shows the trade-off between data misfit χ^2 and regularization term R^2 for different regularization parameters λ . Based on that, the regularization parameter of $\lambda = 10^{-7}$ was selected. Result

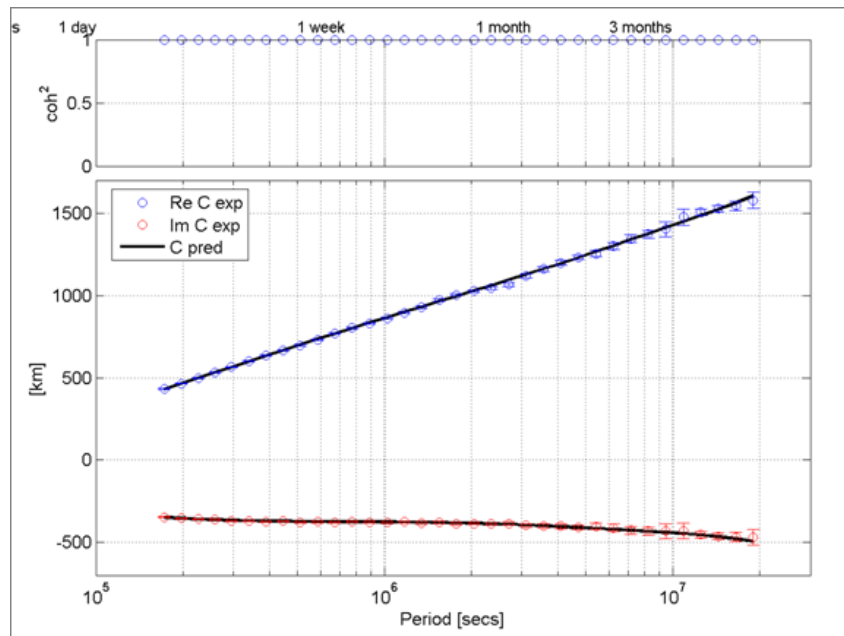


Figure 7.3: "Observed" and predicted C -responses; case of idealistic 3-D data. See details in the text.

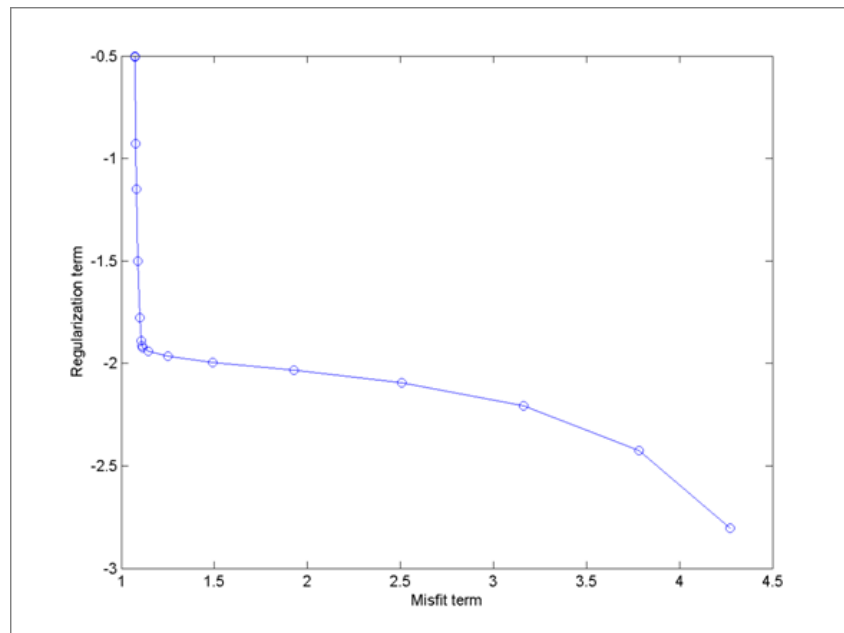


Figure 7.4: L -curve for this inversion.

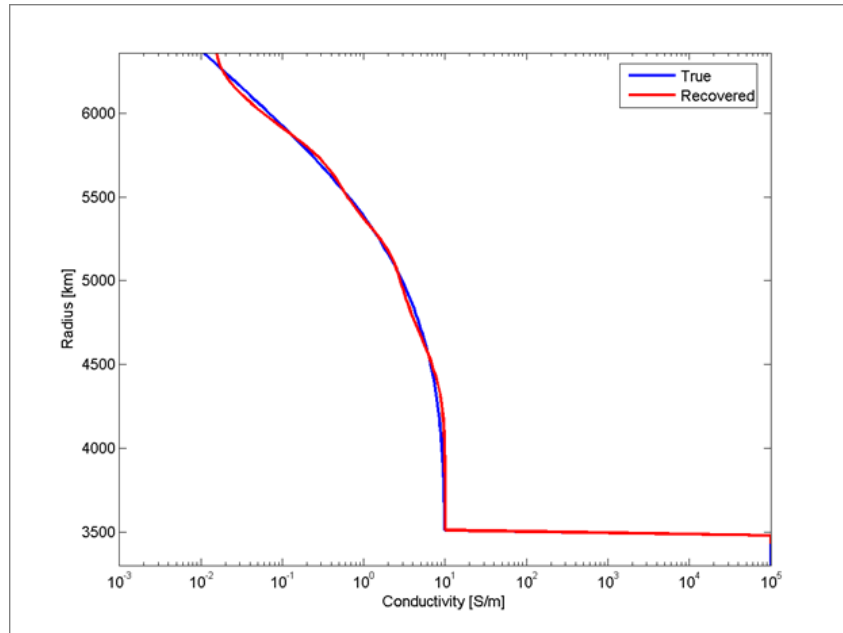


Figure 7.5: True and recovered 1-D conductivity models.

of the inversion is shown in Figure 7.7. Recovery of the model is almost perfect, as can be confirmed by its prediction of synthetic data (Figure 7.8).

7.3 1-D inversion of realistic data II

7.3.1 Frequency domain approach

In this test we use time series of dominant external (inducing) and internal (induced) coefficients, $\epsilon_1^0(t)$ (or $q_1^0(t)$) and $\iota_1^0(t)$ (or $g_1^0(t)$), from realistic data discussed in section 6.3 of Chapter 6. Case A (with sampling interval of 1 h) and case B (with sampling interval of 6 h) are considered. We use the same inversion scheme, the same discretization of the model and the same regularization as in section 7.2.1.

Figure 7.9 shows "observed" C -responses (circles with error bars) and the C -responses calculated from the recovered 1-D structure. Figures 7.10 and Figure 7.11 present L -curve and the recovered and true 1-D conductivity distributions, respectively.

In the same manner Figures 7.12-7.14 presents the results for the case B. In contrast to idealistic 3-D model where background 1-D conductivity changes smoothly with depth, background 1-D model in realistic 3-D model has a jumps at depths 300 and 700 km. Evidently regularized inversion with the smooth constraints cannot reproduce such jumps. Moreover it reproduces some artefacts. Possible remedy to overcome this difficulty is to consider alternative types of regularization.

7.3.2 Time domain approach

The synthetic 4.5 years-long time series of external and internal spherical harmonic coefficient $G_{10}^{(e)}(t)$, $G_{10}^{(i)}(t)$ obtained at 1 hr (case A), and 6 hr (case B) sample rate from simulated mission data (cf. Section 6.3) were directly inverted by the TD approach.

Two different radial parameterizations were used. In setup H, the conductivity is parameterized in 100 km thick layers in the upper mantle, 400 km thick layers in the lower mantle, and a homogeneous

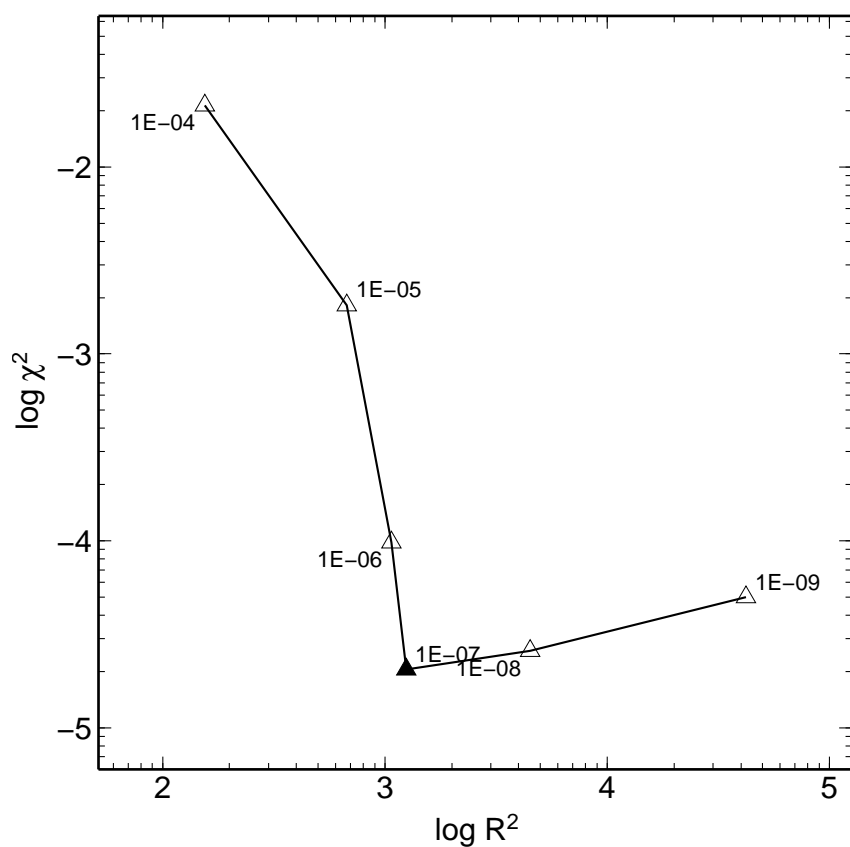


Figure 7.6: Recovery of the 1-D background structure of the idealistic conductivity model. Trade-off between data misfit χ^2 and regularization term R^2 for different regularization parameters λ .

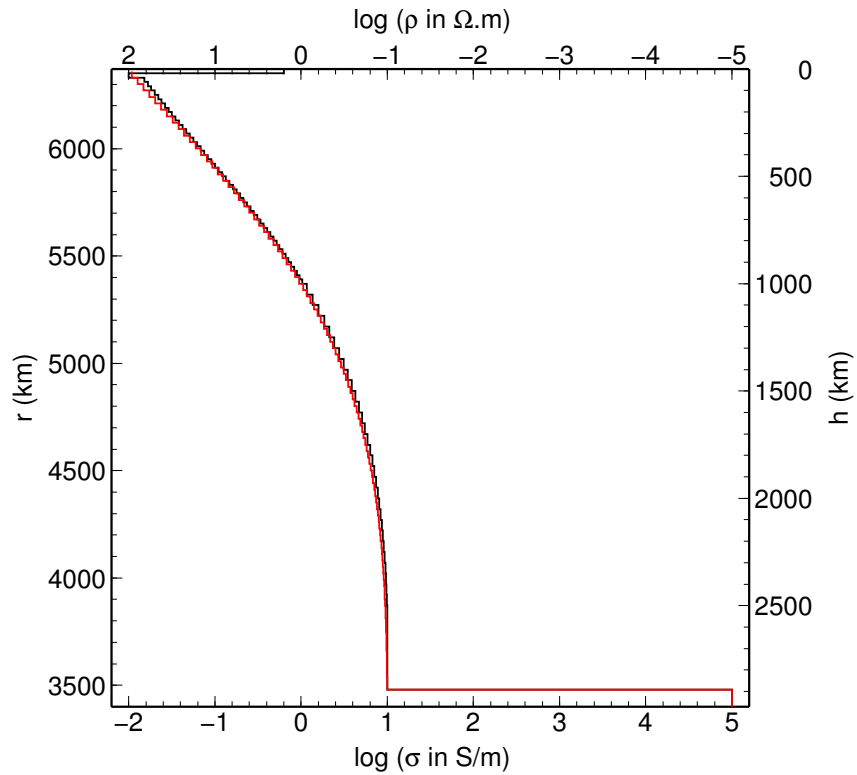


Figure 7.7: Recovery of the 1-D background structure of the idealistic conductivity model (black) by TD approach (red).

core. In setup L, the layer boundaries copy the setup from the known target model, i.e., 12.65 km thick layer at the surface, 400 km and 300 km layers in the upper mantle and transition zone, one layer in the lower mantle, and one in the core. Regularization was applied in terms of minimization of $R^2 = \int_0^a \nabla_r^2 \log \sigma(r) r^2 dr$. The inverse problem was solved by Quasi-Newton (QN) iterations, starting from an initial model of homogeneous mantle of $\sigma = 1 \text{ S/m}$.

Figure 7.15 shows the trade-off curves between data misfit χ^2 and regularization term R^2 for different regularization parameters λ . Based on that, the regularization parameter of $\lambda = 5 \times 10^{-10}$ was selected in all runs (cases A and B with parameterizations H and L). Results of the inversions are shown in Figure 7.16. Differences between cases A and B are small, 1 hr time resolution does not offer any significant advantage over 6 hr time step. In case of H parameterization, conductivity of the lower mantle is well recovered, but the method struggles to recover the relatively large conductivity jumps in the upper mantle. The result is biased towards higher conductivity, probably due to the large highly conductive inclusion in the transition zone below Pacific prescribed in the target model. The low-parameter runs L yield better results. Interestingly, models shown in the bottom row of Figure 7.16, which are considered underregularized ($\lambda = 10^{-11}$ in case A, and $\lambda = 10^{-12}$ in case B) judging from the L-curve analysis (Fig. 7.15), present improved recovery of the uppermost mantle.

7.4 Summary of 1-D benchmarking inversions

Table 7.17 summarizes the results of 1-D benchmarking inversions of two 3-D data sets. Our conclusion is that both frequency domain and time domain approaches produce results of comparable quality.

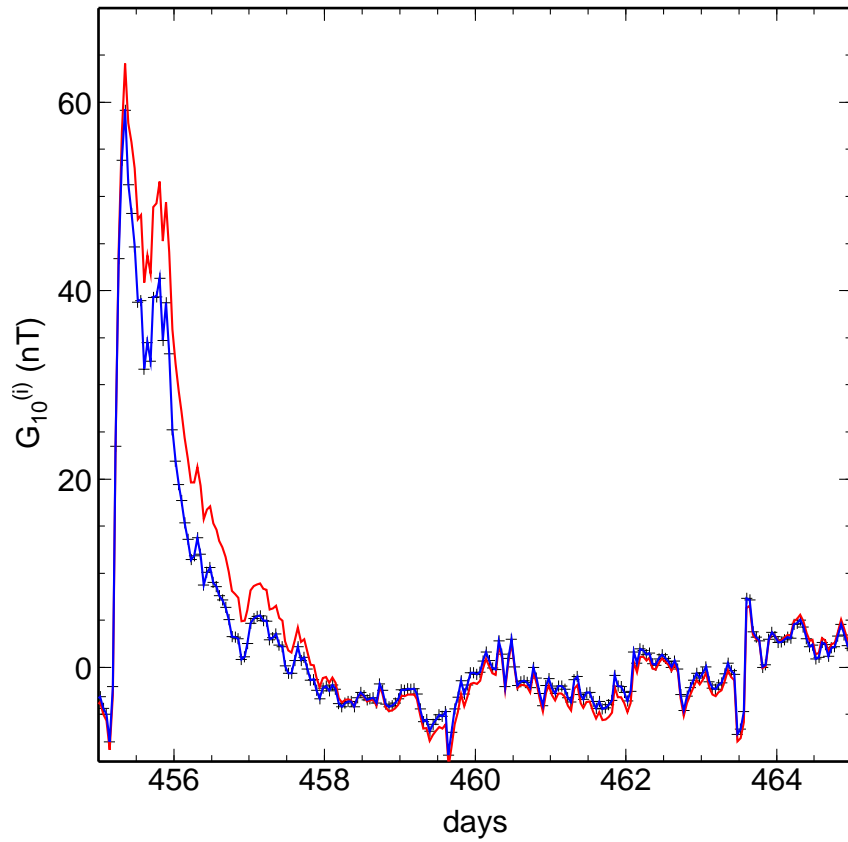


Figure 7.8: Cutout of the time-series of internal coefficient $G_{10}^{(i)}(t)$. Black crosses show the synthetic values to be inverted, red curve marks the predicted coefficient from the initial model of QN iterations, and blue curve corresponds to the optimal model.

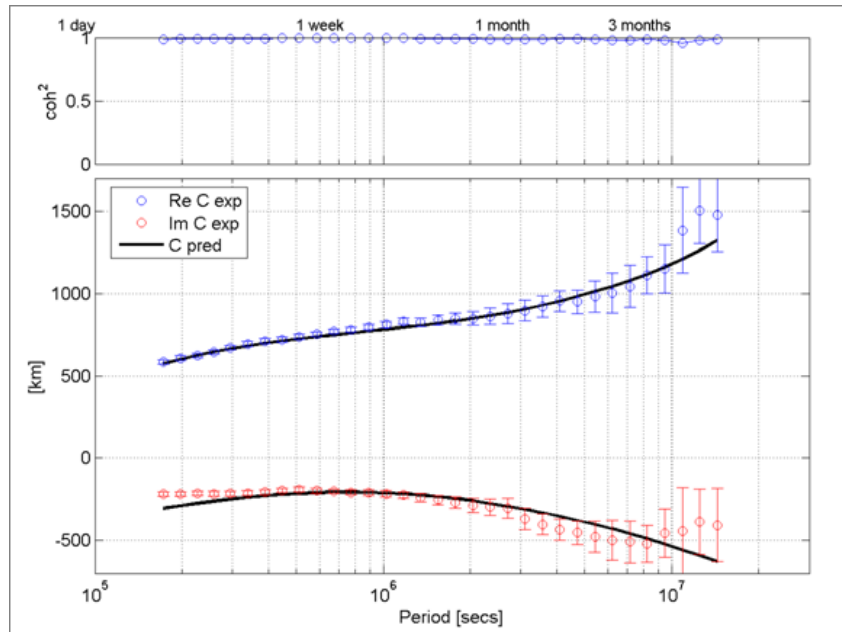


Figure 7.9: "Observed" and predicted C -responses; case A.

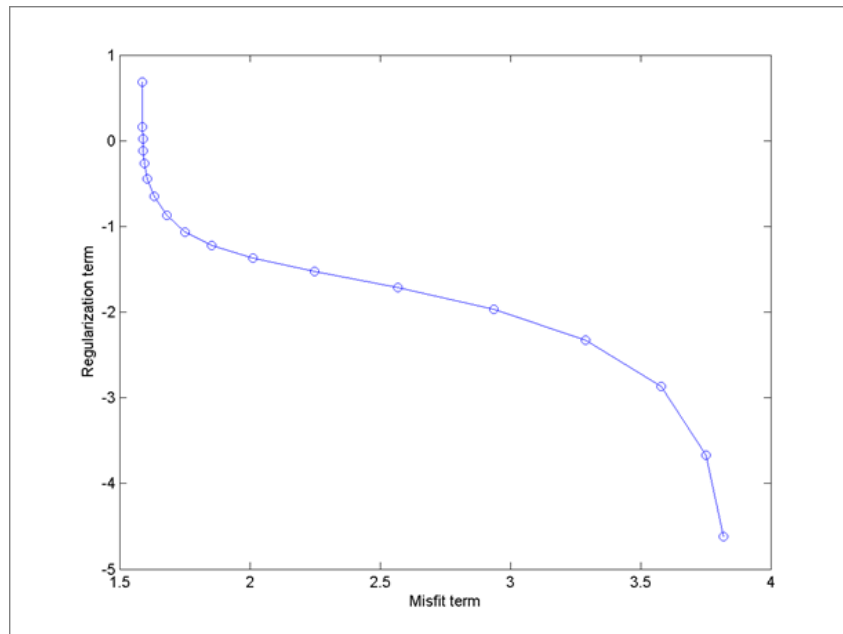


Figure 7.10: *L*-curve for this inversion; case A.

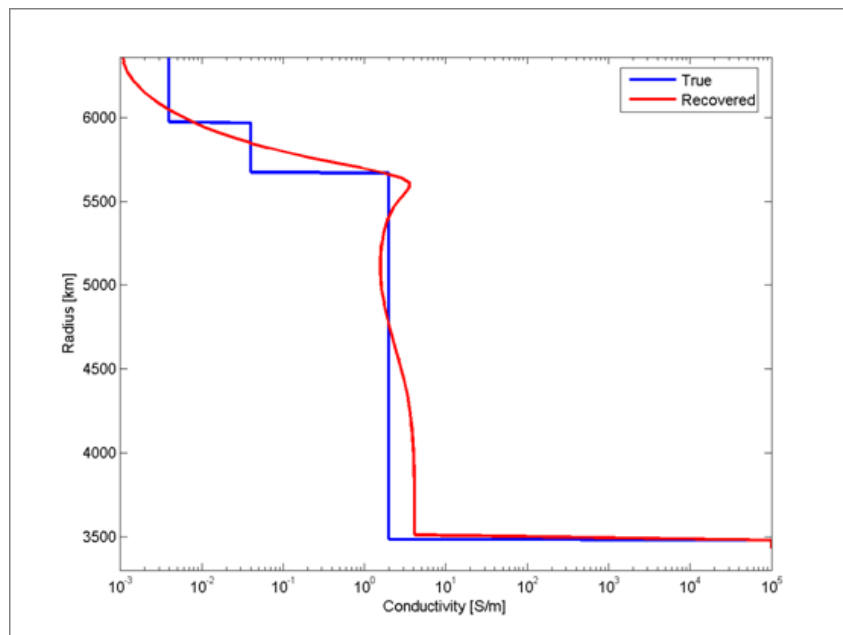


Figure 7.11: True and recovered 1-D conductivity models; case A.

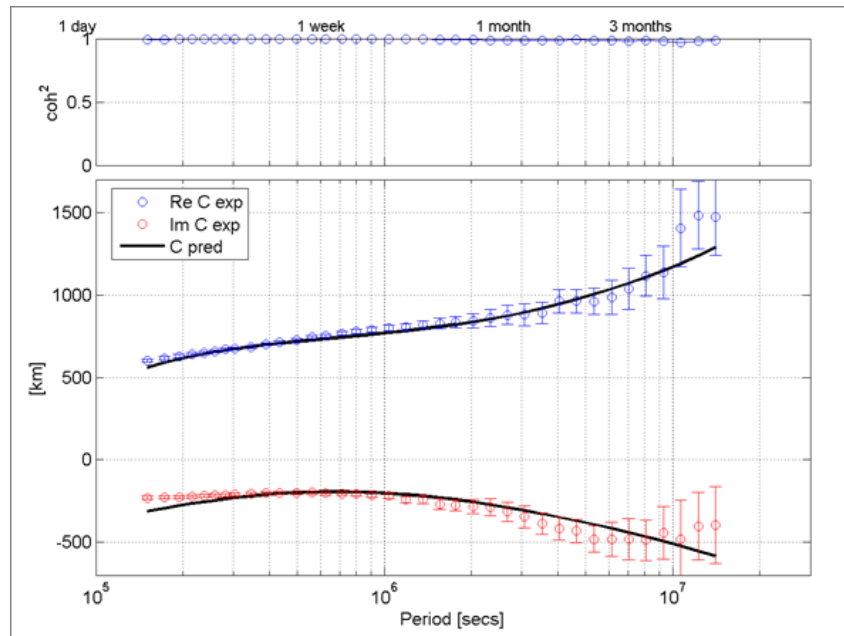


Figure 7.12: "Observed" and predicted C -responses; case B.

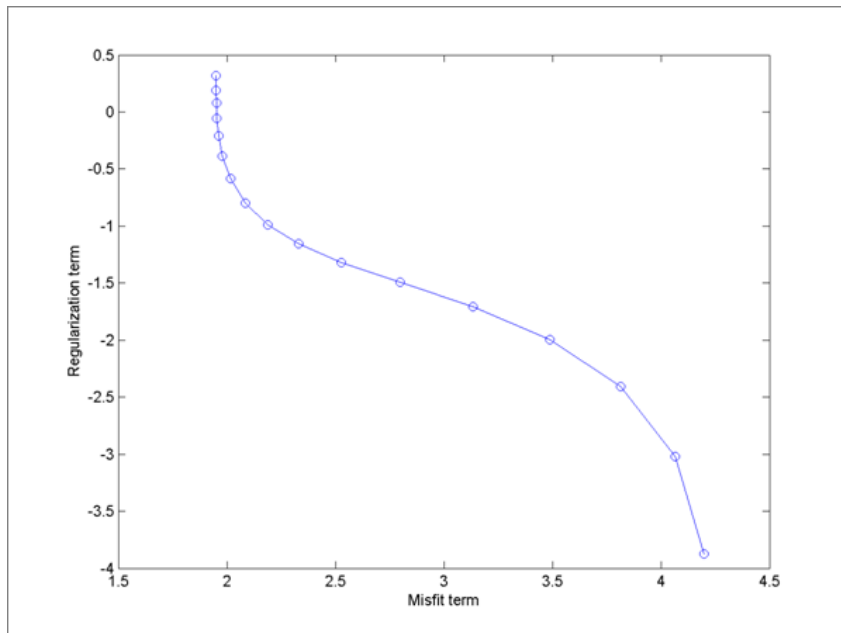


Figure 7.13: L -curve for this inversion; case B.

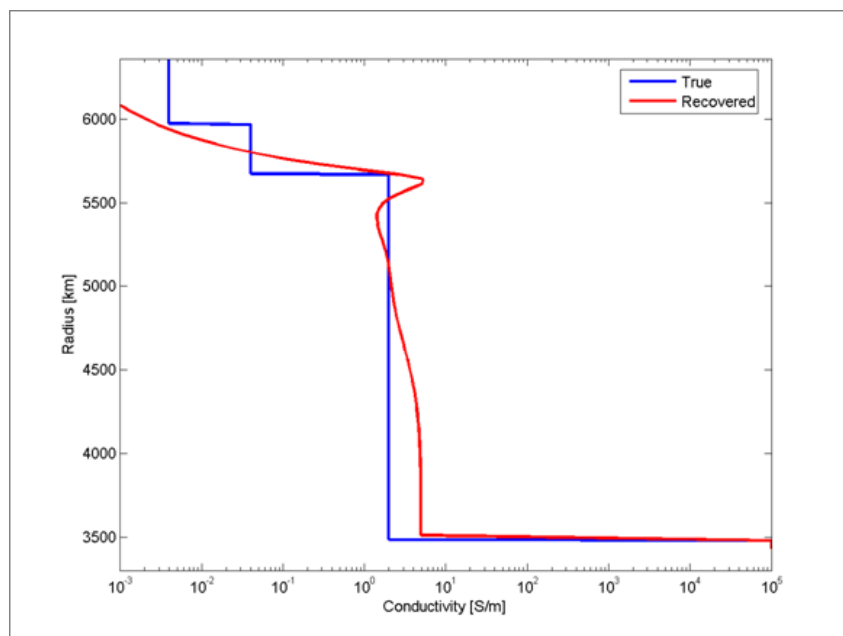


Figure 7.14: True and recovered 1-D conductivity models; case B.

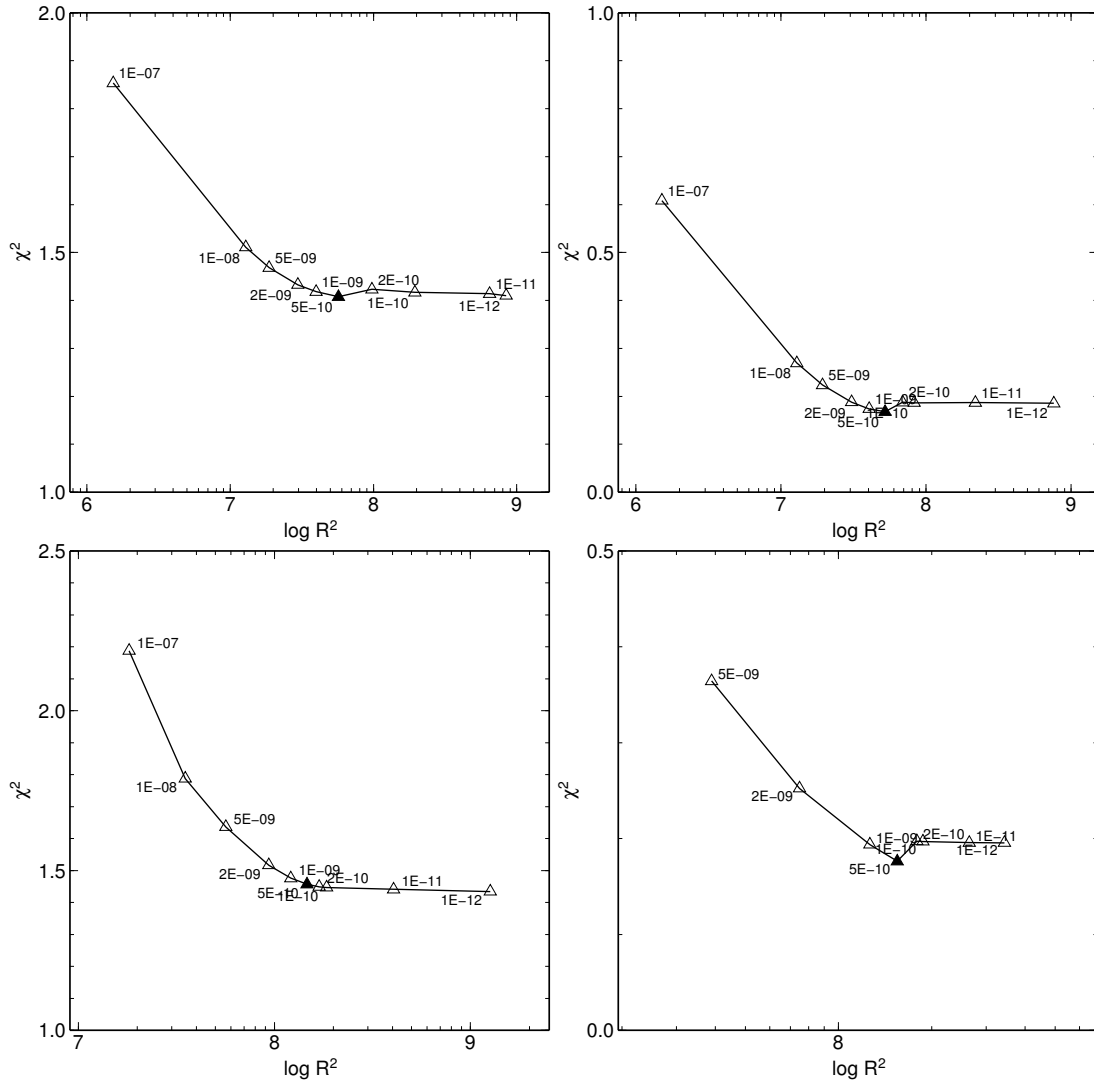


Figure 7.15: Recovery of the 1-D background structure of the realistic conductivity model. Trade-off between data misfit χ^2 and regularization term R^2 for different regularization parameters λ . Left column: case A, right column: case B. Upper row: parameterization H, bottom row: parameterization L (see text).

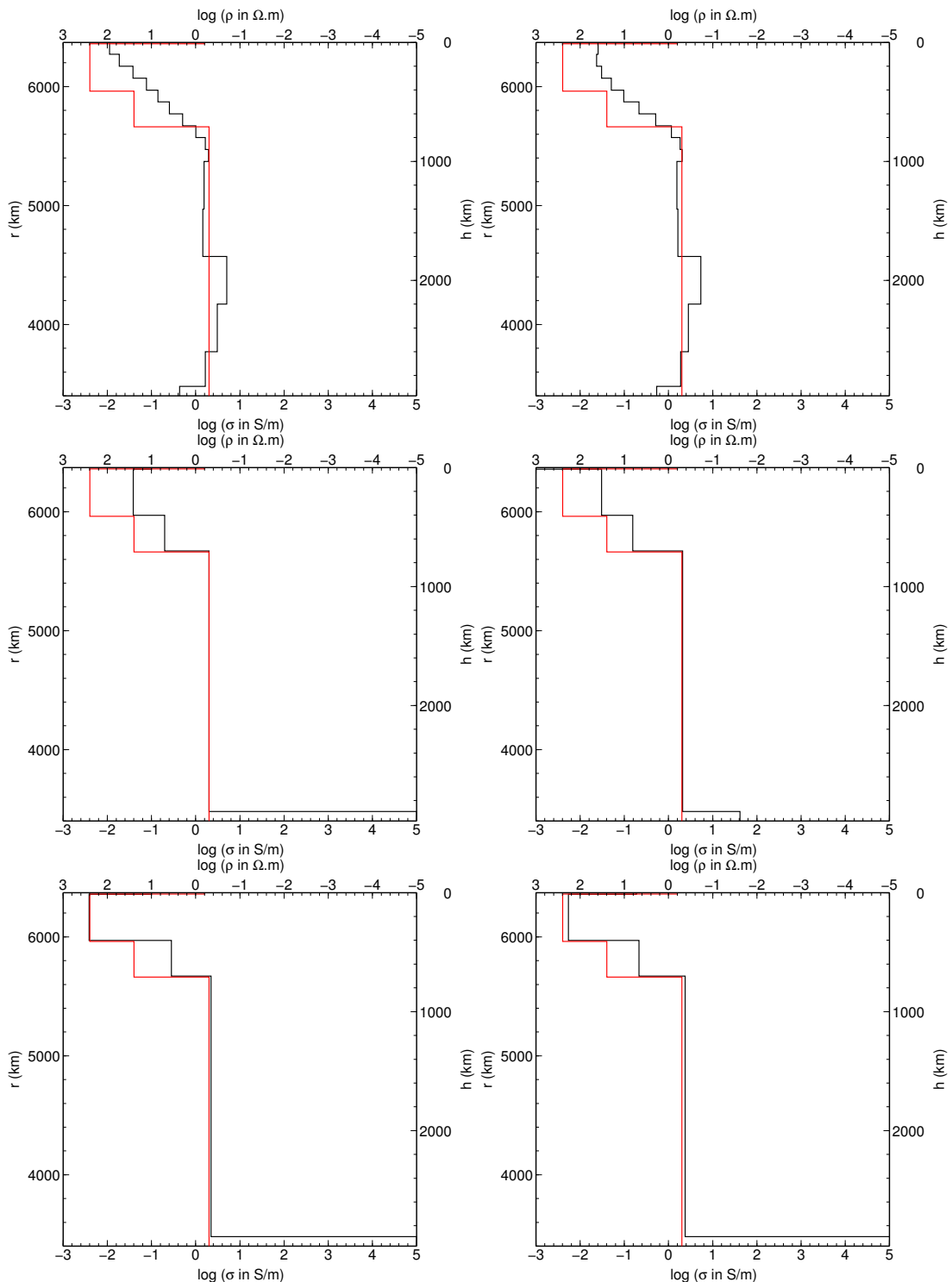


Figure 7.16: Recovery of the 1-D background structure of the realistic conductivity model (red) by TD approach (black). Left column: case A, right column: case B. Upper row: parameterization H; middle row: parameterization L, models for optimal $\lambda = 5 \times 10^{-10}$; bottom row: parameterization L, underregularized models for $\lambda = 10^{-11}$ (case A) and $\lambda = 10^{-12}$ (case B).



<i>Method/Data set</i>	<i>Idealistic</i>	<i>Realistic II</i>	<i>Processing time</i>
<i>Frequency-domain (FD) (C-responses inversion)</i>	very good	satisfactory	small
<i>Time-domain (TD) (internal coefficients inversion)</i>	very good	satisfactory	moderate

Figure 7.17: Summary of 1-D benchmarking inversions.

Chapter 8

Benchmarking of 3-D inversion approaches

Before presenting the results of the 3-D benchmarking studies it is worthwhile to make the following remark. So far the most of 3-D tests of different 3-D inversion schemes were performed in a "closed loop" manner: within each approach the forward modelling of the input data, and the subsequent inversion of these data were based on the same forward solution engine. In this Chapter we perform the tests when one inversion solver uses the data generated by another (independent) forward solver. For example in section 8.1 the frequency domain inversion solvers described in Chapters 2 and 5 use the data generated by the time domain forward solver described in Chapter 3. The reverse situation holds for the tests described in sections 8.2-8.3.

8.1 3-D inversion of idealistic data

8.1.1 Frequency domain inversion of internal coefficients

In this test we use time series of all external (up to degree $n = 6$) and internal (induced) coefficients (up to degree $N_i = 14$) from idealistic 3-D data discussed in section 6.1 of Chapter 6. These data were Fourier transformed and as a result 24 time spectra of the external and internal coefficients have been obtained in period range between 3 days and 100 days.

The model is discretized onto seven spherical inhomogeneous layers. The surface thin (of 10 km thickness) layer of known variable conductance approximates the distribution of land masses and oceans. Six deeper layers (all of 480 km thickness each) fill the whole mantle column down to core-mantle boundary. In the forward/inverse modeling all layers are discretized in horizontal direction by 72×36 cells of size $5^\circ \times 5^\circ$. At each period the model is induced by a source described by the corresponding time spectra of external coefficients. Our aim is to try to recover from spectra of internal coefficients the conductivity distribution in the six mantle layers. As a starting model we took a 1-D model recovered during 1-D benchmarking tests. Note that input 3-D model is not a layered model, thus our layered 3-D model represents only rough approximation of the true model. The idea of this test is to estimate the resolution of our inversions with respect to depth. The results of regularized inversion are presented in Figure 8.1. It is seen that the maximum resolution is achieved in the second layer, thus in depth range between 500 and 1000 km.

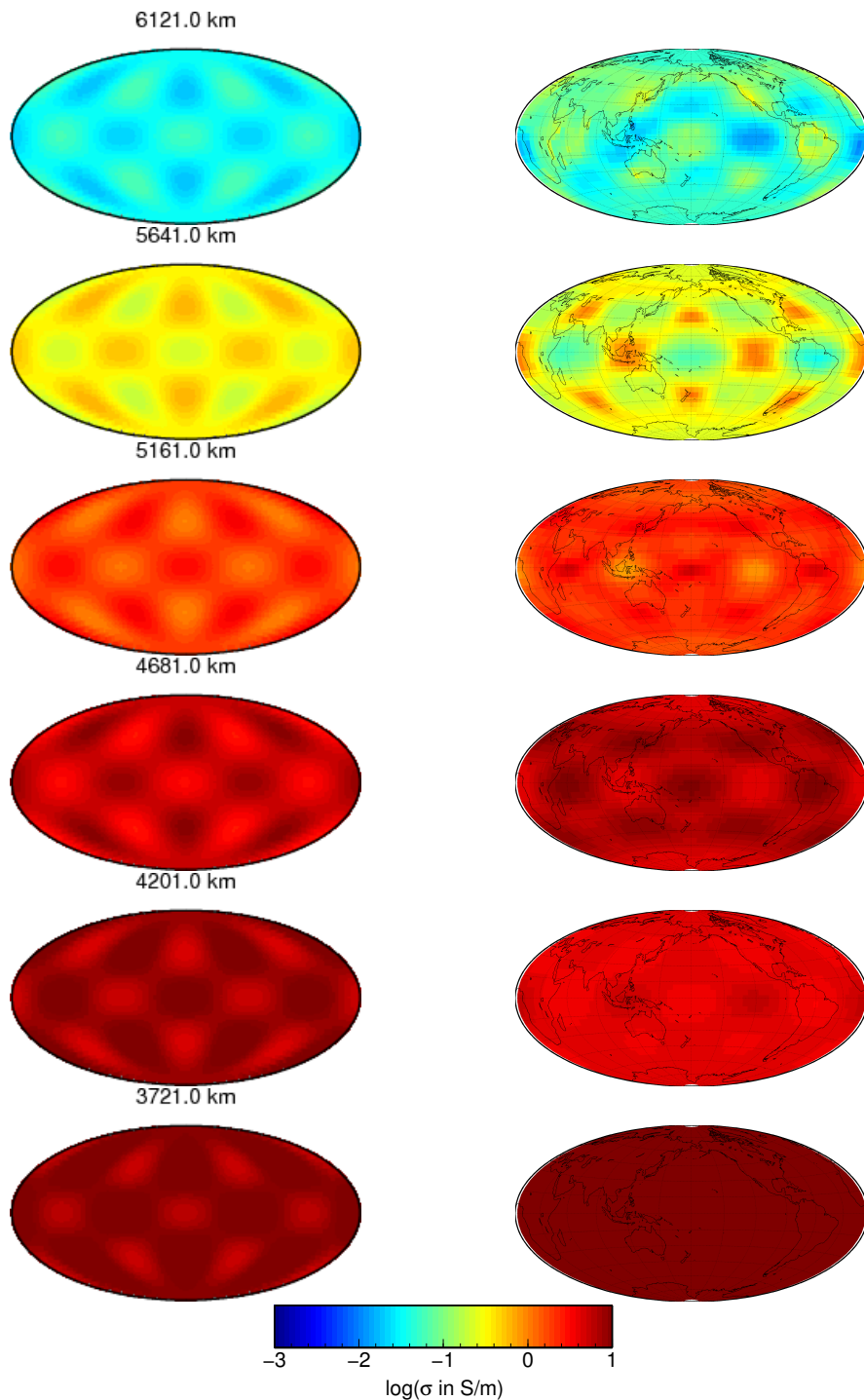


Figure 8.1: Recovery of the 3-D checkerboard structure of the idealistic conductivity model by the FD approach (inversion of internal coefficients). Left column: cross sections of target model positioned at peaks of lobes in the radial direction. Right column: recovered 3-D model.

8.1.2 Frequency domain inversion of C -responses

In this section we report the results of inversion based on analysis of C -responses. These responses are calculated from the time series of external and internal coefficients discussed in previous section. For the details of the responses calculations see Chapter 2. The same discretization, the same starting model and the same type of regularization as discussed in previous section have been applied for these inversion runs. The results of recovery are presented in Figure 8.2. As a whole the recovery is poorer compared with the recovery based on the inversion of internal coefficients.

8.1.3 Time domain inversion of internal coefficients

For the 3-D inversion of the idealistic conductivity model, time series of external coefficients up to degree and order 6, and internal coefficients up to degree and order 8 were downsampled to 6 hr time step for the entire 6 years long interval. The model was parameterized by 6 layers of 480 km thickness in the mantle with 3-D conductivity resolution up to degree 5 in each layer, homogeneous core, and fixed heterogeneous layer at the surface (i.e., 36 model parameters in each layer, 216 in total). Regularization term included both radial and lateral component of Laplacian of conductivity logarithm. Figure 8.3 shows the trade-off L curve between data misfit and regularization. Figure 8.4 compares the result of inversion for $\lambda = 10^{-10}$ with the known target model. In the two uppermost layers, the checkerboard structure is correctly resolved, albeit with slightly overestimated amplitudes in the first layer, and underestimated amplitudes in the second layer. From the third layer downwards, the reconstructed model has similar scale, but opposite signs. Since the checkerboard pattern is sharply recovered, this can be interpreted rather as insufficiency of radial resolution, where the inverse algorithms struggles to assign the lateral heterogeneity to correct depths.

8.2 3-D inversion of realistic data I

We start from the inversions of realistic coefficients that were calculated as input for predicting magnetic signals at satellites' orbits.

8.2.1 Frequency domain inversion of internal coefficients

In this test we use time series of all external coefficients, and internal (induced) coefficients up to degree $N_i = 14$. Note that the full set of the calculated internal coefficients includes the coefficients up to degree $n = 45$. These internal coefficients are calculated for the basic 3-D model described in section 2.1.3.1 of Chapter 2. These data were Fourier transformed and as a result 24 time spectra of the external and internal coefficients have been obtained in the period range between 3 days and 100 days.

The model for inversion is discretized onto six spherical inhomogeneous layers. The surface thin (of 10 km thickness) layer of known variable conductance approximates the distribution of land masses and oceans. Five deeper layers (all of 200 km thickness each) fill the upper and mid mantle column down to depth of 1000 km. In the forward/inverse modeling all layers are discretized in horizontal direction by 72×36 cells of size $5^\circ \times 5^\circ$. At each period the model is induced by a source described by the corresponding time spectra of external coefficients. Our aim is to try to recover from spectra of internal coefficients the conductivity distribution in the five mantle layers. As a starting model we took a background 1-D model. Note that the layering of the "inverse" 3-D model does not coincide with the layering of the "true" 3-D model. The results of the regularized inversion are presented in Figure 8.5. It is seen that the large scale anomaly beneath Pacific plate is recovered pretty well. As expected the shallower, small scale, structures are invisible in the recovered images.

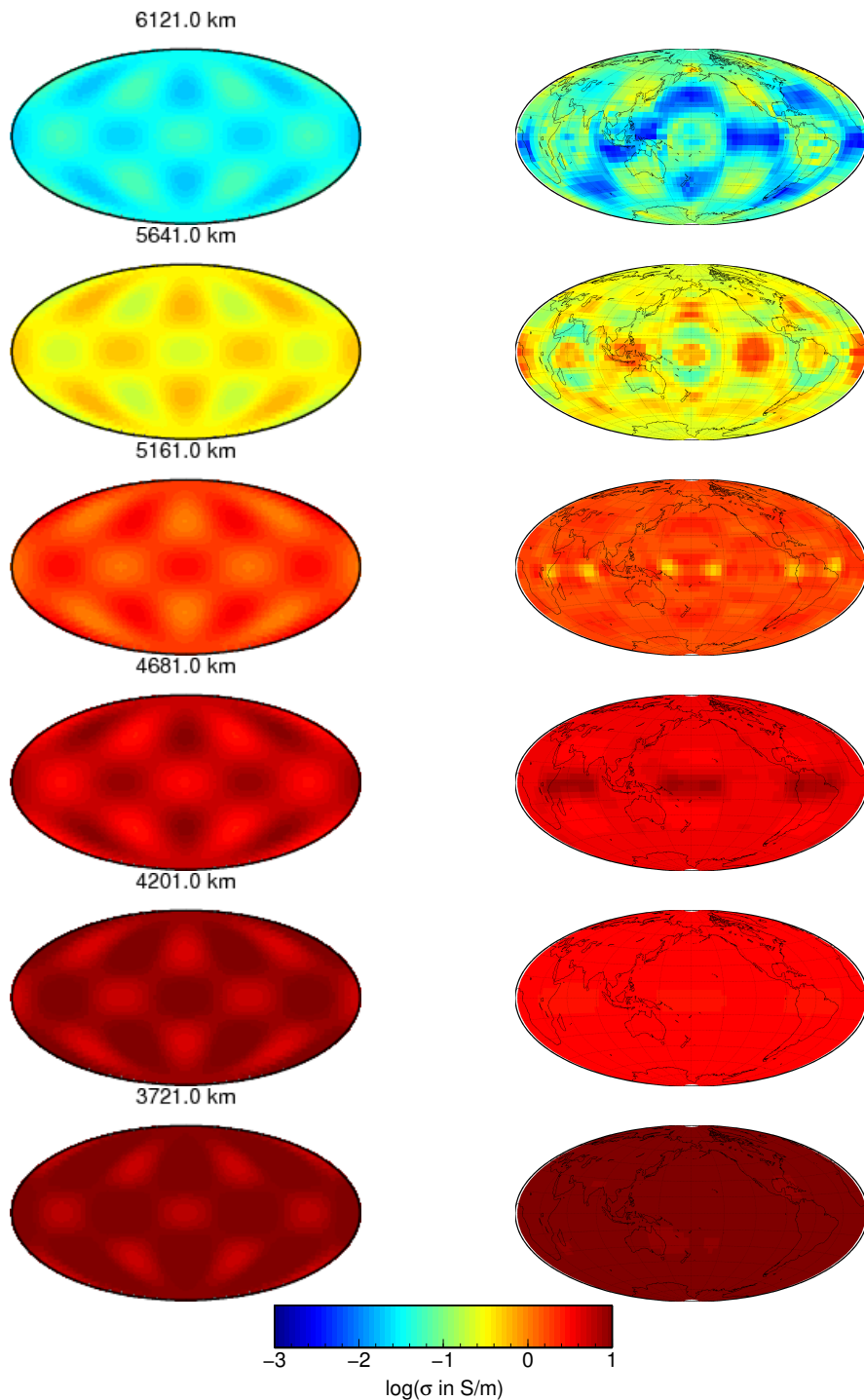


Figure 8.2: Recovery of the 3-D checkerboard structure of the idealistic conductivity model by the FD approach (inversion of C -responses). Left column: cross sections of target model positioned at peaks of lobes in the radial direction. Right column: recovered 3-D model.

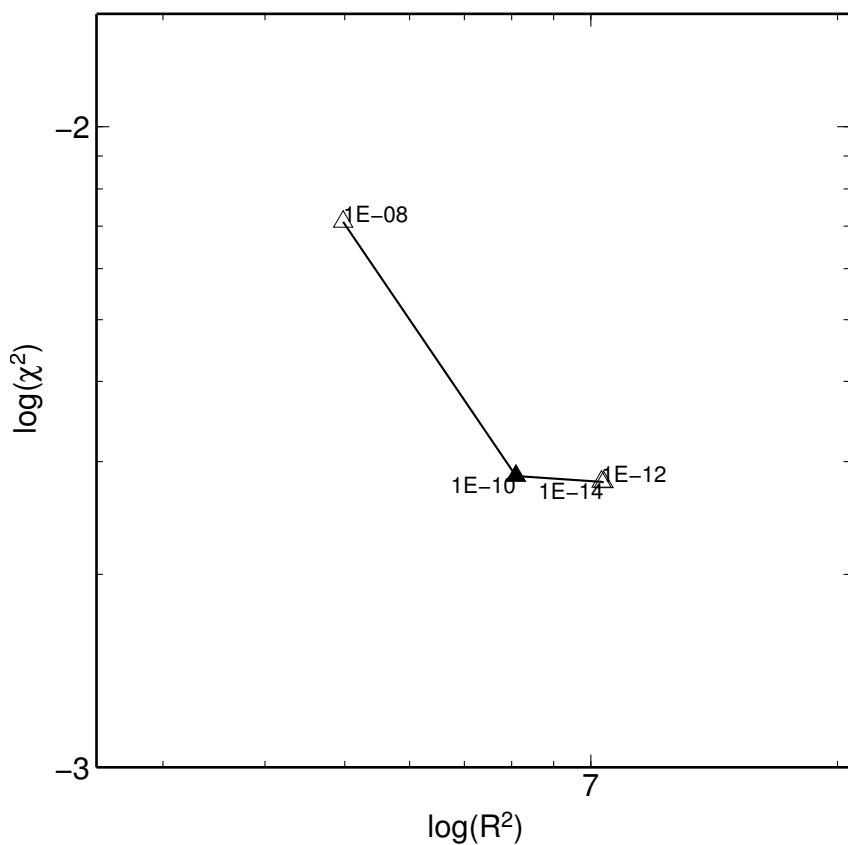


Figure 8.3: Recovery of the 3-D checkerboard structure of the idealistic conductivity model by the TD approach. Trade-off between data misfit χ^2 and regularization term R^2 for different regularization parameters λ .

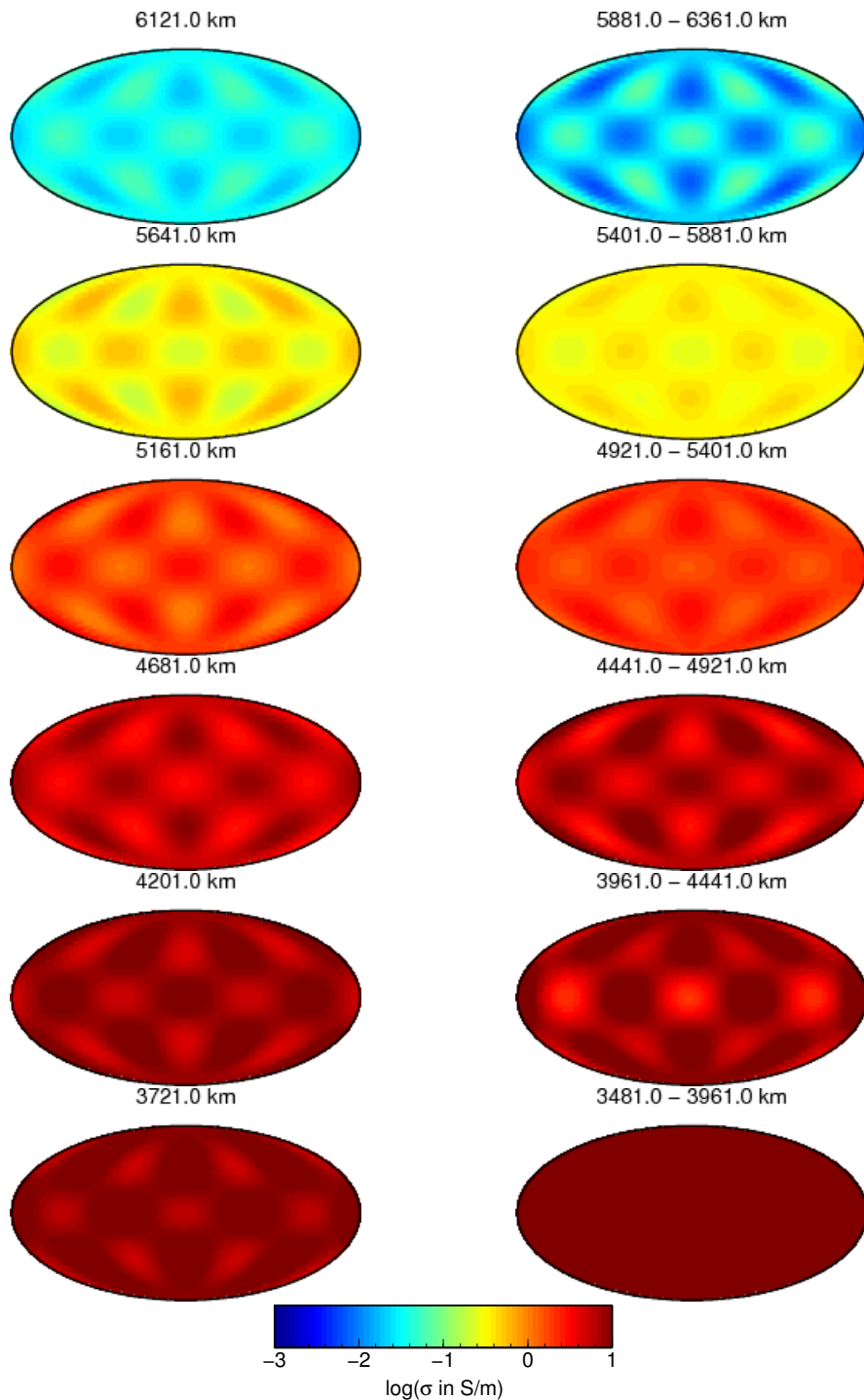


Figure 8.4: Recovery of the 3-D checkerboard structure of the idealistic conductivity model by the TD approach. Left column: cross sections of target model positioned at peaks of lobes in the radial direction. Right column: recovered 3-D model.

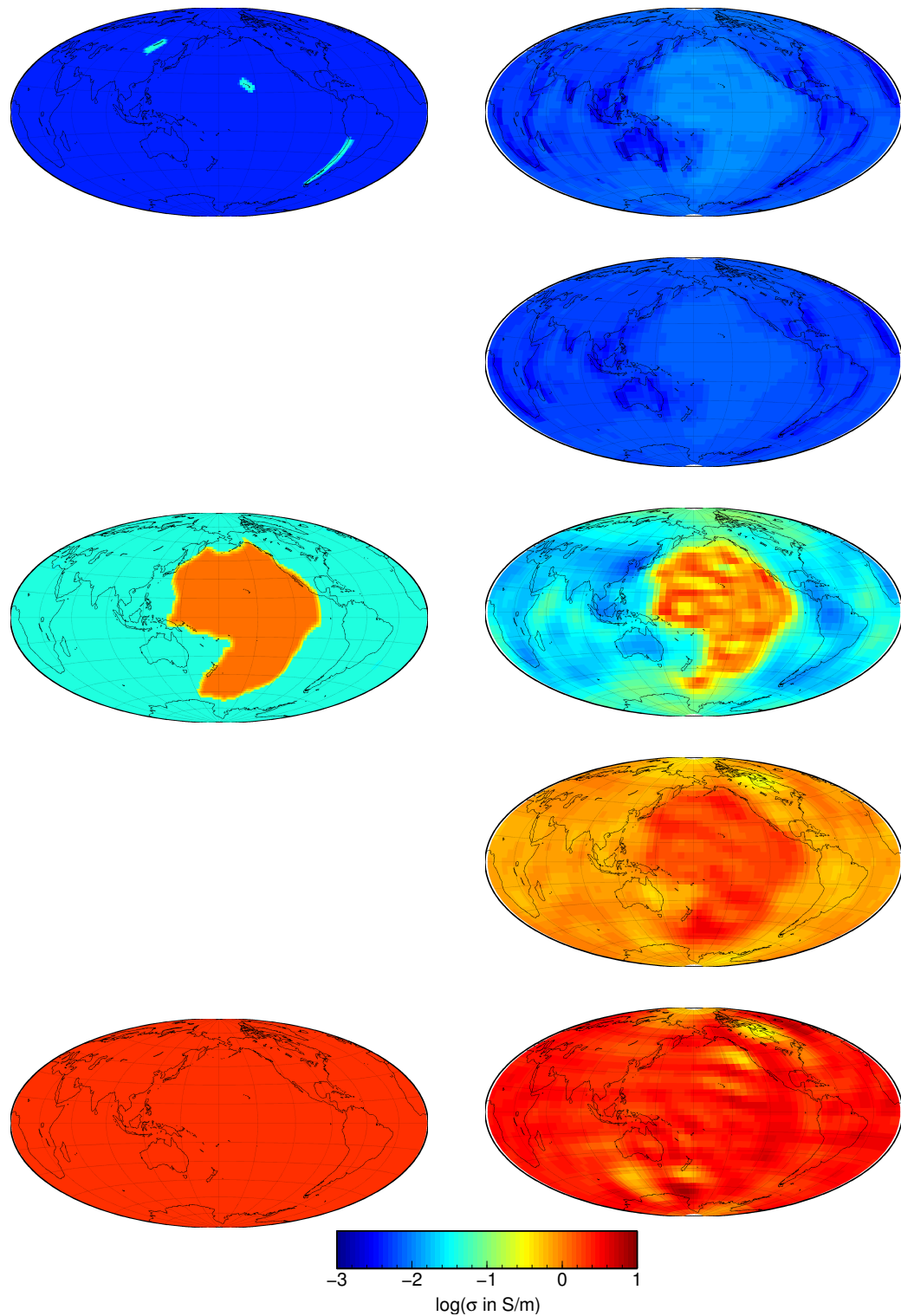


Figure 8.5: Recovery of the realistic conductivity model from original (exact) internal field coefficients by the FD approach (inversion of internal coefficients). Left column: cross sections of target 3-D model. Thickness of layers top to bottom is 400, 300, and 2191 km, respectively. Right column: cross sections of recovered 3-D model in layers of uniform thickness 200 km.

8.2.2 Frequency domain inversion of C -responses

In this section we report the results of inversion based on analysis of C -responses. These responses are calculated from the time series of external and internal coefficients discussed in previous section. For the details of the responses calculations see Chapter 2. The same discretization, the same starting model and the same type of regularization as discussed in previous section have been applied for these inversion runs. The results of recovery are presented in Figure 8.6. Again (as in idealistic 3-D case) the recovery is poorer compared with the recovery based on the inversion of internal coefficients. These results suggest that frequency domain 3-D baseline inversion should rely on inversion of internal coefficients.

8.2.3 Time domain inversion of internal coefficients

For the 3-D inversion of the realistic conductivity model, time series of external coefficients up to degree and order 3, and internal coefficients up to degree and order 8 were at 6 hr time step were used for the entire 5 years long interval. The model was parameterized by 5 layers of 200 km thickness in the upper mantle with 3-D conductivity resolution up to degree 5 in each layer, homogeneous core, and lower mantle, and fixed heterogeneous layer at the surface (i.e., 36 model parameters in each layer, 180 in total). Regularization term included both radial and lateral component of Laplacian of conductivity logarithm. Figure 8.7 shows the trade-off L curve between data misfit and regularization. Figure 8.8 compares the result of inversion for $\lambda = 10^{-9}$ with the known target model. The basic structure of the inclusion is recovered with some leaking of energy to the neighboring layers due to regularization.

8.3 3-D inversion of realistic data II

For the 3-D inversion of the realistic conductivity model, time series of external coefficients up to degree 3 and order 1, and internal coefficients up to degree and order 5 at 6 hr time step (case B) recovered by the Comprehensive inversion, were used for the entire 5 years long interval.

8.3.1 Frequency domain inversion of internal coefficients

The setup is identical to the inversion of the data performed in the previous section. Figure 8.9 shows the results of inversion that are however quite controversial. There is a clear hint on anomaly beneath Pacific plate but the resolution is quite poor most probably due to the insufficient recovery of the internal coefficients by CI.

8.3.2 Time domain inversion of internal coefficients

The setup is identical to the inversion of the data in the previous section, i.e., 5 layers of 200 km thickness in the upper mantle with 3-D conductivity resolution up to degree 5 in each layer, homogeneous core, and lower mantle, and fixed heterogeneous layer at the surface. Regularization term included both radial and lateral component of Laplacian of conductivity logarithm. Figure 8.10 shows the trade-off L curve between data misfit and regularization. Figure 8.11 compares the result of inversion for $\lambda = 10^{-8}$ with the known target model. In spite of rather pessimistic correlations presented in Figure 6.8, the large heterogeneity in the test model was successfully recovered.

8.4 Summary of 3-D benchmarking inversions

Table 8.12 summarizes the results of 3-D benchmarking inversions of three 3-D data sets. Our benchmarking exercises show that both frequency and time approaches as applied directly to internal (induced)

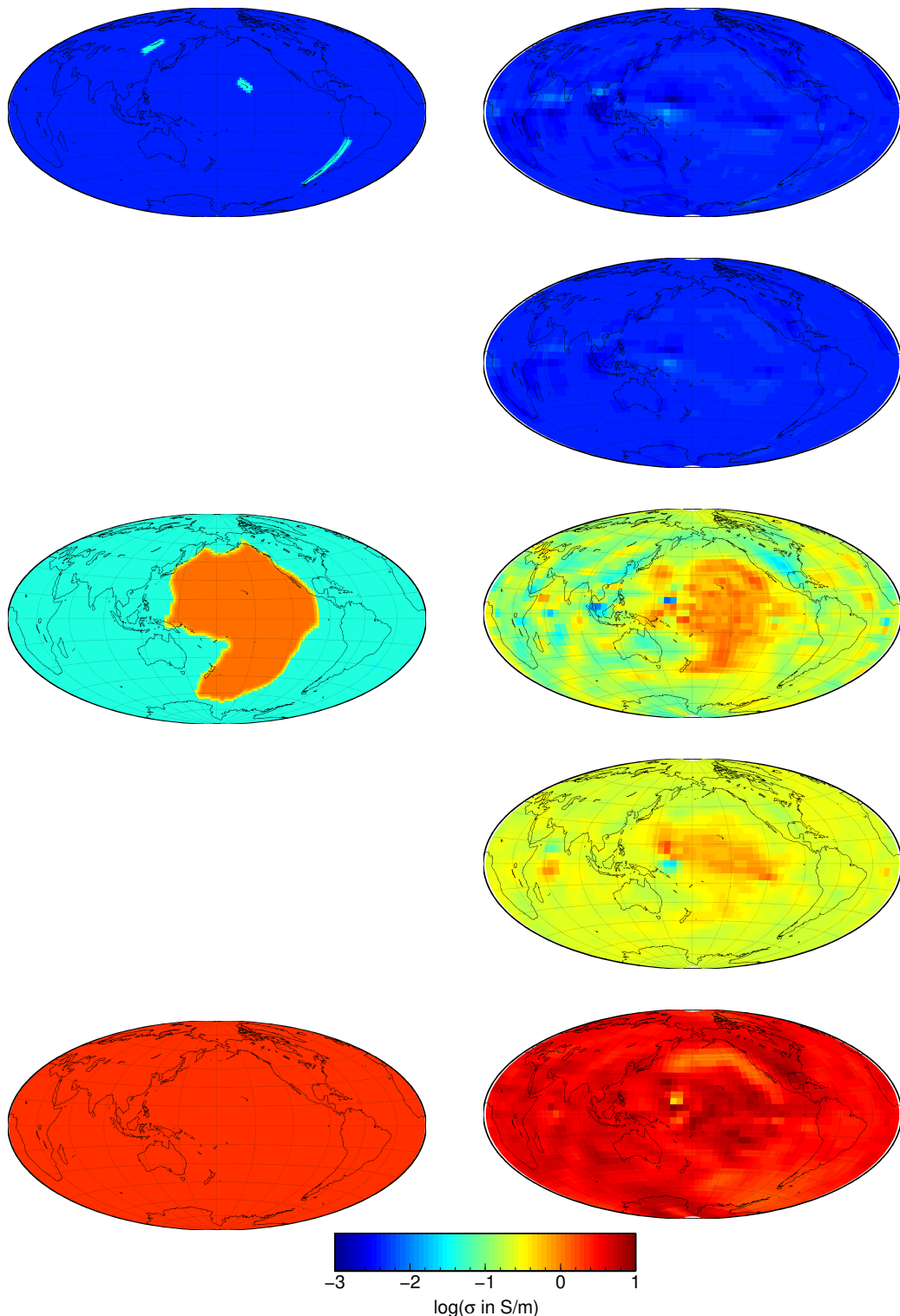


Figure 8.6: Recovery of the realistic conductivity model from original (exact) internal field coefficients by the FD approach (inversion of C -responses). Left column: cross sections of target 3-D model. Thickness of layers top to bottom is 400, 300, and 2191 km, respectively. Right column: cross sections of recovered 3-D model in layers of uniform thickness 200 km.

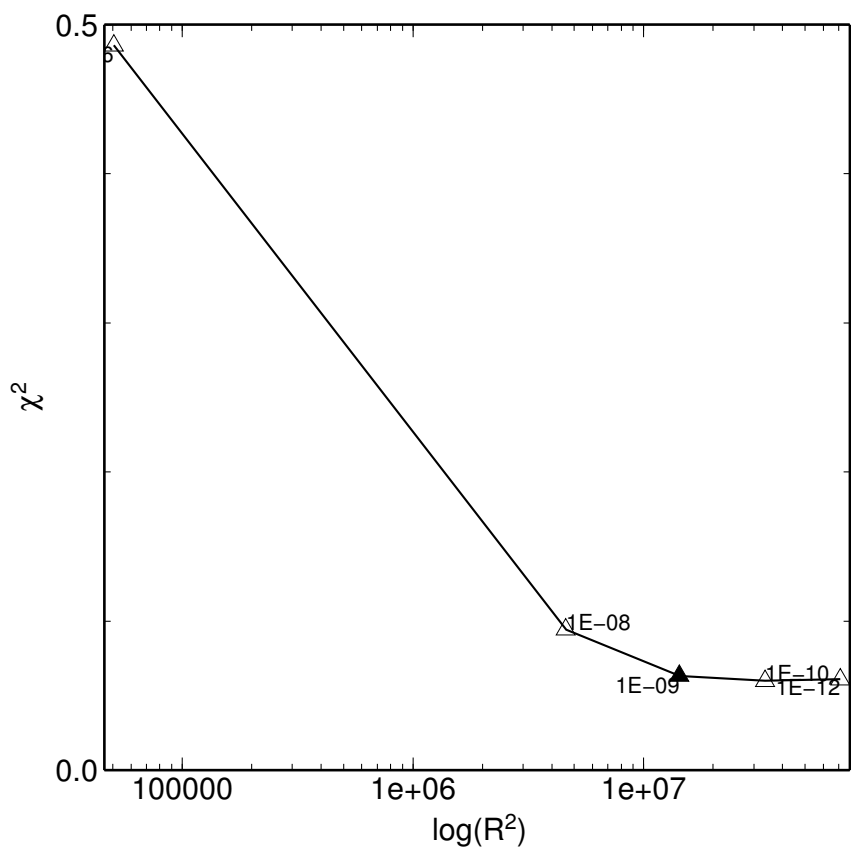


Figure 8.7: Recovery of the realistic conductivity model from original (exact) internal field coefficients by the TD approach. Trade-off between data misfit χ^2 and regularization term R^2 for different regularization parameters λ .

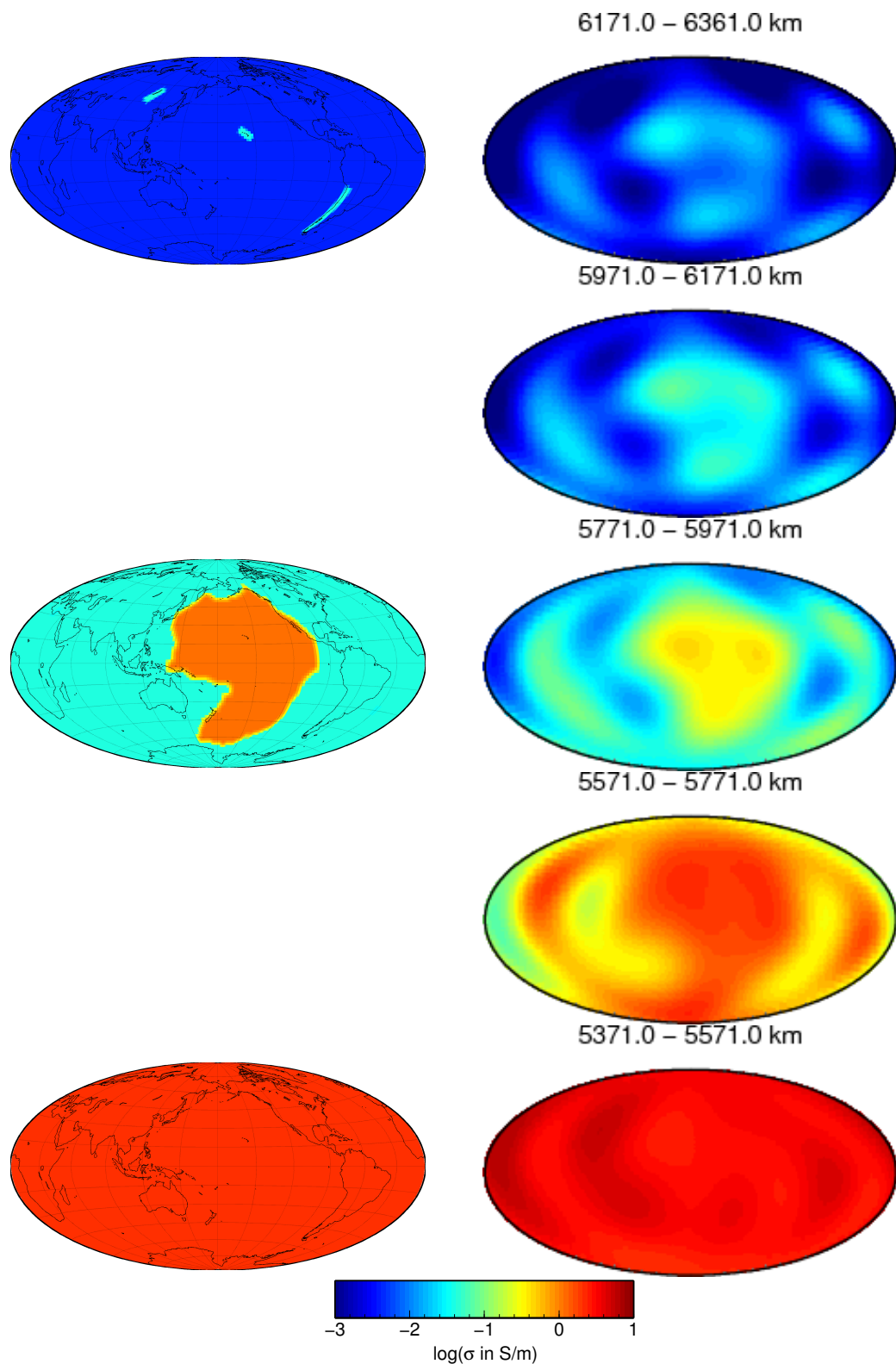


Figure 8.8: Recovery of the realistic conductivity model from original (exact) internal field coefficients by the TD approach. Left column: cross sections of target 3-D model. Thickness of layers top to bottom is 400, 300, and 2191 km, respectively. Right column: cross sections of recovered 3-D model in layers of uniform thickness 200 km.

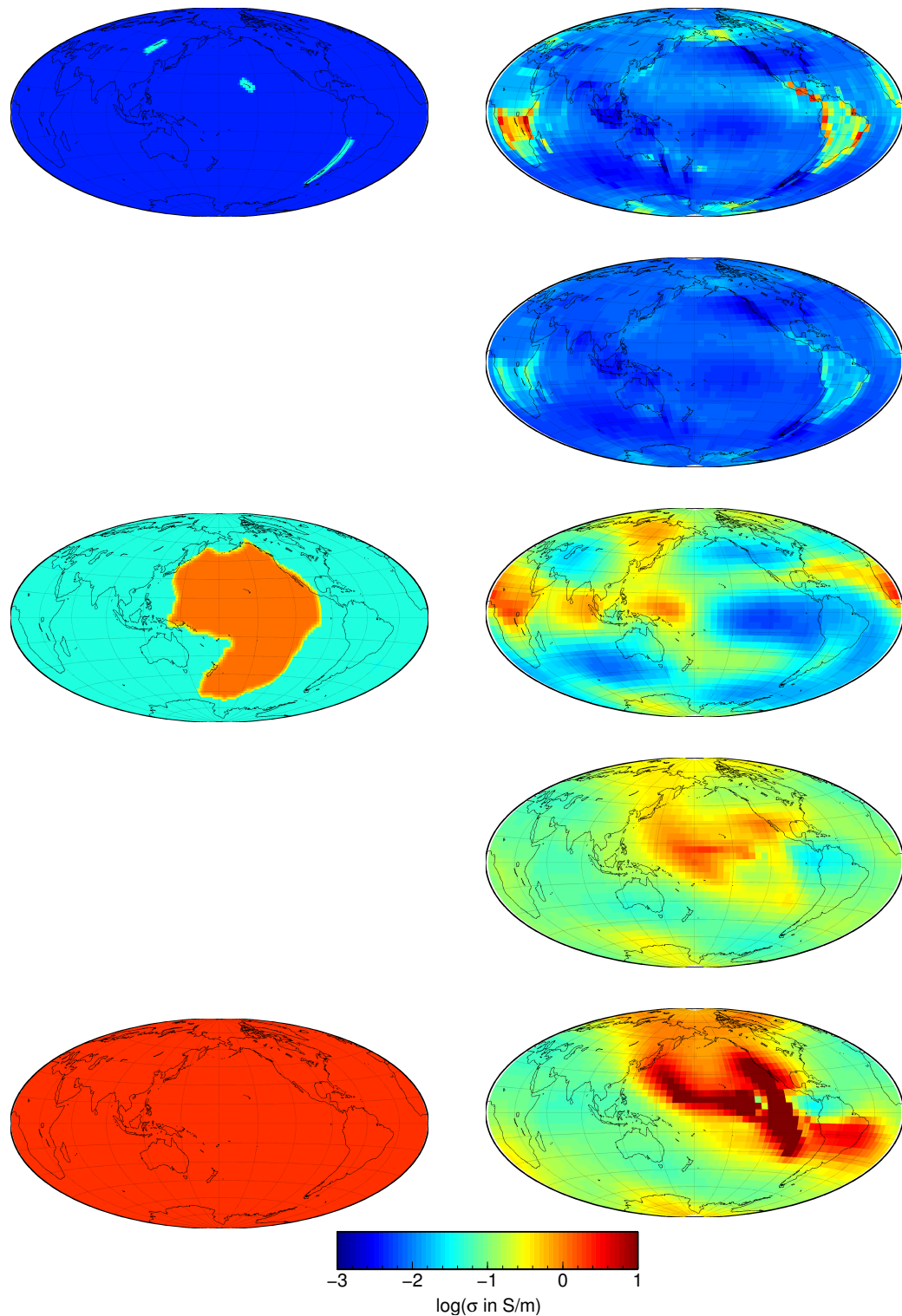


Figure 8.9: Recovery of the realistic conductivity model from “case B” internal field coefficients by the FD approach. Left column: cross sections of target 3-D model. Thickness of layers top to bottom is 400, 300, and 2191 km, respectively. Right column: cross sections of recovered 3-D model in layers of uniform thickness 200 km.

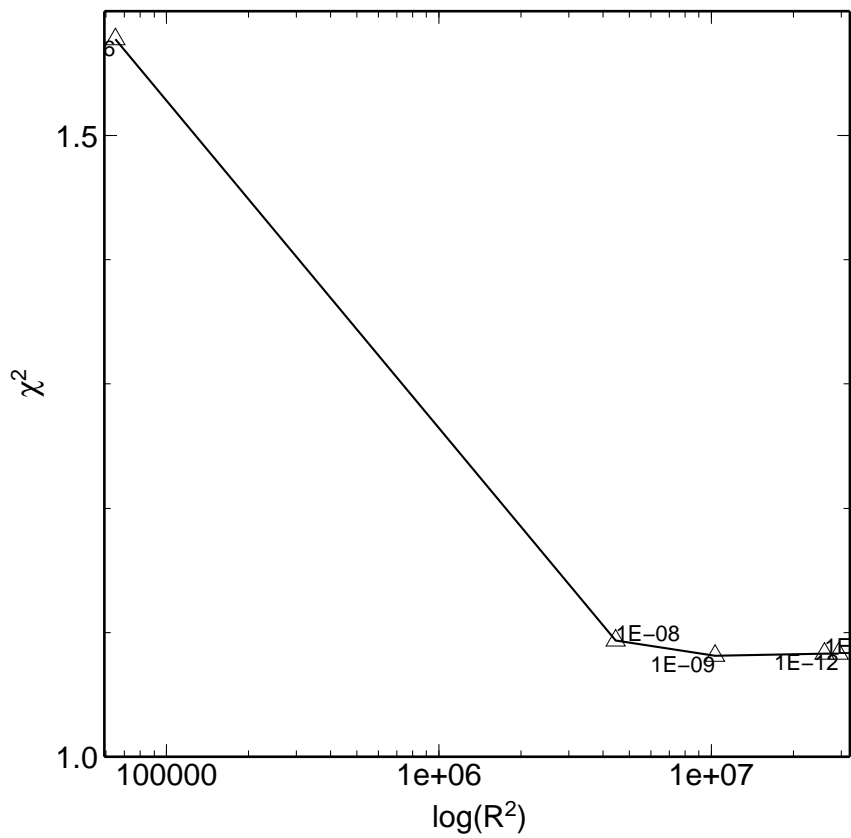


Figure 8.10: Recovery of the realistic conductivity model from “case B” internal field coefficients by the TD approach. Trade-off between data misfit χ^2 and regularization term R^2 for different regularization parameters λ .

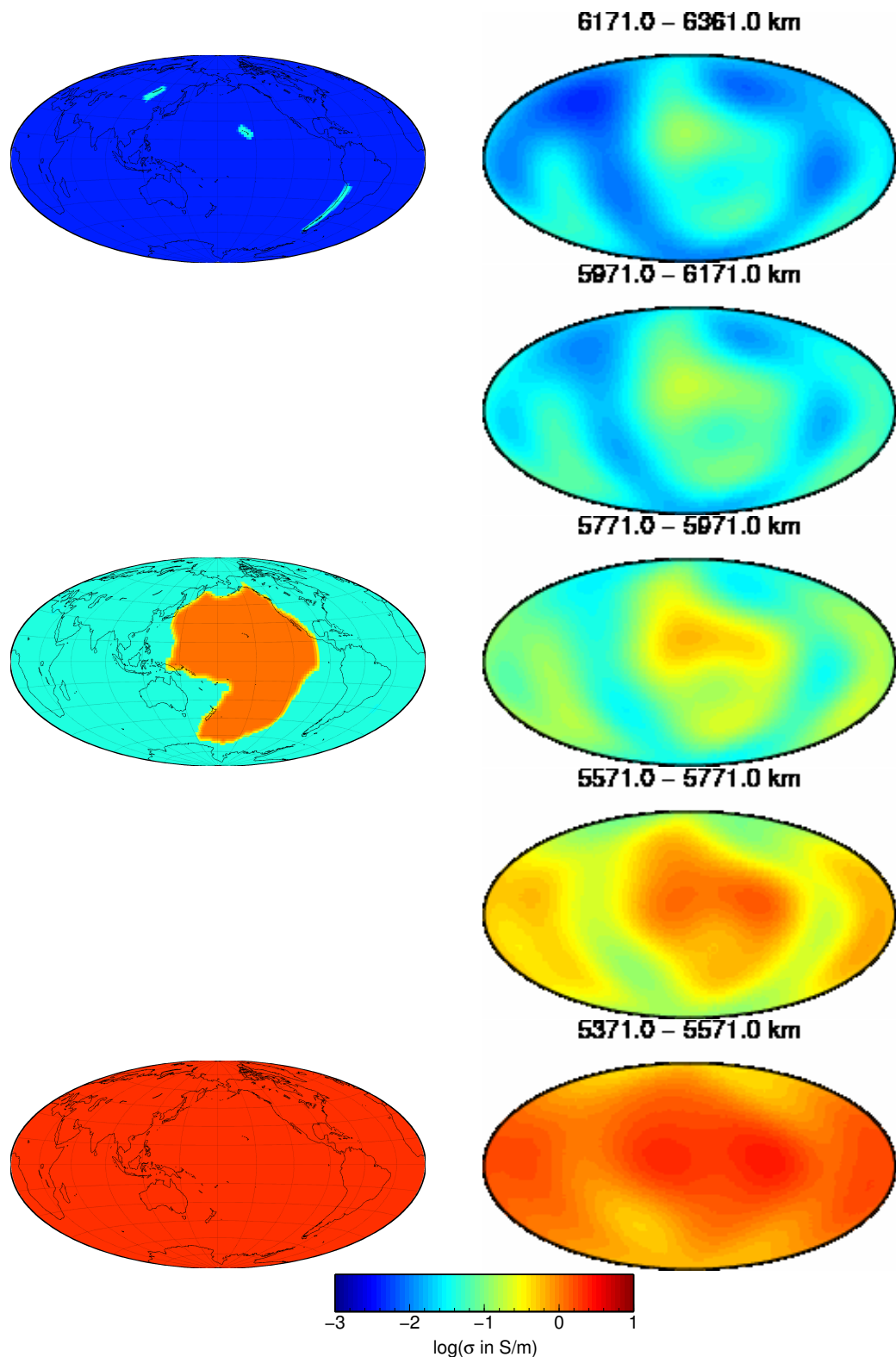


Figure 8.11: Recovery of the realistic conductivity model from “case B” internal field coefficients by the TD approach. Left column: cross sections of target 3-D model. Thickness of layers top to bottom is 400, 300, and 2191 km, respectively. Right column: cross sections of recovered 3-D model in layers of uniform thickness 200 km.

Method/Data set	Idealistic I	Realistic I	Realistic II	Processing time
FD (C-responses inversion)	satisfactory	satisfactory	not tried	moderate
FD (internal coefficients inversion)	good	good	satisfactory	moderate
TD (internal coefficients inversion)	good	good	satisfactory	large (not yet optimized)

Figure 8.12: Summary of 3-D benchmarking inversions.

time series produce results of comparable quality. For realistic data I frequency domain solution seems to perform better, however for realistic data II time domain solution seems to work better. What is also quite clear from the benchmarking results that frequency domain scheme based on analysis of *C*-responses produces less satisfactory 3-D images of the target model.

Chapter 9

Summary of the results and the impact of these results on the proposed Development Plan

9.1 Summary of results

The main objective of the work done in the present and previous studies was to develop inversion algorithms and codes to determine 3-D mantle conductivity from *Swarm* constellation data. Because 3-D induction in a spherical geometry from satellite data was at such a rudimentary stage at the beginning of these studies, the main thrust of the project was to produce a methodology for recovering 3-D electrical conductivity variations. Four alternative approaches have been developed and tested during these studies. Benchmarking of these approaches allows to define one baseline 1-D inversion method and two baseline 3-D inversion methods. In the following we describe these baseline methods and recommend paths for the improvement of them.

9.2 Definition of the baseline 1-D inversion method

Our benchmarking exercises demonstrate that both frequency and time approaches produce results of comparable quality. But bearing in mind that the scientific community is more familiar to work with responses functions rather than directly with the time series, and the fact that *C*-responses will be available as a *Swarm* L2 product, we propose the frequency domain method (based on an analysis of *C*-responses) as the baseline 1-D inversion method.

9.3 Definition of two baseline 3-D inversion methods to be studied further

The results obtained so far are very promising regarding the possibility to determine the 3-D mantle conductivity structure from magnetic field observations. In this study we performed for the first time a full End-to-End simulation starting from synthetic magnetic field observation over the separation of the various source contribution in order to extract time series of magnetospheric (external) and induced spherical harmonic expansion coefficients (Chapter 6) to the inversion of these time series in order to obtain the 3-D mantle conductivity structure (Chapter 8). The obtained results are very promising.

Based on this we propose to concentrate further efforts on a better determination of internal (induced) spherical harmonic expansion coefficients, for instance by inclusion of ground-based observatory mag-



netic field observation in addition to the *Swarm* magnetic data, and on the inversion of these time series in the frequency domain, respectively in the time domain.

Topics that should be further studied within frequency domain approach include an investigation of various schemes for regularizing the inversion, the implementation of a more flexible parameterization of the model, and investigations of the consequences of this.

The most important development needed to fully implement the 3-D time domain method is the enhanced performance by parallelizing the code for distributed memory environment. Currently, with the shared memory setup, solving the inverse problem takes several days of CPU time even at modest spatio-temporal resolution. The parallelization is not trivial due to the nature of the problem (repeated solutions of large, pre-factored linear system with right hand side based on previous time-step). While various blocks of existing code will be reused, the basic structure of the program has to be rewritten with interprocess communication in mind.

Moreover, it will allow to explore in more details the effect of different regularizations and parametrizations (e.g., grid parametrization similar to the one used in the FD methods). Solving the inverse problem in various setups will allow to distinguish robust features of the conductivity model from spurious effects.

Bibliography

- R. C. Aster, B. Borchers, and C. H. Thurber. *Parameter estimation and inverse problems*. Elsevier Academic Press, 2005.
- D. Avdeev, A. Kuvshinov, O. Pankratov, and G. Newman. Three-dimensional induction logging problems, Part I: An integral equation solution and model comparisons. *Geophysics*, 67:413–426, 2002.
- D. B. Avdeev and A. D. Avdeeva. 3D magnetotelluric inversion using a limited-memory quasi-newton optimization. *Geophysics*, 74:45–57, 2009.
- J. Bendat and A. Piersol. Random data: analysis and measurement procedure. *Wiley-Interscience*, 1968.
- R. Blashek, A. Hoerdt, and A. Kemna. A new sensitivity-controlled focusing regularization scheme for the inversion of induced polarization data based on the minimum gradient support. *Geophysics*, 73: 45–54, 2008.
- R. Byrd, P. Lu, J. Nocedal, and C. Zhu. A limited memory algorithm for bound constrained optimization. *SIAM J. Scientific Computing*, 5:1190–1208, 1995.
- S. Constable and C. Constable. Observing geomagnetic induction in magnetic satellite measurements and associated implications for mantle conductivity. *Earth and Planetary Science Letters*, page doi:10.1029/ 2003GC000, 2004.
- S. Constable and G. Heinson. Hawaiian hot-spot swell structure from seafloor MT sounding. *Tectono-physics*, 389:111–124, 2004.
- Y. Dai and Y. Yuan. A nonlinear conjugate gradient method with a strong global convergence property. *SIAM Journal on Optimization*, 10:177–182, 1999.
- O. Dorn, H. Bertete-Aquirre, J. G. Berryman, and G. C. Papanicolaou. A nonlinear inversion method for 3-D electromagnetic imaging using adjoint fields. *Inverse problems*, 15:1523–1558, 1999.
- M. Everett, S. Constable, and C. Constable. Effects of near-surface conductance on global satellite induction responses. *Geophys. J. Int.*, 153:277–286, 2003.
- A. Fichtner, H.-P. Bunge, and H. Igel. The adjoint method in seismology. I. Theory. *Phys. Earth Planet. Int.*, 157:86–104, 2006.
- R. Fletcher and C. M. Reeves. Function minimization by conjugate gradients. *Computer Journal*, 7: 149–154, 1964.
- N. Gillet, A. Jackson, and C. Finlay. Maximum entropy regularization of time-dependent geomagnetic field models. *Geophys. J. Int.*, 171:1005–1016, 2007.

- N. Grammatica and P. Tarits. Contribution at satellite altitude of electromagnetically induced anomalies from a 3-d heterogeneously conducting earth. *Geophys. J. Int.*, 151:913–923, 2002.
- E. Haber. Quasi-newton methods for large-scale electromagnetic inverse problems. *Inverse problems*, 21:305–323, 2005.
- W. W. Hager and H. Zhang. A new conjugate gradient method with guaranteed descent and an efficient line search. *SIAM Journal on Optimization*, 16:170–192, 2005.
- P. Hansen. Analysis of discrete ill-posed problems by means of the L-curve. *SIAM Review*, 34:561–580, 1992.
- G. Jenkins and P. Watts. *Spectral Analysis and its Application*. Holden Day, 1968.
- A. Kelbert, G. Egbert, and A. Schultz. A nonlinear conjugate 3-d inversion of global induction data. resolution studies. *Geophys. J. Int.*, 173:365–381, 2007.
- A. Kuvshinov. 3-d global induction in the oceans and solid Earth: recent progress in modeling magnetic and electric fields from sources of magnetospheric, ionospheric and oceanic origin. *Surveys in Geophysics*, pages doi 10.1007/s10712-008-9045-z, 2008.
- A. Kuvshinov and N. Olsen. New global 1-D conductivity model derived from 5 years of CHAMP, Ørsted, and SAC-C data. In *Proceedings of 1st Swarm meeting*. ESA, 2006a.
- A. Kuvshinov and N. Olsen. 3-D modelling of the magnetic fields due to ocean tidal flow. In C. Reigber, H. Lühr, P. Schwintzer, and J. Wickert, editors, *Earth Observation with CHAMP. Results from Three Years in Orbit*, pages 359–366. Springer Verlag, 2005a.
- A. Kuvshinov and N. Olsen. Modelling the ocean effect of geomagnetic storms at ground and satellite altitude. In C. Reigber, H. Lühr, P. Schwintzer, and J. Wickert, editors, *Earth Observation with CHAMP. Results from Three Years in Orbit*, pages 353–359. Springer Verlag, 2005b.
- A. Kuvshinov and N. Olsen. A global model of mantle conductivity derived from 5 years of CHAMP, Ørsted, and SAC-C magnetic data. *Geophys. Res. Lett.*, 33:L18301, 2006b. doi: doi:10.1029/2006GL027083.
- A. Kuvshinov, T. Sabaka, and N. Olsen. 3-D electromagnetic induction studies using the *Swarm* constellation: Mapping conductivity anomalies in the Earth’s mantle. *Earth, Planets and Space*, 58: 417–427, 2006.
- A. Kuvshinov, C. Manoj, N. Olsen, and T. Sabaka. On induction effects of geomagnetic daily variations from equatorial electrojet and solar quiet sources at low and middle latitudes. *J. Geophys. Res.*, 112 (B10102):doi:10.1029/2007JB004955, 2007.
- A. V. Kuvshinov, D. B. Avdeev, O. V. Pankratov, S. A. Golyshev, and N. Olsen. Modelling electromagnetic fields in 3D spherical Earth using fast integral equation approach. In M. S. Zhdanov and P. E. Wannamaker, editors, *3D Electromagnetics*, chapter 3, pages 43–54. Elsevier, Holland, 2002.
- A. V. Kuvshinov, H. Utada, D. Avdeev, and T. Koyama. 3-D modelling and analysis of Dst C-responses in the North Pacific ocean region, revisited. *Geophys. J. Int.*, 160:505–526, 2005. doi: 10.1111/j.1365-246X.2005.02477.x.
- G. Laske and G. Masters. A global digital map of sediment thickness. *EOS Trans. AGU*, 78:F483, 1997.

- C. Manoj, A. Kuvshinov, S. Maus, and H. Lühr. Ocean circulation generated magnetic signals. *Earth, Planets and Space*, 58:429–439, 2006.
- Z. Martinec. Spectral-finite element approach to three-dimensional electromagnetic induction in a spherical earth. *Geophys. J. Int.*, 136:229–250, 1999.
- Z. Martinec and H. McCreadie. Electromagnetic induction modeling based on satellite magnetic vector data. *Geophys. J. Int.*, 157:1045–1060, 2004.
- S. Maus and A. Kuvshinov. Ocean tidal signals in observatory and satellite magnetic measurements. *Geophys. Res. Lett.*, 31:doi:10.1029/2004GC000634, 2004.
- G. Newman and M. Commer. New advances in three dimensional transient electromagnetic inversion. *Geophys. J. Int.*, 160:5–32, 2005.
- G. A. Newman and D. L. Alumbaugh. Three-dimensional magnetotelluric inversion using non-linear conjugate on induction effects of geomagnetic daily variations from equatorial gradients. *Geophys. J. Int.*, 140:410–424, 2000.
- G. A. Newman and P. T. Boggs. Solution accelerators for large-scale three-dimensional electromagnetic inverse problem. *Inverse problems*, 20:150–170, 2004.
- J. Nocedal and S. J. Wright. *Numerical Optimization*. Springer, 2006.
- R. Nolasco, P. Tarits, J. H. Filloux, and A. D. Chave. Magnetotelluric imaging of the Tahiti Hot Spot. *J. Geophys. Res.*, 103:30287–30309, 1998.
- N. Olsen. Estimation of *C*-responses (3 h to 720 h) and the electrical conductivity of the mantle beneath Europe. *Geophys. J. Int.*, 133:298–308, 1998a.
- N. Olsen. Induction studies with satellite data. *Surveys in Geophysics*, 20:309–340, 1999.
- N. Olsen. Estimation of *C*-responses (3 h to 720 h) and the electrical conductivity of the mantle beneath Europe. *Geophys. J. Int.*, 133:298–308, 1998b.
- N. Olsen and A. Kuvshinov. Modelling the ocean effect of geomagnetic storms. *Earth, Planets and Space*, 56:525–530, 2004.
- N. Olsen, R. Haagmans, T. Sabaka, A. Kuvshinov, S. Maus, M. Purucker, M. Rother, V. Lesur, and M. Mandea. The *Swarm* End-To-End mission simulator study: Separation of the various contributions to earth's magnetic field using synthetic data. *Earth, Planets and Space*, 58:359–370, 2006.
- N. Olsen, T. J. Sabaka, and L. Gaya-Pique. Study of an improved comprehensive magnetic field inversion analysis for *Swarm*. DNSC Scientific Report 1/2007, Danish National Space Center, Copenhagen, 2007.
- O. Pankratov and A. Kuvshinov. General formalism for the efficient calculation of derivatives of EM frequency domain responses and derivatives of the misfit. *Geophys. J. Int.*, *in press*, 2010.
- O. Pankratov, A. Kuvshinov, and D. Avdeev. High-performance three-dimensional electromagnetic modeling using modified Neumann series. Anisotropic case. *J. Geomagn. Geoelectr.*, 49:1541–1547, 1997.

- O. Pankratov, A. Yakovlev, and E. Andreeva. Quasi 3-D inversion: A non-quadratic algorithm in geo-electromagnetic research. In *Abstracts of International conference Tikhonov and contemporary mathematics*. Moscow State University, 2006.
- E. Polyak and G. Ribiere. Note sur la converge de methodes de directions conjugues. *Francaise Informatique et de Recherche Operationelle*, 16:35–43, 1969.
- W. H. Press, B. P. Flannery, S. A. Teukolsky, and W. T. Vetterling. *Numerical Recipes*. Cambridge University Press, Cambridge, 1992.
- W. Rodi and R. L. Mackie. Nonlinear conjugate gradients algorithm for 2-D magnetotelluric inversion. *Geophysics*, 66:174–187, 2000.
- T. J. Sabaka and N. Olsen. Enhancing comprehensive inversions using the *Swarm* constellation. *Earth, Planets and Space*, 58:371–395, 2006.
- U. Schmucker. A spherical harmonic analysis of solar daily variations in the years 1964-1965: response estimates and source fields for global induction-II.Results. *Geophys. J. Int.*, 136:455–476, 1999.
- B. Singer. Method for solution of Maxwell's equations in non-uniform media. *Geophys. J. Int.*, 120: 590–598, 1995.
- A. Tarantola. *Inverse problem theory and methods for model parameter estimation*. SIAM, Philadelphia, 2005.
- P. Tarits. Preliminary investigation of the Oersted data for induction studies. In *Proceedings of Oersted 3rd international Science Team meeting*. 2000.
- P. Tarits and M. Menvielle. Study of an anomalous magnetic field of intralithospheric origin. *Can. J. Earth Sci.*, 20:537–547, 1983.
- P. Tarits, J. Wahr, and P. Lognonne. Influence of conductivity heterogeneities at and near the CMB on the geomagnetic secular variation. In *Proceedings of AGU Fall meeting*. 1998.
- L. Tøffner-Clausen, T. J. Sabaka, and N. Olsen. End-to-end mission simulation study (e2e+). In *Proceedings of the Second International Swarm Science Meeting*. ESA, 2010.
- J. Velímský and Z. Martinec. Time-domain, spherical harmonic-finite element approach to transient three-dimensional geomagnetic induction in a spherical heterogeneous earth. *Geophys. J. Int.*, 160: 81–101, 2005.
- P. Weidelt. The inverse problem of geomagnetic induction. *Z. Geophys.*, 38:257–289, 1972.
- S.-L. Zhang. GPBi-CG: generalized product-type methods based on Bi-CG for solving nonsymmetric linear systems. *SIAM J. Sci. Comput.*, 18:537–551, 1997.